INVESTIGATION OF MAGNETOELASTIC COUPLING IN MULTIFERROIC GEOMETRICALLY FRUSTRATED MAGNETS: $CuFeO_2$, $CuCrO_2$, AND $CuCrS_2$
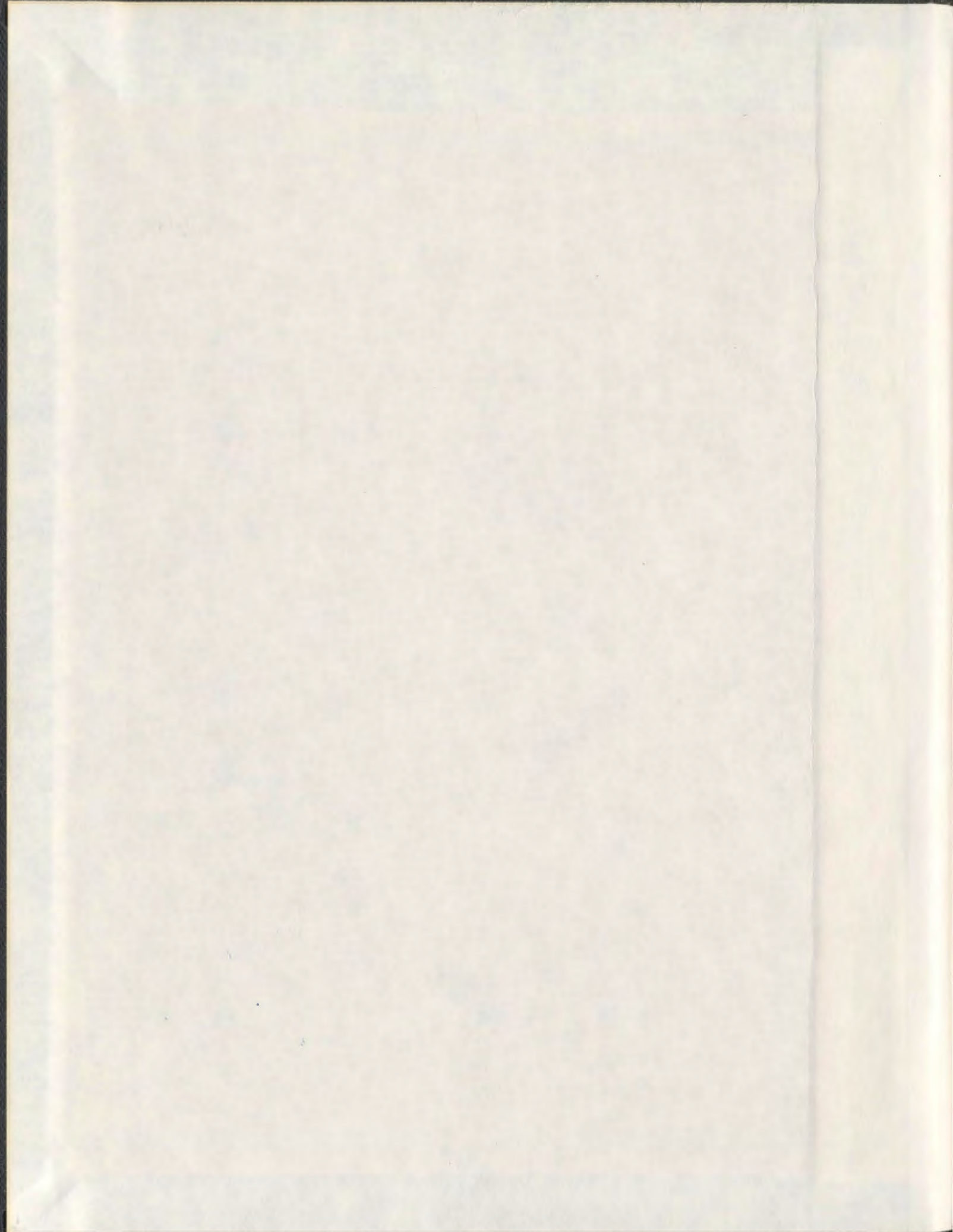
OKTAY AKTAS

Investigation of magnetoelastic coupling in multiferroic geometrically frustrated magnets: $CuFeO_2$, $CuCrO_2$, and $CuCrS_2$

by

© Oktay Aktas
M.Sc. in Physics

A thesis submitted to the
School of Graduate Studies
in partial fulfillment of the
requirements for the degree of
Doctor of Philosophy.

Department of Physics and Physical Oceanography
Memorial University of Newfoundland

November 14, 2012

ST. JOHN'S   NEWFOUNDLAND

Contents

Abstract

Elastic and structural properties of triangular lattice antiferromagnets $CuCrO_2$, $CuFeO_2$, and $CuCrS_2$ were investigated to elucidate the role played by spin-phonon coupling in the magnetic and multiferroic properties of a large class of triangular lattice antiferromagnets.

Using Brillouin scattering, five of six elastic constants of $CuCrO_2$ are determined at room temperature. Low temperature elastic properties of $CuCrO_2$ are extensively investigated with the ultrasonic pulse echo method. According to these measurements, the elastic constants C_{11}, C_{44}, and C_{66} show softening as the temperature is reduced down to the antiferromagnetic transition temperature $T_{N1} = 24.3$ K. The Landau analysis of the ultrasonic data indicates a first order pseudoproper ferroelastic transition at T_{N1}, where magnetic moments can act as a secondary order parameter. The transition corresponds to a structural change from the tetragonal point group $\bar{3}m$ to the monoclinic point group $2/m$. In addition, the symmetry lowering at T_{N1} seems to aid the spin-driven ferroelectricity below $T_{N2} = 23.8$ K, at which the crystal symmetry should change from $2/m$ to 2. The existence of T_{N2} is confirmed by simultaneous measurements of the dielectric constant $\epsilon_{[110]}$ and acoustic modes.

Unlike $CuCrO_2$, isostructural $CuFeO_2$ seems to show a second order $\bar{3}m \rightharpoonup 2/m$ ferroelastic transition coincident with the antiferromagnetic transition at $T_{N1} = 14$ K [1]. In order to confirm if the transition is second order, Brillouin scattering measurements were performed on $CuFeO_2$. Due to the opacity of $CuFeO_2$, Brillouin spectra show only surface acoustic modes for waves propagating in the xy and xz planes. The velocity of the modes

depends on the elastic constants C_{44} and C_{33}.

Raman measurements were performed to possibly determine if the ferroelastic transitions at T_{N1} in $CuFeO_2$ and $CuCrO_2$ and the $R3m \rightharpoonup Cm$ structural and antiferromagnetic transition at $T_N = 38$ K in another geometrically frustrated magnet, $CuCrS_2$, are driven by a soft optic mode. Based on these measurements, the temperature dependencies of all modes in $CuCrO_2$, $CuFeO_2$ and $CuCrS_2$ are attributed to anharmonic phonon-phonon interactions. Therefore, Raman modes in $CuCrO_2$ and $CuFeO_2$ cannot account for the ferroelastic transitions observed at T_{N1}, leaving the driving mechanism of the ferroelastic transitions uncertain. Similarly, measurements on $CuCrS_2$ does not reveal any soft optic modes.

Finally, simultaneous measurements of the dielectric constant and acoustic velocities of $CuCrO_2$ were performed to determine the magnetic phase diagram of $CuCrO_2$ for magnetic fields along the [110] and [1$\bar{1}$0] directions (hexagonal setting). For magnetic fields parallel to the [1$\bar{1}$0] direction the dielectric constant and acoustic modes show an anomaly at $H_{flop} \sim 5$ T between 2 K and 23.7 K, which correspond to a 90° flop in the spin-spiral plane and electric polarization. The anomaly observed in the longitudinal acoustic mode propagating in the basal plane is attributed to the field dependence of magnetic susceptibility. Measurements performed with magnetic fields parallel to the [110] direction suggest a reorientation in the spin-spiral plane.

The ferroelastic transition, coincident with the antiferromagnetic transition at T_{N1} in $CuCrO_2$ as well as acoustic anomalies at the spin flop transition clearly indicate that magnetoelastic coupling has a strong impact on the magnetic and multiferroic properties of $CuCrO_2$. For a complete understanding of the role of magnetoelastic coupling on these properties in $CuCrO_2$ and a large class of triangular lattice antiferromagnets, results on the ultrasonic velocity measurements on $CuCrO_2$ have to be analyzed using a Landau model that includes magnetoelastic coupling terms as well as the coupling between the order parameter

and magnetic moments.

Acknowledgements

I would like to express my sincere appreciation to my supervisor Dr. Guy Quirion for his guidance throughout the course of this project. I would also like to thank him for sharing his expertise in acoustic velocity measurements and helpful discussions.

I am grateful to Dr. Maynard Clouter for allowing me to do Raman and Brillouin scattering measurements in his lab and sharing his expertise in optical spectroscopy.

I would like to acknowledge the generosity of Dr. Tsuyoshi Kimura and Tsuyoshi Otani at Osaka University, Japan for providing $CuCrO_2$ samples, Geetha Balakrishnan at the University of Warwick, England for providing $CuFeO_2$ samples, and Dr. Julia C. E. Rasch previously at ETH Zurich, currently at VDI/VDE Innovation and Technology GmbH, Germany for providing $CuCrS_2$ samples. This project was possible because they kindly provided the samples. I would like to thank Dr. Kim Doan Truong at the University of Sherbrooke for performing Raman scattering measurements using a HeNe laser and Dr. Sergei Jandl for providing his Raman facilities for these measurements at the University of Sherbrooke.

I am thankful to Lance Parsons and Dr. Todd Andrews for fruitful discussions on Brillouin scattering experiments. My special thanks are to Wayne Holly, who provided me with helium and nitrogen for low temperature measurements, Fred Perry for assisting me with software problems and Gordon Whelan for making parts for the experimental setups.

I appreciate the staff members of the Department of Physics and Physical Oceanography. I am especially thankful to Mrs. Joy Simmons for the official letters she wrote for my study

permit, visa and work permit.

I would like to express my gratitude to Carla for her patience, support, and encouragement during the writing of my thesis. Finally, I would like to sincerely express my indebtedness to my family. They have encouraged my academic career and shown unparalleled support. They have been a strong foundation both personally and professionally. They will continue to inspire me as I continue with the next step of my academic career.

I dedicate this thesis to my family.

List of Tables

List of Figures

xvi

xvii

Chapter 1

Introduction

In the past 20 years, multiferroics have received considerable attention due to their fundamental magnetic and electric properties, as well as their potential applications. A material is called multiferroic if it simultaneously possesses two or more of the ferroic properties: ferromagnetism (or antiferromagnetism), ferroelectricity, and ferroelasticity [6]. Ferroelectrics and ferroelastics are electric and mechanical analogs of ferromagnets. For example, a ferroelastic material is defined as a material in which structural domains can be ordered or switched by the application of homogeneous stress [7]. Similarly, in a ferroelectric material, ferroelectric domains can be aligned by the application of an electric field. Combining two or all of these ferroic properties in one material, as in multiferroics, brings about rich fundamental physics. Particularly, coupling between magnetic and electric properties (magnetoelectric coupling) makes these materials promising candidates for potential applications such as in data storage devices [8, 9, 10, 11]. For example, magnetoelectric coupling can be used to design multistate memory devices with electrical writing and nondestructive magnetic reading operations [12]. Early discoveries of multiferroics included $BiFeO_3$, $YMnO_3$, and $BiMnO_3$ [13]. In these materials, ferroelectricity and antiferomagnetism coexist, however, ferroelectricity appears at much larger temperatures than magnetism because these two

1

properties appear independently of each other, which leads to weak magnetoelectric coupling [13]. These materials are classified as type-I multiferroics [10].

Recently, in a new class of magnetoelectric multiferroics, called type-II multiferroics, it was discovered that a ferroelectric polarization is induced upon the emergence of a magnetic ordering [14, 8]. As a result, the magnetic and electric properties are strongly coupled, making possible the electrical control of the magnetic properties, and vice versa [13, 15, 16]. Generally speaking, type-II multiferroics can be divided into 2 groups based on the microscopic mechanism of the multiferroic behavior [10]: materials in which ferroelectricity appears as a result of a spiral spin order through spin-orbit interaction, and those in which ferroelectricity appears in collinear magnetic structures through exchange striction [10]. Before explaining the microscopic mechanism of type-II multiferroics, we illustrate the relevant magnetic orders in Fig. 1.1. The direction of the expected electric polarization $\mathbf{P}$ for each magnetic order is depicted with thick arrows, whereas the direction of magnetic modulation (i.e. magnetic propagation vector) is represented by $\mathbf{q_m}$. If $\mathbf{S}_i$ and $\mathbf{S}_j$ are two neighboring spins on sites i and j, for spiral magnetic orders the cross product of the two spins, $\mathbf{S}_i \times \mathbf{S}_j$, defines the direction of the spin rotation axis. If the spin rotation axis is perpendicular to the propagation vector $\mathbf{q_m}$, the resulting magnetic order is called a cycloidal spiral structure, shown in Fig. 1.1a [15]. If the spin rotation axis is parallel to the propagation vector $\mathbf{q_m}$, then the magnetic order (Fig. 1.1c) is called a proper screw spiral structure. In Fig. 1.1b, we also show a collinear spin order in which magnetic moments are parallel (or antiparallel) to their nearest neighbors.

In the first group of type-II multiferroics, a cycloidal spiral spin order (Fig. 1.1a) as in $TbMnO_3$ [14] and $DyMnO_3$ [17] induces ferroelectric polarization $\mathbf{P}$ through the inverse Dzyaloshinskii-Moriya (DM) interaction [18, 19] such that

$$\mathbf{P} = \mathbf{e}_{ij} \times (\mathbf{S}_i \times \mathbf{S}_j), \tag{1.1}$$

2
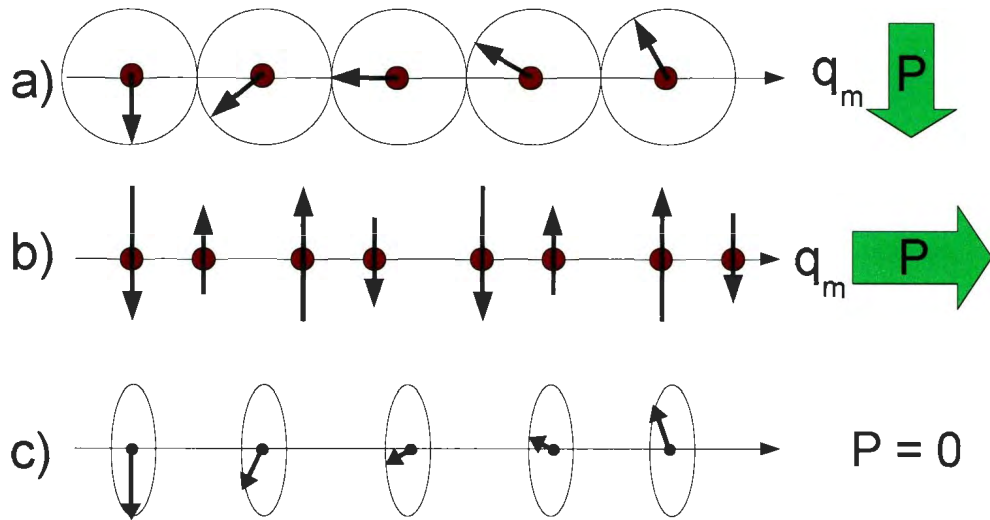
Figure 1.1: Schematic illustrations of spiral and collinear magnetic orders and induced electric polarization: **(a)** Cycloidal spin order where the propagation vector is perpendicular to the spin rotation axis can give rise to polarization through inverse DM interaction. **(b)** 4-sublattice collinear spin configuration can give rise to electric polarization $\mathbf{P}$ in the direction of the modulation vector $\mathbf{q_m}$. Collinear spin order can induce electric polarization through exchange striction. **(c)** Proper screw spiral structure in which the spin rotation axis is parallel to the modulation vector.

where $\mathbf{e}_{ij}$ is a unit vector connecting two magnetic moments $\mathbf{S}_i$ and $\mathbf{S}_j$ parallel to the propagation vector of the cycloid structure, $\mathbf{q_m}||\mathbf{e}_{ij}$. In this case, the induced polarization is perpendicular to both the propagation vector $\mathbf{q_m}$ and spin rotation axis $\mathbf{S}_i \times \mathbf{S}_j$ (see Fig. 1.1a). In these materials, due to the correlation between the electric and magnetic degrees of freedom, the spontaneous polarization can be controlled by an external magnetic field [14]. In TbMnO$_3$, Kimura *et al.* [14] experimentally observed a 90° flop of the electric polarization by applying a magnetic field between 5 T and 9 T along a direction parallel to the cycloidal plane.

In the second group of type-II multiferroics, an electric polarization is induced by a collinear spin order through exchange striction (Fig. 1.1b) [10]. In the collinear ↑↑↓↓ magnetic state of frustrated magnets such as Ca$_3$Co$_{2-x}$Mn$_x$O$_6$ [20] and DyFeO$_3$ [21], the exchange striction coupling pulls parallel spins toward each other and pushes away antiparallel spins, breaking the inversion symmetry and producing an electric polarization in the direction of the magnetic modulation. Microscopically, the local electric polarization is given by [22]

$$\mathbf{P} = \mathbf{p}_0(r)\ \mathbf{S}_i \cdot \mathbf{S}_j, \tag{1.2}$$

where the prefactor $\mathbf{p}_o(\mathbf{r})$ depends on the local structure and exists only when the inversion center between sites i and j is absent [2]. Since the spatial average of $\mathbf{p}_o(\mathbf{r})$ is zero in centrosymmetric materials, ferroelectric polarization can be induced by exchange striction only when the modulation in $\mathbf{S}_i \cdot \mathbf{S}_j$ is commensurate with respect to the lattice [2].

It is important to note that multiferroics in which ferroelectricity is driven by a collinear spin order are rarely discovered [13, 23, 24]. In general, most spin driven multiferroics have a spiral magnetic order (Fig. 1.1a) in the multiferroic state [13, 15, 16]. By using simple symmetry arguments, we can explain how a spiral spin order can induce ferroelectricity. The electric polarization $\mathbf{P}$ changes sign on the spatial inversion ($\mathbf{r} \longrightarrow$ -$\mathbf{r}$) but remains invariant on time reversal ($t \longrightarrow -t$). The magnetization $\mathbf{M}$ transforms in the opposite
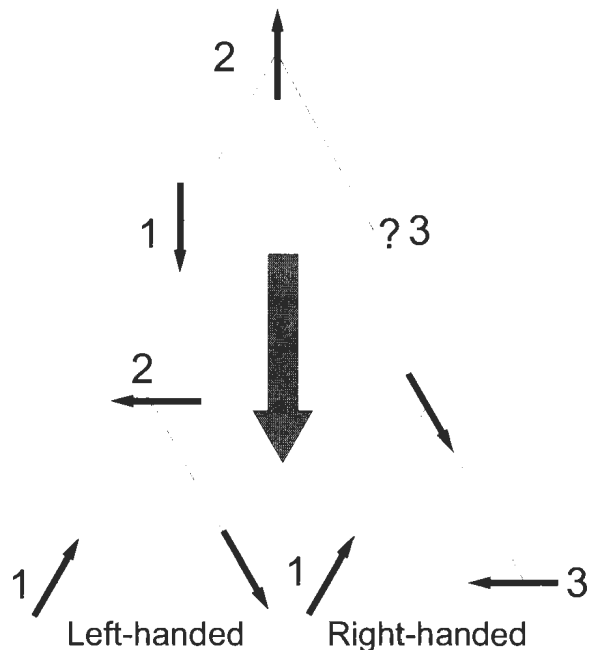
Figure 1.2: Geometrical frustration in a triangular lattice antiferromagnet.

way. While it remains invariant on spatial inversion, it changes sign on time reversal. Like any magnetic order, a spiral magnetic order breaks times reversal symmetry ($t \longrightarrow -t$). In addition, it also breaks spatial inversion symmetry, because upon the application of the spatial inversion, the direction of the rotation of spins in the spiral plane is inverted. Thus, in a material in which spins form a spiral order, an electric polarization is allowed [13]. This makes geometrically frustrated magnets ideal systems for spin-driven ferroelectricity, because geometrically frustrated magnets naturally favor noncollinear magnetic orders as discussed below.

Geometrical frustration occurs on a triangular lattice such as shown in Fig. 1.2. In Fig. 1.2, magnetic moments (spins) 1 and 2 on the triangular lattice are aligned antiparallel to each other. However, the third magnetic moment cannot be aligned simultaneously antiparallel to the other two magnetic moments. Therefore, in order to remove this ambiguity,

the spins adopt a 120° spin configuration and lift the magnetic frustration. In a 120° spin structure, neighboring spins are at 120° to each other and the magnetic propagation constant is $q_m = \frac{1}{3}$. Depending on the sign of the single-ion anisotropy term D in the Hamiltonian $H' = -DS_z^2$, there are two types of 120° spin structures. For $D < 0$, the energy of the system is minimized when the spiral plane is perpendicular to the triangular lattice plane (easy-axis type). For $D > 0$, however, the spiral plane is parallel to the triangular lattice plane (easy-plane type) [16]. Moreover, the spin chirality results in two possible chiral domains, left-handed and right-handed, which leads to additional degeneracy in the ground state. This geometrical frustration leads to a large number of complex spin configurations that occur at low temperatures.

1.1 Motivation

Recently, ferroelectricity was observed in several members of geometrically frustrated magnets with the formula ABO_2. In this chemical formula, A is a nonmagnetic monovalent ion such as Cu, Ag, or Li, whereas B is a magnetic trivalent ion such as Fe or Cr. In ABO_2 compounds, geometrical frustration is due to their trigonal $R\bar{3}m$ symmetry, which leads to interesting spin configurations at low temperatures [3, 25]. Additional studies on $CuFeO_2$, $CuCrO_2$, and $AgCrO_2$ [26, 27, 28] show that an electric polarization $\mathbf{P} \| [110]$ is only induced upon the emergence of a proper-screw spin order (Fig. 1.1). Under this scenario, the usual inverse Dzyaloshinskii-Moriya (DM) interaction $\mathbf{P} \sim \mathbf{r}_{ij} \times (\mathbf{S}_i \times \mathbf{S}_j)$ [18, 19] cannot account for the induced polarization because the propagation vector of the spin modulation is parallel to the spin rotation axis (see Eq. 1.1). Exchange striction (Eq. 1.2) cannot account for the induced polarization either as the magnetic modulation vector in proper screw spirals is incommensurate [2]. An alternative possibility, proposed by Arima et $al.$ [2], is that the polarization is induced by the variation of the metal-ligand hybridization. However,

6

ferroelectricity observed in rhombohedral AgCrS$_2$ upon a helical spin order suggests that there might be other mechanisms that are also responsible for the induced ferroelectricity in these triangular lattice antiferromagnets [29]. This is because the rhombohedral $3m$ point group symmetry ($R3m$ space group) of AgCrS$_2$, as opposed to centrosymmetric $\bar{3}m$ ($R\bar{3}m$) symmetry implies differences in the cation-anion-cation orbital hybridization and thus in the magnetic exchanges [29]. Therefore, even though CuFeO$_2$ and CuCrO$_2$ represent spin-driven ferroelectrics, the mechanism leading to magnetoelectric coupling in these compounds is still uncertain. In the case of CuFeO$_2$, it is pointed out that spin-lattice coupling is crucial in the stabilization of the magnetic states at zero field [1, 30, 31, 32]. At $T_{N1} = 14$ K, an $R\bar{3}m \rightarrow C2/m$ structural transition occurs in coincidence with an antiferromagnetic transition [30]. More importantly, sound velocity measurements and the analysis with a Landau model show strong evidence for an $R\bar{3}m \rightarrow C2/m$ ferroelastic transition at T_{N1}, indicating that the magnetic transitions are stabilized by ferroelastic deformations [1, 31]. Thus, understanding the elastic properties of CuFeO$_2$ and CuCrO$_2$ might help to elucidate the role played by the spin-lattice coupling in the magnetic and magnetoelectric properties of this class of frustrated systems. The comparison between these two isostructural compounds is particularly relevant as their magnetic ground states are different. While CuCrO$_2$ shows the magnetoelectric multiferroic behavior in its ground state below $T_{N2} = 23.6$ K [26, 27], CuFeO$_2$ goes into this state under a magnetic field applied along the c axis [28]. Therefore, we further investigated the ferroelastic transition at T_{N1} in CuFeO$_2$ and extensively studied the elastic properties of CuCrO$_2$.

In the case of CuFeO$_2$, according to the Landau model [1] the transverse acoustic mode propagating along the x axis with a polarization along the y axis, $T_x P_y$, should show complete softening at T_{N1}. The temperature dependence of this mode, based on ultrasonic velocity measurements [1] is depicted in Fig. 1.3 with continuous lines whereas the prediction of the model is shown with a dashed line. As shown in Fig. 1.3, due to large acoustic attenuation,
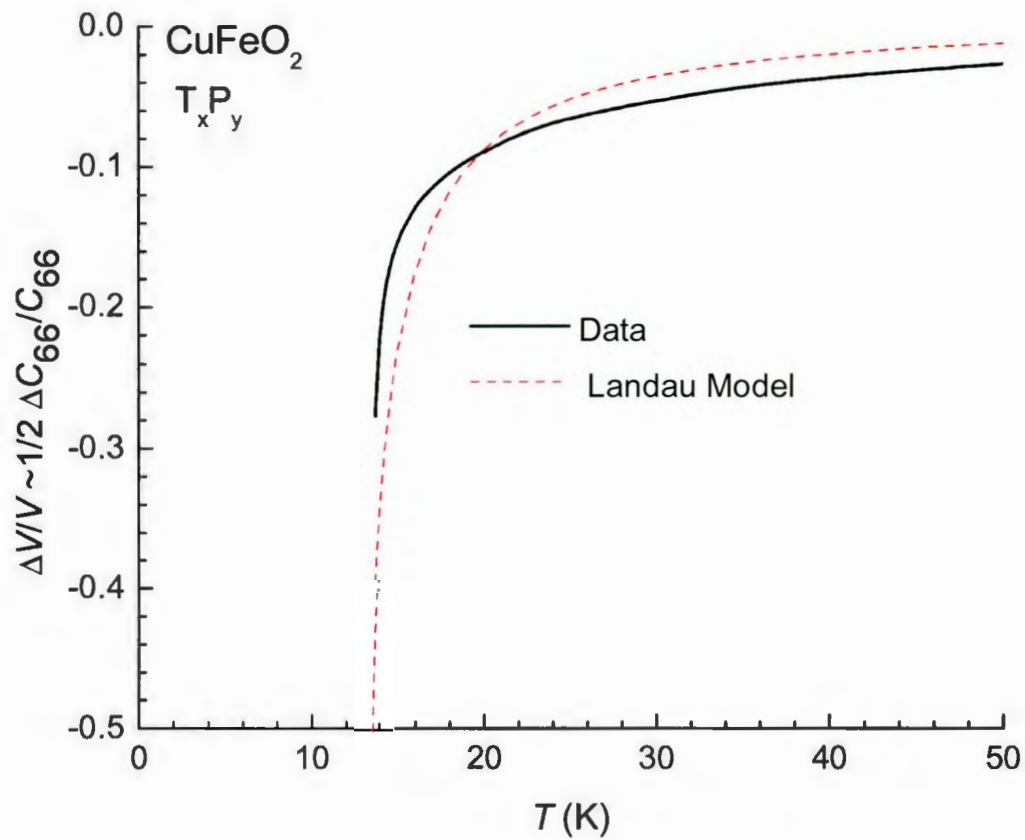
Figure 1.3: Relative velocity variation of the soft acoustic mode $T_x P_y$ in $CuFeO_2$ as a function of temperature. Reprinted figure with permission from [G. Quirion, M. J. Tagore, M. L. Plumer, O. A. Petrenko, Phys. Rev. B **77**, 094111 (2008)]. Copyright (2008) by the American Physical Society

the complete softening on the transverse mode $T_x P_y$ could not be observed. Therefore, we performed Brillouin scattering measurements on $CuFeO_2$ to determine if this mode shows complete softening. Brillouin scattering was performed for the first time on this compound to probe the elastic properties.

For $CuCrO_2$, magnetostriction measurements show evidence for structural deformations at $T_{N1} = 24.3$ K, coincident with an antiferromagnetic transition [33]. Considering that $CuCrO_2$ is isostructural to $CuFeO_2$ at room temperature, $CuCrO_2$ might also undergo a ferroelastic transition at T_{N1}. However, the elastic properties of $CuCrO_2$ are lacking in the literature. Thus, in order to possibly determine ferroelasticity in $CuCrO_2$, we investigated the elastic properties of $CuCrO_2$ using the ultrasonic pulse-echo method as a function of temperature. In addition, for comparison we performed Brillouin scattering measurements down to 30 K. For further investigation of magnetoelastic coupling, as well as magnetic and multiferroic properties in $CuCrO_2$, we performed ultrasonic velocity and dielectric measurements under a magnetic field parallel to the $[1\bar{1}0]$ and $[110]$ directions. With these measurements, we also determined the magnetic field vs temperature phase diagram of $CuCrO_2$ for fields applied along the $[1\bar{1}0]$ and $[110]$ directions.

According to group theory [34], the order parameter of an $R\bar{3}m \rightharpoonup C2/m$ ferroelastic transition belongs to the E_g irreducible representation of the trigonal $R\bar{3}m$ space group. Even though ferroelasticity below T_{N1} in $CuFeO_2$ is confirmed with ultrasonic velocity measurements [1], the order parameter of the ferroelastic transition is still not known. If the order parameter is the spontaneous strains, the transition is called a proper ferroelastic transition and the elastic constants show a linear temperature dependence [35, 36, 37]. Due to the nonlinear temperature dependence of the acoustic modes in $CuFeO_2$ (Fig. 1.3) [1], the transition is identified as pseudoproper ferroelastic, which means that the order parameter is not the spontaneous strains but has the same symmetry properties [1, 35]. In this case, bilinear coupling between the order parameter and the spontaneous strains gives rise to complete

softening on the soft acoustic mode associated with the spontaneous strains. For $CuFeO_2$, one would expect that the magnetic moments could be associated with the order parameter, however, bilinear coupling between the magnetic moments and strains is not allowed due to time reversal symmetry. One possibility is that the transition is driven by a Raman-active E_g mode as in other pseudoproper ferroelastic materials [5, 38, 39, 40]. Thus, we performed Raman scattering measurements on $CuFeO_2$ and $CuCrO_2$ to test this possibility. While unpolarized Raman scattering measurements on $CuFeO_2$ were performed between 80 K and 400 K [41], measurements investigating the antiferromagnetic and structural transition at low temperatures are still lacking. In the case of $CuCrO_2$, only room temperature Raman measurements on polycrystals have been reported [42, 43, 44, 45]. Thus, our Raman measurements represent the first polarized Raman investigation of both $CuFeO_2$ and $CuCrO_2$ as well as the first investigation of phonon behavior at low temperatures. Results were recently published [46].

In order to expand our study to a larger class of geometrically frustrated systems, we also studied $CuCrS_2$ which belongs to the trigonal $R3m$ space group at room temperature [47, 48]. $CuCrS_2$ is possibly a spin-driven ferroelectric material, as in the sister compound $AgCrS_2$ a ferroelectric polarization is induced upon a helical magnetic ordering below T_N = 38 K [29]. Similar to $CuFeO_2$ [1] and possibly $CuCrO_2$ [33], $CuCrS_2$ and $AgCrS_2$ undergo an $R3m \rightarrow Cm$ structural transition at the antiferromagnetic transition temperature $T_N \sim 40$ K, indicating a strong magnetoelastic coupling [29, 47, 48]. According to the Aizu classification of ferroic materials [7, 49], an $R3m \rightarrow Cm$ structural transition can be ferroelastic and simultaneously ferroelectric. Thus, $CuCrS_2$ is an ideal compound to study the role of magnetoelastic coupling in the magnetic and multiferroic properties of geometrically frustrated magnets. Unfortunately, due to the opacity and the platelet structure of $CuCrS_2$ samples, which made it difficult for sample preparation for measurements in the x and y axes, we could not perform ultrasonic velocity and Brillouin scattering measurements on

10

this compound. However, we were able to perform Raman scattering measurements to determine if the order parameter of the $R3m \rightharpoonup Cm$ structural transition is associated with an E symmetry optical mode [34, 50]. Raman measurements were previously performed on single crystals of $CuCrS_2$ down to 80 K [51]. As a result, our measurements provide Raman data lacking at low temperatures.

1.2 Thesis outline

This thesis consists of 10 chapters. In Chapter 2, the topic of discussion is the main structural and ferroic properties of $CuFeO_2$, $CuCrO_2$, and $CuCrS_2$. Chapter 3 is devoted to the optical indicatrix for uniaxial crystals and theory of inelastic light scattering, where Brillouin and Raman scattering are discussed in detail. In Chapter 4, the theory of static and dynamic elasticity is discussed. The solutions of Christoffel's equation for the trigonal $\bar{3}m$ point group are also given. Chapter 5 provides a detailed description of the experimental setups for the ultrasonic pulse echo method, dielectric measurements, and Brillouin and Raman scattering. In Chapter 6, Brillouin scattering measurements on $CuFeO_2$ and $CuCrO_2$ are presented. Brillouin measurements on both $CuFeO_2$ and $CuCrO_2$ were performed at room temperature and low temperatures. With the room temperature measurements on $CuCrO_2$, the elastic constants and refractive indices of $CuCrO_2$ were determined. In Chapter 7, the elastic properties of $CuCrO_2$ obtained using the ultrasonic pulse-echo method are presented. In addition, the magnetic phase diagram of $CuCrO_2$ is determined for fields parallel to the $[1\bar{1}0]$ and $[110]$ directions based on the simultaneous measurements of the ultrasonic velocities and the dielectric constant along the x axis ϵ_x ($\epsilon_{[110]}$ in hexagonal setting). Chapter 7, a comparison of the elastic properties of $CuCrO_2$ obtained using the ultrasonic pulse-echo method and Brillouin scattering is also made. In Chapter 8, a Landau model that accounts for the elastic properties of $CuCrO_2$ is presented. In Chapter 9, Raman scattering measurements

on $CuFeO_2$, $CuCrO_2$, and $CuCrS_2$ as a function of temperature are presented. Finally, a summary and conclusions are made in Chapter 10.

Chapter 2

Properties of CuFeO$_2$, CuCrO$_2$, and CuCrS$_2$

In this chapter, we present the main structural and ferroic properties of CuFeO$_2$, CuCrO$_2$, and CuCrS$_2$.

2.1 CuFeO$_2$ and CuCrO$_2$

CuFeO$_2$ and CuCrO$_2$ crystallize into the delafossite ($R\bar{3}m$) structure at room temperature with the lattice constants $a = b = 3.03$ Å, $c = 17.09$ Å for CuFeO$_2$ [52] and $a = b = 2.98$ Å, $c = 17.11$ Å for CuCrO$_2$ [25]. The delafossite structure is illustrated in Fig. 2.1, where nonmagnetic monovalent Cu ions and magnetic trivalent Fe or Cr ions are represented by green and orange spheres, respectively. ABC stacked triangular layers of Fe or Cr ions are separated by O-Cu-O tri-layers.

Fig. 2.2 illustrates a triangular lattice plane of Fe^{+3} or Cr^{+3} ions between two oxygen layers and the symmetry operations of the delafossite $R\bar{3}m$ space group. The atomic positions and symmetry operations are given with respect to the hexagonal and Cartesian
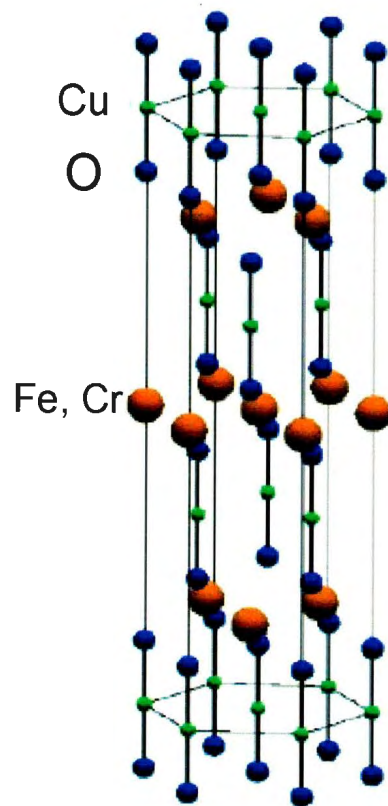
Figure 2.1: Crystal structure of delafossite $CuFeO_2$ and $CuCrO_2$. Reprinted with permission from [T. Arima, J. Phys. Soc. Jpn. **76**, 073702 (2007)]. Copyright (2007) by The Physical Society of Japan.
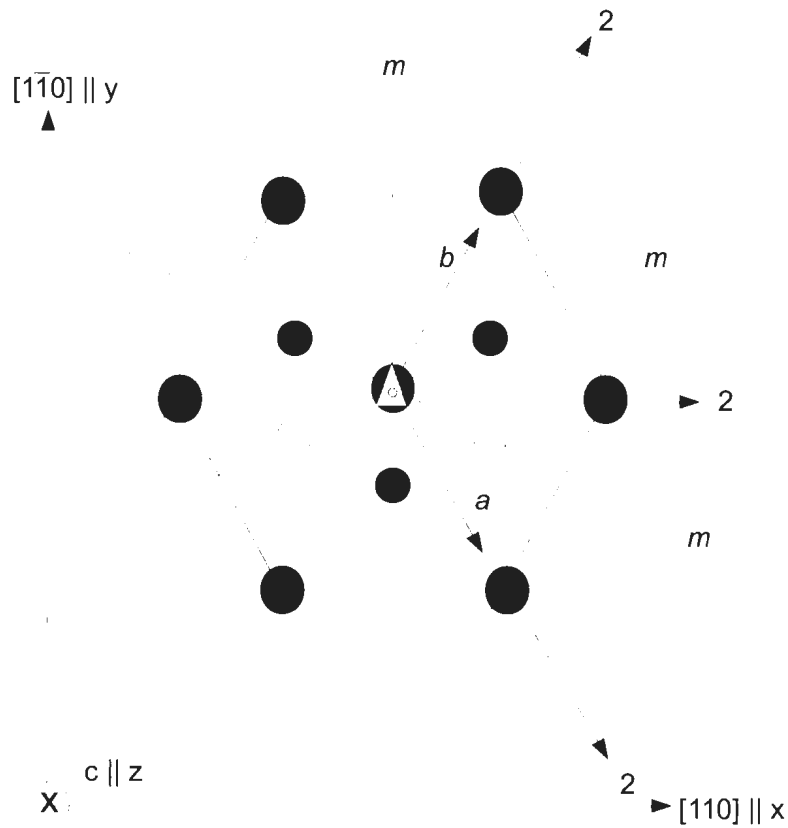
Figure 2.2: The projection of a triangular lattice layer of Cr or Fe ions and two adjacent oxygen layers along the c direction and symmetry operations of $R\bar{3}m$ space group. a, b, c, [110] and [1$\bar{1}$0] designate the directions in the hexagonal basis. In Cartesian coordinates, x and y axes are defined parallel to the [110] and [1$\bar{1}$0] directions of the hexagonal coordinates. Large circles represent the magnetic Cr or Fe ions. Small filled and open circles represent oxygen ions located above and below the Cr or Fe layer, respectively. Thin lines and a triangle with a small white circle at the central Cr or Fe ion indicate mirror planes (m) and a three-fold rotation axis with an inversion center normal to the plane of projection, respectively [2].

coordinates.Throughout the thesis, we will use both Cartesian and hexagonal coordinates depending on their convenience. The labels $a, b, c, [110]$, and $[1\bar{1}0]$ designate the crystallographic directions in the hexagonal basis, whereas x, y and z correspond to those in the Cartesian coordinates. The axes x, y, and z are respectively parallel to the $[110]$, $[1\bar{1}0]$, and c directions of the hexagonal basis. Large circles represent the magnetic Fe or Cr ions, whereas small open and filled circles represent oxygen ions located above and below the Fe or Cr layer, respectively. The symmetry operations of the $R\bar{3}m$ space group are also shown in Fig. 2.2. Thin lines and a triangle with a small white circle at the central Cr or Fe ion indicate mirror planes (m) and a three-fold rotation axis with an inversion center normal to the plane of projection while twofold rotation axes are shown with black arrows. To summarize, the symmetry operations associated with the $R\bar{3}m$ space group are a spatial inversion, a threefold rotation about the c axis, twofold rotations about the a, b, and $[110]$ axes, and mirror planes perpendicular to the twofold rotation axes.

Although $CuFeO_2$ and $CuCrO_2$ are isostructural at room temperature, their magnetic properties at low temperatures are quite different. Because Cu^+ and O^{-2} have filled shells, differences in the magnetic behavior of $CuFeO_2$ and $CuCrO_2$ can be attributed to the magnetic ions: Fe^{+3} ($3d^5, L = 0, S = \frac{5}{2}$) and Cr^{+3} ($3d^3, L = 3, S = \frac{3}{2}$). In particular, no spin-orbit interaction is expected in isolated Fe^{+3} ions since $L = 0$, whereas spin-orbit interaction is allowed in Cr^{+3} as $L = 3$.

The magnetic properties of $CuFeO_2$ are well known and were studied by various groups [1, 53, 28, 52]. In Fig. 2.3, we show the magnetic phase diagram of $CuFeO_2$ obtained using the ultrasonic pulse-echo method [3]. In contrast to other triangular lattice antiferromagnets, such as $CuCrO_2$, $LiCrO_2$, and $AgCrO_2$ [26, 54], $CuFeO_2$ shows a collinear commensurate four-sublattice ($\uparrow\uparrow\downarrow\downarrow$) magnetic structure in its ground state below $T_{N2} = 11$ K [3, 28, 52] (see Fig. 2.3). Note that on a triangular lattice spins normally adopt a $\sim 120°$ spin configuration in order to lift the degeneracy. Between $T_{N2} = 11$ K and $T_{N1} = 14$ K, Fe^{+3} ions order
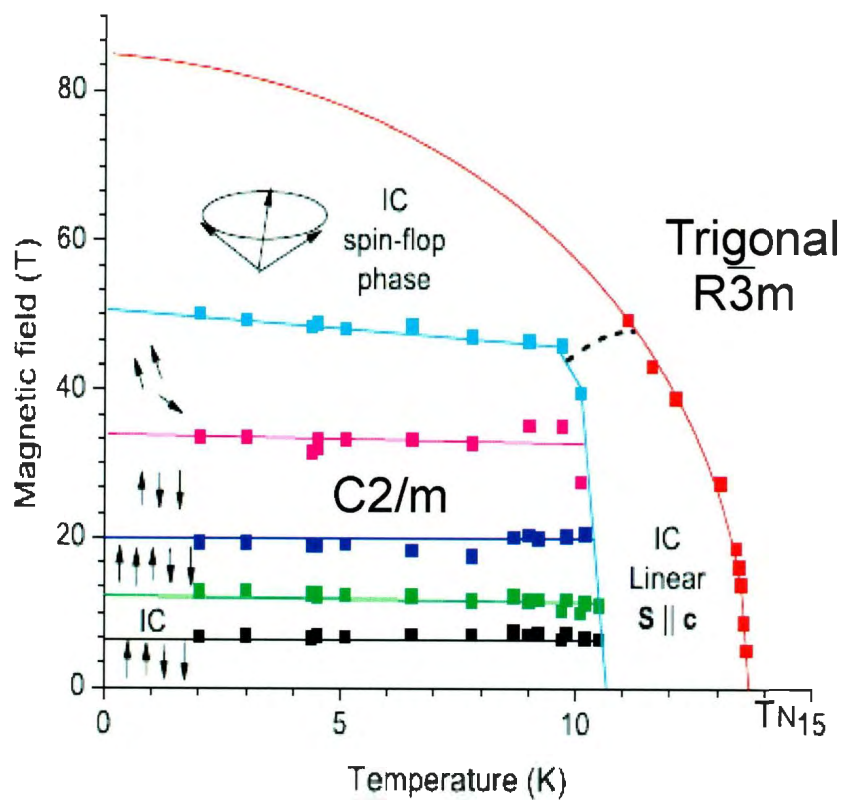
Figure 2.3: Figure is from Quirion et al. [3]. Magnetic field vs. temperature phase diagram of $CuFeO_2$. Reprinted with permission from [G. Quirion, M. L. Plumer, O. A. Petrenko, G. Balakrishnan, and C. Proust, Phys. Rev. B **80**, 064420 (2009)]. Copyright (2009) by the American Physical Society.

into an incommensurate sinusoidally amplitude-modulated spin configuration again with the magnetic moments along the c axis [3, 53]. By the application of a magnetic field along the c axis, $CuFeO_2$ shows rich magnetic properties [3, 28, 52, 53]. Fields between 7 T and 13 T stabilize a proper screw spiral spin configuration. A top view sketch of this spin ordering is presented in Fig. 2.4. In this phase, the magnetic wave vector ($\mathbf{q_m}$) is along the [110] direction (hexagonal basis) and normal to the spin-spiral plane (easy axis) [3, 28, 55, 56]. The green arrow indicates the direction of an electric polarization which is discussed in the next section. The application of larger magnetic fields result in the following spin configurations: a collinear 5-sublattice (↑↑↑↓↓ state with $\mathbf{S} \parallel c$) for 13 T < H < 20 T, a collinear 3-sublattice (↑↑↓) structure with $\mathbf{S} \parallel c$ for 20 T < H < 34 T, a canted 3-sublattice state for 34 T < H < 49 T followed by a nonlinear incommensurate spin-flop phase which is close to the 120° spin structure [3, 57]. The magnetization value saturates above 70 T [3, 56].
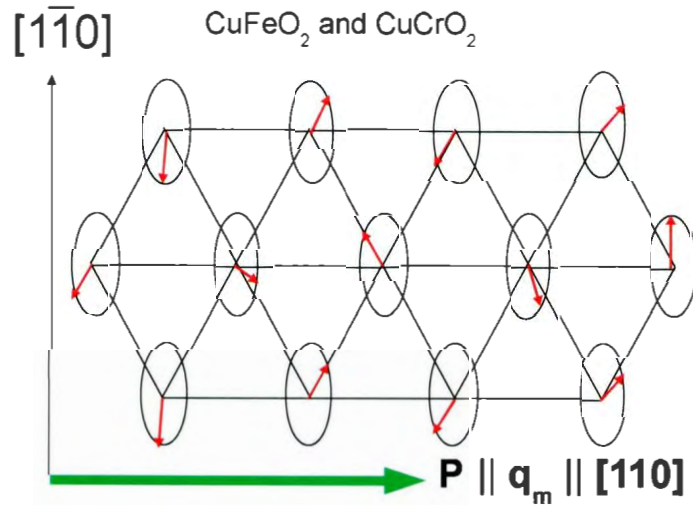
Figure 2.4: A top view sketch of the proper screw spin structure for an arbitrary propagation constant q_m and the direction of the spontaneous polarization observed in $CuFeO_2$ and $CuCrO_2$.

The other delafossite compound studied in this project is $CuCrO_2$ for which the number of transitions is still not clear. In a recent single crystal study by Poienar et al. [58], specific heat, magnetic susceptibility, dielectric, polarization, and resistivity measurements show only one transition at $T_N \sim 24$ K. In addition, there are a number of measurements on $CuCrO_2$ polycrystals [25, 26, 59, 60] which show only one transition at $T_N \approx 24$ K. However, single crystal studies by [27] and Frontzek et al. [61, 62] show evidence of transitions at $T_{N1} = 24.3$ K and $T_{N2} = 23.6$ K. In these measurements, the dielectric constant and electric polarization indicate T_{N2} [27] while magnetic susceptibility [27, 61, 62] and specific heat [27] measurements show transitions at T_{N1} and T_{N2}. In any case, neutron diffraction measurements [62, 63, 64] show that the magnetic order in the ground state of $CuCrO_2$ is an incommensurate proper screw spin structure with $\mathbf{q_m}\|[110]$ (hexagonal basis) below T_{N2}. This spin configuration is very similar to the one observed in $CuFeO_2$ between 7 T and 13 T (see Fig. 2.4), however, the propagation constants of the magnetic modulations in $CuCrO_2$ and $CuFeO_2$ are different. $CuCrO_2$ adopts an almost 120° spin structure with $q_m = 0.329$ in $CuCrO_2$ [25]. On the other hand, the propagation constant of the magnetic modulation in $CuFeO_2$ is $q_m = 0.207$ [65]. Between T_{N1} and T_{N2}, the magnetic order is ambiguous. While Kimura et al. [27] suggest a collinear spin structure with the magnetic moments parallel to the c axis, $\mathbf{S}\|c$, Frontzek et al. [62] interpret the magnetic order as a two dimensional proper screw spin structure based on their neutron diffraction measurements.

Magnetization measurements on $CuCrO_2$ with fields applied up to 53 T along the $[1\bar{1}0]$ (hexagonal basis) direction show only one first order magnetoelectric transition at low temperatures [61, 4, 66]. The transition is observed at 2 K with a field of $H_{flop} = 5.3$ T and is attributed to a 90° spin flop in one of the 3 magnetic structural domains from the (110) plane to the $(1\bar{1}0)$ plane [64, 4, 66]. The magnetic structural domains are illustrated in Fig. 2.5 and are labeled as A, B, and C. Spin-spiral planes are perpendicular to the triangular lattice and represented by thick blue lines. The domains are oriented at 120° relative to each other

due to threefold symmetry of CuCrO$_2$ along the c axis. It is emphasized that domains B and C should undergo a spin flop transition at a field much larger than 9 T [4]. In that case, the spiral plane of each domain will be in the $(1\bar{1}0)$ plane. In addition, it is suggested that a large magnetic field along the [110] direction would align the spiral plane of each domain in the (110) plane [4].
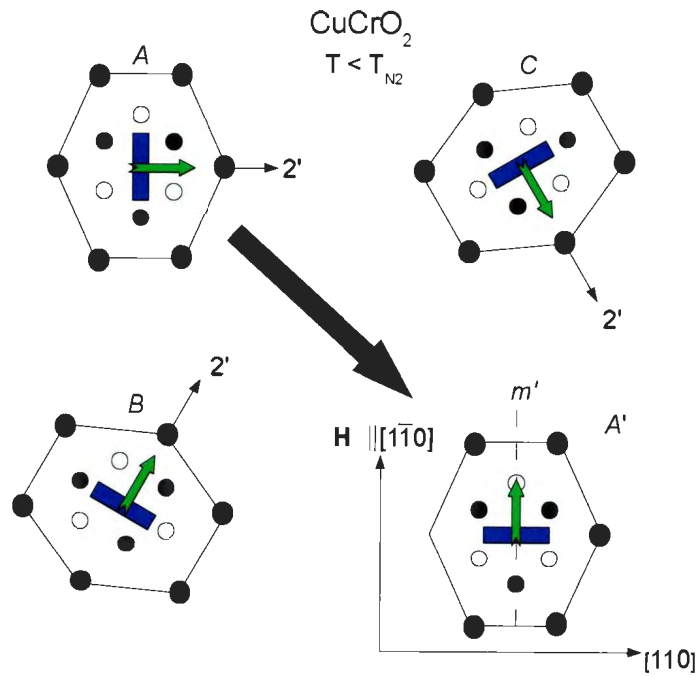
Figure 2.5: Spin-spiral domains A, B, and C in the multiferroic phase of CuCrO$_2$ below $T_{N2} = 23.6$ K and the transition of domain A into domain A' at 2 K with $\mathbf{H}_{1\bar{1}0} = 5.3$ T [4]. Thick lines denote the spiral plane.

2.1.1 Ferroelectricity and magnetoelectric coupling in $CuFeO_2$ and $CuCrO_2$

Even though $CuFeO_2$ and $CuCrO_2$ have different magnetic properties, a proper screw spin structure is stabilized in both compounds with the magnetic propagation vector along the [110] direction [28, 26, 27, 64]. Strikingly, upon the stabilization of the proper screw spin ordering in both compounds, an electric polarization $\mathbf{P}$, represented by a green arrow in Fig. 2.4, is induced in the direction of the magnetic modulation (along the [110] direction) ($\mathbf{P}\|\mathbf{q_m}\|[110]$). Hence, $CuFeO_2$ and $CuCrO_2$ are magnetoelectric multiferroic in the proper-screw spin state.

The ferroelectricity induced upon a proper-screw spin ordering can be explained from the viewpoint of magnetic symmetry [2]. Fig. 2.2 illustrates a triangular lattice plane of Fe^{+3} or Cr^{+3} ions between two oxygen layers and the symmetry operations of the delafossite $R\bar{3}m$ space group. Representing $\mathbf{q_m}$ as $(q, q, 0)$ for the antiferromagnetic phases, either a collinear or a spiral spin configuration breaks the threefold rotation about the c axis and twofold rotations along the a and b axes. In this case, the symmetry should change to monoclinic as the remaining symmetry operations are spatial inversion, two-fold rotation about the [110] axis and a mirror plane normal to the [110] axis. Moreover, the proper screw spin order breaks the inversion and mirror operations; therefore, the only allowed symmetry operation is a $2'$ rotation, which is a time reversal operation followed by a twofold rotation about the [110] axis. As the crystal lattice has no twofold symmetry perpendicular to $\mathbf{q_m}$, the system can be polar in the $2'$ direction ([110] axis), allowing the ferroelectric polarization in the same direction with $\mathbf{E}\|\mathbf{q_m}$ [2].

For $CuCrO_2$, upon the 90° flop of the spiral plane in domain A (Fig. 2.5), the electric polarization also flops as shown in A' [64, 4, 66], demonstrating that the electric polarization is induced by the proper screw spin structure.

A microscopic origin for the spontaneous polarization induced by a proper screw magnetic order is proposed by Arima et al. [2]. The term thought to be responsible [22] originates from the variation of the metal-ligand $(3d - 2p)$ hybridization, which imbalances the charge transfer between neighboring Fe-O pairs. As a result, a net polarization is induced along the direction of the magnetic modulation parallel to the [110] direction [2]. We should note that upon doping the Fe sites with Al [67, 68], Ga [69], or Rh [65], the multiferroic phase of $CuFeO_2$ appears at zero field as in $CuCrO_2$. In Al-doped $CuFeO_2$ [68] and $CuCrO_2$ [64], a direct relationship between the spin helicity and the direction of electric polarization was observed, which is in agreement with the prediction of the proposed microscopic mechanism [2].

2.1.2 Ferroelasticity in $CuFeO_2$

Besides its rich magnetic phase diagram, $CuFeO_2$ has interesting structural properties. At T_{N1}, neutron [30] and x-ray [55] diffraction measurements show that $CuFeO_2$ undergoes a structural transition from the trigonal $R\overline{3}m$ phase to the monoclinic $C2/m$ phase. In addition, ultrasonic velocity measurements on $CuFeO_2$ [1] indicate a second order pseudoproper ferroelastic transition at T_{N1}. According to these measurements [1], some acoustic modes show softening down to T_{N1}, which correspond to a reduction in the elastic constants C_{11}, C_{44}, and C_{66} relative to high temperatures. In particular, the softening observed on the acoustic modes $T_x P_y$ and $T_y P_x$ corresponds to a 50% reduction in the elastic constant C_{66} relative to 100 K (see Fig. 1.3) [1].

Recent studies on the isostructural compound $CuCrO_2$ show evidence for a structural transition at T_{N1} [4, 66]. An indirect indication of a structural transition in $CuCrO_2$ is provided by neutron diffraction measurements on Al- [70] and Ga-doped [69] $CuFeO_2$ which show multiferroicity in its ground state upon a proper screw ordering. These studies show that

the proper screw state is accompanied by a lattice distortion leading to a deformation in the triangular lattice [69, 70]. Moreover, magnetostriction measurements on $CuCrO_2$ show that the Cr triangular lattice is deformed at T_{N1} leading to a lowered crystallographic symmetry at T_{N1} [33]. These results are supported by recent electron spin resonance measurements which have been modeled with a 118° spin configuration on a distorted Cr triangular lattice [66]. As a result, since $CuCrO_2$ is isostructural to $CuFeO_2$ at room temperature, it might also undergo an $R\bar{3}m \rightarrow C2/m$ pseudoproper ferroelastic transition at T_{N1}. Whether or not $CuCrO_2$ is ferroelastic below T_{N1} is still an open question.

2.2 Structural and magnetic properties of $CuCrS_2$

Another triangular lattice antiferromagnet studied in this project is $CuCrS_2$, which drew attention as an ionic conductor [71] and a geometrically frustrated antiferromagnet [48, 47]. It also has a trigonal structure at room temperature, however the $CuCrS_2$ lattice lacks inversion symmetry, therefore, it crystallizes into the trigonal $R3m$ space group with the lattice constants $a = b = 3.48$ Å, $c = 18.72$ Å[47].

Low temperature structural and magnetic properties of $CuCrS_2$ were investigated by neutron diffraction measurements [48]. Despite the quasi-two-dimensional layered structure of $CuCrS_2$, earlier neutron diffraction measurements reveal a complex three dimensional helical magnetic order below $T_N = 38$ K [48]. Recent neutron measurements confirm the three-dimensional order with a propagation vector $\mathbf{q_m} = (-0.493, -0.087, 1.25)$ [47]. In addition to the helical order at $T_N = 38$ K [47, 48], these measurements also show a first order structural transition from the trigonal $R3m$ space group to the monoclinic Cm space group [47]. According to the Aizu classification of ferroic materials [7, 49], an $R3m \rightarrow Cm$ structural transition, as observed in $CuCrS_2$ [47], can result in ferroelastic and simultaneously ferroelectric behavior. However, for $CuCrS_2$ there is no reported ferroelastic and ferroelectric

behavior in the literature. Therefore, additional studies are still required for $CuCrS_2$.

Chapter 3

Theory of light scattering

The propagation characteristics of electromagnetic waves depend on the optical properties and physical structure of the medium. Therefore, we first discuss propagation of monochromatic plane waves in isotropic and anisotropic media. Then, we discuss theory of light scattering from solids. Wave and particle pictures of both Brillouin scattering and Raman scattering are discussed in detail and related derivations are presented.

3.1 Propagation of plane waves in anisotropic media

In this section, we mostly follow the discussion of the books *Lasers and Electro-Optics* by Davis et al. [72] and *Photonic Devices* by Liu et al. [73]. For a more comprehensive discussion of propagation of monochromatic plane waves, one can refer to either book [72, 73]. Let us first consider the propagation of a monochromatic plane wave in free space. The plane wave has the form

$$\mathbf{E} = \mathbf{E_0}e^{i(\mathbf{k}\cdot\mathbf{r}-\omega t)}, \tag{3.1}$$

with an electric field $\mathbf{E}$ of magnitude $|\mathbf{E_0}|$, an angular frequency ω and a wave vector $\mathbf{k}$. The polarization of the wave is specified by the direction of $\mathbf{E}$. In free space, the magnitude

of the wave vector $\mathbf{k}$, called the propagation constant, is given by $k = \omega\sqrt{\mu_0\epsilon_0}$, where ϵ_0 and μ_0 correspond to the electric permittivity and magnetic permeability of free space, respectively. Thus, the phase velocity of the plane wave, or the speed of light, in vacuum, is $c_0 = 1/\sqrt{\mu_0\epsilon_0}$. When the plane wave enters an isotropic medium, its wave vector is modified due to a change in electric permittivity. In the rest of the thesis, the wave vector of a plane wave in any medium is indicated by $\mathbf{K}$ whereas the corresponding wave vector in free space is indicated by $\mathbf{k}$. Here, we assume that the medium is nonmagnetic, therefore, the magnetic permeability is the same as it is in free space, μ_0. If ϵ represents the electric permittivity of the medium, the propagation constant K of the plane wave is given by

$$K = \omega\sqrt{\mu_0\epsilon} = \frac{\omega n}{c_0} = kn = \frac{2\pi n}{\lambda}, \tag{3.2}$$

where

$$n = \sqrt{\frac{\epsilon}{\epsilon_0}} \tag{3.3}$$

is the index of refraction, or the refractive index, of the medium and λ is the wavelength of the plane wave in free space. The ratio $\epsilon_r = \epsilon/\epsilon_0$ is a measure of the change of electric permittivity relative to free space, called the relative electric permittivity or the dielectric constant. In a medium which has a refractive index n, the angular frequency of the plane wave is still ω, but its wavelength is λ/n and the speed of light is $c = c_0/n$. Note that the electric permittivity, and therefore the refractive index n, are functions of frequency. Thus, the speed of light is weakly frequency dependent. In isotropic materials, the relative electric permittivity can be represented by a scalar. In this case the electric displacement vector and associated electric field are parallel,

$$\mathbf{D} = \epsilon_0\epsilon_r\mathbf{E}, \tag{3.4}$$

which imposes that the propagation characteristics of electromagnetic waves are independent of their propagation direction in isotropic media.

26

In anisotropic materials, the relative electric permittivity is expressed by the dielectric tensor $\epsilon_{\mathbf{r}}$,

$$\epsilon_{\mathbf{r}} = \begin{bmatrix} \epsilon_{11} & \epsilon_{12} & \epsilon_{13} \\ \epsilon_{12} & \epsilon_{22} & \epsilon_{23} \\ \epsilon_{13} & \epsilon_{23} & \epsilon_{33} \end{bmatrix}, \tag{3.5}$$

where ϵ_{ij} corresponds to the dielectric constant in the i-th row and j-th column of the dielectric tensor. Therefore, in general $\mathbf{D}$ and $\mathbf{E}$ are no longer parallel because they are related by the dielectric tensor as $\mathbf{D} = \epsilon_0\epsilon_{\mathbf{r}}\mathbf{E}$. In this case, the propagation characteristics of electromagnetic waves depend on the direction of propagation due to the symmetry properties of anisotropic materials. The dielectric tensor in Eq. 3.5 belongs to triclinic crystals. The number of independent elements in the dielectric tensor can be further reduced for crystals of higher symmetry since physical properties of a crystal remain invariant under its symmetry. For example, for a monoclinic crystal, application of a twofold rotation along the z axis in Eq. 3.5 will leave only the diagonal elements and ϵ_{12}. In general, for any given anisotropic crystal, there is a unique set of coordinate axes which diagonalize $\epsilon_{\mathbf{r}}$ with eigenvalues ϵ_x, ϵ_y, and ϵ_z [72, 73]. These axes are called the principal axes of the material. The components of the electric displacement vector $\mathbf{D}$ with respect to the electric field $\mathbf{E}$ along these axes are related by

$$D_x = \epsilon_0\epsilon_x E_x, \ D_y = \epsilon_0\epsilon_y E_y, \ D_z = \epsilon_0\epsilon_z E_z. \tag{3.6}$$

The eigenvalues ϵ_x, ϵ_y, and ϵ_z of the dielectric constant tensor are called the principal dielectric constants. They define three principal refractive indices of the material

$$n_x = \sqrt{\epsilon_x}, \ n_y = \sqrt{\epsilon_y}, \ n_z = \sqrt{\epsilon_z} \tag{3.7}$$

In trigonal, hexagonal, and tetragonal crystals, the physical properties are invariant under a threefold, sixfold and fourfold rotation along the z axis, respectively. Therefore, for crystals

of trigonal, hexagonal, and tetragonal symmetry, the dielectric tensor (3.5) reduces to

$$\epsilon_r = \begin{bmatrix} \epsilon_{11} & 0 & 0 \\ 0 & \epsilon_{11} & 0 \\ 0 & 0 & \epsilon_{33} \end{bmatrix}, \tag{3.8}$$

with corresponding principal refractive indices

$$n_x = n_y = \sqrt{\epsilon_{11}}, \; n_z = \sqrt{\epsilon_{33}}, \tag{3.9}$$

In the case of cubic crystals, the application of a 4 fold rotation along the [111] direction reduces the dielectric tensor to only three diagonal elements with the same value, ϵ_{11}, which defines one distinct refractive index, $n = \sqrt{\epsilon_{11}}$. Therefore, cubic crystals behave like isotropic media in terms of the propagation of plane waves. However, in crystals of lower symmetry, $\mathbf{D}$ and $\mathbf{E}$ are no longer parallel as dictated by Eq. 3.5 and the direction of polarization is specified by the direction of the $\mathbf{D}$ vector. Since $\mathbf{D} \perp \mathbf{K}$ due to the Maxwell equation $\nabla \cdot \mathbf{D} = 0$ in the absence of free charges, $\mathbf{D}$ has no component along the direction of the wave vector and $\mathbf{D}$ has two allowed mutually orthogonal components. In anisotropic materials, each component generally experiences a different index of refraction and therefore has a different propagation constant (see Eq. 3.2). This phenomenon is known as *birefringence* and such a crystal is called a *birefringent crystal* [73].

To clarify birefringence, consider a monochromatic plane wave propagating with an arbitrary polarization propagating along the y axis in a birefringent material. Then, the field will be decomposed into two modes, each of which has a linear polarization along one of the principal axes x and z. According to Eqs. 3.6 and 3.7, each of these modes has a characteristic refractive index n_i and a propagation constant $K^i = n_i \omega / c$, where K^i is used to specify the i-polarized field and does not correspond to a component of the wave vector $\mathbf{K}$. Thus, the x-polarized field travels with a phase velocity $c = c_0/n_x$ whereas the z-polarized field has a velocity of $c = c_0/n_z$. Note that the polarization of the wave depends on the direction

28

of $\mathbf{D}$, and not that of $\mathbf{E}$. In the special case where the plane wave travels along one of the principal axes, $\mathbf{D}$ and $\mathbf{E}$ are parallel [73].

Clearly, when a wave enters an anisotropic medium, in an arbitrary direction with an arbitrary polarization, the allowed polarizations specified by the components of the $\mathbf{D}$ vector will not necessarily be along the principal axes. In that case, we need to specify the polarization directions with respect to the principal axes of the medium to determine the refractive indices. This can be done using a geometric figure called the *optical indicatrix*, or the *index ellipsoid*. The equation for the optical indicatrix is given by [72, 73]

$$\frac{x^2}{n_x^2} + \frac{y^2}{n_y^2} + \frac{z^2}{n_z^2} = 1, \tag{3.10}$$

where n_x, n_y, and n_z correspond to three principal refractive indices of the material [72, 73]. The optical indicatrix allows us to determine the refractive index for monochromatic plane waves as a function of the polarization direction. The principal axes of the optical indicatrix are oriented such that it is consistent with the symmetry axes of the crystal. In any crystal which belongs to cubic, tetragonal, hexagonal, trigonal, and orthorhombic crystal systems, the axes of the ellipsoid are parallel to the crystallographic axes [72, 73]. In a monoclinic crystal, one of the axes of the ellipsoid must coincide with the principal axis along which physical properties are invariant with respect to a twofold rotation. In triclinic crystals, the ellipsoid axes can take any orientation, however it is fixed for a given crystal [72].

We use geometrical properties of the optical indicatrix in order to determine the refractive indices and polarizations of a monochromatic plane wave propagating through a crystal with a given wave vector $\mathbf{K}$. This is illustrated in Fig. 3.1, where the wave vector $\mathbf{K}$ passes through the origin of the indicatrix and is normal to a plane surface represented by the gray area [72, 73]. The plane surface intersects the indicatrix with an ellipse and its semiaxes define the directions of both polarizations determined by the $\mathbf{D}$ vector components $\mathbf{D_1}$ and $\mathbf{D_2}$. The lengths of the semiaxes give the refractive indices experienced by these two polarizations.

29
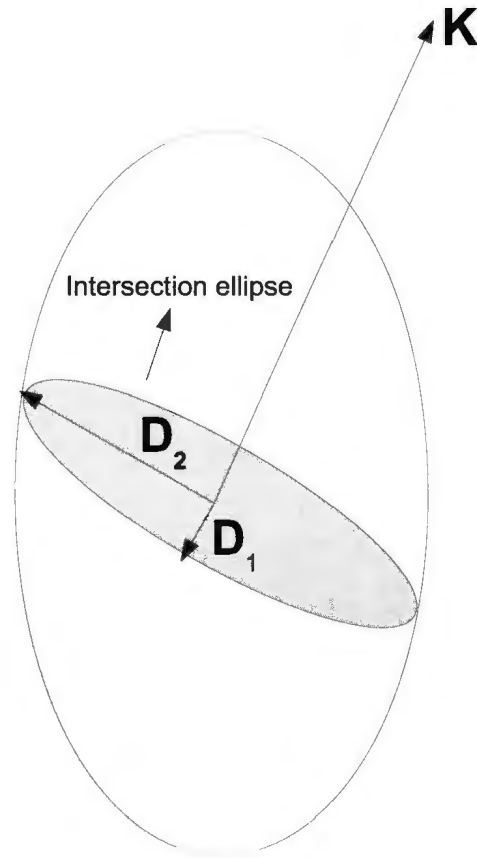
Figure 3.1: Optical indicatrix showing the direction of wave propagation **K** and intersection ellipse which is perpendicular to **K**.

For crystals which do not have cubic symmetry, there is at least one wave vector direction along which the intercepted ellipse is a circle. In this direction, the refractive indices for both polarizations are identical and therefore independent of the polarization [72, 73]. Such a special direction is called the *optic axis*. For crystals in which $n_x \neq n_y \neq n_z$, there are two optic axes, neither of which coincides with any of the principal axes. A crystal with two optic axes is called a *biaxial crystal*. A comprehensive treatment of biaxial crystals can be found in Ref. [72]. In crystals that belong to the trigonal, hexagonal, and tetragonal systems, there exists only one optic axis, which is oriented along the highest symmetry direction of

the crystal, the crystallographic z axis, since $n_x = n_y \neq n_z$. Due to the existence of one optic axis, a crystal that has trigonal, hexagonal or tetragonal symmetry is called a *uniaxial crystal* [72, 73]. In uniaxial crystals, the determination of the polarizations and refractive indices is particularly simple because the optical indicatrix reduces to [72, 73]

$$\frac{x^2 + y^2}{n_o^2} + \frac{z^2}{n_e^2} = 1, \tag{3.11}$$

where $n_x = n_y = n_o$ and $n_z = n_e$. Here, the subscripts o and e refer to the *ordinary index* and *extraordinary index*, respectively. When a monochromatic plane wave propagates in a direction other than the optic axis, it will be resolved into two modes with linear polarizations, each of which experiences a unique refractive index. Clearly, both polarizations are orthogonal to the wavevector $\mathbf{K}$. One of these polarizations, is perpendicular to the optic axis and this mode is called the *ordinary wave* [73]. We use $\hat{e}_o$ to indicate its polarization. The polarization of the other mode is orthogonal to $\hat{e}_o$. This wave is called the *extraordinary wave* and its polarization is indicated by $\hat{e}_e$ [73]. These polarizations are the directions of $\mathbf{D}$ rather than those of $\mathbf{E}$. For the ordinary wave, the polarization $\hat{e}_o$, electric displacement vector $\mathbf{D_o}$, and electric field $\mathbf{E_o}$ are always parallel, $\hat{e}_o \| \mathbf{D_o} \| \mathbf{E_o}$, whereas for the extraordinary wave $\hat{e}_e \| \mathbf{D_e} \nparallel \mathbf{E_e}$. However, when $\mathbf{D_e}$ is parallel to a principal axis, we have $\hat{e}_e \| \mathbf{D_e} \| \mathbf{E_e}$ [73] (see Eq. 3.6).

Knowing the optic z axis of a uniaxial crystal and the direction of the wave vector, $\mathbf{K}$, we can determine both $\hat{e}_o$ and $\hat{e}_e$. Designating the unit vector of the wave vector $\mathbf{K}$ with $\hat{K}$ and that of the optic axis with $\hat{z}$, we can write $\hat{e}_o$ and $\hat{e}_e$ as [73]

$$\hat{e}_o = \frac{\hat{K} \times \hat{z}}{\sin \theta}, \ \hat{e}_e = \hat{e}_o \times \hat{K}. \tag{3.12}$$

If $\hat{K}$ is at angle θ relative to $\hat{z}$ and an angle ϕ relative to $\hat{x}$, being the unit vector for the x axis, we have

$$\hat{K} = \hat{x} \sin \theta \cos \phi + \hat{y} \sin \theta \sin \phi + \hat{z} \cos \theta, \tag{3.13}$$

$$\hat{e}_o = \hat{x} \sin \phi - \hat{y} \cos \phi, \tag{3.14}$$

and

$$\hat{e}_c = -\hat{x} \cos \theta \cos \phi - \hat{y} \cos \theta \sin \phi + \hat{z} \sin \theta. \tag{3.15}$$

The orientations of these vectors with respect to the principal axes are illustrated in Fig. 3.2.

Figure 3.2: Relationships between the direction of wave propagation and polarization directions of the ordinary and extraordinary waves.

The refractive indices associated with the ordinary and extraordinary waves can be found by using the indicatrix equation given in Eq. 3.11 and are shown in Fig. 3.3. The polarizations $\hat{e}_o$ and $\hat{e}_c$ are along the semiaxes of the ellipse and the length of each semiaxis gives the refractive index of each polarization. The refractive index experienced by the ordinary wave
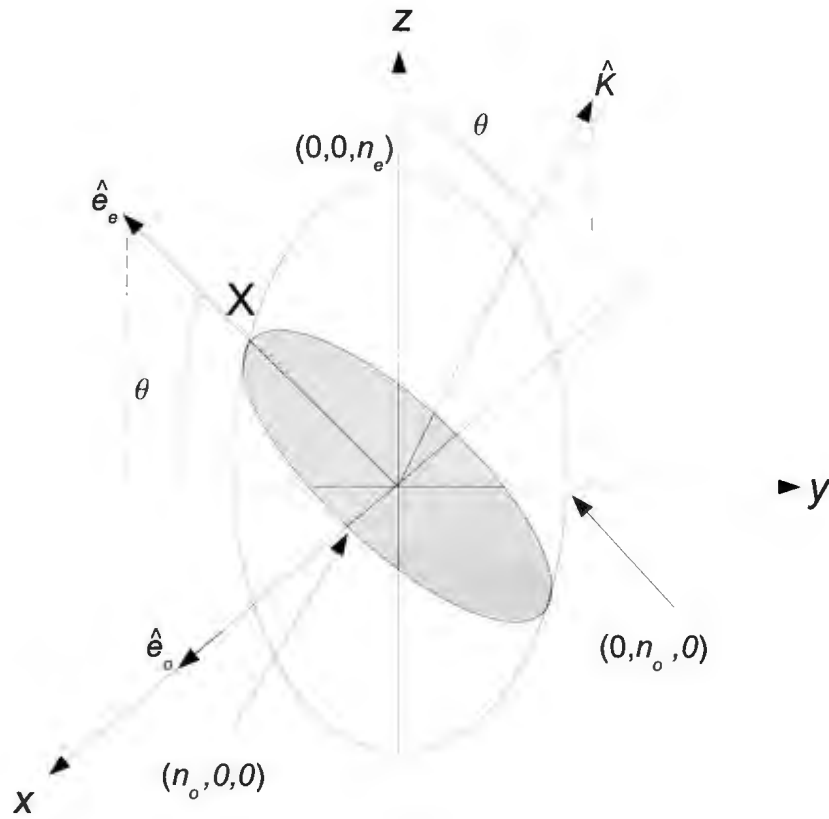
Figure 3.3: Determination of the ordinary and extraordinary refractive indices by optical indicatrix.

(with the polarization $\hat{e}_o$) is always the ordinary index n_o. However, the refractive index for the extraordinary wave is $n_e(\theta)$. Its value depends on the angle θ and is given by the length OX in Fig. 3.3. Using Eqs. 3.12, 3.13, and 3.15, we can write the Cartesian coordinates (x, y, z) of the point X as

$$x = -n_e(\theta)\cos\theta\cos\phi, \tag{3.16}$$

$$y = -n_e(\theta)\cos\theta\sin\phi, \tag{3.17}$$

and

$$z = n_e(\theta)\sin\theta. \tag{3.18}$$

33

Substituting Eqs. 3.16-3.18 in Eq. 3.11, we obtain [73]

$$\frac{1}{n_e^2(\theta)} = \frac{\cos^2\theta}{n_o^2} + \frac{\sin^2\theta}{n_e^2} \tag{3.19}$$

According to Eq. 3.19, a plane wave propagating at an arbitrary direction decomposes into two components with $\mathbf{D}$ vectors, $\mathbf{D_o}$ and $\mathbf{D_e}$,

$$\begin{aligned}\mathbf{D} &= \mathbf{D_o}e^{i\mathbf{K}_o\cdot\mathbf{r}-i\omega t} + \mathbf{D_e}e^{i\mathbf{K}_e\cdot\mathbf{r}-i\omega t} \\ &= \hat{e}_o D_o e^{i\mathbf{K}_o\cdot\mathbf{r}-i\omega t} + \hat{e}_e D_e e^{i\mathbf{K}_e\cdot\mathbf{r}-i\omega t},\end{aligned} \tag{3.20}$$

where $\mathbf{K}_o$ and $\mathbf{K}_e$ are the wave vectors of the components of the plane wave with magnitudes $|\mathbf{K}_o| = n_o\omega/c$ and $|\mathbf{K}_e| = n_e(\theta)\omega/c$, respectively. In general, $\mathbf{E}$ cannot be written in the form of Eq. 3.20 since its longitudinal component does not vanish except when $\theta = 0°$ and $\theta = 90°$ [73]. Note that $n_e(\theta)$ takes values between n_o and n_e. If $n_e > n_o$, the crystal is called *positive uniaxial* whereas it is called *negative uniaxial* if $n_e < n_o$ [72, 73].

3.2 Inelastic light scattering

Inelastic light scattering is one of processes that results from the interaction of electromagnetic radiation with matter. In this process, a light beam with photons of energy $\hbar\omega_i$ and momentum of $\hbar\mathbf{k_i}$ incident on a crystal is inelastically scattered to give photons of energy $\hbar\omega_s$ and momentum of $\hbar\mathbf{k_s}$ through the creation or annihilation of a lattice vibration. If phonons involved in the process have energy $\hbar\Omega$ and momentum $\hbar\mathbf{q}$ the energy and momentum conservation laws give

$$\hbar\omega_s = \hbar\omega_i \pm \hbar\Omega \tag{3.21}$$

and

$$\hbar\mathbf{K_s} = \hbar\mathbf{K_i} \pm \hbar\mathbf{q}, \tag{3.22}$$

where ω_i and $\mathbf{K_i}$ (ω_s and $\mathbf{K_s}$) correspond to the angular frequency and wave vector of the incident (scattered) photons in the scattering medium, whereas Ω and $\mathbf{q}$ are the angular frequency and the wave vector of the lattice vibrations. When the frequency of the scattered light corresponds to $\omega_s = \omega_i - \Omega$, such that a lattice vibration is created, the process is called *Stokes scattering* whereas the process that annihilates a phonon, $\omega_s = \omega_i + \Omega$, is referred as *anti-Stokes scattering*. Thus, the frequency shift of the scattered light depends on the type of the lattice vibration involved in the scattering process. If the scattering of light occurs with the creation or annihilation of optical vibrations, the process is called *Raman scattering* while the scattering phenomenon involving acoustic vibrations is referred as *Brillouin scattering*. The physical processes involved in Raman and Brillouin scattering are different and are discussed in the following two sections in detail. Typical frequency shifts for optical vibrations in Raman scattering range from 10 cm^{-1} to 1000 cm^{-1} while shifts for acoustic vibrations in Brillouin scattering are usually $\sim$1 cm^{-1} [74].

In both Raman and Brillouin scattering experiments, only lattice vibrations near the Brillouin zone center are probed. This is because even in 180° scattering, the wave vector of the acoustic or optical vibrations are on the order of the incident wave vector, $\sim 10^7$ m^{-1}, which is three orders of magnitude smaller than the size of the Brillouin zone, $\frac{\pi}{d} = \sim 10^{10}$ m^{-1}, where d is the lattice spacing [74]. A comprehensive treatment of inelastic light scattering can be found in many text books [74, 75].

3.2.1 Raman scattering

Raman scattering or the Raman effect was discovered by Sir Chandrasekhara Venkata Raman and Kariamanickam Srinivasa Krishnan in liquids in 1928 [76], and by Grigory Landsberg and Leonid Mandelstam in crystals the same year [77]. A comprehensive review of Raman scattering is given by Loudon [78]. Raman scattering can be explained both classically and

quantum mechanically. According to the classical theory, Raman scattering occurs when light interacts with matter via a change in molecular polarizability. The molecular polarizability is a measure of the ability of a material to become polarized under an electric field. A change in the molecular polarizability can be induced, for example, by optical vibrations. If a given molecule vibrates at an angular frequency Ω due to an optical lattice vibration, the molecular polarizability also changes. Then, the components α_{ij} of the molecular polarizability α may be expanded in terms of the normal vibrational coordinate q_n about its equilibrium value q_n^o

$$\alpha_{ij} = \alpha_{ij}^o + \left(\frac{\partial \alpha_{ij}}{\partial q_n} \right)_0 q_n \tag{3.23}$$

where

$$q_n = q_n^o \cos \Omega t. \tag{3.24}$$

In Eq. 3.23, the first term corresponds to the equilibrium value of the polarizability whereas the second term is the change induced by optical vibrations. A light beam with an electric field

$$\mathbf{E} = \mathbf{E_0} \cos \left(\omega_i t \right) \tag{3.25}$$

induces an oscillating dipole moment in the material given as

$$\begin{bmatrix} p_x \\ p_y \\ p_z \end{bmatrix} = \begin{bmatrix} \alpha_{xx} & \alpha_{xy} & \alpha_{xz} \\ \alpha_{yx} & \alpha_{yy} & \alpha_{yz} \\ \alpha_{zx} & \alpha_{zy} & \alpha_{zz} \end{bmatrix} \begin{bmatrix} E_x \\ E_y \\ E_z \end{bmatrix} . \tag{3.26}$$

Therefore, the induced dipole moment component p_i can be expressed as

$$p_i(t) = \alpha_{ij}^o E_j^o \cos \left(\omega_i t \right) + \left(\frac{\partial \alpha_{ij}}{\partial q_n} \right)_0 q_n E_j^o \cos \left(\Omega t \right) \cos \left(\omega_i t \right). \tag{3.27}$$

where repeated indexes represent a sum and ω_i corresponds to the angular frequency of the incident light. Using the trigonometric relations

$$\cos \left(x \mp y \right) = \cos \left(x \right) \cos \left(y \right) \pm \sin \left(x \right) \sin \left(y \right), \tag{3.28}$$

36

the induced dipole moment $p_i(t)$ becomes

$$p_i(t) = \alpha_{ij}^o E_j^o \cos{(\omega_i t)} + \frac{1}{2}\left(\frac{\partial \alpha_{ij}}{\partial q_n}\right)_0 q_n E_j^o \cos{(\omega_i - \Omega)t} + \frac{1}{2}\left(\frac{\partial \alpha_{ij}}{\partial q_n}\right)_0 q_n E_j^o \cos{(\omega_i + \Omega)t}.$$

(3.29)

Here, the scattered radiation consists of both elastically and inelastically scattered light. The first term represents an oscillating dipole associated with an elastic process (Rayleigh scattering) since there is no frequency shift with respect to ω_i. The last two terms correspond to Raman scattering with Stokes $(\omega_i - \Omega)$ and anti-Stokes $(\omega_i + \Omega)$ bands (modes) for which the frequency difference between the incident and scattered light is equal to the lattice vibration Ω. As Eq. 3.29 dictates, a lattice vibration is Raman active only if at least one of the elements of the derivative of the polarizability tensor is non-zero, i.e. $\left(\frac{\partial \alpha_{ij}}{\partial q_n}\right)_0 \neq 0$.

According to the quantum mechanical picture, Raman scattering is an inelastic collision between an incident photon and a molecule which changes the vibrational state of the molecule. The diagram in Fig. 3.4 illustrates the vibrational and electronic states of the molecule as well as the transitions giving rise to Raman scattering. The electronic ground state is assumed to have several vibrational energy levels represented by $m = 0, 1, 2, 3$. The incident photon excites the molecule from the ground sate $(m = 0)$ to a virtual electronic state shown with dashed lines. Since the virtual level is not stable, the molecule immediately loses energy and goes down to its ground state $(m = 0)$. In this case, the photon will be elastically scattered with an energy equal to that of the incident photon, corresponding to Rayleigh scattering. However, a small portion of molecules in the virtual level may go down to the excited vibrational level $(m = 1)$ and the incident photon loses an energy equal to the energy difference between the ground and excited $(m = 1)$ states, $h(\nu_1 - \nu_0)$. This scattered photon gives rise to a Stokes band in the Raman spectrum. The final possibility is that the molecule which is initially in an excited vibrational state absorbs the incident photon and rises to a higher virtual state (see Fig. 3.4). Then, the molecule goes down to the ground
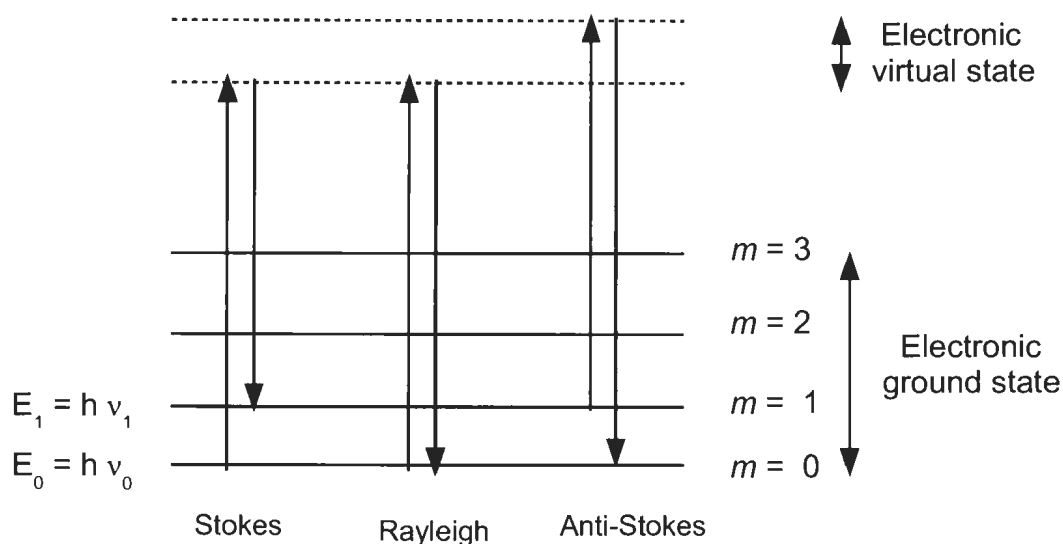
Figure 3.4: A schematic diagram of vibrational transitions for Raman and Rayleigh Scatterings

state ($m = 0$) while the energy loss is compensated for by the emission of a photon the energy of which equals that of the incident light plus the energy difference between the ground ($m = 0$) and the excited ($m = 1$) vibrational states. This scattered photon gives rise to an anti-Stokes line in the Raman spectrum. According to the Boltzman distribution function, designating the number of molecules in the vibrational ground state $m = 0$ with N_0, the number of molecules in the excited vibrational level ($m = 1$) is given by [79]

$$N = N_0 \exp\left(-\frac{h\nu_1}{k_B T}\right). \tag{3.30}$$

According to Eq. 3.30, most of the molecules exist in the ground state ($m = 0$) at low temperatures and therefore the intensity of the Stokes lines is normally larger than that of the anti-Stokes counter part. The ratio of the anti-Stokes and Stokes line intensity is [79]

$$\frac{I^{anti-St}}{I^{St}} = \frac{(\nu_i + \nu)^4}{(\nu_i - \nu)^4} \exp\left(\frac{-h\nu}{k_B T}\right) \tag{3.31}$$

where ν_i is the frequency of the incident light, ν is the frequency of the molecular vibrations,

and T is the temperature. While k_B is known as the Boltzman constant, the exponential term is called the Boltzman factor. Referring to Eq. 3.31, one can see that the relative intensity of the anti-Stokes line rapidly decreases as the temperature approaches zero due to the Boltzman factor. For that reason, as both lines give the same information, the Stokes lines are usually preferred to anti-Stokes lines.

3.2.2   Polarizability and Raman Tensors

As mentioned earlier, a vibrational transition is Raman active only if the derivatives of the polarizability tensor have a non-zero element. Since the molecular polarizability for an anisotropic crystal is a tensor, its derivatives with respect to a given normal coordinate q_n are also expressed as tensors and are defined as *Raman tensors*. If the elements of a Raman tensor, for a given normal coordinate q_n, are represented by a_{ij}, the Raman tensor and the electric fields of the incident and scattered light are related as [80]

$$
\begin{bmatrix} E_x^s \\ E_y^s \\ E_z^s \end{bmatrix} = \begin{bmatrix} a_{xx} & a_{xy} & a_{xz} \\ a_{yx} & a_{yy} & a_{yz} \\ a_{zx} & a_{zy} & a_{zz} \end{bmatrix} \begin{bmatrix} E_x^i \\ E_y^i \\ E_z^i \end{bmatrix}
\tag{3.32}
$$

where E_x^s, E_y^s, and E_z^s are the components of the electric field of the scattered light along the x, y, and z axes, while E_x^i, E_y^i, and E_z^i are those of the incident light. Hence, if the element a_{ij} of the Raman tensor given in Eq. 3.32 is non-zero, Raman scattering is possible for the electric fields E_i^s and E_j^i; that is, if the incident light is polarized along the i axis and the scattered light is polarized along the j axis. In this case, the intensity of the Raman line is proportional to [79]

$$
I \propto a_{ij}^2.
\tag{3.33}
$$

Raman tensors, for possible vibrational modes, are derived according to the symmetry of the crystallographic point groups. These vibrational species are labeled using irreducible

representations (IR) listed in character tables reported in various textbooks such as Ref. [81]. These IRs describe how properties of molecules, such as vibrational (phonon) modes, transform under symmetry operations of the molecular point group. They are represented by symbols such as A, B, E and F. A vibration belongs to the A type if the vibration is symmetric with respect to the rotation about the principal axis of symmetry, whereas it belongs to B if it is anti-symmetric [82]. A and B are one dimensional, non-degenerate representations. Types E and F, on the other hand, correspond to doubly and triply degenerate representations, respectively [82]. IRs may also have subscripts depending on the point group [81]. The subscript g is used when the vibration is symmetric with respect to a center of symmetry whereas u is used when it is antisymmetric. Moreover, the subscript 1 (or 2) is used when the vibration is symmetric (or antisymmetric) with respect to a rotation axis or rotation-reflection axis other than the principal axis or in point groups which have only one symmetry axis with respect to a plane of symmetry.

Raman tensors are different for each irreducible representation for a given point group (see Chapter 9). Thus, in a Raman experiment, one can identify the symmetries of optical vibrations in a crystal with known orientation and point group by choosing the appropriate polarizations for the incident and scattered light according to Eq. 3.32 (see Chapter 9).

3.3   Brillouin Light Scattering

Brillouin light scattering (BLS) from acoustic waves may occur due to two different mechanisms. One of these mechanisms is (bulk) *elasto-optic scattering* mechanism. Acoustic waves present in a solid move in thermal equilibrium and modulate the dielectric constant of the medium. Since atomic displacements due to acoustic waves are nearly constant over distances on the order of 100 unit cells, one may discuss the acoustic waves in terms of an elastic continuum model [83]. In this case, we can explain elasto-optic scattering mecha-
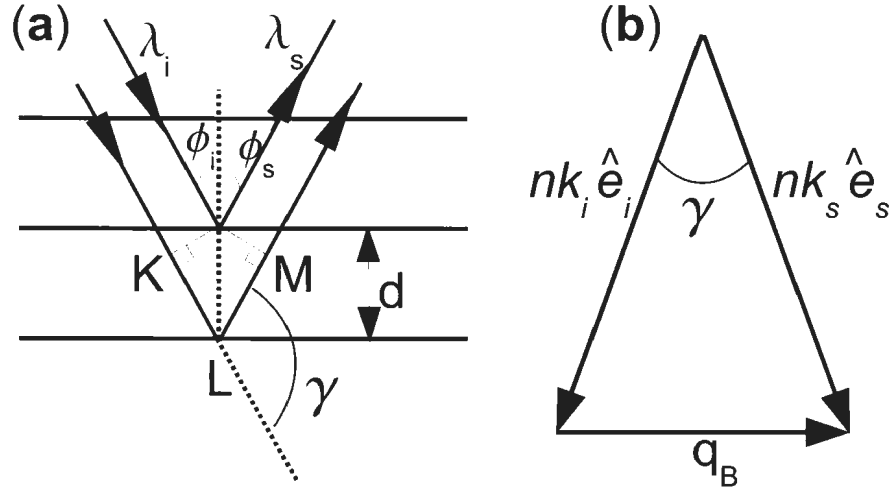
Figure 3.5: **a)** Wave and **b)** particle pictures of Brillouin light scattering.

nism as Bragg scattering from acoustic waves. According to this analogy, acoustic waves are viewed by an incident light wave as a moving diffraction grating and the incident light is scattered with (Doppler) shifted frequencies. This is illustrated in Fig. 3.5a, where acoustic waves are represented by parallel planes. The angles ϕ_i and ϕ_s are equal in this geometry. The spacing d between the plane parallel regions correspond to the wavelength Λ_B of the acoustic waves in the solid. Note that throughout the text, Λ represents the wavelength of acoustic waves and the subscript B is used to represent bulk acoustic waves. For constructive interference to occur, the path difference must be an integral multiple m of the wavelength of the incident light, λ_i,

$$KL + LM = 2KL = m\lambda_i = 2nd\cos\left(\phi_i\right),\tag{3.34}$$

where n is the refractive index of the solid. Considering the first order constructive interference ($m = 1$), and using $d = \Lambda_B = V/\nu_B$, where V and ν_B are the acoustic velocity and frequency, Eq 3.34 becomes

$$\lambda_i = 2n\frac{V}{\nu_B}\sin\left(\frac{\gamma}{2}\right),\tag{3.35}$$

41

where γ is the scattering angle given by $\gamma = \pi - 2\phi_i$. Eq. 3.35 can be organized to express the Brillouin frequency shift

$$\Delta\nu_B = \pm\nu_B = \pm2n\frac{V}{\lambda_i}\sin\left(\frac{\gamma}{2}\right), \tag{3.36}$$

called the *Brillouin equation*.

The Brillouin equation can also be derived by considering that the acoustic phonon wave vector $\mathbf{q_B}$ is very small compared to those of the incident and scattered photons, $\mathbf{k_i}$ and $\mathbf{k_s}$. Therefore, the propagation constants will be nearly the same and we can use the approximation $nk_i \approx nk_s$, where $\mathbf{K_i}$ and $\mathbf{K_s}$ are the wave vector of the incident and scattered light inside the medium. Therefore, the triangle in Fig. 3.5b, where $\hat{e}_i$ and $\hat{e}_s$ are the unit vectors giving the directions of the incident and scattered light wave vectors inside the medium, is nearly isosceles which allows us to write the magnitude of the phonon wave vector as

$$q_B = nk_i\sin\left(\frac{\gamma}{2}\right). \tag{3.37}$$

Using that $V = \nu_B\Lambda_B$, we obtain the Brillouin equation, Eq. 3.36.

If the refractive indices for the incident (n_i) and scattered (n_s) light are different, the propagation constants of the incident and scattered light in the scattering medium are n_ik_i and n_sk_s. Referring to Fig. 3.5b and using the cosine law, the magnitude of the phonon wave vector can be written as

$$q_B = k_i(n_i^2 + n_s^2 - 2n_in_s\cos\gamma)^{1/2}, \tag{3.38}$$

where $\gamma = \pi - \Theta_i + \Theta_s$ is the scattering angle inside the crystal. In Eq. 3.38, we have assumed that $k_i \approx k_s$. The substitution of the relation $\Omega_B = Vq_B$ into Eq. 3.38 will yield the Brillouin frequency shift $\Delta\nu_B = \pm\nu_B = \Omega_B/2\pi$ as

$$\Delta\nu_B = \pm\frac{V}{\lambda_i}(n_i^2 + n_s^2 - 2n_in_s\cos\gamma)^{1/2}. \tag{3.39}$$

42
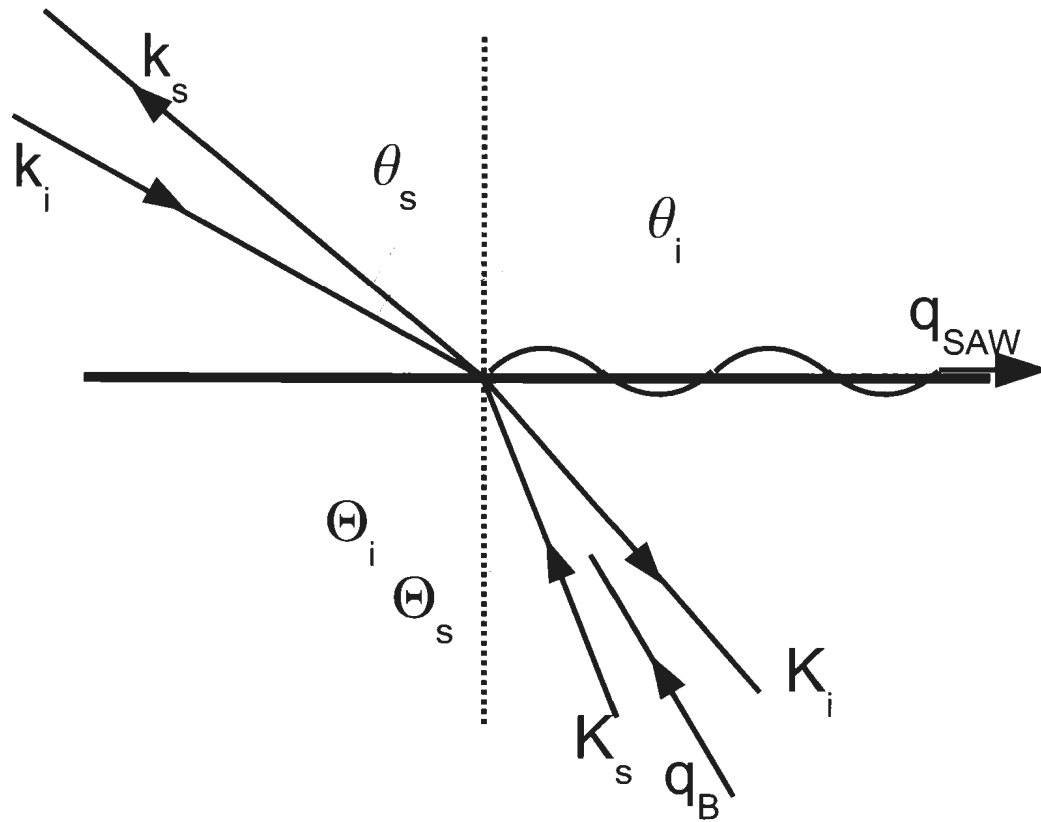
Figure 3.6: Brilluin scattering geometry.

Brillouin scattering in an arbitrary direction is illustrated in Fig. 3.6, where $\mathbf{k_i}$ ($\mathbf{K_i}$) and $\mathbf{k_s}$ ($\mathbf{K_s}$) are the external (internal) incident and scattered photon wave vectors whereas $\mathbf{q_B}$ corresponds to the bulk acoustic wave vector. θ_i (Θ_s) and Θ_i (θ_s) are the angle of incidence and the angle of refraction of the incident (scattered) light. From Snell's law, we can see that $\sin\theta_i = n\sin\Theta_i$ and $\sin\theta_s = n\sin\Theta_s$ (see Fig. 3.6). If the sample transparency decreases, the incident light is not able to penetrate deep below the sample surface. Hence, a range of possible acoustic wave vectors couple to the incident light according to the uncertainty principal. This causes broadening in the bulk acoustic modes [84, 85, 86]. With increasing opacity in the material, the scattering cross section for the bulk elasto-optic mechanism

43

decreases and bulk acoustic waves may not even be observed [87]. In that case, another mechanism, the *surface-ripple effect*, takes place to give rise to Brillouin scattering. As the name suggests, scattering by this mechanism occurs due to acoustic phonons present on the surface of the solid, or surface acoustic waves (SAW). The wave vector of a surface acoustic wave is shown in Fig. 3.6 and is represented by $\mathbf{q_{SAW}}$. The magnitude of the surface acoustic wave vector can be expressed as

$$q_{SAW} = k_i \sin\theta_i + k_s \sin\theta_s \approx k_i(\sin\theta_i + \sin\theta_s) \tag{3.40}$$

Using the dispersion relation, the frequency shift reduces to

$$\Delta\nu_{SAW} = \pm\frac{V_{SAW}}{\lambda_i}(\sin\theta_i + \sin\theta_s) \tag{3.41}$$

It should be noted that Brillouin light scattering does not allow direct sound velocity measurements. In a backscattering geometry, $\gamma = 180°$ and $\theta_i = \theta_s$, rearranging Eqs. 3.39 and 3.41, the velocities of the bulk and surface phonons can be calculated using

$$V = \frac{\lambda_i \Delta\nu_B}{n_i + n_s} \text{ if } n_i \neq n_s \tag{3.42}$$

$$V_{SAW} = \frac{\lambda_i \Delta\nu_{SAW}}{2\sin\theta_i}. \tag{3.43}$$

In Eq. 3.43, the frequency shift $\Delta\nu_{SAW}$ of a surface acoustic wave is independent of the refractive index of the solid and is proportional to the sine of the angle of incidence, $\sin\theta_i$. Thus, the frequency shift goes to zero as θ_i approaches zero. Hence, one can unambiguously distinguish surface acoustic modes from bulk acoustic modes in a Brillouin spectrum.

After determining the bulk acoustic mode velocities from the frequency shifts and using Eq. 3.42, one can calculate the elastic constants using Christoffel's equation. Christoffel's equation is derived in Chapter 4 for the trigonal $\bar{3}m$ point group. In the case of surface acoustic waves, the relationship between the velocity and elastic constants is not straightforward. Except for crystals of cubic and hexagonal symmetry, numerical calculations are required for the determination of the elastic constants [88, 89, 90].

3.3.1 Acoustic velocities and refractive indices of a birefringent crystal

As discussed in Sec. 3.3, Brillouin scattering can be employed to determine acoustic velocities in a material. However, determination of acoustic velocities with Brillouin scattering experiments normally requires that the refractive index of the sample be known (see Eq. 3.39). There are several experimental geometries which do not require the refractive index of the material for the calculation of the acoustic velocities, however, these geometries are for transparent materials [91, 92]. Recently, it has been shown [93] that a pseudoreflection geometry (Fig. 3.7) can be successfully used to simultaneously determine the acoustic velocities and refractive index of anisotropic materials from Brillouin scattering measurements. This geometry can also be employed for opaque materials provided that one observes bulk acoustic modes. Below, we derive the frequency shifts of bulk acoustic modes in a solid for reflection geometry Brillouin scattering experiments [91].
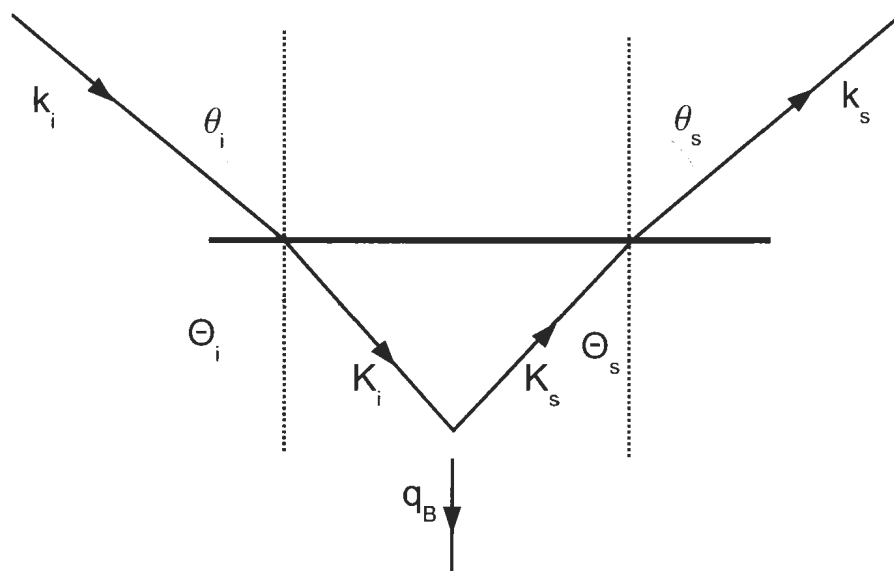
Figure 3.7: Brillouin light scattering in a reflection geometry.

In the reflection geometry [91] shown in Fig 3.7, $\mathbf{k_i}$ ($\mathbf{K_i}$) and $\mathbf{k_s}$ ($\mathbf{K_s}$) are the external (internal) incident and scattered photon wave vectors, whereas $\mathbf{q_B}$ is the bulk acoustic wave vector q_B. θ_i (Θ_s) and Θ_i (θ_s) are the angle of incidence and the angle of refraction of the incident (scattered) light. Note that $\theta_i = \theta_s$ in this geometry. In addition, Snell's law relates these angles as $\sin\theta_i = n_i \sin\Theta_i$ and $\sin\theta_s = n\sin\Theta_s$, where n_i and n_s are the refractive indices for the incident and scattered light. Since $\theta_i = \theta_s$ and $k_i \approx k_s$, $\mathbf{q_B}$ has no component parallel to the sample surface. Thus, the acoustic wave propagates along the surface normal with the wave vector

$$
\begin{aligned}
\mathbf{q_B} &= \mathbf{q_{B\perp}} && (3.44) \\
&= \hat{e}_\perp K_s \cos\Theta_s + \hat{e}_\perp K_i \cos\Theta_i \\
&= \hat{e}_\perp k_s n_s \cos\Theta_s + \hat{e}_\perp k_i n_i \cos\Theta_i \\
&\approx \hat{e}_\perp k_i (n_s \cos\Theta_s + n_i \cos\Theta_i),
\end{aligned}
$$

where $\mathbf{q_{B\perp}}$ corresponds to the perpendicular and only component of the acoustic wave vector whereas $\hat{e}_\perp$ is a unit vector parallel specifying the direction of the acoustic wave vector, which is normal to the sample surface. Using $\sin\Theta_i{}^2 = 1 - \cos\Theta_i{}^2 = 1$ and Snell's law, $n_i \sin\Theta_i = n_s \sin\Theta_s$, the acoustic wave vector takes its form in terms of the external parameters

$$
\mathbf{q_B} = \hat{e}_\perp k_i \left(\sqrt{n_s^2 - \sin\theta_i{}^2} + \sqrt{n_i^2 - \sin\theta_i{}^2} \right) \tag{3.45}
$$

Substitution of the dispersion relation, $\Omega_B = V\, q_B$, in Eq. 3.45 yields the frequency shift as

$$
\Delta\nu_B = \frac{V}{2\pi} \left(\sqrt{k_i^2 n_s^2 - k_m^2} + \sqrt{k_i^2 n_i^2 - k_m^2} \right), \tag{3.46}
$$

where we drop the vector notation. Here, $k_m = k_i \sin\theta_i$ is the in-plane component of the incident light wave vector. According to Eqs. 3.46, fits to experimentally determined $\Delta\nu_B$ vs. k_m data will give the acoustic velocities and refractive indices of the sample solid.

46

Chapter 4

Elasticity

This chapter introduces some basic terms of elasticity theory such as *stress, strain,* and *elastic constants.* The discussions follow those of the book *Elastic Waves in Solids* by Dieulesaint et al. [94]. The number of independent stress components, strains, and elastic constants depends solely on the crystal point group. Therefore, symmetry properties of crystals are also discussed. Forming the background for dynamic elasticity, Christoffel's equation is solved for plane waves propagating in a trigonal crystal with point group $\overline{3}m$. As mentioned in earlier sections, $CuFeO_2$ and $CuCrO_2$ belong to the trigonal point group $\overline{3}m$ (space group $R\overline{3}m$). These solutions are required to determine the elastic constants using the ultrasonic pulse-echo method and Brillouin scattering measurements.

4.1 Static elasticity

A force acting on a unit area is defined as the *stress.* Hence, the stress components are expressed as

$$\sigma_{ij} = \frac{\Delta F_i}{\Delta S_j},$$ (4.1)

where ΔF_i is the i_{th} component of the force exerted on the surface element ΔS_j. Thus, σ_{ij} represents the i_{th} component of the force acting on a unit area normal to the j-axis. Forces normal to the surface are called *tensile*, or *normal stress* (σ_{ii}), whereas forces applied in a direction parallel to the surface are associated with *shear stress*. As a result, there are 9 stress components. However, if one considers an elementary cube in static equilibrium, the net force and torque acting on the cube must be zero, which requires

$$\sigma_{ij} = \sigma_{ji}, \tag{4.2}$$

reducing the number of independent stress components to 6. Thus, the stress tensor is written as a symmetric 3×3 matrix

$$\sigma = \begin{bmatrix} \sigma_{11} & \sigma_{12} & \sigma_{13} \\ \sigma_{12} & \sigma_{22} & \sigma_{23} \\ \sigma_{13} & \sigma_{23} & \sigma_{33} \end{bmatrix}. \tag{4.3}$$

The stress applied on a material causes *strain* which can be defined as the deformation of a solid induced by the action of a stress. As illustrated in Fig. 4.1, when a stress is applied on a string, its length will change from L to L'. Let us define the deformation of a small element in the string. Consider the section between the points M and N located at x and $x + \Delta x$ in Fig. 4.1. After the force is applied, these points move to M' and N' at $x + u(x)$ and $x + u(x + \Delta x) + \Delta x$. The relative deformation of the section MN is then

$$\frac{\overline{M'N'} - \overline{MN}}{\overline{MN}} = \frac{u(x + \Delta x) - u(x)}{\Delta x}, \tag{4.4}$$

where $\overline{MN}$ and $\overline{M'N'}$ are the lengths of the sections MN and $M'N'$, respectively. The strain e of the string is defined as the limit when Δx goes to 0, i.e.,

$$e = \lim_{\Delta x \to 0} \frac{u(x + \Delta x) - u(x)}{\Delta x} = \frac{du}{dx}, \tag{4.5}$$

which is a dimensionless quantity. In the case of a one-dimensional object, the deformation is along the same direction as that of the stress and the *strain* is called a *normal* or *tensile*

48
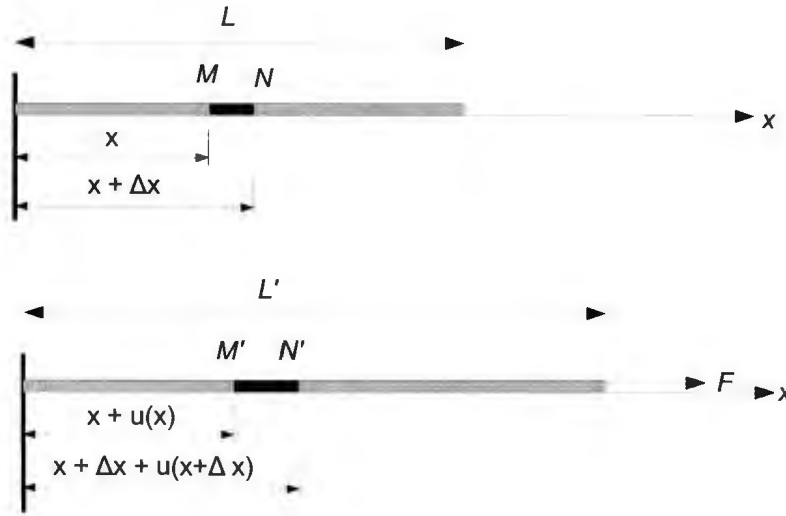
Figure 4.1: Deformation of a spring

strain. However, for two or three-dimensional objects, shear stress (e_{ij}, $i \neq j$) causes angular distortions, giving rise to *shear strain*. For small deformations, the strain components can be expressed as

$$e_{ij} = \frac{1}{2} \left(\frac{\partial u_i}{\partial x_j} + \frac{\partial u_j}{\partial x_i} \right) \tag{4.6}$$

where u_i ($i, j = 1, 2, 3$) is the i-th component of the displacement vector and x_j (i is the j-th component of the position vector $\mathbf{x}$. According to Eq. 4.6, elements e_{ij} are invariant under the interchange of the indices,

$$e_{ij} = e_{ji}, \tag{4.7}$$

leaving only 6 independent strain components

$$e = \begin{bmatrix} e_{11} & e_{12} & e_{13} \\ e_{12} & e_{22} & e_{23} \\ e_{13} & e_{23} & e_{33} \end{bmatrix}. \tag{4.8}$$

49

For small deformations, the strain is proportional to the stress so that the generalized Hookes law is written as

$$\sigma_{ij} = C_{ijkl}\ e_{kl};\ i,\ j,\ k,\ l = 1, 2, 3, \tag{4.9}$$

where repeated indices are summed over. The constants C_{ijkl} are known as the *elastic constants* which form a fourth-rank tensor called the *elastic stiffness tensor*. As each index i, j, k, l can take three possible values, the elastic stiffness tensor has 81 elements. However, due to the symmetry properties of the stress (Eq. 4.2) and the strain (Eq. 4.7) tensor, we have

$$C_{ijkl} = C_{jikl};\ C_{ijkl} = C_{ijlk}, \tag{4.10}$$

which reduces the number of independent elastic constants to 36.

The number of independent elastic constants can be further reduced by thermodynamic considerations as follows: the energy variation per unit volume can be expressed as

$$dU = \sigma_{ik}de_{ik} + TdS, \tag{4.11}$$

where T is the temperature and S is the entropy. Here, the first term represents the work done by the external forces while the second term corresponds to heat received per unit volume. Using

$$\sigma_{ik} = \left(\frac{\partial U}{\partial e_{ik}} \right)_S, \tag{4.12}$$

the elastic constants can be expressed in terms of the internal energy as

$$C_{ijkl} = \frac{\partial \sigma_{ij}}{\partial e_{kl}} = \frac{\partial^2 U}{\partial e_{ij} \partial e_{kl}} = \frac{\partial^2 U}{\partial e_{kl} \partial e_{ij}} = C_{klij}. \tag{4.13}$$

The symmetry property in Eq. 4.13 not only reduces the number of independent elastic constants from 36 to 21 but also allows one to label the elastic constants using the Voigt notation where α are β represent pairs of Cartesian indices (i, j) according to

$$1 \leftrightarrow (1, 1),\ 2 \leftrightarrow (2, 2),\ 3 \leftrightarrow (3, 3)$$

$$4 \leftrightarrow (2, 3) = (3, 2),\ 5 \leftrightarrow (1, 3) = (3, 1),\ 6 \leftrightarrow (1, 2) = (2, 1).$$

The elastic tensor can then be more conveniently expressed as a 6×6 matrix

$$
C = \begin{bmatrix}
C_{11} & C_{12} & C_{13} & C_{14} & C_{15} & C_{16} \\
C_{12} & C_{22} & C_{23} & C_{24} & C_{25} & C_{26} \\
C_{13} & C_{23} & C_{33} & C_{34} & C_{35} & C_{36} \\
C_{14} & C_{24} & C_{34} & C_{44} & C_{45} & C_{46} \\
C_{15} & C_{25} & C_{35} & C_{45} & C_{55} & C_{56} \\
C_{16} & C_{26} & C_{36} & C_{46} & C_{55} & C_{66}
\end{bmatrix}, \tag{4.14}
$$

where $C_{\alpha\beta} = C_{ijkl}$ with $\alpha \leftrightarrow (ij)$ and $\beta \leftrightarrow (kl)$. The elastic tensor in Eq. 4.14 belongs to triclinic crystals. The number of independent elastic constants can be further reduced for a crystal that belongs to other crystal systems because its physical properties remain invariant under its symmetry properties. In other words, the invariance condition requires that the elastic tensor must be invariant under all transformations of the reference frame, such as rotations, inversion, and mirror planes,

$$
C'_{ijkl} = \alpha_i^p \alpha_j^q \alpha_k^r \alpha_l^s C_{pqrs}, \tag{4.15}
$$

where α_i^p is the element of the symmetry operation α in the i-th row and $p-$th column. As an example, for trigonal point groups $\bar{3}m$, $3m$, and 32, the elastic stiffness tensor has to be invariant under C_{3z}^+ (3-fold rotation with respect to z axis), C_{2x} (2-fold rotation with respect to x axis), and I (spatial inversion), which can be written in the matrix form as

$$
\alpha_{3z}^+ = \begin{bmatrix}
-\frac{1}{2} & \frac{\sqrt{3}}{2} & 0 \\
-\frac{\sqrt{3}}{2} & -\frac{1}{2} & 0 \\
0 & 0 & 1
\end{bmatrix}, \tag{4.16}
$$

$$
\alpha_{2x} = \begin{bmatrix}
1 & 0 & 0 \\
0 & -1 & 0 \\
0 & 0 & -1
\end{bmatrix}, \tag{4.17}
$$

and

$$\alpha_{\bar{1}} = \begin{bmatrix} -1 & 0 & 0 \\ 0 & -1 & 0 \\ 0 & 0 & -1 \end{bmatrix}. \tag{4.18}$$

If we apply the symmetry operations in Eqs. 4.16-4.18 on Eq. 4.14, we see that the elastic tensor for the trigonal point groups $\bar{3}m$, $3m$, and 32 has only 6 independent elastic constants,

$$C_{\alpha\beta} = \begin{bmatrix} C_{11} & C_{12} & C_{13} & C_{14} & 0 & 0 \\ C_{12} & C_{11} & C_{13} & -C_{14} & 0 & 0 \\ C_{13} & C_{13} & C_{33} & 0 & 0 & 0 \\ C_{14} & -C_{14} & 0 & C_{44} & 0 & 0 \\ 0 & 0 & 0 & 0 & C_{44} & C_{14} \\ 0 & 0 & 0 & 0 & C_{14} & C_{66} \end{bmatrix}, \tag{4.19}$$

where $C_{66} = \frac{C_{11} - C_{12}}{2}$.

The energy provided by the external forces during the deformation is stored in the medium as elastic energy. In the approximation of Hooke's law (Eq. 4.9), this elastic energy G_e is a function of strains e_i and elastic constants C_{ij},

$$G_e = \sum_{i,\,j} C_{ij} e_i e_j. \tag{4.20}$$

Using Eq. 4.20, the elastic energy for the trigonal point group $\bar{3}m$ can be written as

$$\begin{aligned} G_e(e) &= \frac{1}{2}C_p(e_1 + e_2)^2 + \frac{1}{2}C_{33}e_2^3 + \frac{1}{2}C_{44}(e_4^2 + e_5^2) \\ &+ \frac{1}{2}C_{66}e_6^2 + C_{66}(e_1 - e_2)^2 + C_{13}(e_1 + e_2)e_3 + C_{14}(e_1 e_4 - e_2 e_4 + e_5 e_6), \end{aligned} \tag{4.21}$$

where $C_p = \frac{C_{11} + C_{12}}{2}$.

4.2 Dynamic elasticity and plane wave propagation in crystals

The propagation of acoustic waves in solid can be described by utilizing Newton's second law and Hooke's law. The force density per unit volume for a solid under stress is given by

$$f_i = \frac{\partial \sigma_{ij}}{\partial x_j}. \tag{4.22}$$

According to Newton's second law, the force density f_i gives rise to an acceleration $\frac{\partial^2 u_i}{\partial t^2}$ of an infinitesimal element as

$$f_i = \rho \frac{\partial^2 u_i}{\partial t^2}, \tag{4.23}$$

where ρ represents the density and u_i corresponds to the i-th component of the displacement u. Combining Eqs. 4.22 and 4.23, the equation of motion for an elastic medium can be written as

$$\rho \frac{\partial^2 u_i}{\partial t^2} = \frac{\partial \sigma_{ij}}{\partial x_j}. \tag{4.24}$$

Making use of Hooke's law (Eq. 4.9), the equation of motion becomes

$$\rho \frac{\partial^2 u_i}{\partial t^2} = C_{ijkl} \frac{\partial^2 u_l}{\partial x_j \partial x_k}. \tag{4.25}$$

For plane waves, the solutions of this wave equation have the form

$$u_i = u_{0i} e^{i(\mathbf{q} \cdot \mathbf{r} - \Omega t)}, \ i = 1, 2, 3, \tag{4.26}$$

where u_{0i} is the wave polarization or the particle displacement direction, $\mathbf{q}$ is the wave vector corresponding to $q = 2\pi/\Lambda$ with Λ representing the wavelength and Ω is the angular frequency. Substituting Eq. 4.26 into Eq. 4.25, one obtains

$$\rho \Omega^2 u_{0i} = C_{ijkl} q_j q_k u_{0l}, \tag{4.27}$$

where q_j and q_k are the components of the wave vector along the principal axis. Using $u_{0i} = \delta_{il} u_{0l}$ and dividing by q^2, Eq. 4.27 can be written as

$$(\rho V^2 \delta_{il} - C_{ijkl} n_j n_k) u_{0l} = 0, \tag{4.28}$$

where $V = \frac{\Omega}{q}$ is the phase velocity and n_j and n_k are the cosine directions of the wave vector $\mathbf{q}$. After introducing a second rank tensor, called the *propagation tensor*,

$$\Gamma_{il} = C_{ijkl} n_j n_k, \tag{4.29}$$

Eq. 4.28 takes its final form

$$(\Gamma_{il} - \rho V^2 \delta_{il}) u_{0l} = 0, \tag{4.30}$$

which is known as Christoffel's equation. Christoffel's equation has 3 real and positive eigenvalues, which means that there are three waves propagating in the same direction with mutually orthogonal polarizations. One of these waves is longitudinal, hence the direction of polarization (particle displacement) is parallel to the wave vector. The other two waves are called transverse (or shear) waves as the direction of polarization is perpendicular to the wave vector. The velocities of these waves can be obtained by solving the secular equation

$$\left| \Gamma_{il} - \rho V^2 \delta_{il} \right| = 0, \tag{4.31}$$

which gives

$$V = \sqrt{\frac{C_{eff}}{\rho}}, \tag{4.32}$$

where C_{eff} corresponds to a combination of independent elastic constants given in Eq. 4.19. Consider as an example elastic waves propagating along the x direction in $CuFeO_2$ or $CuCrO_2$ single crystals (which belong to the trigonal $\overline{3}m$ point group). In this case, the cosine directions are $n_1 = 1$, $n_2 = 0$, $n_3 = 0$, and Γ_{il} can be written as

$$\Gamma_{il} = C_{i11l} \tag{4.33}$$

54

or in the matrix form

$$\Gamma_{[100]} = \begin{bmatrix} C_{11} & 0 & 0 \\ 0 & C_{66} & C_{14} \\ 0 & C_{14} & C_{44} \end{bmatrix}. \tag{4.34}$$

The substitution of Eq. 4.34 in Eq. 4.31 yields the expressions for the velocities and polarizations of the three waves propagating along the x ([100]) axis in terms of the elastic constants, as shown in Table 4.1. The expressions for the velocities ρV^2 of acoustic waves propagating in the y ([010]) and z ([001]) axes can be determined in a similar way and are also shown in Table 4.1. For convenience, acoustic modes are labeled as L_i or $T_i P_j$, where L_i corresponds to the longitudinal mode propagating along the i axis and $T_i P_j$ is the transverse mode propagating along the i axis with a polarization along the j axis. Note that the transverse modes propagating along the z axis are degenerate and have the same expression for their velocities.

Table 4.1: Solutions of Christoffel's equation for a monochromatic plane wave propagating along the three crystallographic axes for trigonal $\bar{3}m$ point group. Modes are designated with L_i or T_iP_j. L_i corresponds to the longitudinal mode propagating along the i axis whereas T_iP_j corresponds to the transverse mode propagating along the i axis with a polarization along the j axis.

Direction	Mode	ρV^2
[100]	L_x	C_{11}
	T_xP_y	$\frac{1}{2}(C_{44} + C_{66} - \sqrt{(C_{44} - C_{66})^2 + 4C_{14}^2})$
	T_xP_z	$\frac{1}{2}(C_{44} + C_{66} + \sqrt{(C_{44} - C_{66})^2 + 4C_{14}^2})$
[010]	L_y	$\frac{1}{2}(C_{11} + C_{44} + \sqrt{(C_{11} - C_{44})^2 + 4C_{14}^2})$
	T_yP_x	C_{66}
	T_yP_z	$\frac{1}{2}(C_{11} + C_{44} - \sqrt{(C_{11} - C_{44})^2 + 4C_{14}^2})$
[001]	L_z	C_{33}
	[010]	C_{44}
	T_zP_x	C_{44}

Chapter 5

Experimental Setup

In this work, four experimental techniques were employed. Two of these techniques are ultrasonic pulse echo method and Brillouin scattering. These techniques can be used to measure the velocity of zone-center acoustic phonons from which one can obtain elastic constants through Christoffel's equation. We also performed capacitance measurements using a capacitance bridge. Therefore, we briefly describe how a capacitance bridge works. Finally, Raman scattering measurements were performed to measure zero wave vector optical phonons. While all measurements were performed as a function of temperature, ultrasonic velocity and dielectric measurements were also performed in a magnetic field. Cryogenic systems and a superconducting magnet for field dependent measurements are described in the relevant sections.

5.1   Ultrasonic Pulse Echo Method

Sound velocity can be measured by using the ultrasonic pulse echo method. Sound waves are generated with a transducer glued on two parallel surfaces of the sample. A transducer is a piezoelectric crystal coated with gold electrodes. When a pulsed radio frequency (RF) signal

is applied to the electrodes of the transducer, the piezoelectric crystal mechanically vibrates at the same frequency (inverse piezoelectric effect) and generates an ultrasonic pulse in the crystal. A piezoelectric crystal can also convert mechanical energy into an electrical signal, called the piezoelectric effect. Thus, a transducer can serve as both a sound wave generator and a detector. Measurements can be done in both reflection and transmission configurations (see Fig. 5.1). In the reflection configuration, the induced sound waves travel back and forth between the parallel surfaces of the crystal due to reflection at the surfaces. Each time the sound waves return the transducer, it converts a small portion of the mechanical energy into an electrical signal. If the acoustic attenuation is not too large, several echoes can be detected as shown in Fig. 5.2. In Fig. 5.2, the amplitude of the second echo is less than that of the first echo due to acoustic attenuation. In the reflection configuration, the sound velocity can be determined using

$$V = \frac{2L}{t},$$ (5.1)

where t is the time of flight for the acoustic wave which travels a total distance of $2L$, L being the sample length. In the transmission configuration, two transducers, glued on the parallel surfaces of the sample, serve as the acoustic generator and detector, respectively. The sound velocity can be obtained using

$$V = \frac{L}{t},$$ (5.2)

when the first echo is measured.

5.1.1 Acoustic Interferometer

The typical sample length used in the standard pulse-echo method is between 2 mm and 5 mm, giving a time of flight between 0.5 μs and 3 μs. The uncertainty associated with the sample length is 0.01 mm. If we assume an uncertainty of 0.01 μs for the time of flight, the
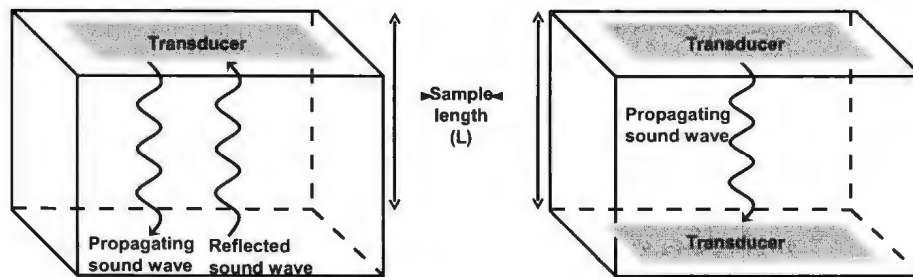
Figure 5.1: Sound velocity measurements in **Left:** Reflection configuration and **Right:** Transmission configuration.
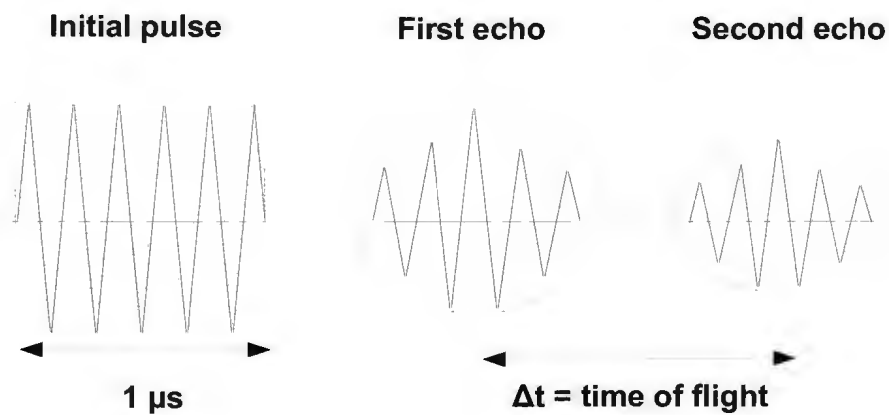
Figure 5.2: Consecutive echoes detected by the receiver in a sound velocity measurement.

resolution in the absolute velocity measurements will be around 0.5 %. We can increase the resolution by using longer samples, however, the acoustic attenuation and the finite space of the sample holder are the limiting factors. In order to obtain a higher resolution, an acoustic interferometer is used. In that case, the measured quantity is the relative change in velocity, $\frac{\Delta V}{V}$, instead of the absolute velocity V, and a resolution of as high as 1 part per million (ppm) can be achieved. The main principle of the acoustic interferometer is to detect the phase difference between a reference signal and an echo. As seen in Fig. 5.3, the continuous signal, generated by the radio frequency (RF) synthesizer opearting at 30 MHz, is split into two parts by the power splitter. The first part is used as the reference signal. The other part is shaped into short pulses of one μs at a repetition rate of 1 kHz using the first gate. After the signal is amplified by the broad band amplifier, it reaches the transducer via the circulator. The main purpose of the circulator is to prevent any reflected signal from going back to the RF synthesizer. The acoustic wave produced by the transducer travels in the sample and gets reflected from the parallel surface. The reflected wave (echo) is converted into an electrical signal by the transducer and it passes through the circulator from the position 1 to the position 3. The second gate eliminates the initial pulse from the echo pattern to prevent the saturation of the low noise RF amplifier. The echo pattern, after being amplified by the low noise RF amplifier, is compared to the reference signal at the phase detector, which produces a signal that is proportional to the phase difference. Provided that the acoustic attenuation is not too large, a multi-echo pattern can be observed on the oscilloscope as shown in Fig. 5.4.

For the m-th reflected echo, the phase difference Φ_m can be expressed in terms of the time of flight, $\Delta t_m = \frac{m2L}{V}$, and the period T of the radio frequency signal as

$$\Phi_m = 2\pi \frac{\Delta t_m}{T} = \frac{4\pi mLf}{V}. \tag{5.3}$$

60
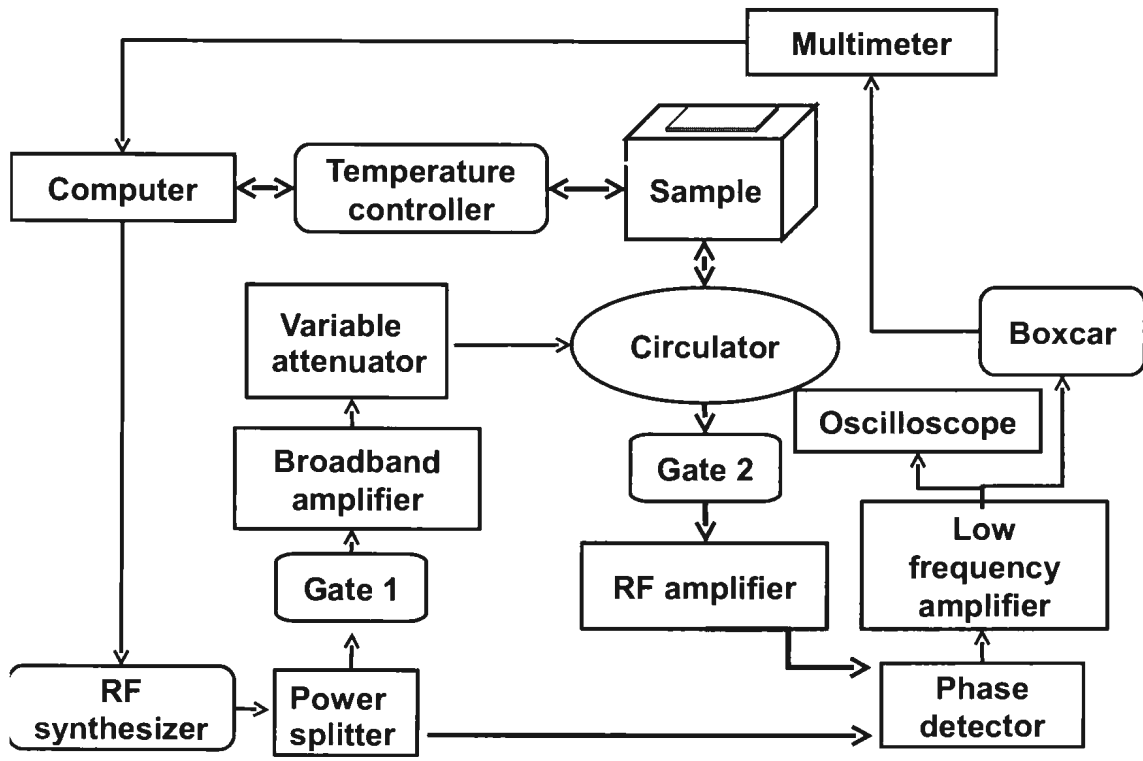
Figure 5.3: A block diagram of an acoustic interferometer
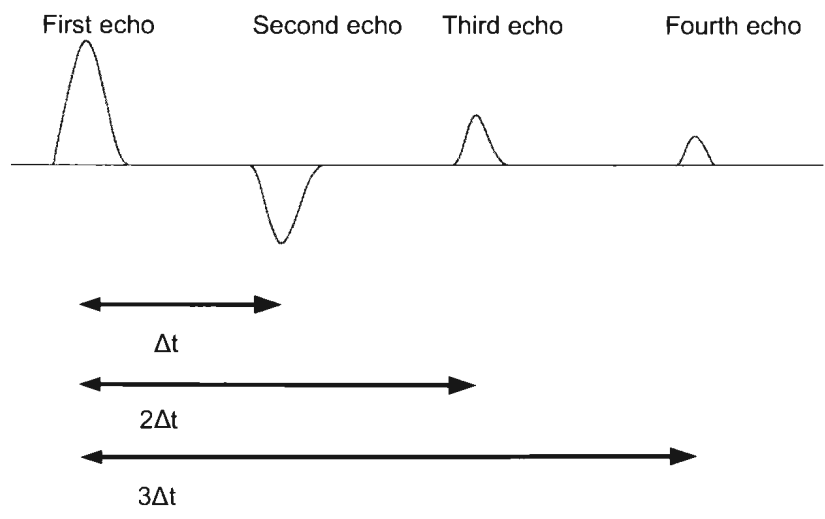
Figure 5.4: An illustration of a multi echo pattern observed using an oscilloscope.

The relative phase change of the m-th echo can be expressed as

$$\frac{\Delta \Phi_m}{\Phi_m} = \frac{\Delta f}{f} + \frac{\Delta L}{L} - \frac{\Delta V}{V}. \tag{5.4}$$

During the experiment, a boxcar, which measures the phase of one specific echo (in general the first echo), functions as a part of a retroaction loop. In this loop, a computer is also used to maintain a zero phase difference ($\Delta \phi = 0$) by changing the frequency of the radio frequency synthesizer. In general, the variation of the relative sample length $\frac{\Delta L}{L}$, as a function of temperature or magnetic field, is an order of magnitude smaller than $\frac{\Delta V}{V}$. Hence, neglecting the thermal expansion of the sample, we can directly measure the variation of the relative velocity variation by measuring the variation of the relative frequency $\frac{\Delta f}{f}$

$$\frac{\Delta V}{V} \cong \frac{\Delta f}{f}. \tag{5.5}$$

5.1.2 A helium bath cryostat

A continuous flow helium bath cryostat equipped with a superconducting magnet was used for most of the sound velocity and dielectric measurements (Fig. 5.5). The temperature of this cryogenic system can go down to 2 K with the use of liquid helium as cryogen. At this temperature, the superconducting magnet can achieve a variable magnetic field up to 15 T.

The helium reservoir is vacuum insulated by an outer chamber to reduce conductive and convective heat transfer due to the outside wall of the cryostat at room temperature. When the liquid helium is transferred, the lower part of the reservoir is cooled down to 4.2 K by liquid helium. Meanwhile, radiation baffles are cooled down by the cold gas which evaporates from liquid helium. Therefore, the radiation baffles further reduce heat flow due to room temperature radiation. The sample is mounted on the sample holder of a long probe located in the sample chamber. In order to cool down the sample, the capillary is adjusted to let the helium flow into the sample chamber. Moreover, the pressure in the sample chamber can

Sample probe

Safety pressure relief

Insert evacuation valve

Lambda plate
Pumping port

Outer chamber

Outer chamber
Pumping port

Helium vapor
shield

Radiation baffles

Helium reservoir

Insert Liquid helium flow
valve (capillary)

Liquid helium at 4.2 K

Magnet support rods

Lambda plate liquid
helium valve

Lambda plate

Superconducting
magnet

Sample holder
with heater

Convection of liquid
Helium below 4.2 K

Vaporizer with heater

Liquid helium
near 2.2 K

Figure 5.5: Helium bath cryostat equipped with a superconducting magnet.

be decreased using a mechanical pump connected to the sample chamber evacuation valve. As the boiling point of helium decreases with low pressure, a temperature of 2 K can be achieved around the sample holder. The temperature regulation is provided by adjusting the input power of a resistive heater in the sample chamber and monitoring the temperature with a diode. Both the resistive heater and diode are connected to a temperature controller. Using a temperature controller, one can set the cooling or warming rate of the sample at a specific value with a high accuracy and achieve a temperature stability better than 0.01 K. In addition, measurements performed as a function of magnetic field requires a constant temperature, which requires a high temperature stability to obtain the field dependence of the acoustic velocity or dielectric constant.

The superconducting magnet in the helium bath cryostat is a solenoid. This magnet normally produces a variable magnetic field up to 13 T at 4.2 K (See Fig. 5.5). However, it is possible to enhance its performance using the lambda refrigerator (also called the lambda plate) [95]. Lambda refrigerators consist of a liquid helium valve and a chamber with a pumping line. Liquid helium continuously flows into the chamber and is pumped to a low pressure. Cold helium below the lambda plate sinks to the bottom of the chamber and sets up convection currents, maintaining the temperature of the magnet at 2.2 K. In this way, the magnet can produce a variable field up to 15 T.

5.2 Dielectric measurements

Dielectric constants of a solid can be determined by measuring capacitance. The dielectric constant and capacitance are related by the equation

$$C = \epsilon_r \epsilon_0 \frac{A}{d},$$

(5.6)

where ϵ_r is the dielectric constant of the material and ϵ_0 is the vacuum permittivity. Here, A
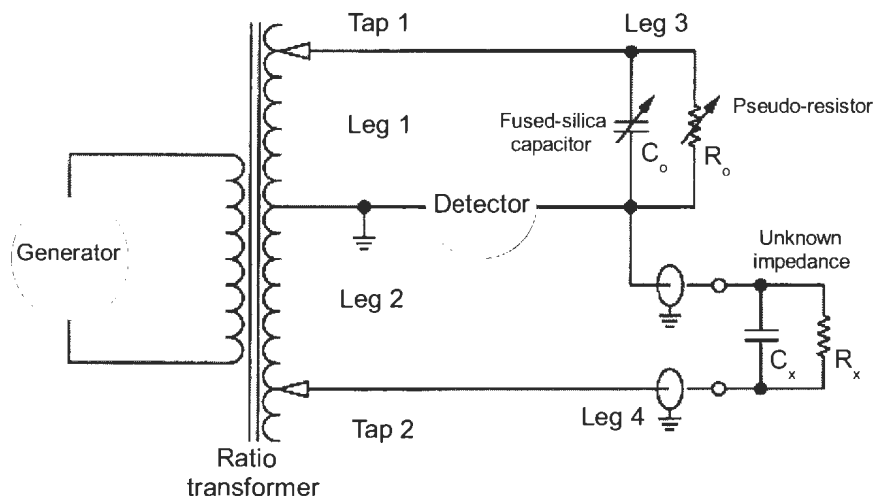
Figure 5.6: A schematic diagram of the basic capacitance bridge circuit, the Andeen-Hagerling Inc., model AH2550A.

corresponds to the area of two parallel plates separated by a distance d. In order to measure the capacitance of the sample, two thin brass plates were glued on two parallel surfaces of the sample using silicone. Measurements were performed using a 1 kHz ultra-precision capacitance bridge (Andeen-Hagerling Inc., model AH2550A). The basic bridge circuit is shown in Fig. 5.6. A generator excites the ratio transformer with a 1 kHz oscillating electrical signal. The ratio transformer consists of leg 1 and leg 2 of the basic bridge. A large number of transformer taps available in leg 1 and leg 2 allows the selection of precisely defined voltage values to drive leg 3 and leg 4. Leg 3 is comprised of several fused-silica capacitors and other circuit elements in order to form a stable resistor. The sample is connected on leg 4. The basic function of the microprocessor in the instrument is to minimize the voltage at the detector by selecting (or balancing) taps 1 and 2 and selecting C_o and R_o. The detector can measure both in-phase and quadrature (90°-out-of-phase) voltages with respect to the voltage of the generator so that the resistive and capacitive components of the sample

65

is independently balanced. When the minimum voltage at the detector is achieved, the capacitance of the sample can be determined since the ratio of the sample capacitance to C_o is equal to the ratio of the Tap 1 voltage to Tap 2 voltage.

5.3 Brillouin Scattering

The experimental setup for Brillouin scattering measurements in backscattering geometry is shown in Fig. 5.7. A single mode Ar^+ laser (Coherent Inc.) operating at 514.5 nm or a solid state laser (Coherent DPSS 532) with an output wavelength of 532 nm is used as the incident light source. The incident beam from the laser is split into two beams by using a beam splitter. One of the beams is used as the reference beam to stabilize the alignment of a Sandercock-type 3+3 tandem Fabry-Perot (FP) interferometer. The other beam serves as the incident light beam. The polarization of the incident light is adjusted using a half-wave plate (HWP). The incident beam is directed towards lens L_1 (f/2.2, f = 5.5 cm) with prism Pr. L_1 both focuses the incident beam on the sample and collects the scattered beam from the sample. A microscope (MS) is used for visual observation of the sample in order to accurately focus the beam on the sample surface and collect the scattered beam using L_1. Considering that the scattered beam collected by the lens (L_1) will have the same diameter, an alternative way is to adjust the spot diameter of the scattered beam such that the spot diameter remains the same between the lens L_1 and interferometer. A polarizer (P) is used to obtain the desired polarization of the scattered light. A lens (L_4) focuses the scattered beam onto pinhole (A_1) for data collection and acquisition.

In a typical Brillouin light scattering experiment, acoustic waves can be revealed in the frequency range between 1 and 150 GHz. Since the inelastically (Brillouin) scattered light is weak compared to the elastically scattered contribution, a high resolution spectrometer with a high contrast is required. This can be provided by a Fabry-Perot (FP) interferometer. A
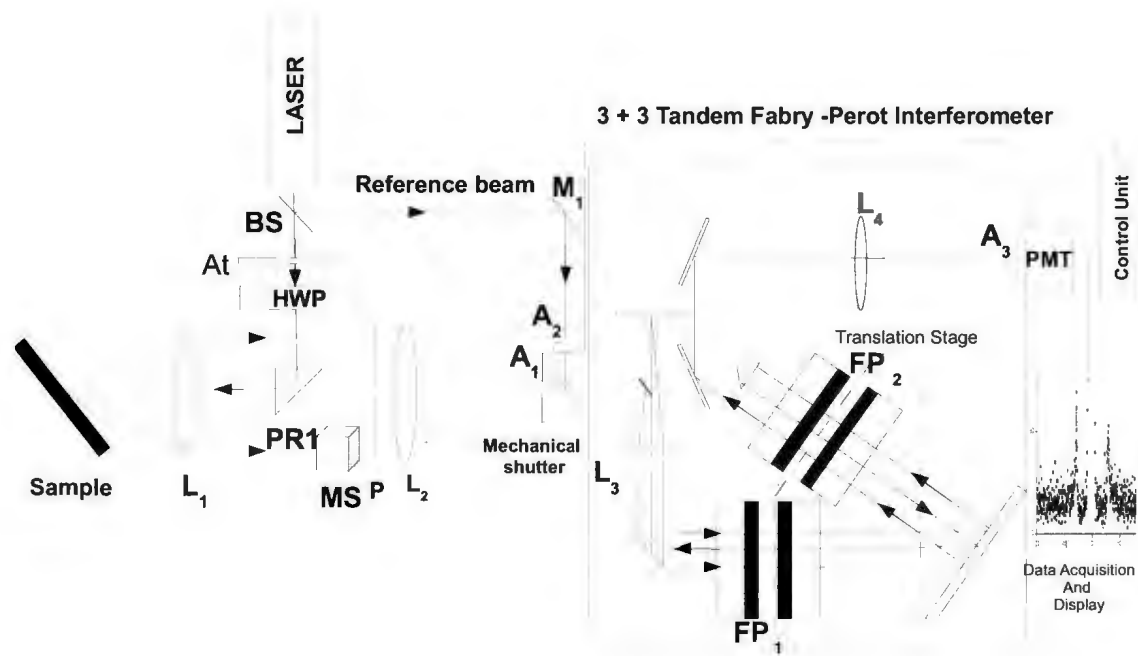
Figure 5.7: Experimental setup for Brillouin light scattering measurements. Incident light is shown by continuous lines while the scattered light entering the FP interferometer is shown by dashed lines. At = attenuator; HWP = half-wave plate; Pr = prism; L_j = lens; M_j = mirror; P = polarizer; MS = microscope; A_j = pin hole; FP = Fabry-Perot interferometer; PMT = photomultiplier tube.
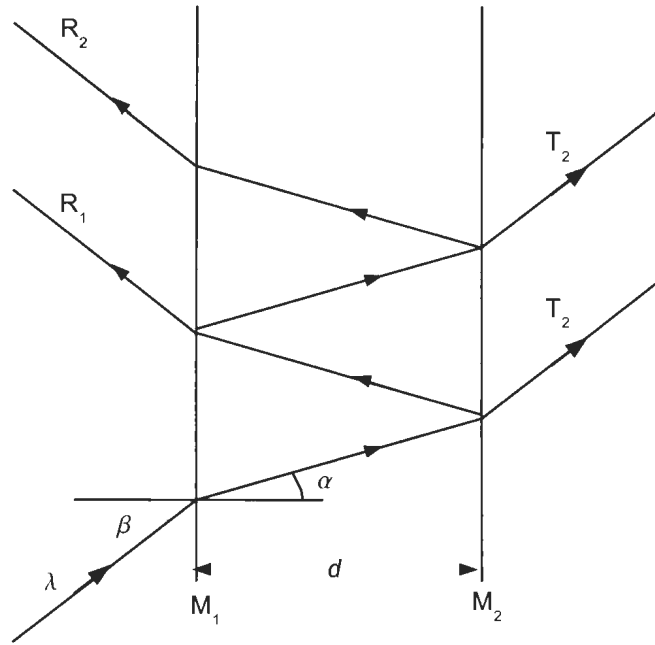
Figure 5.8: The sketch of a Fabry-Perot etalon consisting of two plane parallel mirrors. M_j: mirror, R_j: j-th reflected beam, $T_j = j$-th transmitted beam.

brief theory explaining how a Fabry-Perot interferometer is given in the following paragraphs.

A Fabry-Perot interferometer consists of two parallel, highly reflecting plane surfaces, called an *etalon* (Fig. 5.8). In a Fabry-Perot interferometer, the spacing between the parallel surfaces is variable so that it serves as a spectrometer. Assume a plane wave of wavelength λ is incident at angle α on the etalon as shown in Fig. 5.8. The plane wave is multiply reflected on both surfaces while a small portion is transmitted at each reflection. Reflected beams are indicated with R_j while transmitted beams are labeled as T_j. The path difference between each succeeding reflection is given by

$$l = 2nd \cos \alpha, \tag{5.7}$$

where n is the refractive index of the medium between the mirrors separated by d. The

phase difference is then

$$\delta = \frac{2\pi l}{\lambda} = \frac{4\pi nd \cos \alpha}{\lambda}. \tag{5.8}$$

If the reflectivity R of the parallel surfaces is known, then the intensities of the reflected and transmitted light, I_R and I_T, can be calculated as

$$I_R = I_0 R \frac{4 \sin^2 \delta/2}{(1 - R^2) + 4R \sin^2 \delta/2} \tag{5.9}$$

and

$$I_T = I_0 \frac{1 - R^2}{(1 - R^2) + 4R \sin^2 \delta/2}, \tag{5.10}$$

where I_0 is the intensity of the incident plane wave. Eqs. 5.9 and 5.10 are known as Airy formulae. When the spacing between the parallel surfaces is an integer multiple of wavelength λ, the boundary conditions require that the phase difference be given by $\delta = 2m\pi$, where m is an integer specifying the order of interference. Therefore, for each interference order m, we can see from Eq. 5.10 that a transmission maximum, $I_T = I_0$, occurs. The frequency spacing between the transmission maximum of each successive interference order $(m \to m + 1)$ is known as the *free spectral range* (FSR). Using Eq. 5.8 and $\lambda = c/\nu$, we obtain the free spectral range as

$$FSR = \frac{c}{2d\sqrt{n^2 - \sin^2 \alpha}}. \tag{5.11}$$

In most cases, the incident beam is normal to the parallel surfaces, i.e., $\alpha = 0$. In addition, the space between the parallel surfaces is filled with air, which has a refractive index $n = 1$. Then, the free spectral range (Eq. 5.11) can be written as

$$FSR = \frac{c}{2d}. \tag{5.12}$$

A measure of the resolution of the interferometer is the *finesse* (F). The finesse is defined as the ratio of FSR to the full width at half maximum of the transmission maxima, $\delta\nu$,

$$F = \frac{FSR}{\delta\nu} = \frac{\pi\sqrt{R}}{1 - R}. \tag{5.13}$$

69

The width of each transmission peak is determined by the reflectivity R of the parallel surfaces. Therefore, the finesse also depends on the reflectivity R. Another important term determined by the mirror reflectivity is the contrast C, which is defined as the ratio of the peak height to the minimum intensity. The contrast is given by

$$C = 1 + \frac{4F^2}{\pi^2}. \tag{5.14}$$

In practice, the finesse value is less than 100 which places an upper limit to the contrast $C \leq 10^4$ [84]. For transparent samples, this contrast value is sufficient [84]. However, for opaque samples, a higher contrast is normally required since the intensity of the Brillouin peaks is much smaller [84]. A way to increase the contrast is to introduce multi-pass operation, that is, to pass the light through the interferometer several times. An alternative approach is to combine two interferometers of unequal mirror spacing such as in a Sandercock type six-pass tandem Fabry-Perot interferometer (see Fig. 5.7). A tandem instrument consists of two FP interferometers of unequal mirror spacing d_1 and d_2. This prevents the overlap of neighboring interference orders, hence providing a higher free spectral range by a factor of 10-20 as compared to a single FP instrument. The FP interferometer serves as a spectrometer by varying the mirror spacings d_1 and d_2 to scan the light intensity at different wavelengths (Fig. 5.7). The variable mirror spacing is provided by the translation stage (enclosed by red fine-dashed lines) on which one mirror from each FP interferometer is mounted as shown in Fig 5.7. Focused scattered beam entering pinhole A_1 is recollimated using lens L_3 to pass 3 times through each FP interferometer. The scattered light is then focused onto pinhole A_3 using lens L_4 and detected by a photomultiplier tube (PMT). Pinholes A_1 and A_3 are opened to 200-450 μm and 300-700 μm, respectively. Light detected by the photomultiplier tube can be viewed on a computer.

5.3.1 The cryogenic system for the optical setups

In order to perform Brillouin and Raman scattering experiments between room temperature and low temperatures, a two-stage closed-cycle helium refrigerator was used. The two-stage closed-cycle helium refrigerator consists of two units: a compressor module (APD Cryogenics Inc., model HC2 or model HC4) and an expander module (Air products, model DE202). The compressor is connected to the expander with two pressurized gas lines. The refrigeration in the expander is achieved in two stages (see Fig. 5.9). The temperature in the first stage is approximately 80 K and is not regulated. The sample is mounted in the second stage which is surrounded by a brass radiation shield. The temperature in this stage is regulated using a cryogenic temperature controller (LakeShore Cryotronics, model DTC 500). A silicon diode and two resistive heaters are used to stabilize the temperature. A diffusion pump system is used to keep the sample under high vacuum in order to provide thermal insulation.

5.4 Raman scattering

A schematic diagram used for Raman backscattering measurements is shown in Fig. 5.10. The incident light is generated by either a tunable Ar^+ laser (Spectra Physics, series 2000) or a solid state laser (Coherent DPSS 532) operating at 532 nm. The Ar^+ laser operates at wavelengths of 514.5 nm, 501.7 nm, 496.5 nm, 488.0 nm, 476.5 nm, 472.9 nm, 465.8 nm, and 457.9 nm. Usually a 514.5 nm or 488 nm output is used. A mirror (M_0) and a prism (Pr) are used to direct the incident beam toward the sample. Then, the incident beam is focused on the sample using lens L_1 (f = 20.0 cm). The backscattered light is collected by the same lens (i.e., L_1). Focusing the incident beam on the sample and the collimation of the scattered light is achieved with the same procedure as in Brillouin scattering measurements. The polarization of the scattered light is selected by using a polarizer (P). The scattered light is

Vacuum shroud
And
radiation shield
windows

Sample holder
Sample
Second stage heat station
Radiation shield

First resistive heater

First stage heat station

Vacuum shroud

Low pressure
gas line

high pressure
gas line

Valve disk

Valve motor

Valve motor assembly
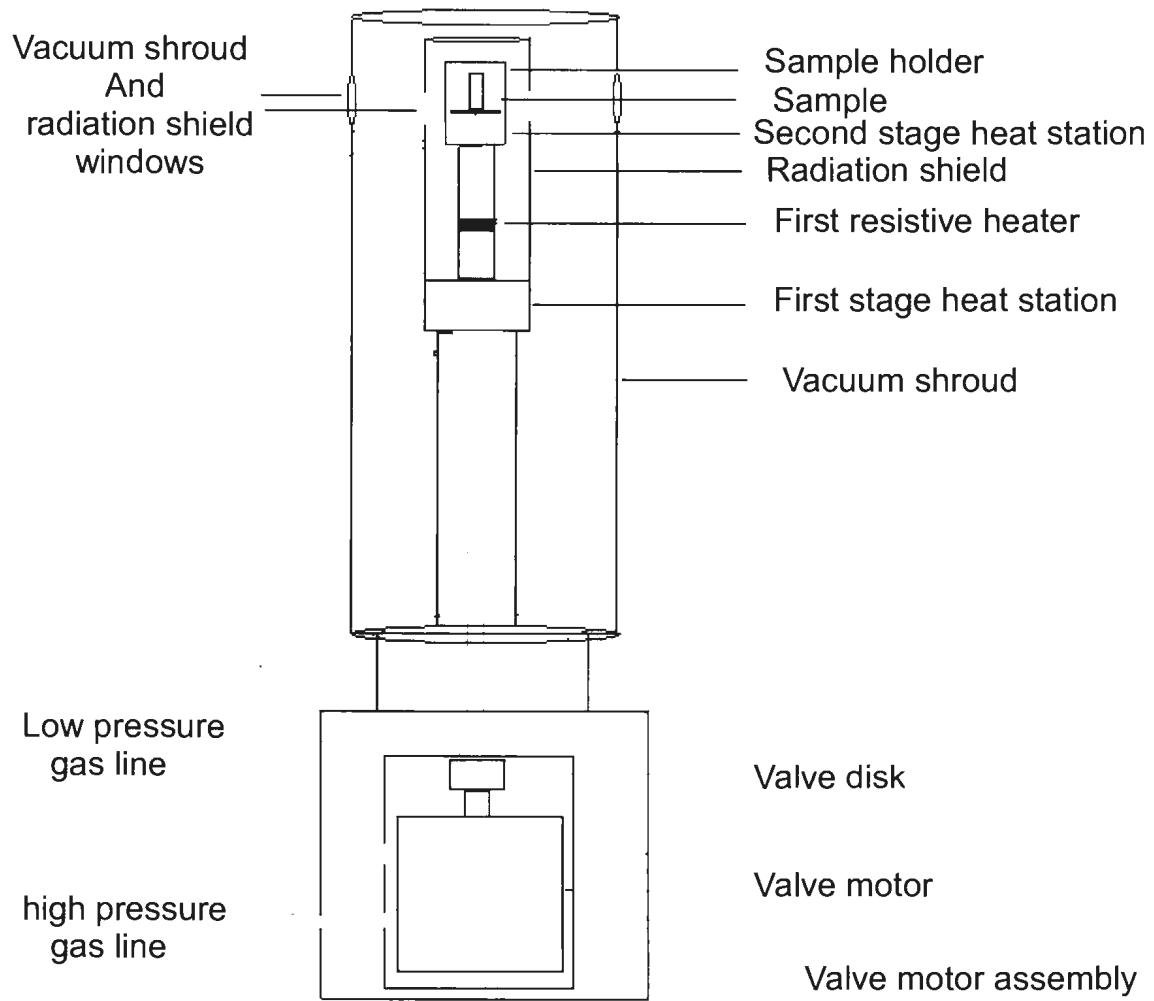
Figure 5.9: The expander module of the closed-cycle helium refrigeration system.
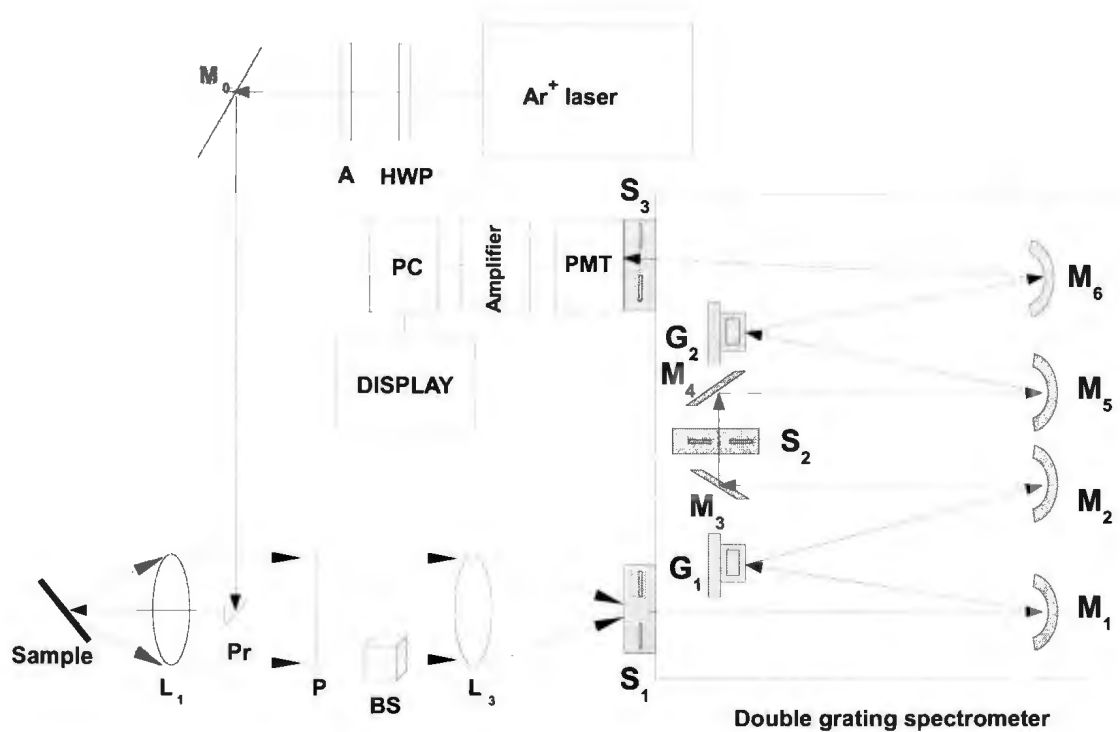
Figure 5.10: Experimental setup for Raman scattering.

focused onto the entrance slit of the spectrometer using a lens (L_3, f = 40 cm) and detected using a data collection and acquisition system consisting of a double grating spectrometer (Spex Industries Inc., model 1401), a photomultiplier tube (Perkin Elmer, model MP900), an amplifier-discriminator, a photon counter (Princeton Applied Research, model 1109), and a computer.

Raman Spectrometer

The Raman spectra were collected using a double grating monochromator (Spex Industries Inc., model 1401) with a focal length of 85 cm and an f-number of 7.8 (See Fig. 5.10). It employs first order diffraction from the gratings which follows the fundamental grating

equation

$$m\lambda = s(\sin\alpha + \sin\beta) \tag{5.15}$$

where m is the order of diffraction, λ is the wavelength of light, and s is the grating spacing. The symbols α and β represent the angle of incidence, and angle of diffraction, respectively. The theoretical resolving power of a grating is given by

$$R_T = \frac{\lambda}{\Delta\lambda} = \frac{\nu}{\Delta\nu} = Mm, \tag{5.16}$$

where M is the total number of the grating grooves, and m is the order of diffraction. Each grating (with an area of 102 mm x 102 mm) consists of 1800 grooves per mm which corresponds to a theoretical resolving power of $R_T = Mm \sim 10^5$. In general, the theoretical resolution is reduced by aberrations and imperfections associated with mirrors, lenses, and the width of the slits. In order to obtain optimum resolution, the first collimating mirror M_3 must be completely illuminated by the scattered light entering from slit S_1. Therefore, lens L_3 (f/8) is selected to have a similar f-number to that of the spectrometer (f/7.8). The light diffracted by grating G_1 is focused by mirror M_2 onto plane mirror M_3. After the light passes through intermediate slit S_2 and gets reflected from plane mirror M_4, it is sent to second grating G_2 by mirror M_5. Then, it is focused by mirror M_6 onto exit slit S_3 for detection by the photomultiplier tube PMT. Entrance and exit slits, S_1 and S_3, of the spectrometer are opened to 300 μm while intermediate slit S_2 is opened to 400 μm to a spectral resolution of ~ 4 cm^{-1}. The scanning step size is set to 0.5-0.8 cm^{-1} with a dwell time of 5-120 s per step.

Chapter 6

Brillouin Scattering Measurements on CuFeO$_2$ and CuCrO$_2$

As shown in Ref. [1], softening of the elastic constants in CuFeO$_2$ at the magnetic and structural transition, $T_{N1} = 14$ K, is well accounted for using a Landau model for a pseudoproper ferroelastic transition from the trigonal $R\bar{3}m$ phase to the monoclinic $C2/m$ phase. According to the Landau model, the transverse acoustic mode propagating along the x axis with a polarization along the y axis, $T_x P_y$, in CuFeO$_2$ should show complete softening. However, due to acoustic attenuation, the complete softening of this mode could not be observed with sound velocity measurements [1]. As a result, we made an attempt to measure the soft acoustic mode down to T_{N1} using Brillouin scattering. These results are presented in Sec. 6.1. Because multiferroic CuCrO$_2$ is isostructural to CuFeO$_2$ at room temperature, it might also show an $R\bar{3}m \rightharpoonup C2/m$ ferroelastic transition at low temperatures. Therefore, we investigated acoustic waves in CuCrO$_2$ using Brillouin measurements down to low temperatures. Before doing the low temperature measurements, we also performed a set of room temperature measurements to determine the elastic constants. Since the refractive indices of CuCrO$_2$ are not reported, we performed a set of reflection geometry Brillouin scattering

measurements to simultaneously determine the acoustic velocities and refractive indices of $CuCrO_2$. We present the results on $CuCrO_2$ in Sec. 6.2.

6.1 $CuFeO_2$

In order to determine whether the soft acoustic mode $T_x P_y$ shows complete softening at the ferroelastic and antiferromagnetic transition at T_{N1}, we performed Brillouin scattering measurements on single crystals of $CuFeO_2$. Single crystals of $CuFeO_2$ were grown by the floating zone method using a four mirror image furnace by Dr. Geetha Balakrishnan at the Department of Physics, University of Warwick [52]. All samples were cut from a large single crystal which has the shape of a long cylinder with the cylindrical axis close to the crystallographic z axis. Dimensions of the samples vary but have approximately an area of 2 mm $\times$ 2 mm on the studied surface and 1 mm along the surface normal (see Fig. 6.1). To minimize surface scattering, samples were polished using abrasive slurry with 50 nm Al_2O_3 grains in order to minimize surface scattering. Room temperature Brillouin measurements on $CuFeO_2$ were performed with a single mode solid state laser operating at 532 nm. An incident beam of 80 mW was focused on the sample surface with a lens which has a focal length of 5.5 cm and an f-number of 2.4 (f/2.4). The free spectral range was set to 25 GHz. The frequency shifts and linewidths of the modes were determined with a fit to a Gaussian profile.

Even though Brillouin scattering can occur at any angle, backscattering and right-angle scattering are more commonly used since they are easy to carry out. Backscattering and right-angle scattering geometries are illustrated in Fig. 6.2. The wave vectors of incident and scattered light outside the sample are represented by $\mathbf{k_i}$ and $\mathbf{k_s}$. The acoustic waves observed with both geometries are also shown in Fig. 6.2, where the wave vectors of bulk and surface acoustic waves are denoted by $\mathbf{q_B}$ and $\mathbf{q_{SAW}}$. Sample in Fig. 6.2a is represented as
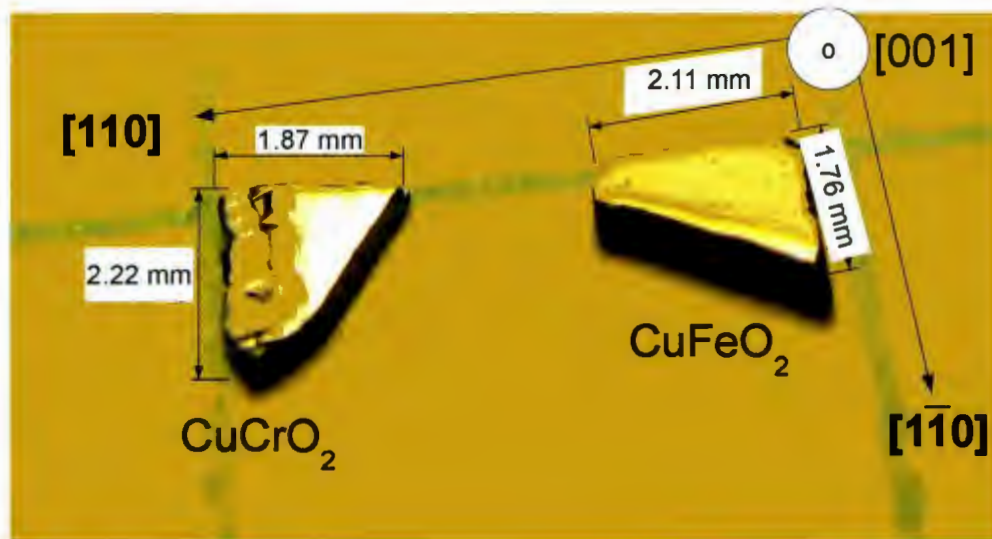
Figure 6.1: Two of the **a)** CuCrO$_2$ and **b)** CuFeO$_2$ samples used in Brillouin and Raman scattering experiments.
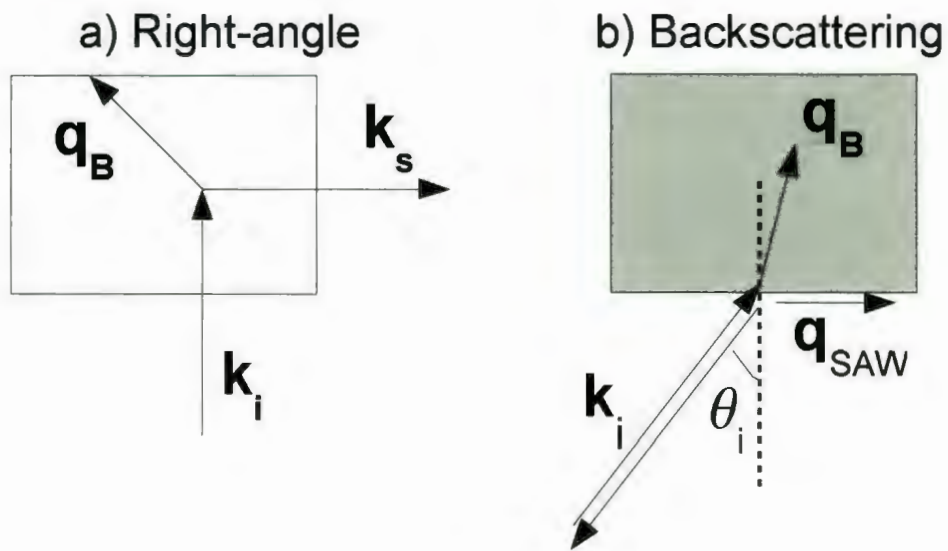
Figure 6.2: Common scattering geometries for Brillouin light scattering **a)** Right angle scattering **b)** Backscattering.

transparent to point out the requirement for sample transparency in right-angle scattering measurements. $CuFeO_2$ is an opaque material (semiconductor) with a direct band gap of 1.67 eV [96]. The incident light in our experiments is 532 nm which corresponds to an energy of 2.33 eV. Therefore, we cannot use right-angle scattering on $CuFeO_2$. The backscattering geometry is illustrated in Fig. 6.2b, where θ_i and broken lines correspond to the angle of incidence and surface normal. In contrast to right-angle scattering geometry, backscattering can also be used on opaque samples, which is why the sample in Fig. 6.2b is represented with a gray color. In semiconductors, usually Brillouin scattering occurs via both elasto-optic and surface-ripple mechanisms, that is, both bulk acoustic waves and surface acoustic waves can be observed [84]. Therefore, we used backscattering geometry in the Brillouin scattering measurements on $CuFeO_2$. Measurements performed at normal backscattering ($\theta_i = \theta_s = 0$) did not show any acoustic modes. As a result, all measurements were done with a backscattering geometry at an oblique incidence as shown in Fig. 6.2.

Fig. 6.3 shows the sample orientation for the backscattering measurements. The polarization of the incident light was in the plane of incidence, which is defined as the plane spanned by the surface normal and incident light wave vector. The polarization of the scattered light was not measured. The incident and scattered light propagated at an angle θ_i with respect to the surface normal, which is parallel to the z axis in Fig. 6.3. Note that we can represent the scattering geometry in Fig. 6.3 in a convenient way using the Porto notation, $k_i(e_i e_s)k_s$. In this representation, k_i and k_s correspond to the propagation directions of the incident and scattered light, whereas e_i and e_s are the polarizations. When the direction of the incident (scattered) light propagates at angle θ relative to one of the crystallographic axes, we use an apostrophe as a superscript. For example, the scattering geometry in Fig. 6.3 can be represented by $z'(pu)\bar{z}'$, where the label z' corresponds to an incident light direction at an angle θ_i with respect to the surface normal which is parallel to the z axis. In addition, p corresponds to a polarization in the plane of incidence and u means unpolarized.
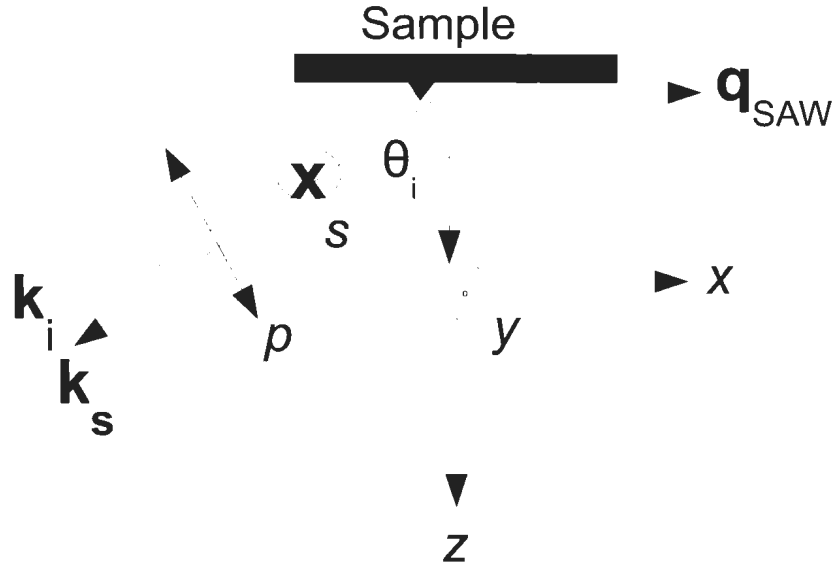
Figure 6.3: Experimental geometry and sample orientation in Brillouin scattering measurements on $CuFeO_2$.

Spectra obtained with backscattering geometry are shown in Fig. 6.4; the angle of incidence is indicated on the right hand side of each spectrum. We observe only one mode in all spectra obtained with an angle of incidence varying from 40° to 80°. As the angle of incidence is decreased, the frequency shift also decreases. In order to determine whether or not the mode is a bulk or surface acoustic wave, we present in Fig. 6.5 the frequency shift vs. $\sin \theta_i$. Dominant sources of uncertainty in the frequency shift are the angle of incidence θ_i and mirror spacing of the interferometer while the uncertainty in $\sin \theta_i$ is due to θ_i. As seen in Fig. 6.5, the frequency dependence is linear and the frequency shift extrapolates to zero as expected for surface acoustic waves

$$\Delta \nu_{SAW} = \pm \frac{2 \sin \theta_i V_{SAW}}{\lambda_i}. \tag{6.1}$$

Therefore, we conclude that the mode observed in our spectra is a surface acoustic mode.

79
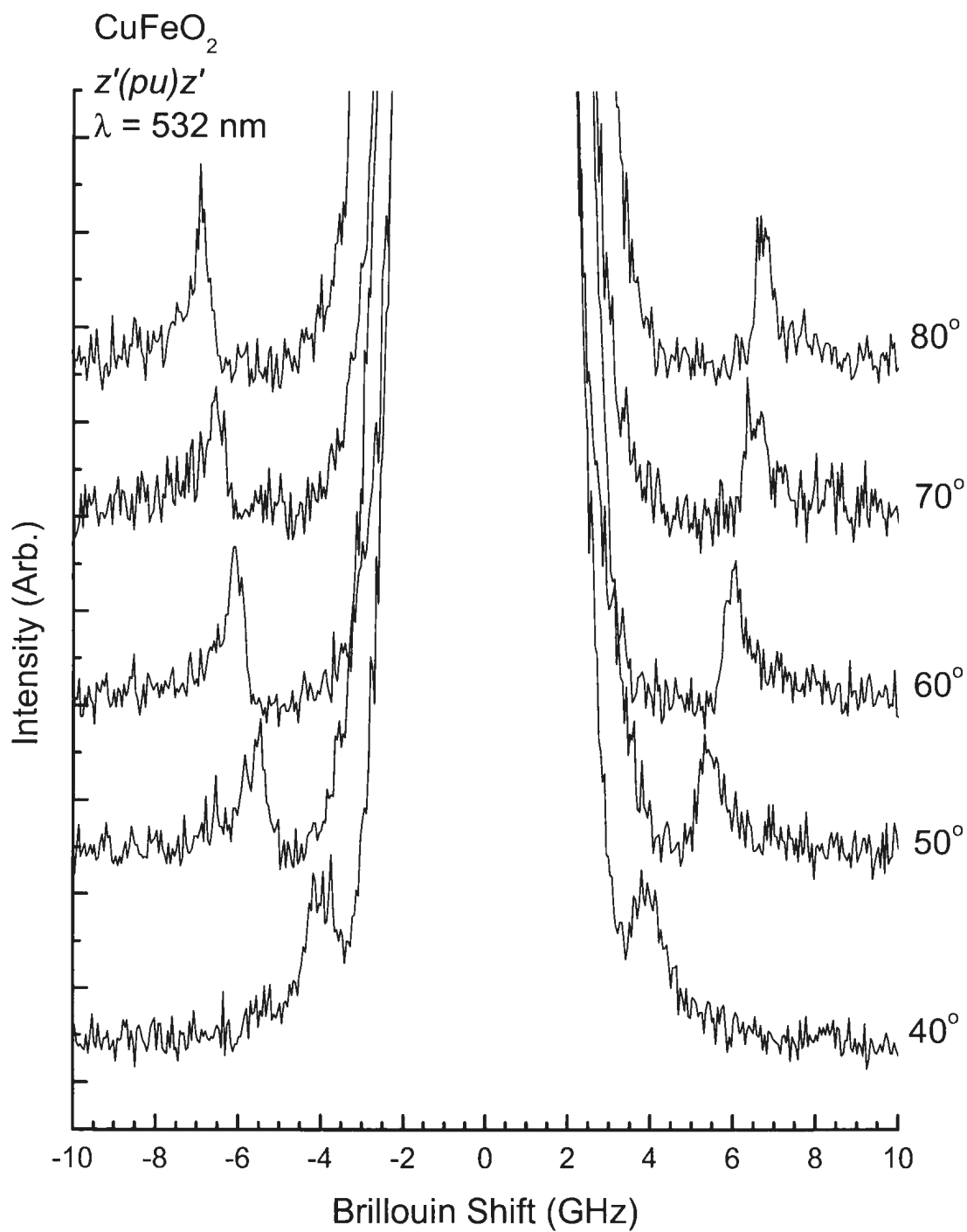
Figure 6.4: Brillouin spectra of $CuFeO_2$ obtained with a backscattering geometry at an angle of θ_i relative to the z axis.

From the linear fit to the data in Fig. 6.5, we obtain $V_{SAW} = 1800 \pm 40$ m/s for the velocity of the surface acoustic wave (; to improve the linear fit, a point at $\theta_i = 0$ was added to the data. Without the point at $\theta_i = 0$, the frequency shift still extrapolates to zero within the uncertainty). It might be worth mentioning that measurements performed with polarized incident and scattered light, (ss), (sp), (pp), and (ps), show that the surface acoustic mode is observed only in the pp polarization (not shown). Here, s corresponds to a light polarization perpendicular to the plane of incidence.

The fact that we cannot observe any bulk modes is due to the high opacity of $CuFeO_2$ crystals. In an opaque material, scattering from a bulk acoustic wave occurs in a volume close to the surface due to the high value of the *extinction coefficient* κ [84]. The extinction coefficient is the imaginary part of the complex refractive index given by $n_c = n + i\kappa$. In that case, the incident light penetrates a short distance beneath the sample surface and is coupled to phonons with a large range of wavevectors. This causes broadening in the linewidth $\delta\nu_B$ of the Brillouin peaks in a Brillouin spectrum. The linewidths of the Brillouin peaks for opaque materials $\delta\nu_B = 4VK_i\kappa/\pi$, where K_i is the incident light wave vector in the sample, mainly depend on the extinction coefficient. With increasing opacity, the surface ripple mechanism may dominate and bulk modes may not even be observed [84, 97] as shown in $CuFeO_2$ (Fig. 6.4).

Unfortunately, as our measurements on $CuFeO_2$ show only one surface acoustic mode (Fig. 6.4), we are not able to determine whether the bulk mode T_xP_y shows complete softening as expected for the ferroelastic transition observed in $CuFeO_2$ [1]. At this point, it is important to note that a soft bulk mode implies the existence of a soft surface mode [98, 99]. If the velocity of the surface acoustic wave (Fig. 6.4) is related to the elastic constants that determine the velocity of T_xP_y, then we can still determine if T_xP_y shows complete softening by measuring the soft acoustic mode velocity down to T_{N1}.

The elastic constants of $CuFeO_2$ have already been determined by ultrasonic measure-
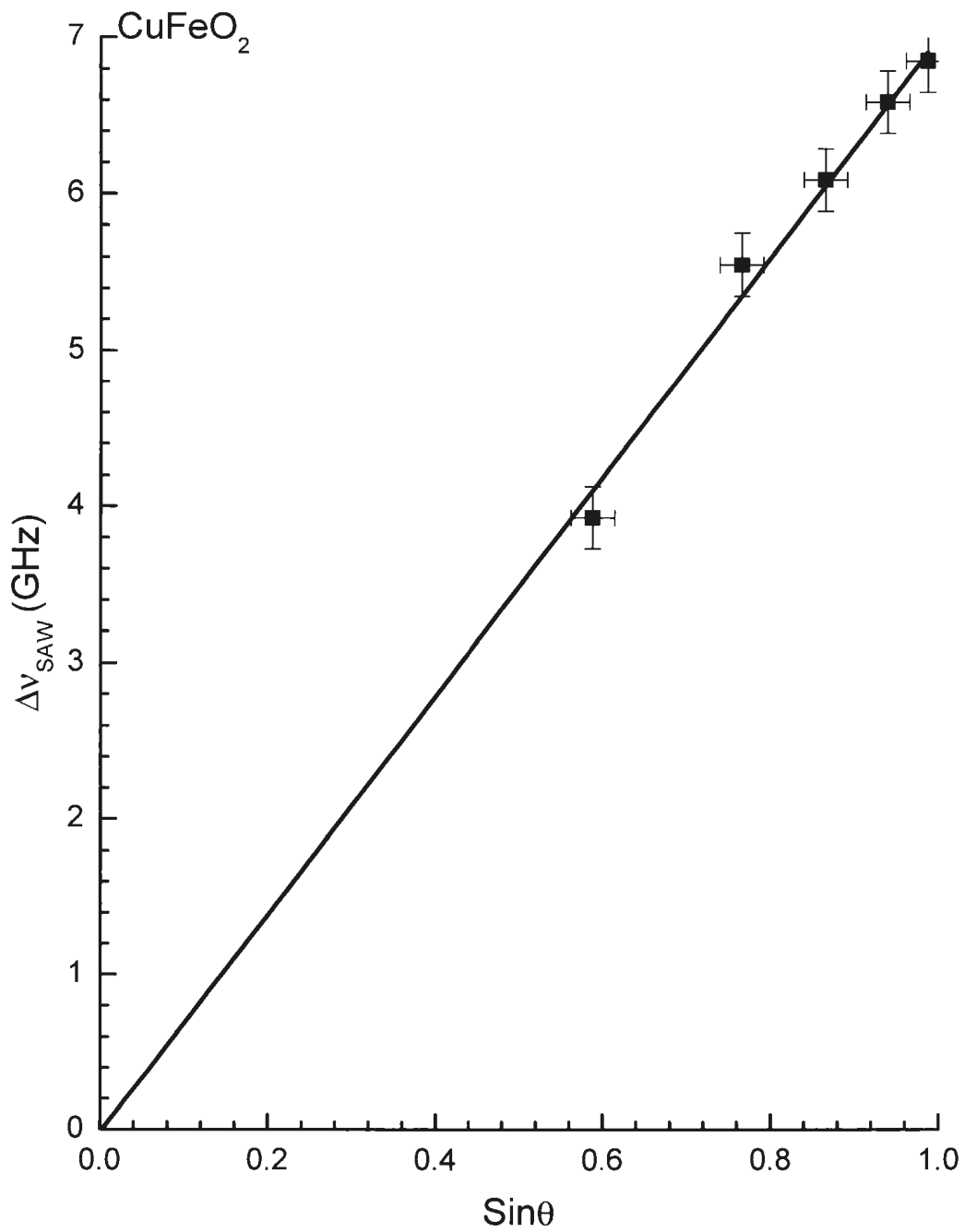
Figure 6.5: Frequency shift of the surface acoustic wave in $CuFeO_2$ propagating along the x axis against the sine of the angle of incidence θ_i. The angle θ_i is relative to the normal of the sample surface which is parallel to the z axis.

ments [1]. Using the elastic constants of $CuFeO_2$ [1], we can plot the angular dependence of the bulk mode velocities and compare them with the angular dependence of the surface acoustic mode velocity. By comparison, we can find out which elastic constants determine the surface acoustic mode velocity. Therefore, we measured the angular dependence of the frequency shift of the surface acoustic mode in the xy and xz planes. The experimental geometries for these measurements are illustrated in Fig. 6.3. If we keep the angle of incidence (θ_i) constant and rotate the sample parallel to xy plane, the propagation direction of the surface acoustic wave rotates in the xy plane. Measurements in the xz plane were done in a similar way. Using the frequency shifts, we calculate the velocity of the surface acoustic wave according to Eq. 6.1 and plot it against the angle relative to x axis in Fig. 6.6, where squares represent surface modes propagating in the xy plane whereas circles are used for modes propagating in the xz plane. According to Fig. 6.6, the velocity of the surface acoustic mode does not change in the xy plane within the uncertainty. On the other hand, the measurements in the xz plane show a large anisotropy. The velocity increases from 1800 $\pm$ 40 m/s along the x direction to 3100 ± 40 m/s along the z direction, giving an anisotropy ratio of 1.72 ± 0.06.

In Figs. 6.7-6.8, we compare the angular dependence of the inverse velocities of the surface (squares) and bulk (lines) modes using a polar plot. The polar plots for the bulk modes are obtained using the elastic constants determined by ultrasonic velocity measurements [1]. In the xy plane (Fig. 6.7), the velocity of the surface wave is close to that of the fast transverse mode velocity (continuous line) which mainly depends on the elastic constant C_{44}. In the xz plane, along the directions close to the x axis, the velocity of the surface acoustic mode is close to the fast transverse mode velocity (continuous line), which is dominated by C_{44} (Table 4.1). However, in the directions close to the z axis, the surface mode velocity is between the longitudinal (dashed line) and fast transverse mode velocities. According to Table 4.1, the longitudinal mode velocity mainly depends on C_{33} along these directions.
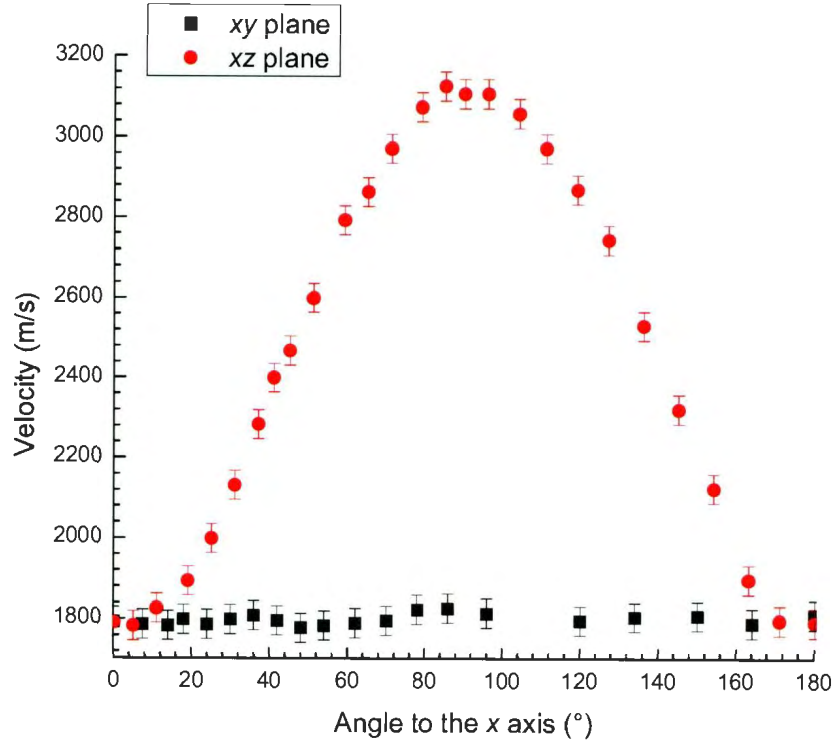
Figure 6.6: Velocity variations of the surface acoustic wave in the xy and the xz planes of $CuFeO_2$.

These results show that the surface mode velocity mainly depends on C_{44} and C_{33}. According to Table 4.1 and Ref [1], softening observed on the T_xP_y mode (Fig. 1.3) is primarily due to the C_{66} elastic constant. Unfortunately, as the surface acoustic mode velocity depends on C_{44} and C_{33}, we cannot determine whether the soft acoustic mode T_xP_y shows complete softening.
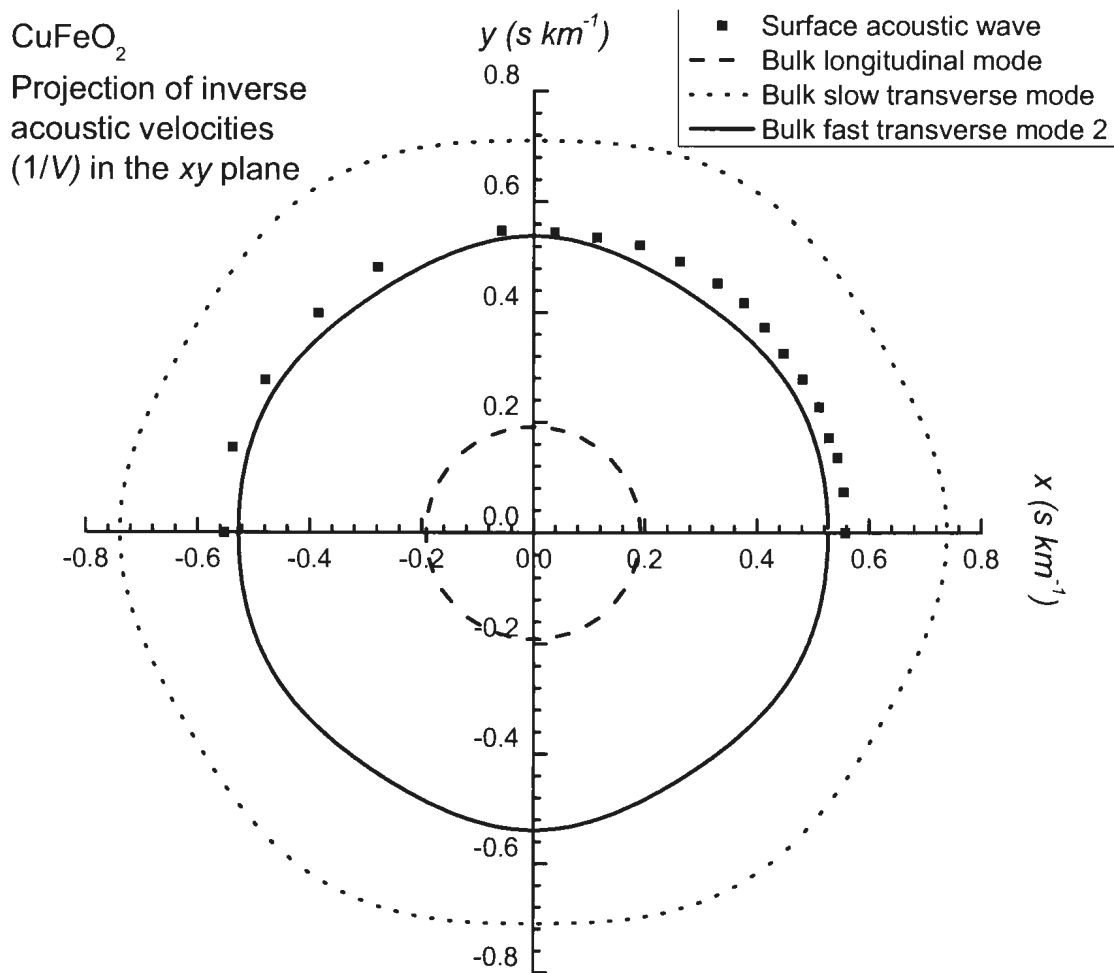
Figure 6.7: Projection of inverse bulk and surface acoustic velocities in the xy plane of CuFeO$_2$. Inverse velocities of bulk modes in CuFeO$_2$ were calculated using the values of elastic constants presented in Ref. [1].
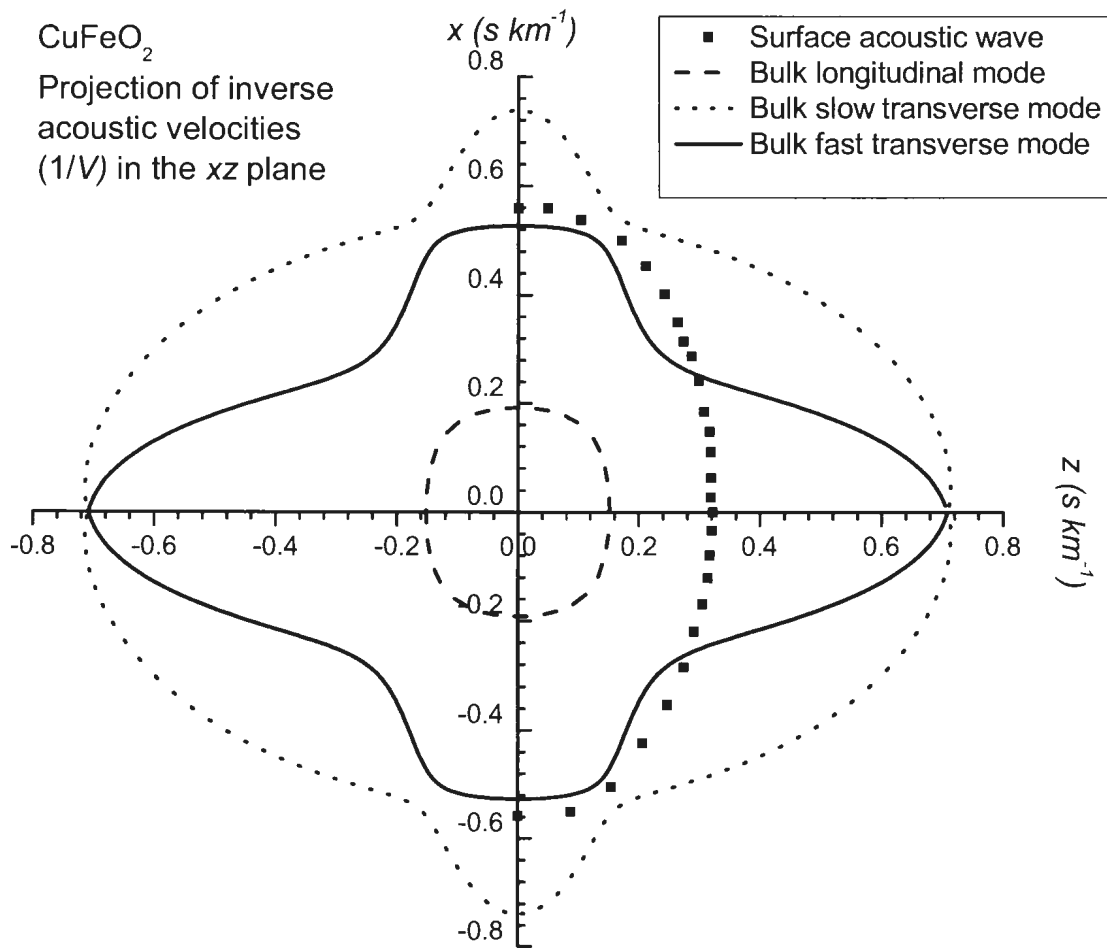
Figure 6.8: Projection of inverse acoustic velocities in the xz plane of $CuFeO_2$. Inverse velocities of bulk modes in $CuFeO_2$ were calculated using the values of elastic constants presented in Ref. [1].

6.2 CuCrO$_2$

In this section, we investigate the temperature dependence of the elastic properties of CuCrO$_2$. At room temperature, we identify the acoustic modes propagating along the x, y, and z axes. Then, using reflection geometry, we determine the acoustic velocities and refractive indices of CuCrO$_2$. Finally, we present low temperature measurements.

6.2.1 Elastic constants and refractive indices of CuCrO$_2$

Brillouin scattering measurements were performed on single crystals of CuCrO$_2$ which were grown from Bi$_2$O$_3$ flux [27] by Dr. Tsuyoshi Kimura and Dr. Tsuyoshi Otani at Osaka University. The samples were platelets with a surface area of 2 mm x 2 mm in the triangular lattice plane (xy plane) and about 0.4 mm long along the c axis (See Fig. 6.1). Similar to the preparation of CuFeO$_2$ samples, CuCrO$_2$ samples were mechanically polished using abrasive slurry with 50 nm Al$_2$O$_3$ grains. As CuCrO$_2$ is not transparent, we could not apply the right-angle scattering configuration for Brillouin scattering measurements. Instead, measurements were performed using the geometry illustrated in Fig. 6.9 with 532 nm or 514.5 nm incident light and a beam power of 40 mW. The incident and scattered light wave vectors outside the sample are represented by $\mathbf{k_i}$ and $\mathbf{k_s}$. The wave vectors of bulk and surface acoustic waves are denoted by $\mathbf{q_B}$ and $\mathbf{q_{SAW}}$.

The backscattering spectra obtained at an angle θ_i relative to the z axis (Fig. 6.9) are shown in Fig. 6.10. The angle of incidence is indicated on the right hand side of each spectrum ($z'(pu)\bar{z}'$). As seen in Fig. 6.10, each spectrum shows three modes. At 76°, the frequency shifts are 7.5 GHz, 28.5 GHz and 25.6 GHz. As the angle of incidence is reduced, the frequency shift of each mode decreases. It is also noticeable that the high frequency modes start to merge as the angle of incidence decreases. In order to identify these modes, we follow the same procedure as for CuFeO$_2$. From the Brillouin equations of bulk and

87
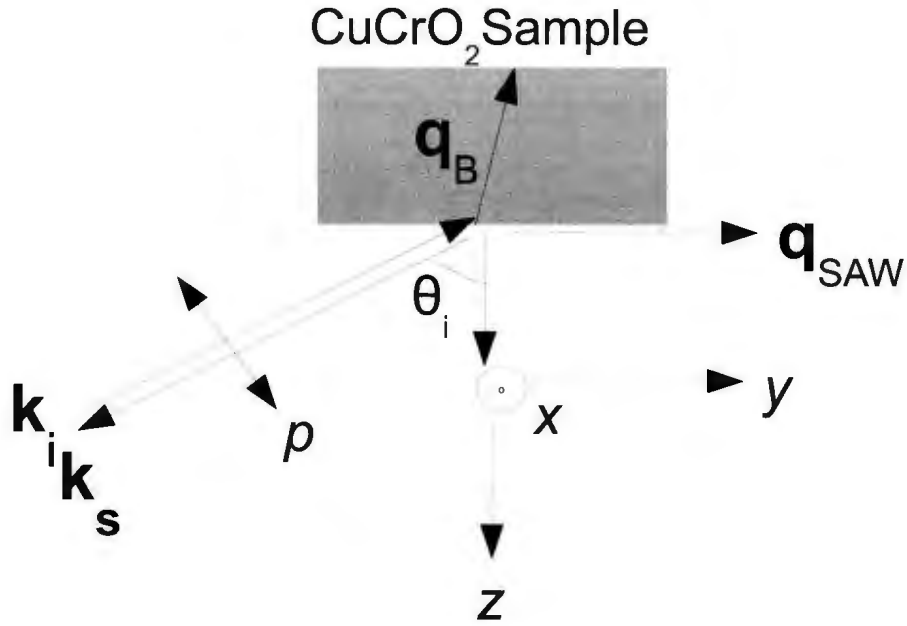
Figure 6.9: Sample orientation in backscattering measurements on CuCrO$_2$ at an oblique angle of incidence.

surface acoustic modes for backscattering, we have that

$$\Delta\nu_B = \pm\frac{V(n_i + n_s)}{\lambda_i} \tag{6.2}$$

and

$$\Delta\nu_{SAW} = \pm\frac{2\sin\theta_i V_{SAW}}{\lambda_i}. \tag{6.3}$$

Thus, we present in Fig. 6.11 the frequency shifts vs $\sin\theta_i$. With a decrease in $\sin\theta_i$, the frequency shifts of the modes observed at 28.5 GHz and 25.6 GHz slightly decrease, however, from extrapolation we see that the frequency shifts are not zero at normal incidence, as expected for bulk acoustic modes (Eq. 6.2). Therefore, we identify these modes as bulk acoustic modes. However, the frequency shift of the low frequency mode extrapolates well to zero (Eq. 6.3), indicating that this mode is a surface acoustic mode. Fitting the data for this mode (red line), we obtain $V_{SAW} = 2000 \pm 50$ m/s.
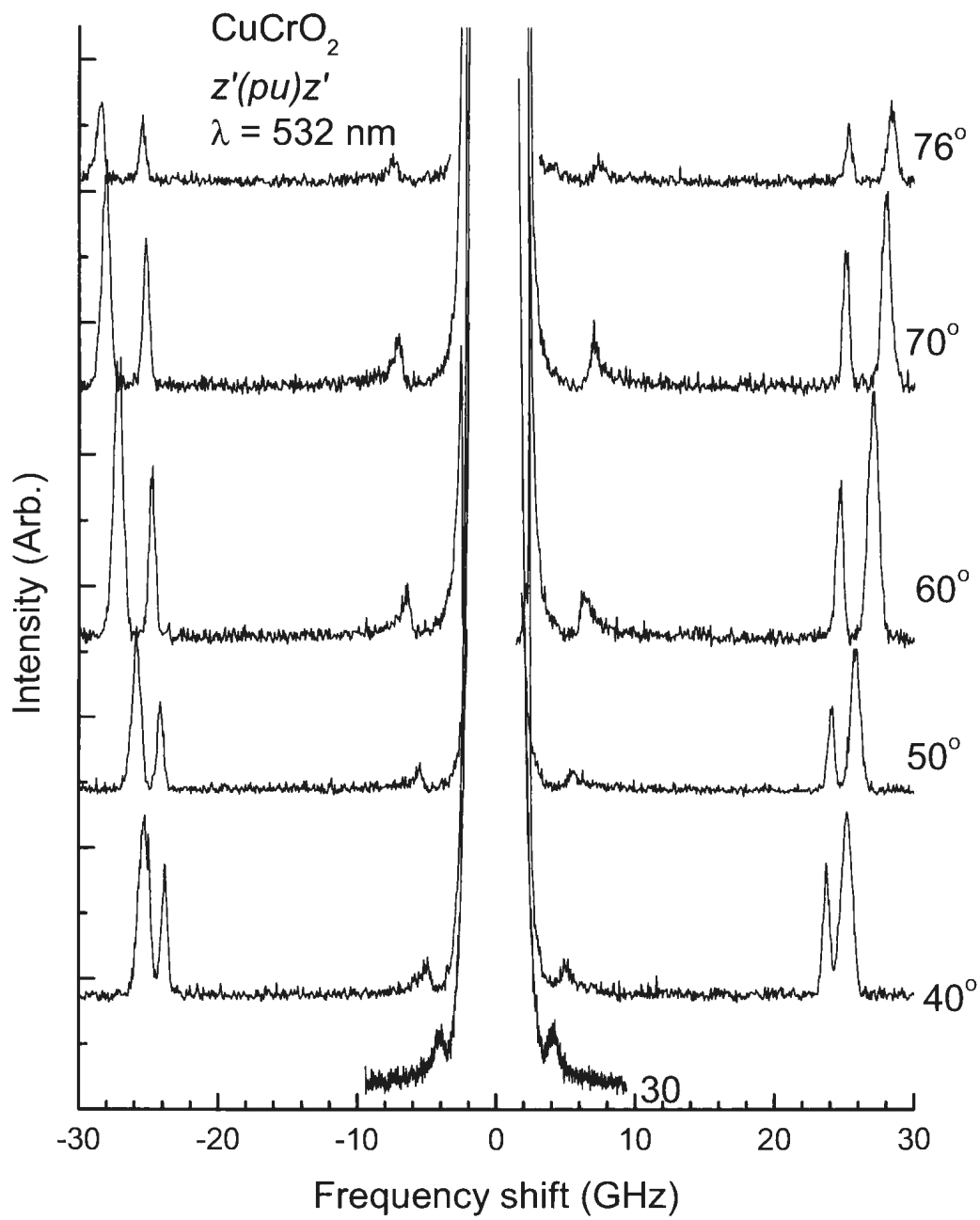
Figure 6.10: Backscattering spectra of $CuCrO_2$ obtained with an oblique angle of incidence relative to the z axis. The scattering geometry is $z'(pu)z'$.
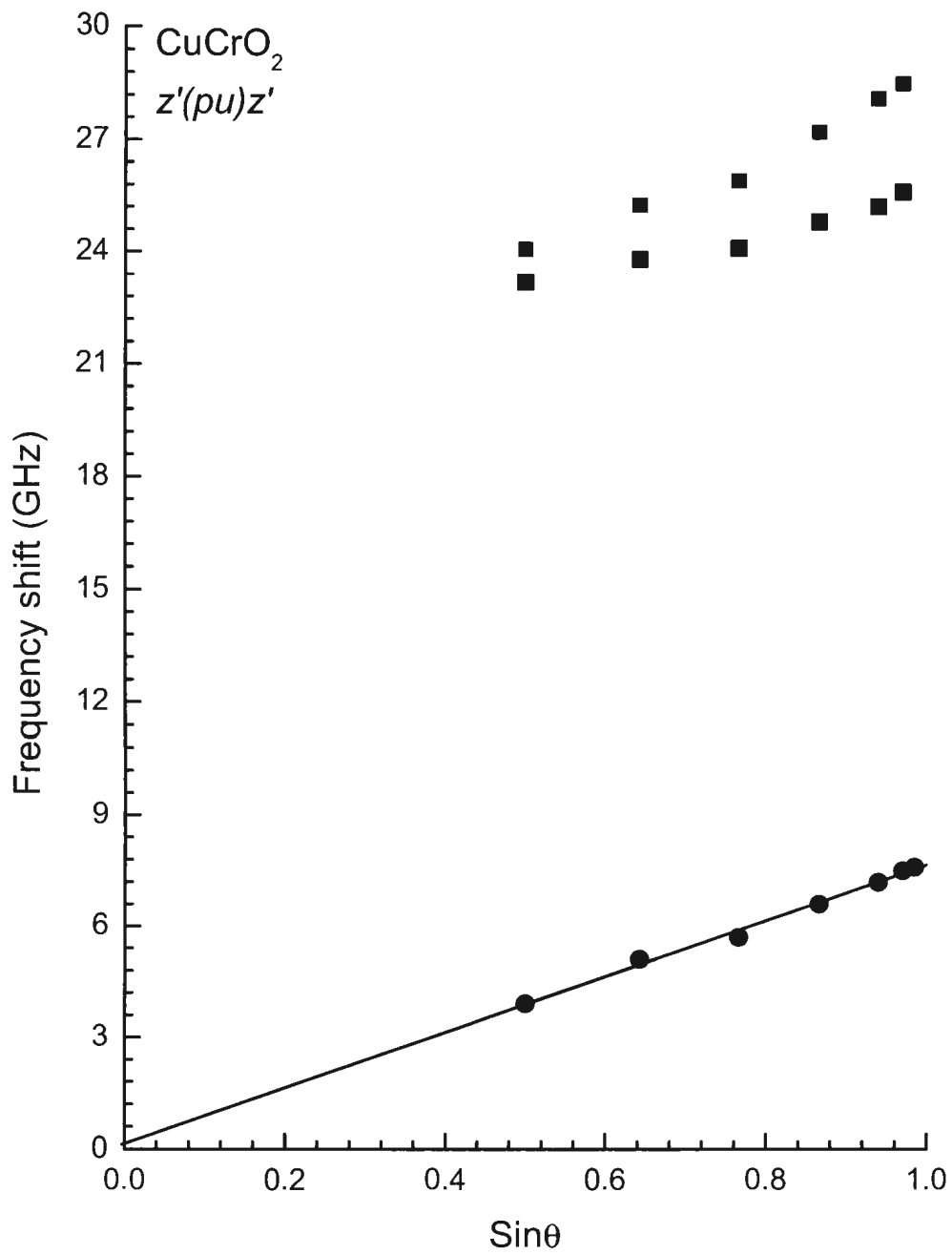
Figure 6.11: Frequency shifts of modes in CuCrO$_2$ observed with an oblique angle of incidence relative to the z axis. The scattering geometry is $z'(pu)z'$.

Table 6.1: Probed acoustic modes in CuCrO$_2$ with Brillouin backscattering in the trigonal R$\bar{3}m$ phase ($\bar{3}m$ point group) [100].

Direction	Scattering geometry	Mode	Expressions of ρV^2
[100]	$x(yy)\bar{x}$, $x(zz)\bar{x}$, $x(zz)\bar{x}$	L_x	C_{11}
[010]	$y(xx)\bar{y}$, $y(zz)\bar{y}$	L_y	$\frac{1}{2}(C_{11} + C_{44} + \sqrt{(C_{11} - C_{44})^2 + 4C_{14}^2})$
	$y(xx)\bar{y}$, $y(zz)\bar{y}$	$T_y P_z$	$\frac{1}{2}(C_{11} + C_{44} - \sqrt{(C_{11} - C_{44})^2 + 4C_{14}^2})$
	$y(xz)\bar{y}$	$T_y P_x$	C_{66}
[001]	$z(xx)\bar{z}$, $z(yy)\bar{z}$	L_z	C_{33}
	$z(xx)\bar{z}$, $z(yy)\bar{z}$, $z(xy)\bar{z}$	$T_z P_y, T_z P_x$	C_{44}

In the backscattering geometry at an oblique angle of incidence (Fig. 6.9), bulk acoustic phonons propagate at an angle θ_i relative to the z axis. Along such directions, that is, directions that are not along the high symmetry axes of the crystal, selection rules allow the observation of all bulk phonons. Moreover, expressions of the velocities in terms of elastic constants are complicated. An alternative way is to use backscattering along crystallographic axes (Table 6.1), along which selection rules are satisfied [100]. As a result, we performed backscattering measurements on CuCrO$_2$ along the x, y, and z crystallographic axes. Measurements were performed with 514.5 nm and 532 nm incident light. The incident light with a beam power of 40 mW was focused on the sample surface using a 5.5 cm lens ($\sim$ 12000 W/cm^2).

Backscattering spectra obtained for modes propagating along the x, y and z axes are presented in Figs. 6.12-6.14. The scattering geometries are designated with the Porto notation, $k_i(e_i e_s)k_s$. We first discuss backscattering spectra for propagation along the z axis shown in Fig. 6.12. The wavelength of the incident light is 532 nm. In Fig. 6.12, we see modes at 22.5 GHz and 100.4 GHz. The transverse modes along the z axis are degenerate

[83], which is why we observe only two modes. Since the intensity of the mode at 100.4 GHz is weak, the frequency range between 90 GHz and 110 GHz was scanned 10 times more than the rest of the spectrum (Fig. 6.12). The intensity of the mode at 100.4 GHz is weak probably due to the small value of the elasto-optic coefficient in the selection rules [100], which we present in Table 6.1 for trigonal symmetry. Selection rules for Brillouin scattering are derived using elasto-optic (or photoelastic) tensors for each point group and depend on both the propagation direction of the acoustic modes and the polarizations of incident and scattered light [100]. Therefore, we present the selection rules for each acoustic mode in terms of its propagation direction and scattering geometry. For a discussion and derivation of the selection rules, one can refer to Ref. [100]. In Table 6.1, we label the acoustic modes as L_i and $T_i P_j$, where L_i corresponds to a longitudinal mode propagating along the i axis and $T_i P_j$ is a transverse mode propagating along the i axis with a polarization along the j axis. The elastic constant combinations that determine the acoustic mode velocities are also given according to Christoffel's equation. According to the selection rules [100] (Table 6.1) for backscattered light along the z axis, a parallel polarization configuration such as $z(yy)z$ or $z(xx)z$ allows for the observation of both longitudinal and transverse modes (see Fig. 6.12). On the other hand, a cross polarization geometry such as $z(xy)z$ should only allow for the observation of the transverse mode [100]. Therefore, we assign the mode at 22.5 GHz to the transverse acoustic mode ($T_z P_x$), the velocity of which can be directly used to determine the elastic constant C_{44} (Table 6.1). The other mode at 100.4 GHz is attributed to the longitudinal mode L_z depending on C_{33} (Table 6.1).

Brillouin spectra for backscattering along the y axis are shown in Fig. 6.13. Results obtained with $\lambda = 514.5$ nm are presented in Fig. 6.13. For the spectrum labeled as $y(z'u)y$, z' corresponds to the polarization of the incident light at angle of 30° relative to the z axis, whereas u corresponds to the unpolarized scattered light. In a Brillouin scattering experiment, one can generally observe 3 pairs of peaks, each of which corresponds to one of
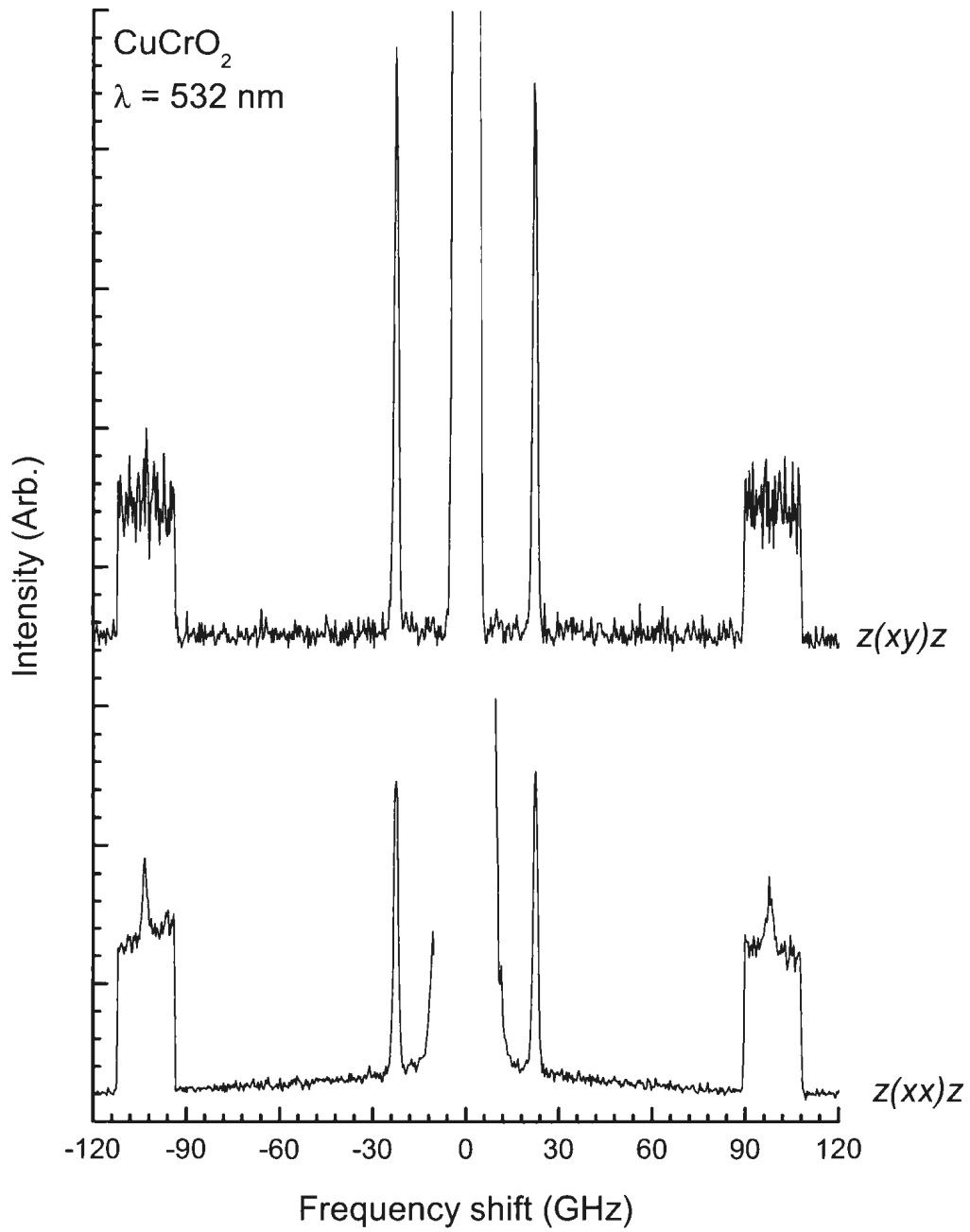
Figure 6.12: Polarized Brillouin backscattering spectra of CuCrO$_2$ obtained along the z axis with $\lambda = 532$ nm.

the three acoustic modes. However, the spectrum obtained with unpolarized scattered light (Fig. 6.13) shows 6 pairs of peaks with frequency shifts ranging from 20 GHz to 80 GHz (See Table 6.2). In birefringent crystals, a wave of arbitrary polarization can be decomposed into two orthogonal polarizations. In this case, the polarization directions are along the x and z axes (Eq. 3.6). When light is polarized in the xy plane, the refractive index is the ordinary index n_o. However, when light is polarized along the z axis, the refractive index is the extraordinary index n_e. Referring to Eq. 6.2, we see that the frequency shift of an acoustic mode depends on the refractive index of the incident and that of the scattered light. As a result, if the selection rules allow the observation of an acoustic mode with (xx), (zz), and (xz) polarizations, a spectrum obtained with $(z'u)$ polarization should show frequency shifts that depend on n_o, n_e, and both n_o and n_e, respectively, giving rise to three peak pairs.

In order to identify the peaks for acoustic modes propagating along the y axis (Fig. 6.13, we refer to the selection rules presented in Table 6.1 [100, 83]. In Fig. 6.13, with (xx) polarization two well-defined modes are observed at 75.6 GHz and 23.7 GHz. With (zz) polarization, two modes are observed at 61.9 GHz and 19.8 GHz. According to the selection rules (Table 6.1), these configurations should allow longitudinal and quasitransverse modes [100]. Hence, the high frequency peaks at 75.6 GHz and 61.9 GHz are assigned to the longitudinal mode (L_y) whereas modes observed at 23.7 GHz and 19.8 GHz are attributed to the quasitransverse mode $(T_y P_z)$. The fact that the frequency shifts are different for (xx) and (zz) polarizations clearly shows the effect of birefringence. Fig. 6.13 also shows the spectrum with cross polarization (xz). In this configuration, a strong peak is observed at 39.8 GHz. According to the selection rules (Table 6.1), only the pure transverse mode should be observed. Therefore, we assign the mode at 39.8 GHz to the pure transverse mode $(T_y P_x)$ related to the elastic constant C_{66}. As seen in the spectrum, there are two additional pairs observed with weak intensities at 61.9 GHz and 68.8 GHz. As the mode at 61.9 GHz has

94
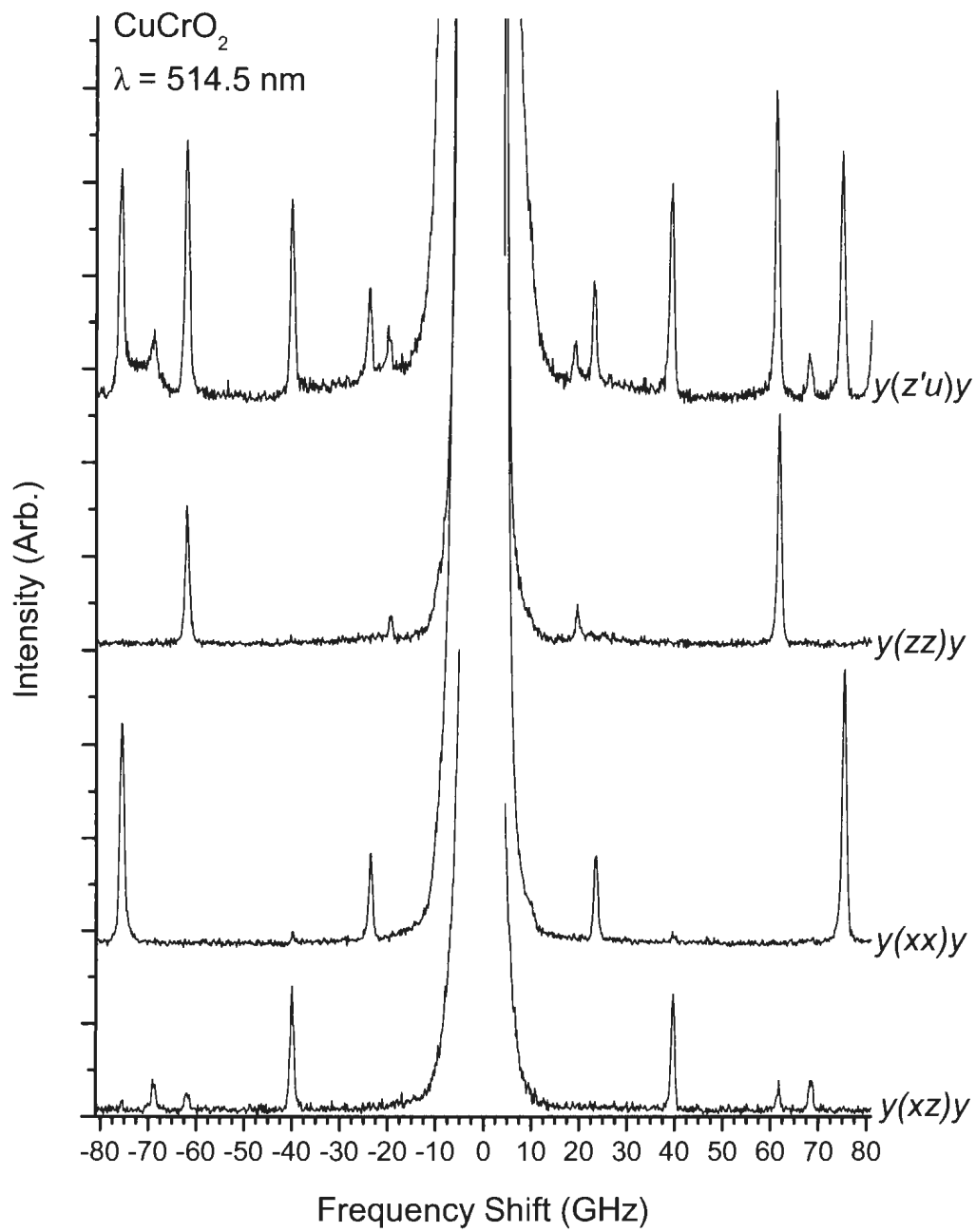
Figure 6.13: Polarized Brillouin backscattering scattering spectra of CuCrO₂ obtained along the y axis with λ =514.5 nm.

the same frequency shift as the longitudinal mode (L_y) observed with a (zz) polarization configuration, this suggests that the polarization of the incident light was at a small angle relative to the x axis. The other mode at 68.8 GHz can also be assigned to the longitudinal mode. Its frequency shift is different due to different refractive index in the basal plane (n_o) and that in the z axis (n_e). The cross polarization configuration does not normally allow for the observation of the longitudinal mode along the y axis [100]. However, probably the large collection angle (due to an f-number of 2.4) lifts the selection rules since acoustic modes propagating in the directions within the scattering cone (of $\sim 30°$) formed by the lens can be observed. This explains why the longitudinal mode is also observed with a lower amplitude [101].

Finally, we also performed backscattering measurements to determine the frequency of acoustic modes propagating along the x axis. The spectra obtained along the x axis are presented in Fig. 6.14. Normally, the selection rules impose that backscattering measurements along the x axis only allow longitudinal modes [100]. However, with unpolarized scattered light $x(z'u)x$, we observe a total of 6 modes, which have frequency shifts similar to those obtained for modes propagating along the y axis (Table 6.2). We attribute the observation of these modes to the large collecting angle (f/2.4) in our measurements [101].

Frequency shifts of the bulk acoustic modes propagating along the three axes are tabulated in Table 6.2. The frequency shifts are given for both 514.5 nm and 532 nm incident light beams. The frequency shifts obtained with two excitation lines are different because the frequency shifts depend on the wavelength of the incident light as well as the refractive indices of the incident and scattered light (Eq. 6.2), which are weakly frequency dependent. Here, we should note that normal incidence backscattering spectra cannot show surface acoustic waves because the frequency shift of a surface acoustic wave is zero at normal incidence (Eq. 6.1).

For the calculation of the acoustic velocities, we need to know the refractive indices of
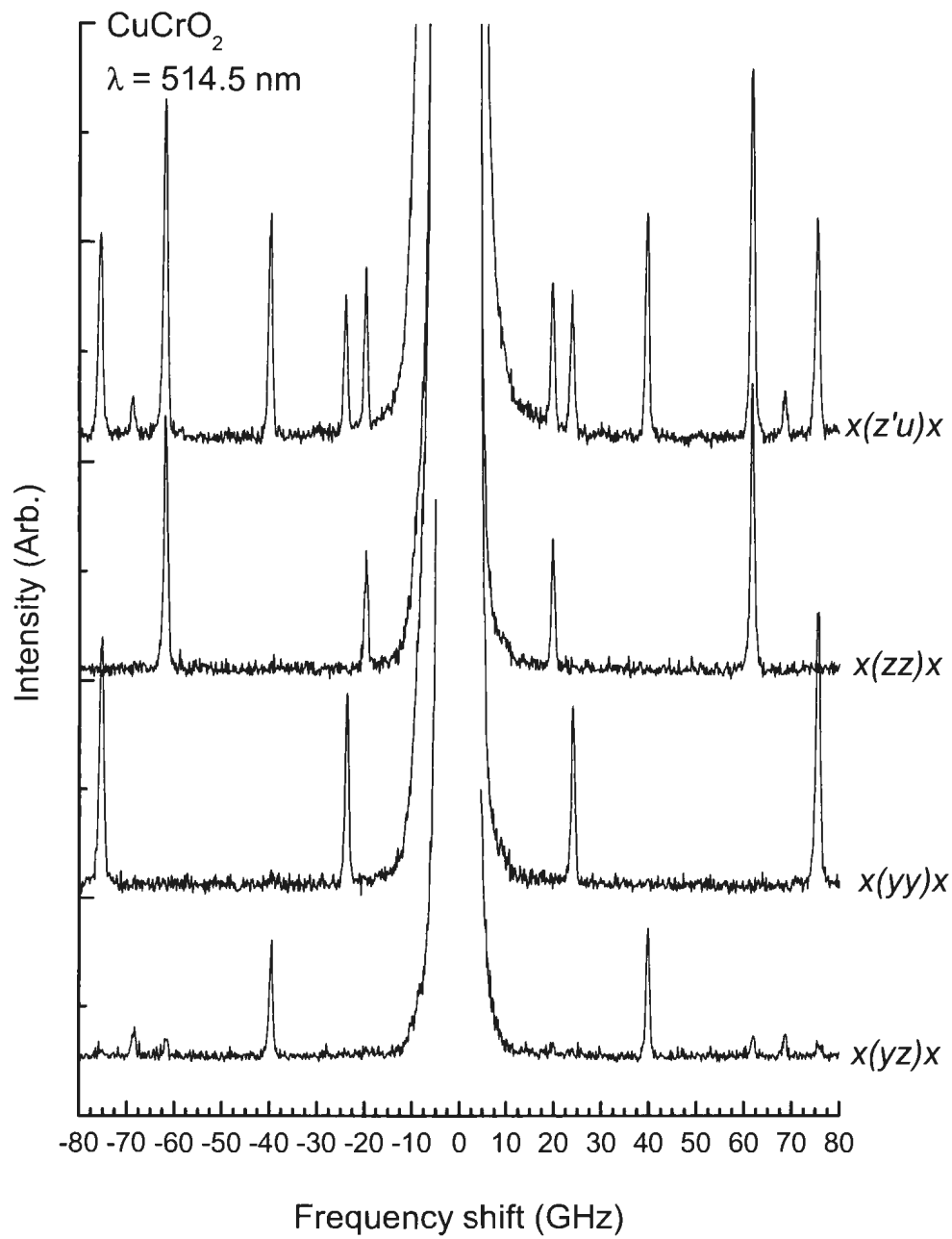
Figure 6.14: Polarized Brillouin backscattering spectra of $CuCrO_2$ obtained along the x axis with $\lambda = 514.5$ nm.

Table 6.2: Frequency shifts of the acoustic modes observed with Brillouin backscattering experiments along x, y, and z axes observed at room temperature in $R\bar{3}m$ phase of CuCrO$_2$. The uncertainty associated with the frequency shifts is 0.5%.

Direction	Acoustic mode	Light Polarization	$\Delta\nu_B$ for $\lambda = 514.5$ nm Uncertainty: 0.5%	$\Delta\nu_B$ for $\lambda = 532nm$ Uncertainty: 0.5%
[001]	L_z	$(xx), (yy)$		100.4
	T_zP_x	$(xx), (yy), (xy)$	23.5	22.5
[010]	L_y	(xx)	75.6	72.0
	L_y	(xz)	68.6	65.4
	L_y	(zz)	61.9	59.4
	T_yP_z	(xx)	23.7	22.7
	T_yP_z	(zz)	19.8	19.7
	T_yP_x	(xz)	39.8	38.2
[100]	L_x	(yy)	75.4	
	L_x	(yz)	68.6	
	L_x	(zz)	61.8	
	T_xP_z	xx	23.8	
	T_xP_z	(zz)	19.7	
	T_xP_y	(yz)	39.7	

CuCrO$_2$ (Eq. 6.2). As discussed in Chapter 3, reflection geometry illustrated in Fig. 3.7 can be used to determine acoustic velocities and refractive indices of an isotropic material [93]. In that case, the acoustic modes propagate normal to the surface and the frequency shift is given by (Eq. 3.46)

$$\Delta \nu_B = \frac{V}{2\pi} \left(\sqrt{k_i^2 n_s^2 - k_m^2} + \sqrt{k_i^2 n_i^2 - k_m^2} \right),$$ (6.4)

where k_i is the incident light wave vector whereas $k_m = k_i \sin \theta_i$ is the component parallel to the sample surface (in-plane component). V is the acoustic velocity and n_i and n_s are the refractive indices associated with the incident and scattered light, respectively. If the refractive indices for the incident and scattered light are equal, i.e., $n_i = n_s = n$, the frequency shift can be written as

$$\Delta \nu_B = \pm \frac{V}{\pi} \sqrt{k_i^2 n^2 - k_m^2}$$ (6.5)

Note that CuCrO$_2$ has trigonal symmetry ($\overline{3}m$ point group) which means that it is a uniaxial birefringent material (see Sec. 3.1). Along the optic axis, which is parallel to the crystallographic z axis, the refractive index is independent of the polarization direction and given by the ordinary index n_o. For other directions, light will be resolved into two orthogonal modes, each of which experiences a unique refractive index. One of these polarizations is in the xy plane, which experiences the ordinary index n_o. The other polarization experiences a refractive index which depends on the polar angle θ between the z axis and direction of the light propagation

$$\frac{1}{n_e^2(\theta)} = \frac{\cos^2 \theta}{n_o^2} + \frac{\sin^2 \theta}{n_e^2},$$ (6.6)

where n_e corresponds to the extraordinary index. The extraordinary index n_e is experienced by light polarized along the z axis (optic axis). For a derivation of Eq. 6.6 using the optical indicatrix for uniaxial materials, one can refer to Sec. 3.1. As seen in Eq. 6.6, depending on the polar angle θ, the refractive index $n_e(\theta)$ will take a value between the ordinary index n_o and the extraordinary index n_e.

Consider the reflection geometry with respect to the y axis shown in Fig. 6.15a. In this geometry, the plane of incidence is parallel to the xy plane. If we set the polarization of the incident and scattered light in the xy plane, we observe acoustic modes L_y and T_yP_z with frequency shifts associated with (xx) polarization. Performing measurements at different angles of incidence θ_i, a fit of $\Delta\nu_B$ vs. k_m using Eq. 6.5 will provide the velocities of the L_y and T_yP_z acoustic modes and the value of the ordinary index n_o. Similarly, if we perform measurements with (zz) polarization, we can determine the velocities of the L_y and T_yP_z modes and the extraordinary index n_e. If the reflection geometry measurement is performed with respect to the y axis (Fig. 6.15) using cross polarized light, (xz) or (zx), then we determine the velocity of the T_yP_x mode and refractive indices n_o and n_e by a fit using Eq. 6.4. Even though the longitudinal L_y mode is normally forbidden in cross polarization, it is observed with a weak intensity due to a large collecting angle in our experiments (Fig. 6.13). Therefore, we can determine the velocity of the L_y mode also using cross polarization. Measurements can be done in a similar way with respect to the x axis. In that case, the velocities of the acoustic modes propagating along the x axis, L_x, T_xP_y, and T_xP_z, as well as n_o and n_e can be obtained.

The same approach can be used to determine the velocities of acoustic modes propagating along the z axis and ordinary index n_o as illustrated in Fig. 6.15b. In this case, the plane of incidence is parallel to the xz plane. The symbol $\otimes$ is used to indicate that the polarization of the incident and scattered light is along the y axis, that is, perpendicular to the plane of incidence. In this case, the refractive index for the incident and scattered light is the ordinary index n_o. Then, fitting $\Delta\nu_B$ vs. k_m using Eq. 6.5, we can determine the velocities of T_zP_y and L_z modes as well as the ordinary index n_o. The same results can be obtained if the plane of incidence is parallel to the yz plane and the incident and scattered light are polarized along the x axis.

In order to determine the refractive indices n_o and n_e and the velocities of the acoustic
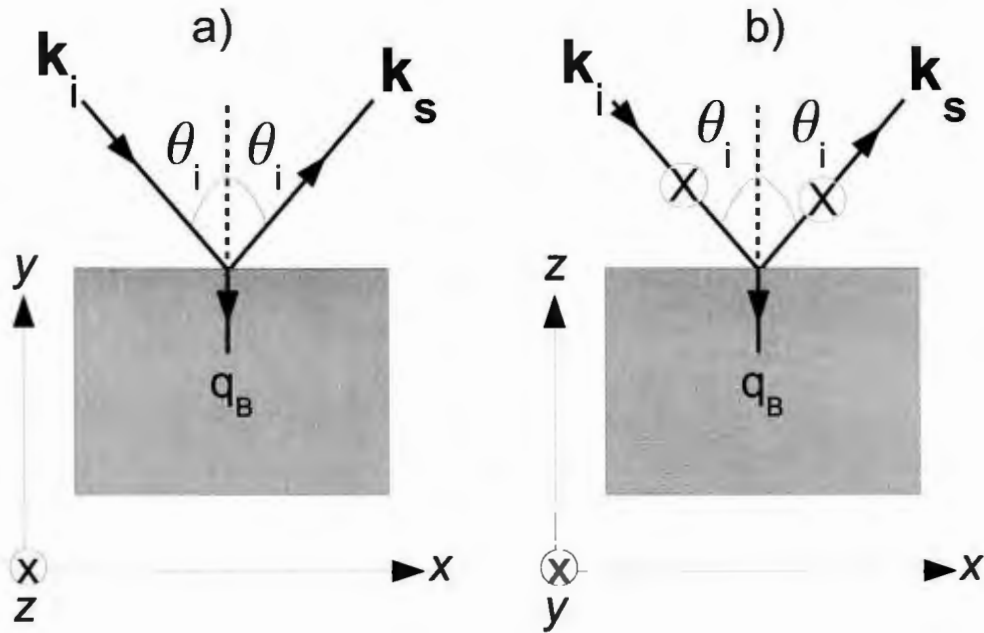
Figure 6.15: Reflection geometries used to determine the ordinary and extraordinary refractive indices and velocities of the acoustic modes propagating along the **a)** y **b)** z axes

modes propagating along the y and z axes, we performed Brillouin scattering measurements with reflection geometries illustrated in Fig. 6.15. Measurements were performed at angles of incidence θ_i varying from $0°$ to $80°$ relative to y and z axes. The wavelength of the incident light was 514.5 nm for all measurements. Spectra obtained with polarized incident and scattered light are shown in Fig. 6.16 while those obtained with unpolarized (u) scattered light are presented in Fig. 6.17. Incident angles θ_i are shown on the right hand side of each spectrum. Polarizations are shown above each spectrum in both figures (Figs. 6.16 and 6.17). Whenever necessary, the propagation and polarization directions are labeled with an apostrophe. For example, in the notation $y'(x'x')y'$, incident and scattered light directions (y') are at angle θ_i with respect to the y axis whereas light polarizations (x') are in the xy plane. In Fig. 6.17, when $(x'u)$ is used, the spectra show modes that are observed with (xx) and (xz) polarizations while (zu) polarization allows modes observed with (zz)
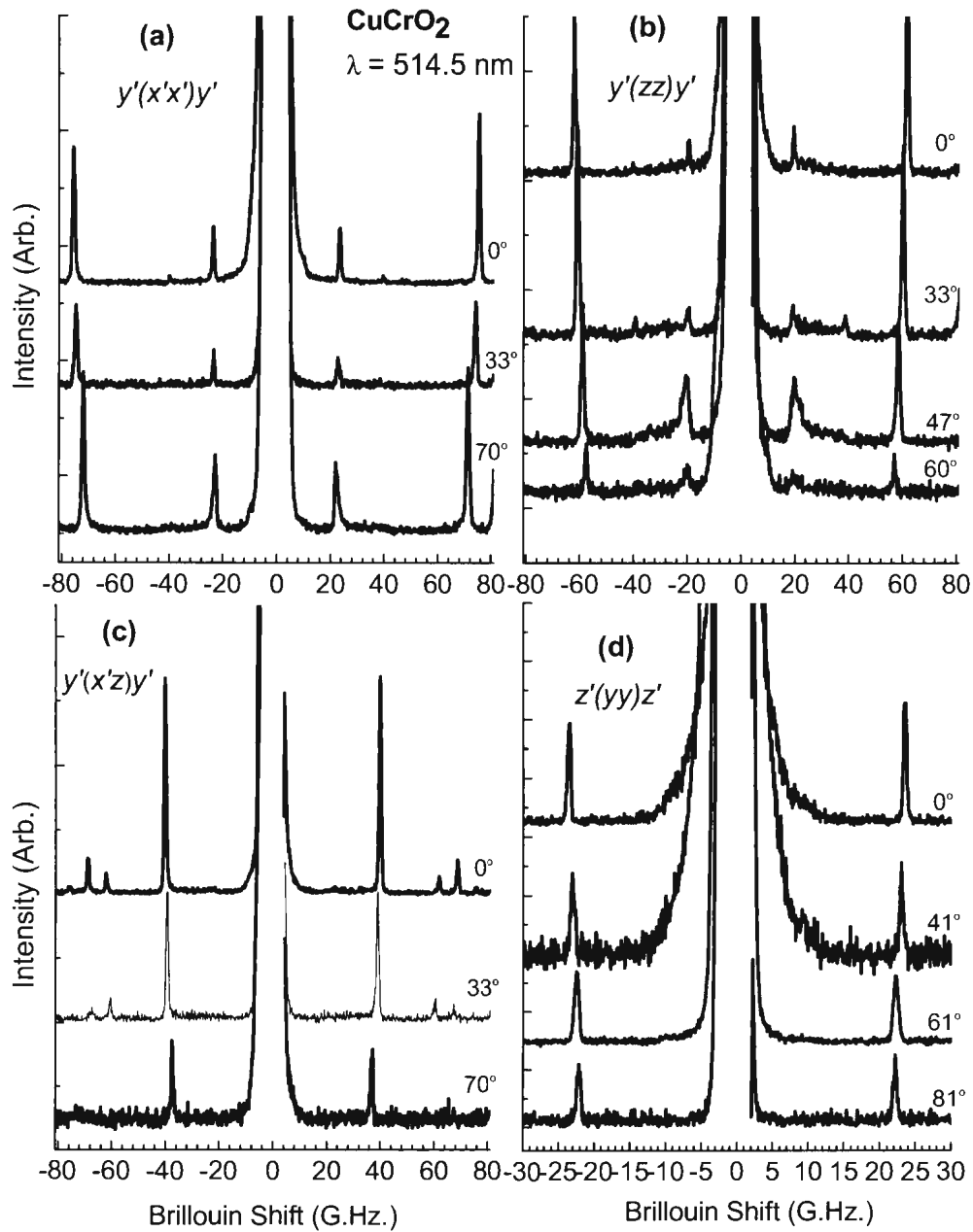
Figure 6.16: Polarized Brillouin scattering spectra obtained by using reflection geometry for modes propagating along the y and z axes. Employed scattering geometries are **a)** $y'(x'x')y'$, **b)** $y'(zz)y'$, **c)** $y'(x'z)y'$, and **d)** $z'(y'y')z'$.
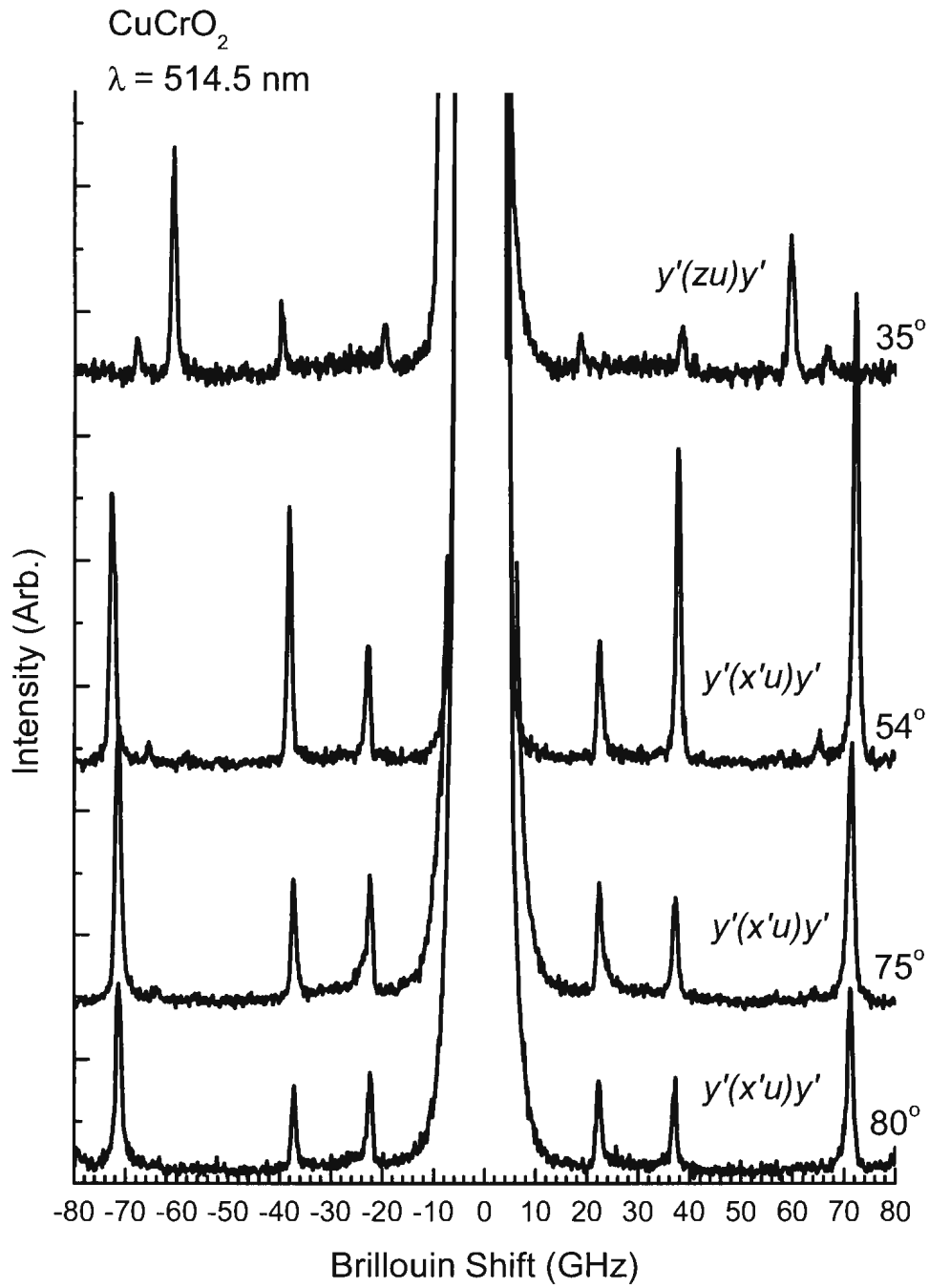
Figure 6.17: Brillouin scattering spectra obtained using reflection geometry with unpolarized scattered light for modes propagating along the y axis.

and (zx) polarizations. At normal incidence, approximately 5000 scans ($\sim$1 hour) were enough to obtain a spectrum with strong mode intensities for the L_y, T_yP_z and T_yP_x modes (Figs. 6.16and 6.17). The observation of other modes required as high as 40000 scans (17 hours) for angles larger than 40°. The longitudinal mode observed with (xz) polarization and the quasitransverse mode (T_yP_z) observed with (zz) polarization could not be observed for angles larger than 60°.

The linewidths of the modes in the spectra shown in Figs. 6.16 and 6.17 are about 1.2 GHz, comparable to the instrumental linewidth (0.5 GHz). An increase in θ_i in reflection geometry experiments did not considerably change the linewidths with the exception for the T_yP_z mode at 19.8 GHz (Fig. 6.16). Severe broadening and asymmetry of this mode shifted the intensity distribution to higher frequencies. Therefore, the frequency variation of this mode was not used.

The frequency shifts of the acoustic modes are plotted against the in-plane component of the incident light wave vector k_m in Fig. 6.18. A simultaneous fit to the data obtained using Eqs. 6.4 and 6.5 is represented by continuous lines. From the fit, we determine the acoustic mode velocities V_L, L_y, V_{TyPx}, V_{TyPz}, and V_{TzPx} as well as the refractive indices (n_o and n_e). The results are tabulated in Tables 6.3 and 6.4. The uncertainties are approximately 3%.

We first discuss the results for the refractive indices. The fit to the frequencies of the modes propagating along the y and z axes gives the ordinary and extraordinary refractive indices as $n_o = 2.92 \pm 0.3$ and $n_e = 2.39 \pm 0.3$ for $\lambda = 514.5$ nm (Table 6.3). Since the ordinary index n_o is greater than the extraordinary index n_e, $CuCrO_2$ can be classified as a negatively birefringent material [72] (see Sec. 3.1). The birefringence magnitude of $CuCrO_2$ is then $\Delta n = n_e - n_o = $ -0.53 $\pm$ 0.06. This value is larger than that of the well-known negatively birefringent material $CaCO_3$, in which $n_o = 1.66$ and $n_e = 1.49$, giving $\Delta n = $ -0.17 [102].

The ratio of $\frac{n_o}{n_e} = 1.22 \pm 0.03$ can be tested using the frequency shifts of the L_y, L_x, T_yP_z
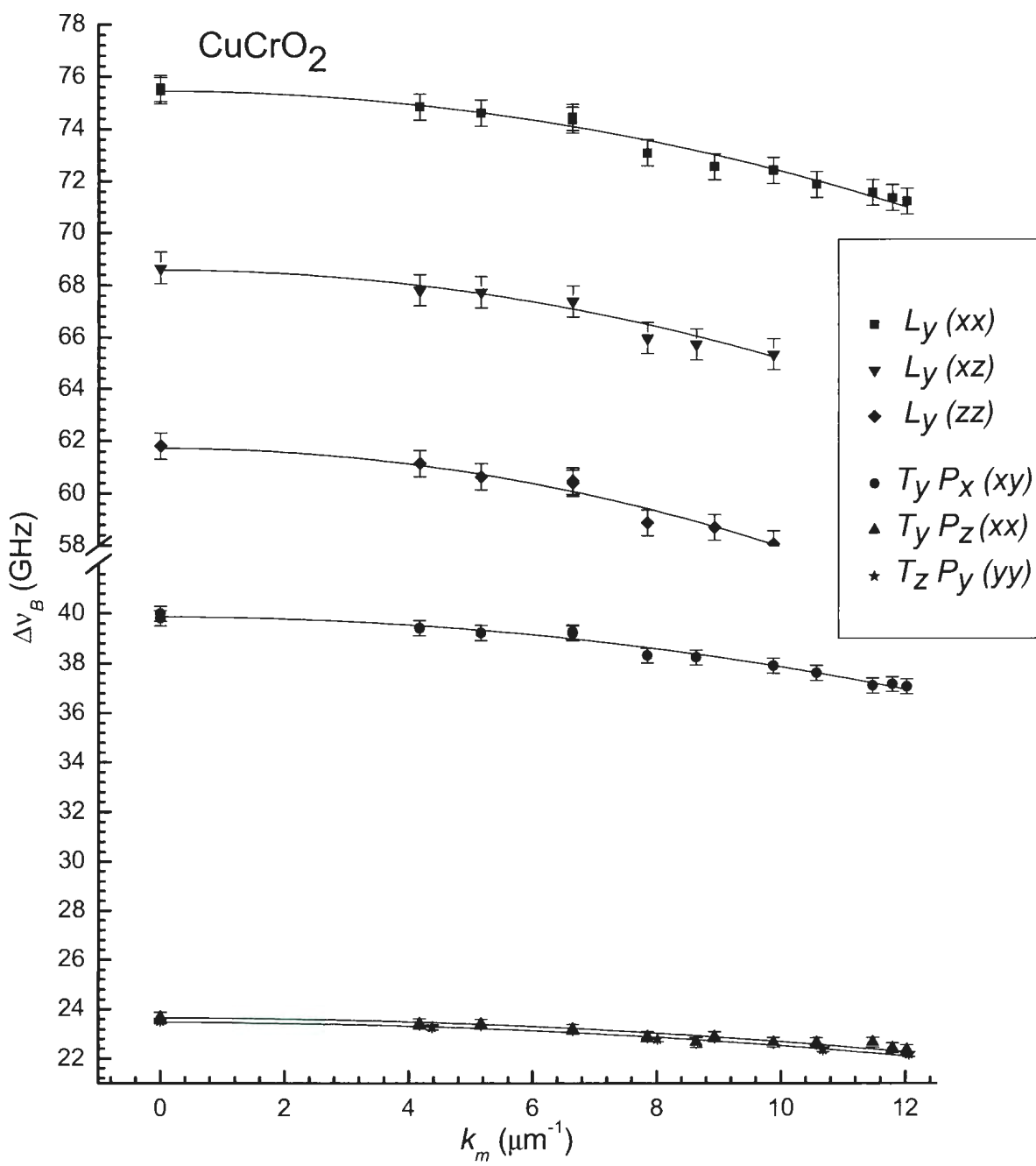
Figure 6.18: Frequency shift plotted against the in-plane component of the incident light for modes propagating along the y and z axis (L_y, $T_y P_x$, $T_y P_z$, $T_z P_x$) and nonlinear fits using Eqs. 6.4 and 6.5 (continuous lines).

Table 6.3: Refractive indices of $CuCrO_2$ for $\lambda = 514.5$ nm and $\lambda = 532$ nm at room temperature

Wavelength (nm)	n_o	n_e
514.5	2.92 ± 0.03	2.39 ± 0.03
532	2.88 ± 0.05	2.38 ± 0.04

and $T_x P_z$ modes associated with (xx) and (zz) polarizations. This can be done by rewriting Eq. 6.2 for $n_i = n_s$, so that

$$\frac{\Delta \nu_B(xx)}{\Delta \nu_B(zz)} = \frac{n_o}{n_e}. \tag{6.7}$$

Using the frequency shifts in Table 6.2, the longitudinal modes (L_x and L_y) give 1.22 ± 0.01 whereas the shifts for the transverse modes $T_x P_y$ and $T_y P_z$ give 1.21 ± 0.01. Thus, the ratio determined by the fitting procedure agrees with those obtained from the frequency shifts observed with backscattering (Figs. 6.13 and 6.14). The overall quality of the fitting procedure can be further tested if one organizes Eq. 6.5 as

$$\left(\frac{\pi \Delta \nu_B}{V k_i}\right)^2 = n_o^2 - \left(\frac{k_m}{k_i}\right)^2, \tag{6.8}$$

where $n_i = n_s = n_o$. Eq. 6.8 can be used for all modes observed with (xx) polarization, as shown in Fig. 6.19. In Fig. 6.19, squares, triangles, and stars represent data for the modes L_y, $T_y P_z$, and $T_z P_x$, respectively. According to Eq. 6.8, the intercept determined from a linear fit (black line) to the data gives the square of the ordinary refractive index n_o^2, from which we obtain $n_o = 2.92 \pm 0.01$ in agreement with the value of n_o presented in Table 6.3.

The refractive indices for $\lambda = 532$ nm are also presented in Table 6.4. These values are determined using Eq. 6.2, the frequency shifts, and velocities (Tables 6.2 and 6.4). Except for the asymmetric low frequency (19.7 GHz) mode obtained with (zz) polarization, all modes give the ordinary (n_o) and extraordinary n_e index values as presented in Table 6.3.
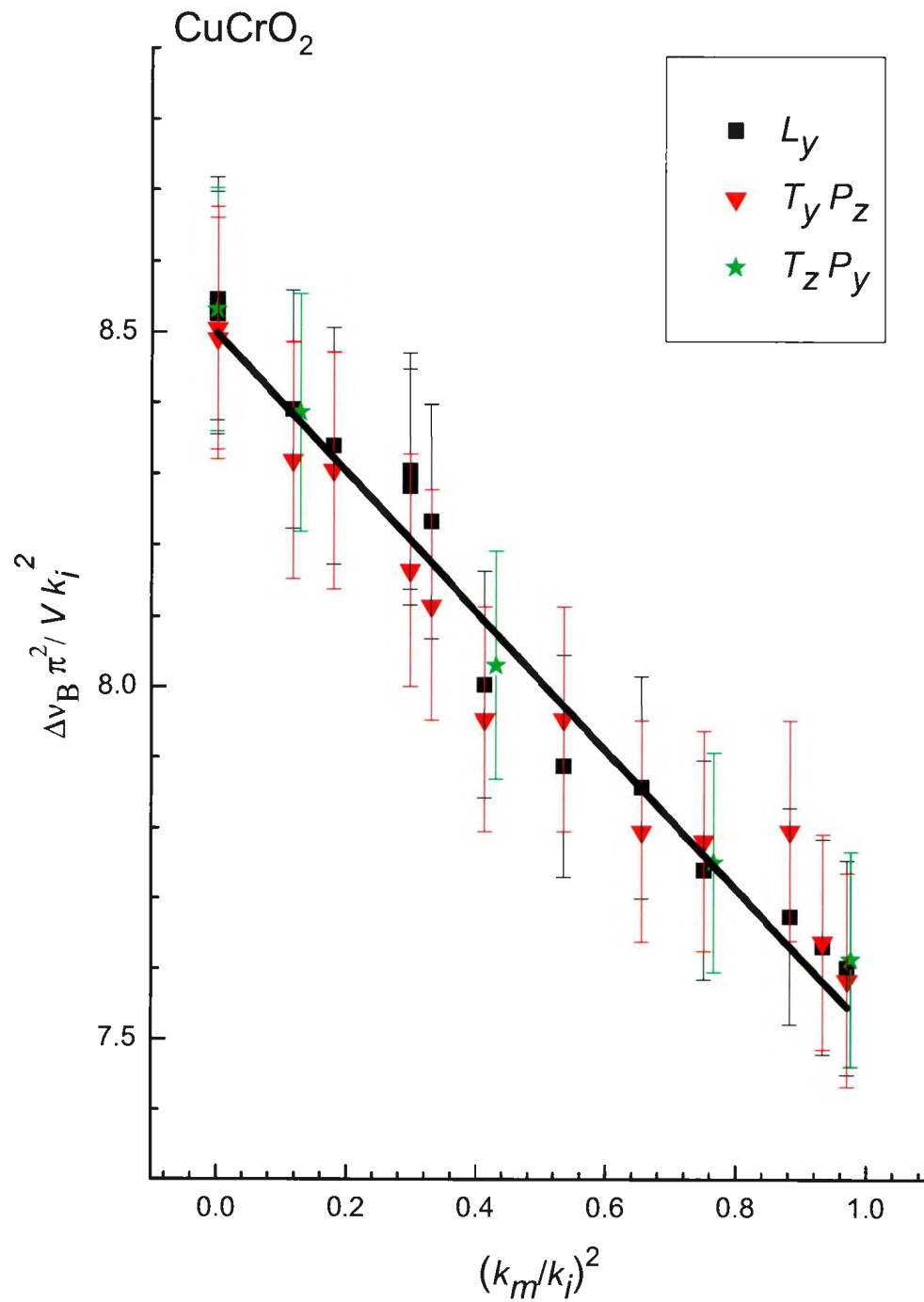
Figure 6.19: A plot of $(\pi \Delta \nu_B / V k_i)^2$ vs. $(k_m/k_i)^2$ for modes observed with (xx) polarization.

Table 6.4: Experimentally determined acoustic velocities for modes propagating along x, y, and z axes in the trigonal $R\bar{3}m$ phase of $CuCrO_2$ at room temperature.

Acoustic mode	Velocity (ms^{-1})
L_z	9200 ± 200
$T_z P_x$, $T_z P_y$	2070 ± 30
L_y	6650 ± 80
$T_y P_z$	2090 ± 30
$T_y P_x$	3870 ± 50
L_x	6640 ± 100
$T_x P_y$	2110 ± 40
$T_x P_z$	3850 ± 70

Table 6.5: Experimental values of the bare elastic constants in $CuCrO_2$ at room temperature.

Bare values	C_{11}	C_{12}	C_{33}	C_{44}	C_{66}
10^{10} N/m^2	24.2 ± 0.7	7.8 ± 1	47 ± 3	2.35 ± 0.07	8.2 ± 0.2

Acoustic velocities obtained using Eqs. 6.4 and 6.5 are presented in Table 6.4. Using these velocities (Table 6.4) and the solutions of the Christoffel's equation (Table 6.1), we determine the elastic constants C_{11}, C_{12}, C_{33}, C_{44}, $C_{66} = (C_{11} - C_{12})/2$, which are given in Table 6.5. The uncertainties associated with C_{11}, C_{44}, and C_{66} are about 3%. The velocities of the acoustic modes $T_z P_x$, $T_y P_z$ and $T_y P_x$ are equal within the uncertainties, therefore, we could not determine the value of C_{14}. From the acoustic velocities presented in Table 6.4, we estimate the absolute value of C_{14} to be less than 1.4×10^{10} N/m^2.

As discussed earlier, transverse modes are forbidden in the backscattering measurements

along the x axis (see Fig. 6.14). Modes located at 19.7 GHz and 23.7 GHz observed with parallel ((zz) and (xx)) polarization are assigned to the transverse mode $T_x P_z$ whereas mode located at 39.7 GHz observed with cross (xz) polarization is assigned to the transverse mode $T_x P_y$ (see Table 6.1). In order to test our mode selection we calculate the transverse mode velocities using the elastic constant values presented in Table 6.5. We obtain $V_{T_x P_y} = 3900 \pm 100$ m/s and $V_{T_x P_z} = 2100 \pm 100$ m/s. These values are in agreement with the velocities presented in Table 6.4 which are calculated using the frequency shifts. Thus, we confirm that our mode selection for the transverse modes is correct. Finally, using the extraordinary index n_e, we can obtain the velocity associated with the $T_y P_z$ mode observed with $y(zz)y$ geometry. The velocity is calculated as 2130 ± 40 m/s, which falls in the velocity range for this mode (Table 6.4).

6.2.2 Measurements between 295 K and 30 K

Ultrasonic velocity measurements on CuFeO$_2$ indicate an $R\bar{3}m \rightharpoonup C2/m$ pseudoproper ferroelastic transition at $T_{N1} = 14$ K. These measurements show significant softening of some acoustic modes propagating along the x and y axes. [1]. Particularly, the transverse modes $T_x P_y$ and $T_y P_x$ show softening up to 35% just above T_{N1}, which correspond a 50% reduction in the value of C_{66} relative to its maximum value at high temperatures. In addition, according to the Landau analysis [1], the temperature dependence of $T_x P_y$ is consistent with complete softening. This observation is direct evidence that the transition at T_{N1} is a second order ferroelastic transition. Considering that CuCrO$_2$ is isostructural to CuFeO$_2$ at room temperature, it might also undergo a ferroelastic transition at $T_{N1} = 24.3$ K, which could be identified through the observation of softening of the modes $T_x P_y$ and $T_y P_x$. Therefore, we performed Brillouin scattering measurements on CuCrO$_2$ to determine the temperature dependence of acoustic modes propagating along the x and y axes. Because we can measure

the transverse acoustic modes $T_x P_y$ and $T_y P_x$ with backscattering along the x and y axes (Figs. 6.13, 6.14), we used backscattering along these directions down to ~30 K using a single mode Ar^+ laser operating at 514.5 nm. The incident beam power for the measurements along the x axis was 12 mW (3800 W/cm^2) whereas it was 20 mW (6400 W/cm^2) for the y axis.

Low temperature backscattering spectra on CuCrO$_2$ are shown in Figs. 6.20-6.21. Since the intensity of each mode decreases as the temperature is lowered, the spectra had to be recorded for up to 40 hours at low temperatures to obtain an acceptable signal-to-noise ratio. Unfortunately, the lowest temperature we could achieve with the cryogenic system is 30 K, therefore, we could not obtain the temperature dependence of the acoustic modes down to the antiferromagnetic transition at $T_{N1} = 24.3$ K and multiferroic transition at $T_{N2} = 23.6$ K [27, 62, 62].

The backscattering spectra obtained along the y axis, Fig. 6.20, were collected with an incident light polarization along the x axis and unpolarized (u) scattered light, giving a scattering geometry as $y(xu)\overline{y}$. As determined in Sec. 6.2.1, modes at 23.7 GHz and 39.8 GHz are due to the quasi transverse mode ($T_y P_z$) and the pure transverse mode ($T_y P_x$), respectively. The modes at 61.9 GHz, 68.6 GHz, and 75.6 GHz correspond to the longitudinal mode L_y.

The backscattering spectra obtained along the x axis are shown in Fig. 6.21. The incident light was polarized along the y axis, whereas the polarization of the scattered light was not measured. The spectra in Fig. 6.21 show four modes at 23.8 GHz, 39.7 GHz, 68.6 GHz, and 75.4 GHz. The modes at 24 GHz, and 40 GHz correspond to the quasi transverse modes $T_x P_z$ and $T_x P_y$. The modes at 68.6 GHz and 75.4 GHz are the frequency shifts due to the longitudinal mode L_x observed with (yz) and (yy) polarized light, respectively.

In Fig. 6.22, we present the temperature dependence of the relative acoustic velocity variations determined from the frequency shifts normalized with respect to their maximum
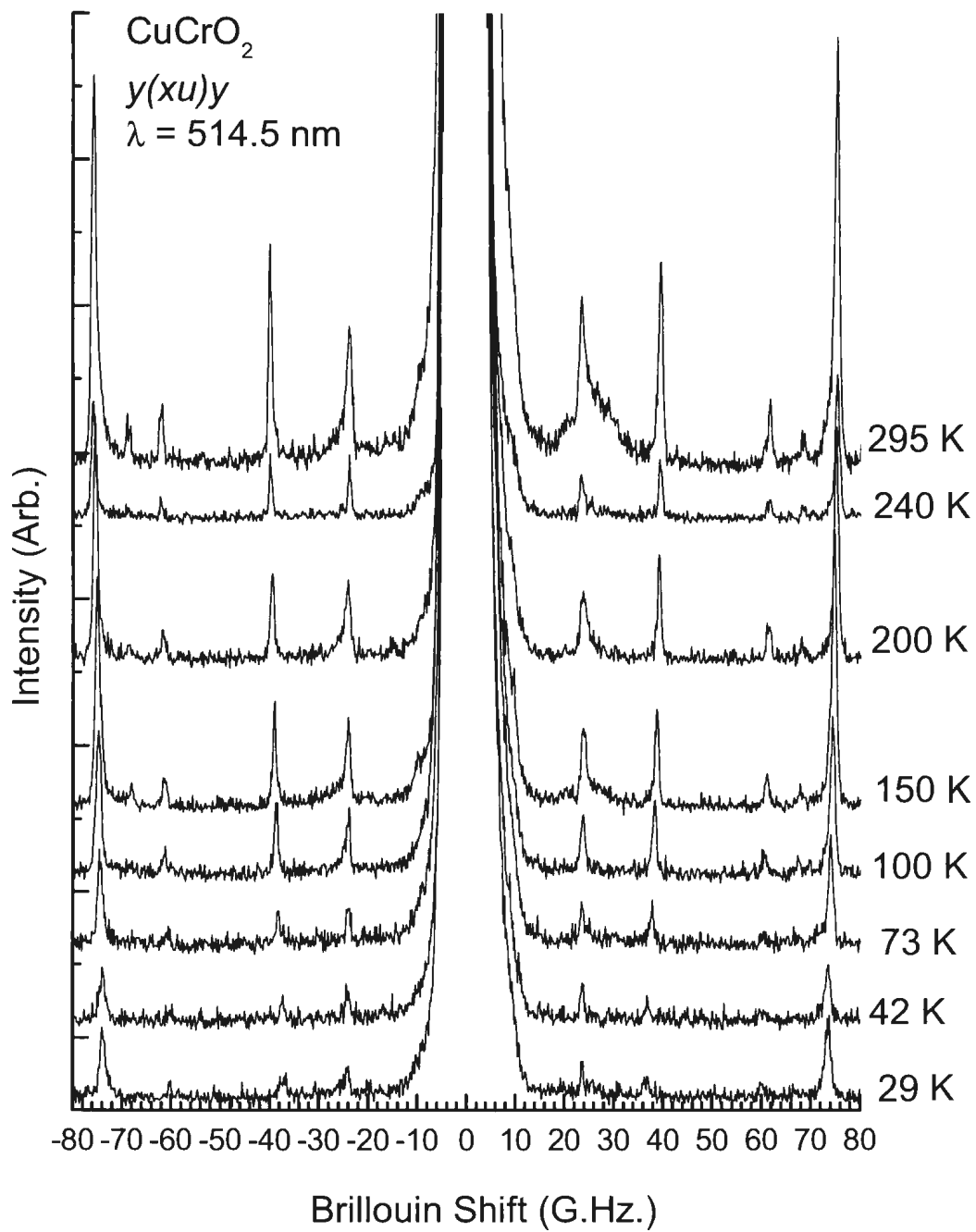
Figure 6.20: Brillouin spectra of CuCrO$_2$ obtained with $y(xu)\overline{y}$ geometry at temperatures between 31 K and 295 K using a 20 mW incident beam power ($\lambda = 514.5$ nm).
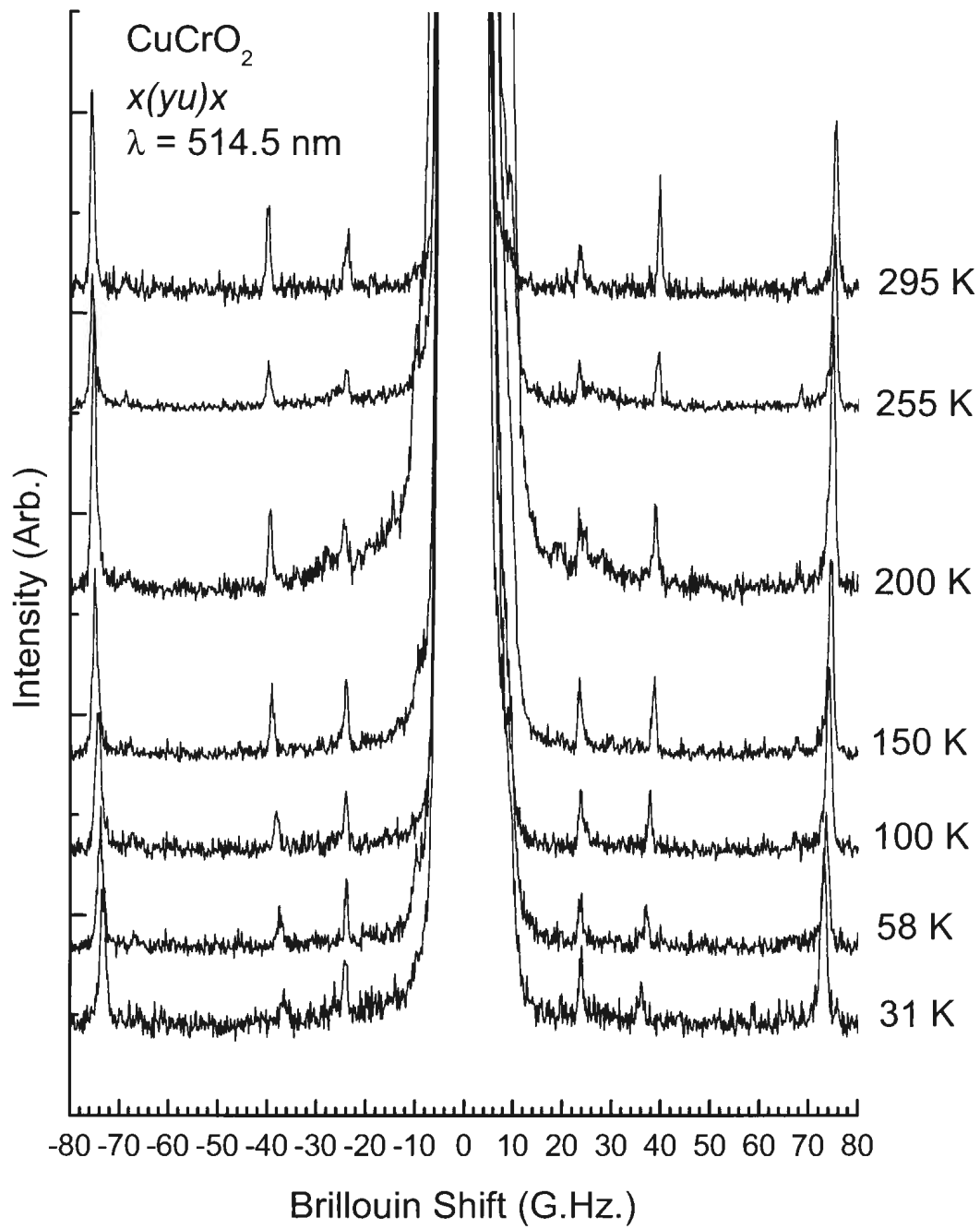
Figure 6.21: Brillouin spectra of $CuCrO_2$ obtained with $x(yu)\bar{x}$ geometry at temperatures between 31 K and 295 K using a 12 mW incident beam power ($\lambda = 514.5$ nm).

112
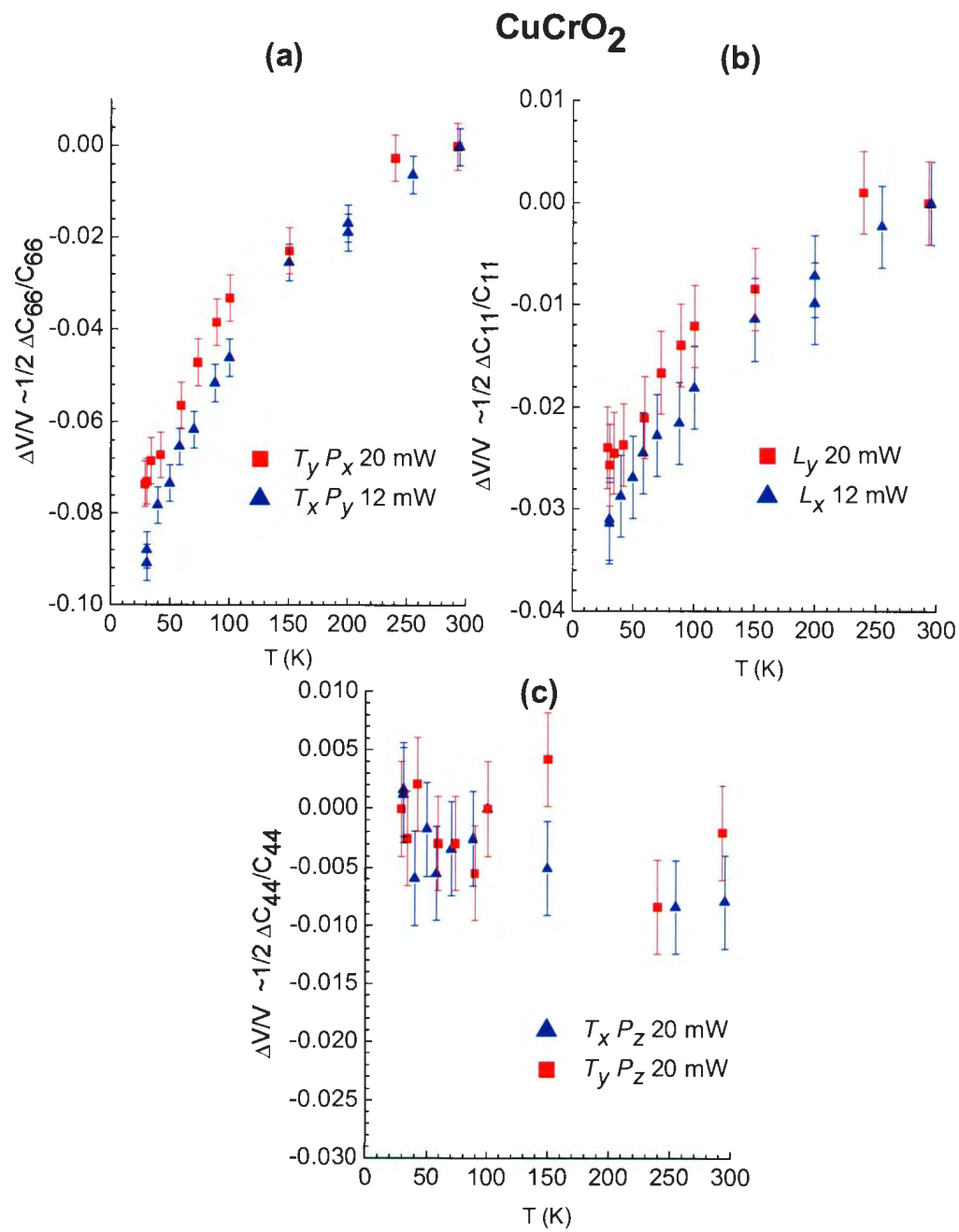
Figure 6.22: Relative velocity variations of the acoustic modes of CuCrO$_2$ observed along the x (triangles) and y axes (squares).

values at high temperatures. Modes propagating along the y axis are shown as squares while those propagating along the x axis are represented with triangles. The relationship between the acoustic velocities and associated effective elastic constants are given in Table 4.1. According to Table 4.1, Fig. 6.22a-c reflect the temperature dependence of the elastic constants C_{66}, C_{11}, and C_{44}, respectively. At 30 K, the temperature variation of the velocity for the modes T_yP_x and T_xP_y shows 7% and 9% softening relative to the value at room temperature. This softening corresponds to a decrease of about 11% in C_{66} (Table 6.5). Even though the velocity of T_xP_y is primarily determined by C_{66} (Table 4.1), it also depends on C_{14} and C_{44}, which might explain the difference in the temperature variation of both modes. In Fig 6.22b, we show the velocity variations of both longitudinal modes, L_y and L_x. Similar to transverse modes presented in Fig. 6.22a, both modes soften as the temperature is decreased down to 30 K. Softening observed in these modes is about 3%, which corresponds to a $\sim 5\%$ decrease in C_{11} relative to room temperature. Finally, we present the temperature dependence of the modes T_yP_z and T_xP_z in Fig. 6.22c. The velocities of these modes remain almost the same throught the temperature range, which indicates that C_{44} shows no variation with temperature.

Even though we could not obtain data down to the antiferromagnetic transitions, the softening observed on the elastic constant C_{66} implies that CuCrO$_2$ possibly undergoes a ferroelastic transition at $T_{N1} = 24.3$ K. However, in order to make a conclusive statement, the temperature dependence of the elastic constants around T_{N1} is still required. In that case, an alternative method, such as the ultrasonic pulse echo method [1], can be used to investigate the elastic properties of CuCrO$_2$ at lower temperatures.

Chapter 7

Ultrasonic velocity and dielectric measurements on CuCrO$_2$

Brillouin scattering measurements on CuCrO$_2$ show that acoustic modes related to C_{66} and C_{11} show softening as the temperature is decreased down to 30 K. Unfortunately, the minimum temperature achievable for the Brillouin measurements is 30 K, just above the antiferromagnetic transition at $T_{N1} = 24.3$ K. For that reason, we used the ultrasonic pulse-echo method to determine the elastic properties of CuCrO$_2$ down to ~ 4 K. In addition, ultrasonic velocity and dielectric measurements were simultaneously performed to further investigate magnetoelastic coupling and determine the magnetic phase diagram of CuCrO$_2$ for fields up to 8 T along the [1$\bar{1}$0] direction. Besides, these measurements aimed at clarifying whether there is one or two zero-field phase transitions at low temperatures [27, 58].

7.1 Ultrasonic velocity measurements

In this section, elastic properties of CuCrO$_2$ are determined using the ultrasonic pulse echo method. The difference between the ultrasonic pulse echo method and Brillouin scattering

is that the ultrasonic pulse echo method measures acoustic waves induced by a transducer, whereas Brillouin light scattering experiments investigate phonons that already exist in the crystal. The two techniques have several advantages and disadvantages compared to each other. One of the disadvantages of the ultrasonic pulse echo method is that samples of 0.5 mm long are normally required. On the other hand, Brillouin scattering can be used to study bulk modes in much smaller samples as thin as 1 μm [103]. In addition, the surface area required for Brillouin scattering can be of the order of several hundred μm, which is large enough for the spot size of the focused light. Another disadvantage of the ultrasonic pulse-echo method is that below ferroic transitions, domains may cause large acoustic attenuation. More importantly, the velocity measured in that case is the average velocity of the domains. In the case of Brillouin scattering, domains may cause broadening in the line shape and therefore a decrease in the intensity of phonon peaks [104]. However, even if the incident light is focused on several structural domains [104], Brillouin peaks associated with different domains can be resolved [104]. One of the disadvantages of Brillouin scattering over the ultrasonic pulse echo method was that the contrast provided by the single Fabry-Perot interferometers is not sufficient to study opaque materials [84]. Therefore, the development of multi-pass interferometers in the past 40 years has made this technique more convenient, although local heating due to the incident beam power has to be taken into account [84]. Moreover, Brillouin scattering techniques cannot provide the resolution provided by the ultrasonic pulse-echo method. The ultrasonic pulse echo method can provide a resolution as high as 1 part per million [1], whereas Brillouin scattering is limited to 0.1% [84].

Regardless of the advantages and disadvantages, both techniques are complementary. In our case, due to the small sizes and dimensions of the samples, uncertainties on the absolute acoustic velocities obtained with the ultrasonic pulse-echo method were large. Along the z axis, we could not even measure the acoustic velocity as the samples are only 0.5 mm long (see Fig. 6.1). However, along the other directions, relative variations of the acoustic

velocities are obtained with a resolution as high as a few parts per million down to 4 K.

CuCrO$_2$ samples were platelets with a surface area of 2 mm$\times$2 mm in the triangular lattice plane (xy plane) and about 0.5 mm along the z axis (See Fig. 6.1). Prior to ultrasonic velocity measurements, samples were polished using abrasive slurry which is a mixture of glycerin and SiC grains (White Abrasives Inc., 1200 RA SiC) in order to obtain parallel and smooth surfaces. Acoustic waves were generated at $\sim$30 MHz with a repetition rate of 1 kHz. The temperature dependent measurements of the acoustic modes were performed along the x and y directions (the [110] and [1$\bar{1}$0] directions in the hexagonal basis).

The temperature dependences of all acoustic modes propagating along the x and y axes in CuCrO$_2$ are presented in Fig. 7.1. Modes propagating along the x axis are plotted using green lines, whereas modes propagating along the y axis are plotted using red lines. The data presented in Fig. 7.1 are normalized relative to the maximum value at high temperatures. All modes show only one distinct anomaly at $T_{N1} = 24.3 \pm 0.2$ K, below which a collinear phase is expected down to $T_{N2} = 23.6$ K [27, 61]. As seen in Fig. 7.1, none of the acoustic modes show an anomaly at T_{N2} which is the transition temperature to the proper-screw spin structure [25, 27]. In addition, no thermal hysteresis was observed at T_{N1} in any of the modes. Thermal hysteresis is a characteristic of first order phase transitions which manifests itself with two different critical temperatures for warming and cooling cycles (see Chapter 8). This observation agrees with magnetic susceptibility, [27, 61], dielectric constant [27], specific heat [27] and polarization measurements [26, 27] on CuCrO$_2$. The most interesting feature of the results is that the velocities decrease as the temperature is reduced down to T_{N1}. Especially, the transverse modes $T_x P_y$ and $T_y P_x$ show softening up to 20% (Fig. 7.1a), which corresponds to a reduction of about 35% in the elastic constant C_{66} relative to room temperature (Table 4.1). For convenience, the room temperature values of the elastic constants determined by Brillouin scattering are presented in Table 7.1. In Fig. 7.1b, temperature dependences of the longitudinal modes L_x and L_y indicate a decrease of $\sim$6%
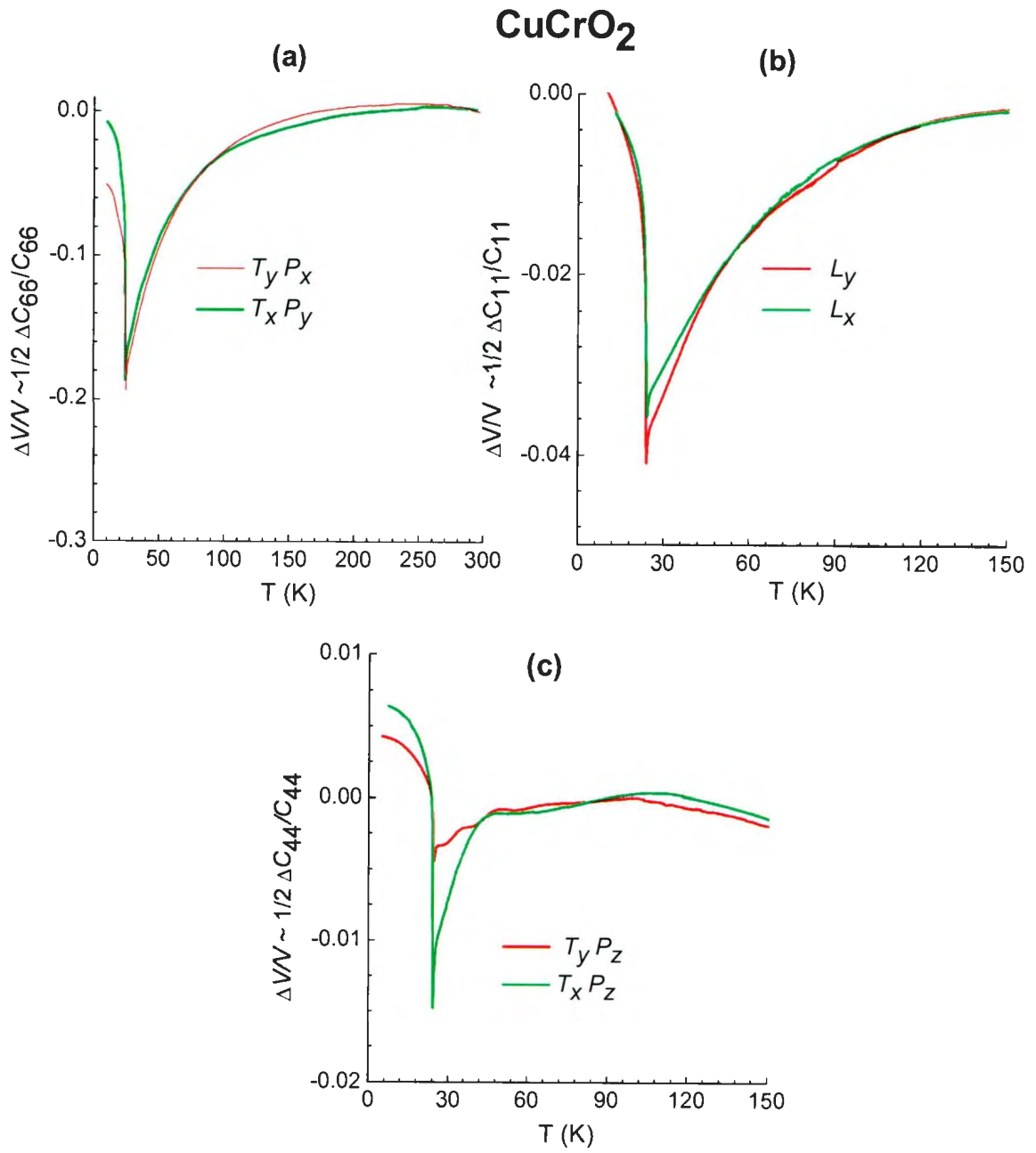
Figure 7.1: Temperature dependence of the normalized acoustic mode velocities in $CuCrO_2$: **a)** $T_x P_y$ and $T_y P_x$ **b)** L_y and L_x **b)** $T_y P_z$ and $T_x P_z$

118

Table 7.1: Experimental values of the bare elastic constants in $CuCrO_2$ at room temperature

Bare values	C_{11}	C_{12}	C_{33}	C_{44}	C_{66}
10^{10} N/m^2	24.2 ± 0.7	8 ± 1	47 ± 3	2.35 ± 0.07	8.0 ± 0.2

in C_{11} relative to high temperatures. The decrease in the velocity of transverse modes $T_y P_z$ and $T_y P_x$ (Fig. 7.1c) corresponds to a softening of 2% in C_{44}.

As discussed previously, sound velocity measurements on $CuFeO_2$ show evidence of a second order $R\bar{3}m \rightharpoonup C2/m$ pseudoproper ferroelastic transition at $T_{N1} = 14$ K [1]. All modes in $CuFeO_2$ show softening down to T_{N1}, similar to our results obtained on $CuCrO_2$. In Fig. 7.2a, we compare the temperature behavior of the transverse mode $T_x P_y$ in $CuCrO_2$ and that in $CuFeO_2$ [1]. In Fig. 7.2, the dotted lines represent the data for $CuFeO_2$, while the continuous lines are for $CuCrO_2$. Although the softening on both modes is comparable, $T_x P_y$ in $CuFeO_2$ seems to show complete softening whereas the softening observed in $CuCrO_2$ is clearly incomplete. According to the Landau model for $CuFeO_2$ [1], complete softening of this mode is expected when the transition is second order. Large softening of the transverse mode $T_x P_y$ in $CuCrO_2$ suggests that the transition at T_{N1} is also ferroelastic [105]. In order to further investigate the order of the transition at T_{N1} in $CuCrO_2$, we compare in Fig. 7.2b the temperature dependence of the longitudinal mode L_x in $CuCrO_2$ and $CuFeO_2$ [1]. Both modes show a decrease in the velocity with significant differences below T_{N1}. As seen in the inset of Fig. 7.2b, below T_{N1} the velocity in $CuCrO_2$ (continuous line) increases more rapidly compared to results obtained on $CuFeO_2$ (dotted line). The temperature dependence of L_x in $CuCrO_2$ is similar to the behavior obtained in NaN_3 at $T_c = 293$ K [105]. This particular behavior in NaN_3 was considered as evidence for a weakly first order $R\bar{3}m \rightharpoonup C2/m$ ferroelastic transition [105]. Thus, in order to determine whether the transition at T_{N1} in $CuCrO_2$ is first order, we compare in Chapter 8 the data to predictions
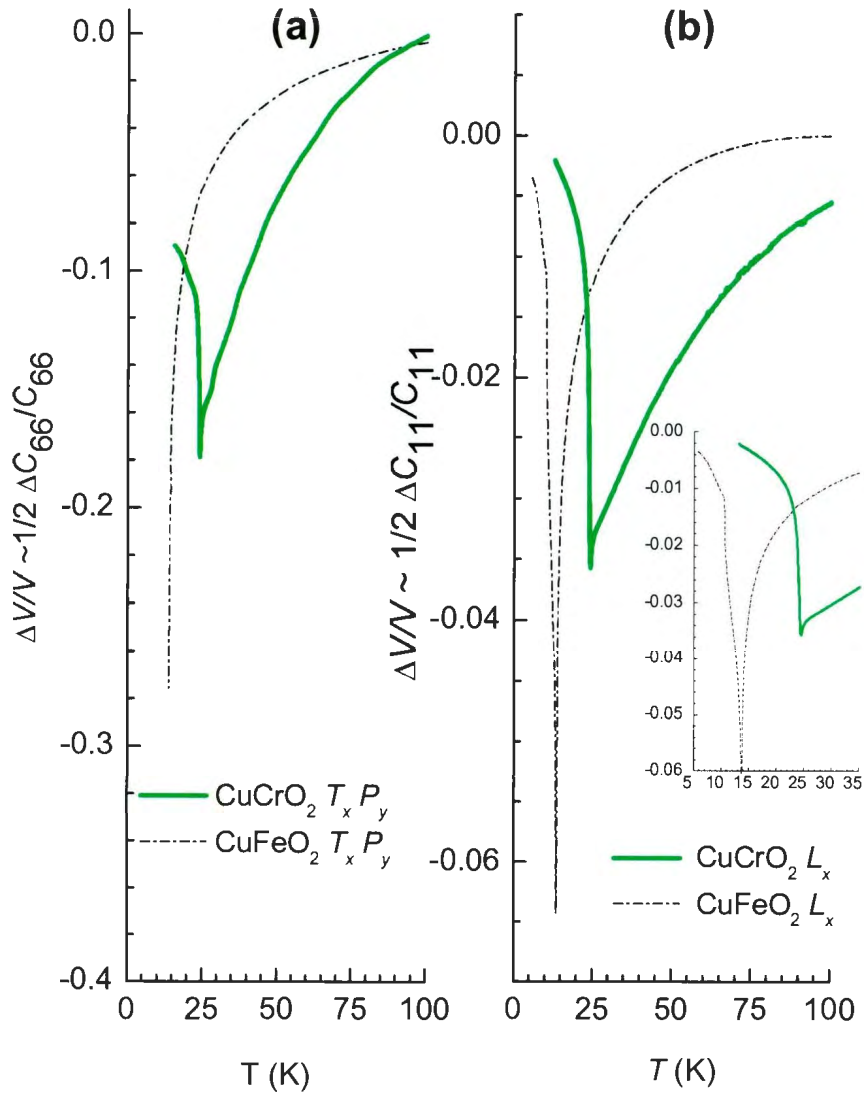
Figure 7.2: The relative velocity variations of **a)** $T_x P_y$ in CuCrO$_2$ (continuous lines) and CuFeO$_2$ (dashed lines) and **b)** L_x in CuCrO$_2$ and CuFeO$_2$. The experimental data for CuFeO$_2$ are reprinted with permission from [G. Quirion, M. J. Tagore, M. L. Plumer, O. A. Petrenko, Phys. Rev. B **77**, 094111 (2008)]. Copyright (2008) by the American Physical Society.

derived from a first order Landau model.

7.1.1 Magnetic phase diagram of CuCrO$_2$

In this section, we determine the magnetic phase diagram of CuCrO$_2$ for fields applied along the [1$\bar{1}$0] and [110] directions (hexagonal basis). So far, the Cartesian coordinate system has been mostly used throughout the text. In this section, it is more convenient to use hexagonal axes since we refer to the symmetry properties of the triangular lattice of CuCrO$_2$ to explain our findings. Therefore, the sketch of the projection of the Cr and O ions along the z axis shown in Fig. 2.2 is also presented in Fig. 7.3 to define the Cartesian and hexagonal axes. Large circles represent the chromium ions, whereas small open and filled circles represent oxygen ions located above and below the Cr layer, respectively. The crystallographic directions in the hexagonal basis are represented by a, b, c, [110] and [1$\bar{1}$0], whereas Cartesian axes are designated by x, y, and z. The axes x, y, and z are defined parallel to the [110], [1$\bar{1}$0], and c directions of the hexagonal basis. Thin lines and a triangle with a small white circle at the central Cr ion indicate mirror planes (m) and a threefold rotation axis with an inversion center normal to the plane of projection. The twofold rotation axes are shown with black arrows. In the $R\bar{3}m$ space group, the symmetry operations are a spatial inversion, a threefold rotation about the c axis, twofold rotations about the a, b, and [110] axes, and mirror planes perpendicular to the twofold rotation axes. Using the hexagonal coordinates, the notations for acoustic modes should also be changed. In that case, L_y, $T_y P_x$, and $T_y P_z$ read as $L_{[1\bar{1}0]}$, $T_{[1\bar{1}0]}P_{[110]}$, and $T_{[1\bar{1}0]}P_{[c]}$, respectively.

We first determine the number of magnetic phase transitions in CuCrO$_2$ at zero field. Our acoustic velocity measurements show only one transition at the antiferromagnetic transition at T_{N1} = 24.3 K (Fig. 7.1). While a single crystal study by Poienar et al. [58] and a number of measurements on polycrystals indicate one phase transition at $\sim$ 24.3 K, single
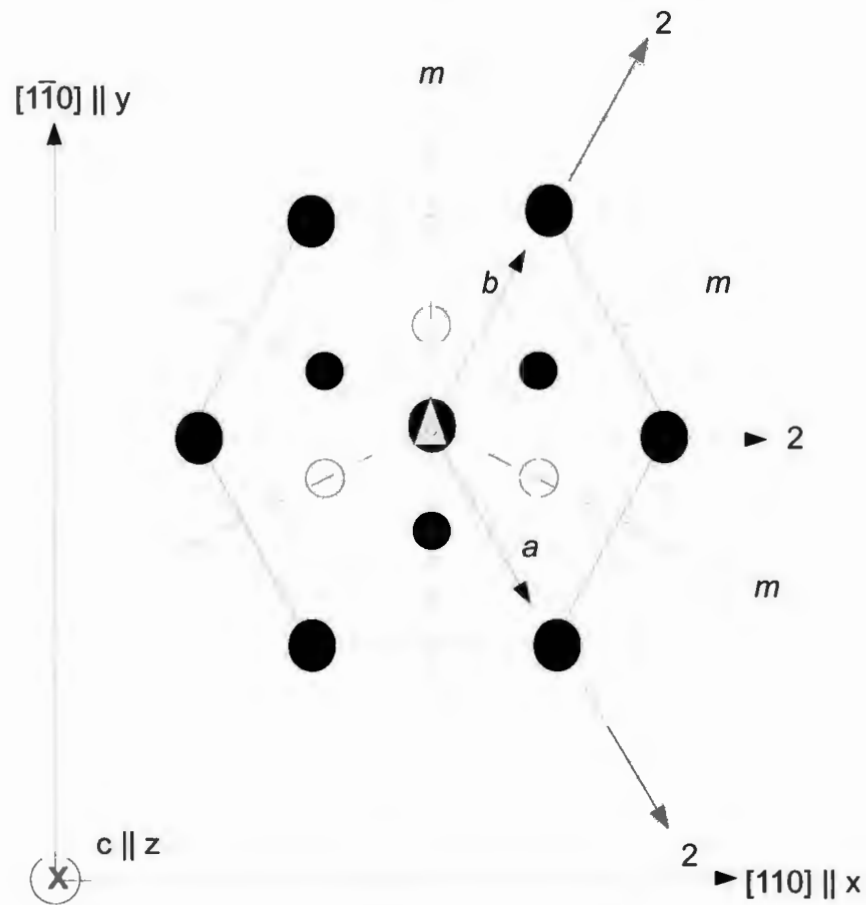
Figure 7.3: Identical to Fig. 2.2. The projection of a triangular lattice layer of Cr ions and two adjacent oxygen layers along the c direction in $CuCrO_2$ and symmetry operations of $R\bar{3}m$ space group. a, b, c, [110] and [1$\bar{1}$0] designate the directions in the hexagonal basis. In Cartesian coordinates, x and y axes are defined parallel to the [110] and [1$\bar{1}$0] directions of the hexagonal coordinates. The figure is identical to Fig. 2.2 and is replotted for convenience.

crystals studies by Kimura et al. [27] and Frontzek et al. [61, 62] indicate two transitions at $T_{N1} = 24.2$ K and $T_{N2} = 23.6$ K [27]. In particular, according to dielectric constant and polarization measurements by Kimura et al. [27], an electric polarization emerges at $T_{N2} = 23.6$ K. To clarify the number of low temperature phase transitions at zero field in $CuCrO_2$ and which phases are ferroelectric, we performed simultaneous measurements of capacitance $C_{[110]}$ and the velocities of acoustic modes $L_{[1\bar{1}0]}$ and $T_{[1\bar{1}0]}P_{[1\bar{1}0]}$ in $CuCrO_2$. It should be noted that our $CuCrO_2$ samples were provided by Kimura et al. [27] but are not the same samples as those used in their measurements. Measuring the capacitance $C_{[110]}$, the temperature dependence of the dielectric constant $\epsilon_{[110]}$ was determined using

$$C_{[110]} = \epsilon_{[110]}\epsilon_0\frac{A}{d}, \tag{7.1}$$

where $C_{[110]}$ is the capacitance along the [110] direction and ϵ_0 is the vacuum permittivity. Here, A corresponds to the area of two parallel plates separated by a distance d. In order to measure the capacitance of the sample, two thin brass plates were glued by using silicone on two parallel surfaces of the sample.

Results for $\epsilon_{[110]}$, performed with the longitudinal mode $L_{[1\bar{1}0]}$, are presented in Fig. 7.4a while those measured simultaneously with $T_{[1\bar{1}0]}P_{[110]}$ are shown in Fig. 7.4b. The absolute values of the dielectric constant $\epsilon_{[110]}$ shown in Fig. 7.4a-b are different. Our values are also smaller by a factor of 3 compared to earlier results [27]. Considering that the dielectric constant $\epsilon_{[110]}$ is calculated according to Eq. 7.1, our results clearly indicate considerable parasitic capacitance C_{probe} due to the experimental setup. One possibility is that the parasitic capacitance C_{probe} acts as a capacitor connected in series to the capacitance $C_{[110]}$ of the sample. In that case, what we measure could be less than $C_{[110]}$ because the equivalent capacitance C_{eq} would be given by $\frac{1}{C_{eq}} = \frac{1}{C_{probe}} + \frac{1}{C_{[110]}}$. Therefore, it is plausible that we obtain smaller values for the dielectric constant ($\epsilon_{[110]}$) of $CuCrO_2$ than those reported in literature [27]. Even though the absolute value for $\epsilon_{[110]}$ deviates from other results [27],

123
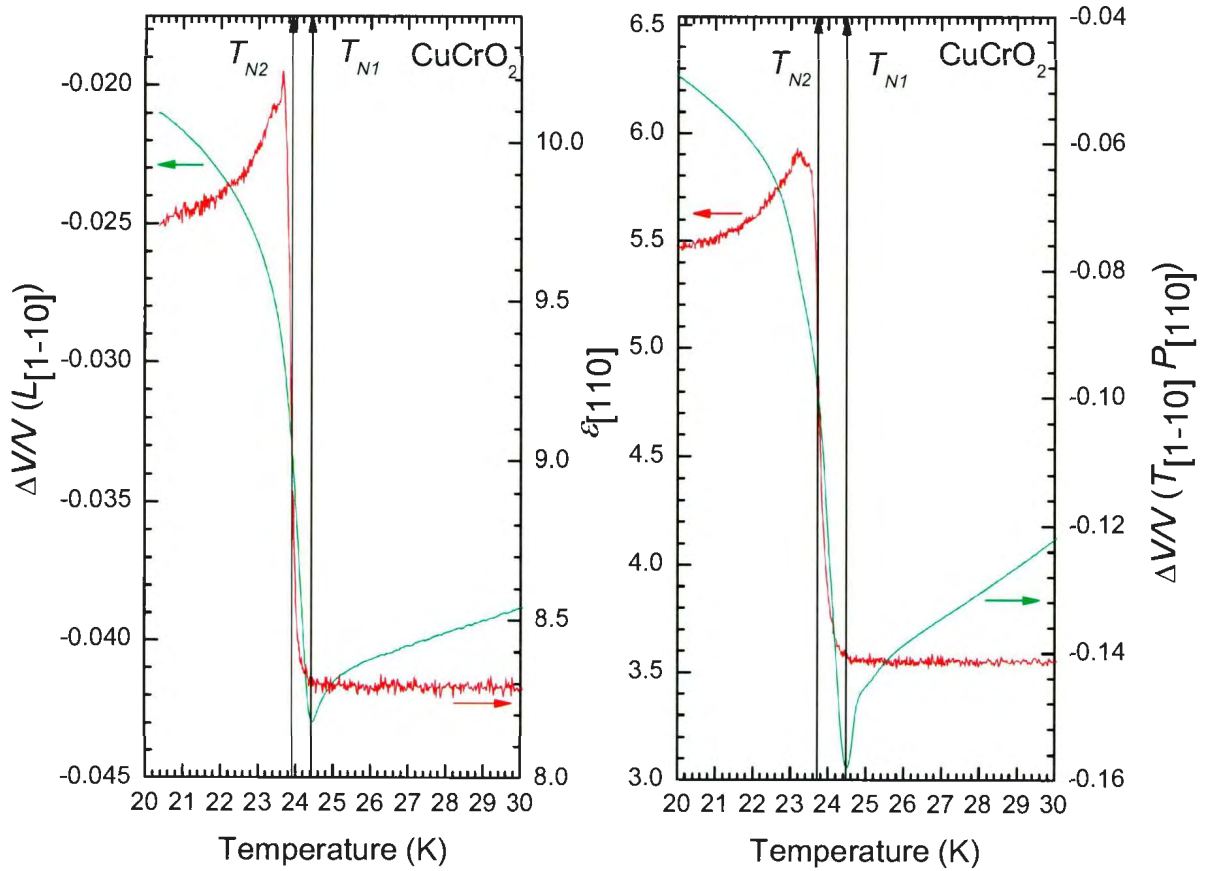
Figure 7.4: Temperature dependence of the dielectric constant $\epsilon_{[110]}$ simultaneously measured with the relative velocity variations of the acoustic modes **a)** $L_{1\bar{1}0}$ and **b)** $T_{1\bar{1}0}P_{[110]}$ in CuCrO$_2$.

our measurements consistently show a step-like anomaly with an increase between 2 and 2.5 in the dielectric constant at $T_{N2} = 23.8$ K, indicating that $CuCrO_2$ is ferroelectric below T_{N2} in agreement with Kimura et al. [27]. On the other hand, the velocities presented in Fig. 7.4 show a minimum at $T_{N1} = 24.3$ K. Therefore, we conclude that at zero field, $CuCrO_2$ undergoes a transition at $T_{N1} = 24.3$ K and a second one at $T_{N2} = 23.8$ K, in agreement with Refs. [27, 61, 62]. The absence of an acoustic anomaly at T_{N2} is indicative of weak magnetoelastic and piezoelectric coupling at this temperature.

Next, the field dependence of the transition at T_{N1} was determined through the measurements of acoustic mode velocities at a magnetic field. Therefore, at fields parallel to the $[1\bar{1}0]$ direction the relative velocity variations of the acoustic modes $L_{[1\bar{1}0]}$, $T_{[1\bar{1}0]}P_c$, and $T_{[1\bar{1}0]}P_{[110]}$ were measured. According to these measurements (not shown), the transition temperature T_{N1} is field independent up to 8 T. In order to obtain the field dependence of the transition at T_{N2}, we measured the capacitance along the [110] direction along with the transverse mode $T_{[1\bar{1}0]}P_{[110]}$. The variation of the dielectric constant $\epsilon_{[110]}$ is shown in Fig. 7.5 together with the acoustic mode $T_{[1\bar{1}0]}P_{[110]}$. The relative velocity variation of $T_{[1\bar{1}0]}P_{[110]}$ is shown with dashed lines, whereas the dielectric constant $\epsilon_{[110]}$ is shown with black lines. Since the acoustic mode velocity is independent of the magnetic field, we only show the temperature dependence of the acoustic mode at zero field. Unlike the transverse mode $T_{[1\bar{1}0]}P_{[110]}$, the dielectric constant significantly changes with the magnetic field. The largest increase in the dielectric constant is observed at zero field. With an increase in the magnetic field, the increase in the dielectric constant is gradually suppressed. When the field is 6 T or larger, the dielectric constant shows a minimum. Taking the transition temperature as the midpoint of the step like increase in the dielectric constant (indicated by the black arrow), we see that T_{N2} slightly changes with the magnetic field.

Possible new phases in $CuCrO_2$ were also investigated by measurements of acoustic modes as a function of magnetic field at a constant temperature. These measurements were per-
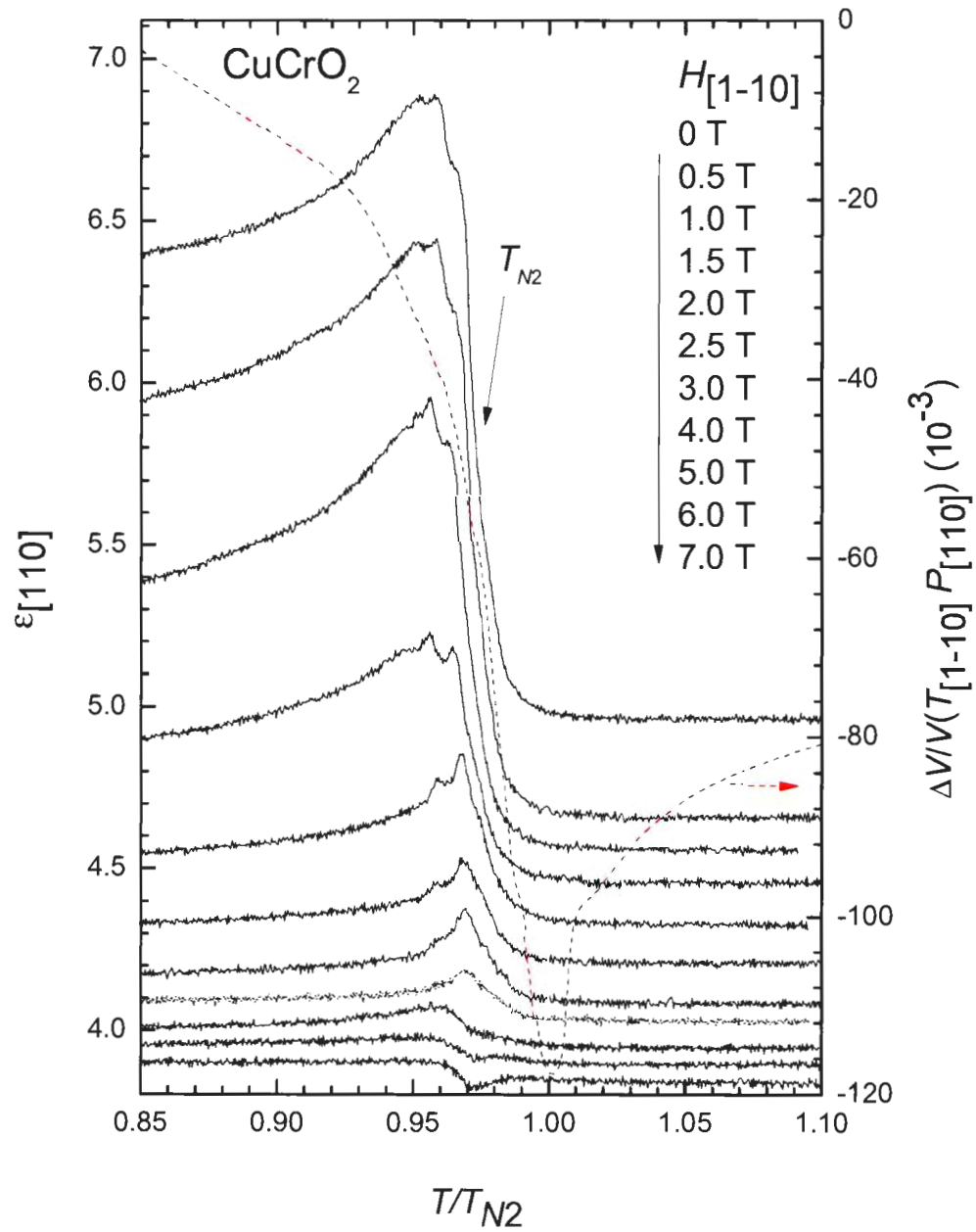
Figure 7.5: Temperature dependence of the dielectric constant along the [110] direction ($\epsilon_{[110]}$) simultaneously measured with the transverse mode $T_{[1\bar{1}0]}P_{[110]}$ in CuCrO$_2$ at constant fields parallel to the [1$\bar{1}$0] direction.

formed at temperatures between 2 K to 26 K. Previous magnetization measurements on $CuCrO_2$ indicate a first order magnetoelectric transition at 5.3 T at 2 K when the field is applied along the $[1\bar{1}0]$ direction [4, 66]. Therefore, we applied the magnetic field along the $[1\bar{1}0]$ direction.

The field dependence of the longitudinal mode $L_{1\bar{1}0}$ at 2 K and 23 K is shown in Fig. 7.6. At 2 K, the acoustic velocity shows a minimum at $H_{flop} \approx 5.3$ T, whereas at 23.7 K, a minimum is observed at $H_{flop} \approx 4.4$ T. At both temperatures, the velocity minimum is at different fields for increasing and decreasing magnetic fields, indicating that the transition is first order. In Fig. 7.7, we show the field dependence of the velocity of $L_{1\bar{1}0}$ for increasing fields. The velocity minimum first appears at slightly higher fields for temperatures up to 20 K and then goes down to 4.4 T at 23.7 T. The field scans performed on the transverse mode $T_{[1\bar{1}0]}P_c$ are shown in Fig. 7.8. In agreement with $L_{[110]}$, $T_{[1\bar{1}0]}P_c$ shows a minimum in its velocity at 5.3 T at 2.5 K. At 17 K, the minimum observed in the velocity is at higher field, 5.4 T. At 26 K, i.e. in the paramagnetic phase, no change is observed in the velocity with the magnetic field, which shows that the the acoustic anomalies have a magnetic origin. We also measured the velocity of the transverse mode $T_{[1\bar{1}0]}P_{[110]}$ as a function of magnetic field along the $[1\bar{1}0]$ direction. Results are shown in Fig. 7.9. Unlike the modes $L_{[110]}$ and $T_{[1\bar{1}0]}P_c$, the field dependence of $T_{[1\bar{1}0]}P_{[110]}$ shows a double minimum feature. However, the anomaly shows a similar behavior with temperature. Finally, in the paramagnetic phase (at 26 K), Fig. 7.9 shows no variation in velocity of $T_{[1\bar{1}0]}P_{[110]}$ with a magnetic field, as observed in the velocity of the mode $T_{[1\bar{1}0]}P_c$ (Fig. 7.8).

The field dependences of the acoustic modes $L_{[1\bar{1}0]}$ and $T_{[1\bar{1}0]}P_c$ presented in Figs. 7.6-7.8 are similar to the ones observed in the antiferromagnetic compounds $\alpha-$ Fe_2O_3 [106] and $CsNiCl_3$ [107]. In $\alpha-$ Fe_2O_3 [106] and $CsNiCl_3$ [107], the velocity dips observed at a critical field are explained by magnetoelastic coupling and are attributed to a spin-flop transition [106, 107]. Thus, we also associate the acoustic anomalies on $CuCrO_2$ (Figs. 7.6, 7.7, 7.8,
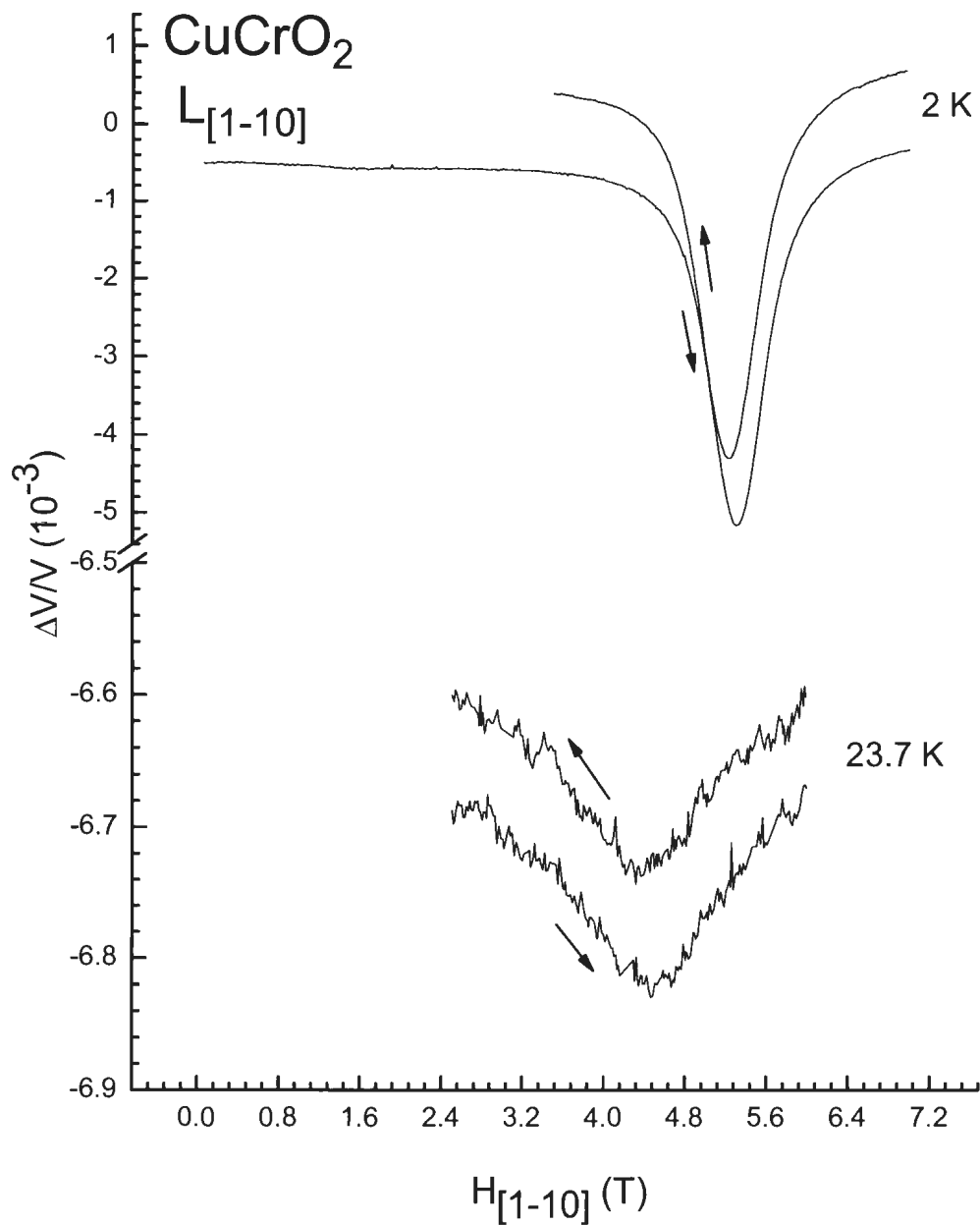
Figure 7.6: Relative velocity variation of the longitudinal acoustic mode $L_{[1\bar{1}0]}$ as a function of magnetic field parallel to the $[1\bar{1}0]$ direction in $CuCrO_2$. The data were collected at 2 K and 23.7 K for increasing and decreasing fields which were indicated by arrows.

128
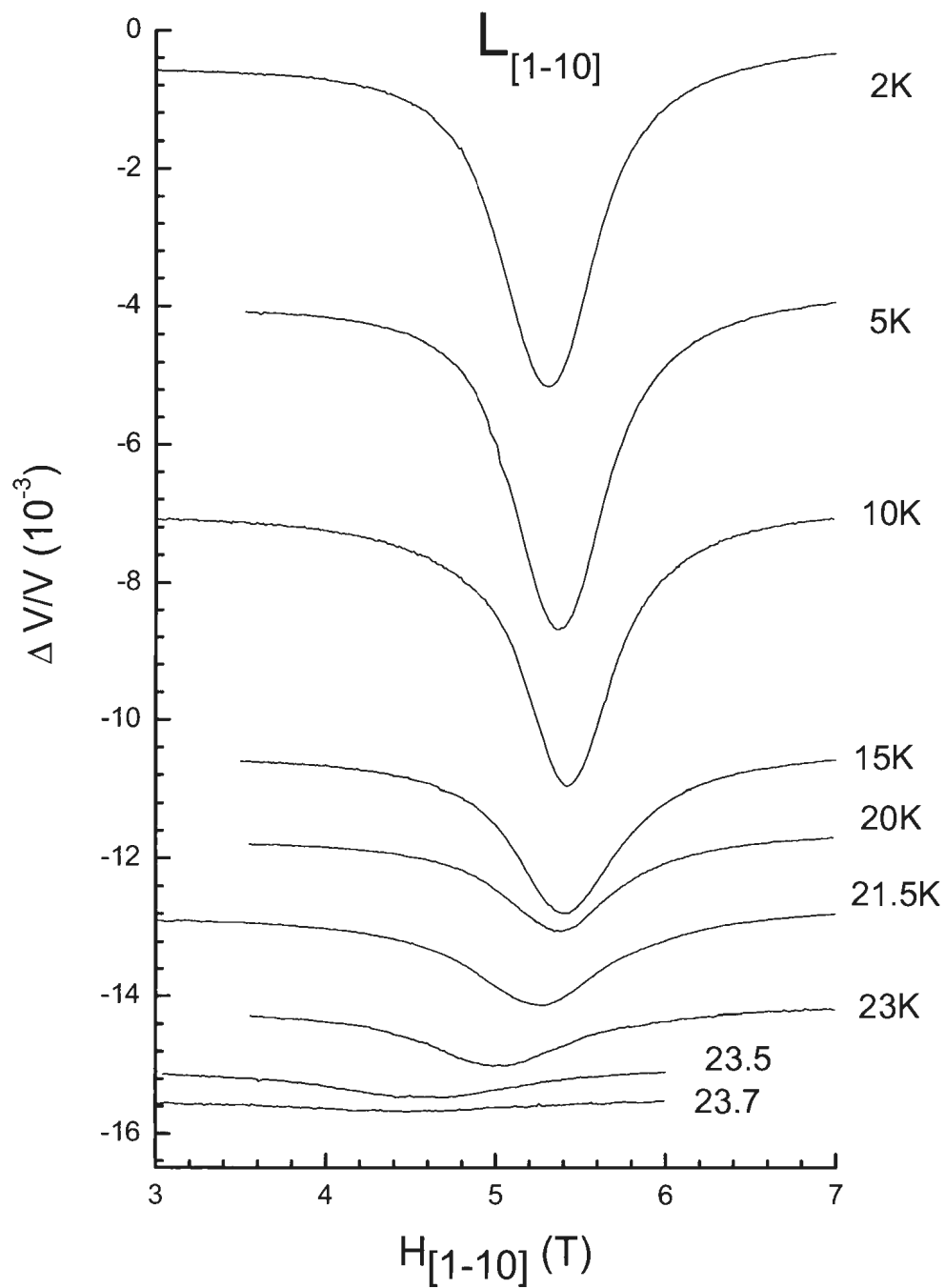
Figure 7.7: Relative velocity variation of the longitudinal acoustic mode $L_{[1\bar{1}0]}$ as a function of magnetic field parallel to the $[1\bar{1}0]$ direction in $CuCrO_2$ at temperatures between 2 K and 23.7 K. Data were collected for increasing magnetic field.
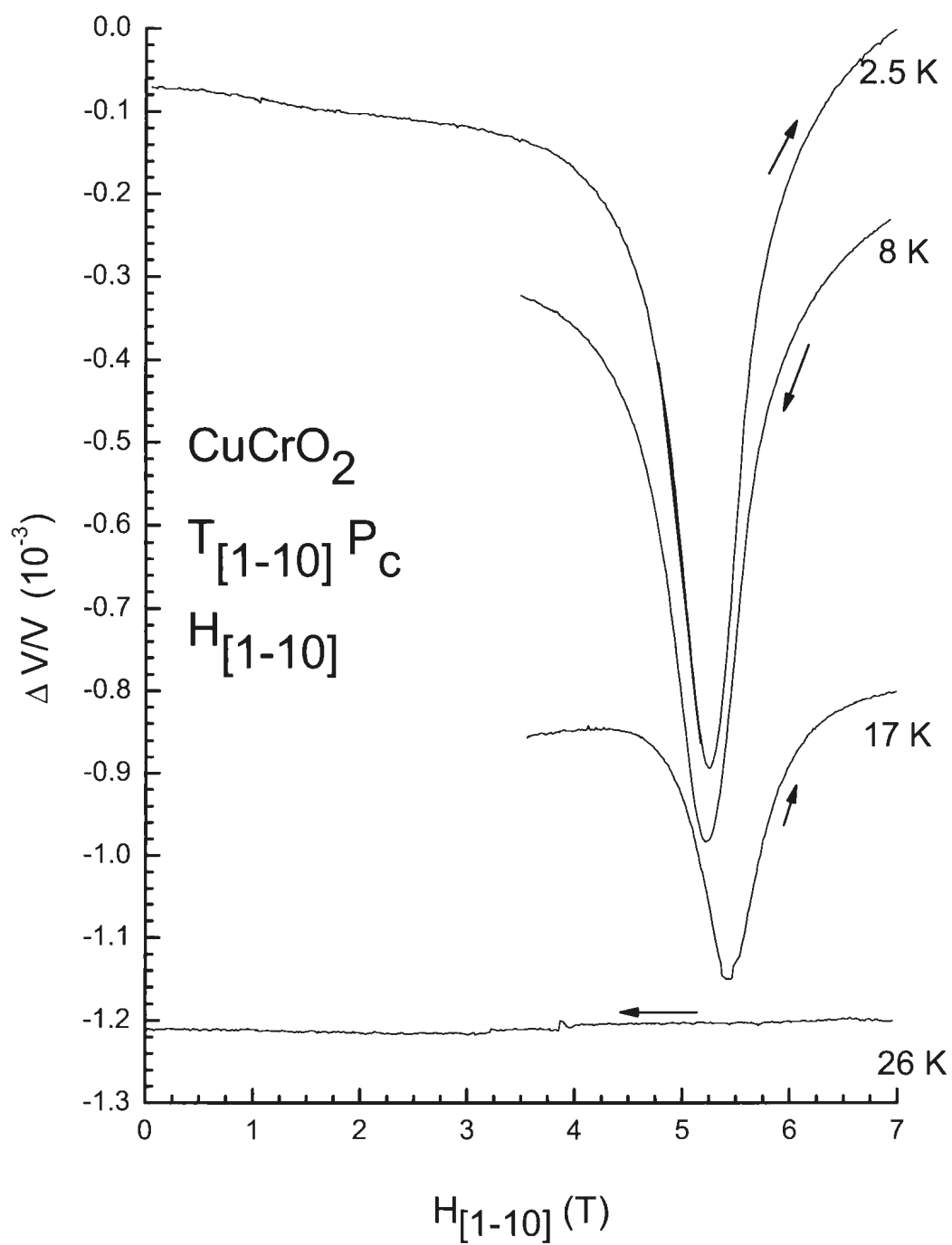
Figure 7.8: Relative velocity variation of the transverse acoustic mode $T_{[1\bar{1}0]}P_c$ as a function of magnetic field parallel to the $[1\bar{1}0]$ direction in $CuCrO_2$.

Figure 7.9: Relative velocity variation of the transverse acoustic mode $T_{[1\bar{1}0]}P_{[110]}$ as a function of magnetic field parallel to the $[1\bar{1}0]$ direction in CuCrO$_2$.

7.9) to a spin flop transition for fields applied along the $[1\bar{1}0]$ direction. In addition, in the case of $CsNiCl_3$ [107], the velocity dip observed in the longitudinal mode L_c is accounted for by the field dependence of the magnetic susceptibility. Thus, the ultrasonic data for $CuCrO_2$ suggest that the minimum observed in the longitudinal mode $L_{[1\bar{1}0]}$ (Figs. 7.6 and 7.7 is also due to the field dependence of the magnetic susceptibility.

A spin flop scenario in $CuCrO_2$ for the acoustic anomalies presented in Figs. 7.6-7.8 is in agreement with results obtained by magnetization, dielectric constant, polarization [4], and electron spin resonance measurements [66] on $CuCrO_2$. These measurements performed as a function of magnetic field along the $[1\bar{1}0]$ direction show a first order transition at 5.3 T at 2 K [4, 66]. The transition is attributed to a 90° flop of the spin-spiral plane in one of the magnetic structural domains A, B, and C [4, 66]. The flop of the spin-spiral plane is illustrated in Fig. 7.10, where rectangles denote the spiral plane whereas green arrows in each domain indicate the direction of the electric polarization induced by the proper screw spin structure. Considering the evidence for a structural transition at T_{N1} [4, 66], the domains are shown as slightly distorted relative to an equilateral triangle. In addition, if the structural transition is to the monoclinic $C2/m$ phase as in the case of $CuFeO_2$, the loss of three fold symmetry below T_{N1} should result in three structural domains which are at 120° relative to each other [66]. In Fig. 7.10, the spiral plane of each domain is shown with thick blue lines whereas the direction of the electric polarization is given by thick green arrows. The increase in the free energy due to the field is proportional to the dot product of a magnetic moment and the magnetic field. At a certain field, H_{flop}, the free energy of domain A becomes higher than domain A'. Therefore, in order to minimize the free energy, the magnetic domain A shows a transition to domain A' and the spiral plane flops by 90° as shown in Fig. 7.6. Domains B and C can also show a spin flop transition [4]. In that case, higher fields are required for a spin flop transition [4] as the spiral planes in B and C domains make an angle of 60° relative to the field direction.
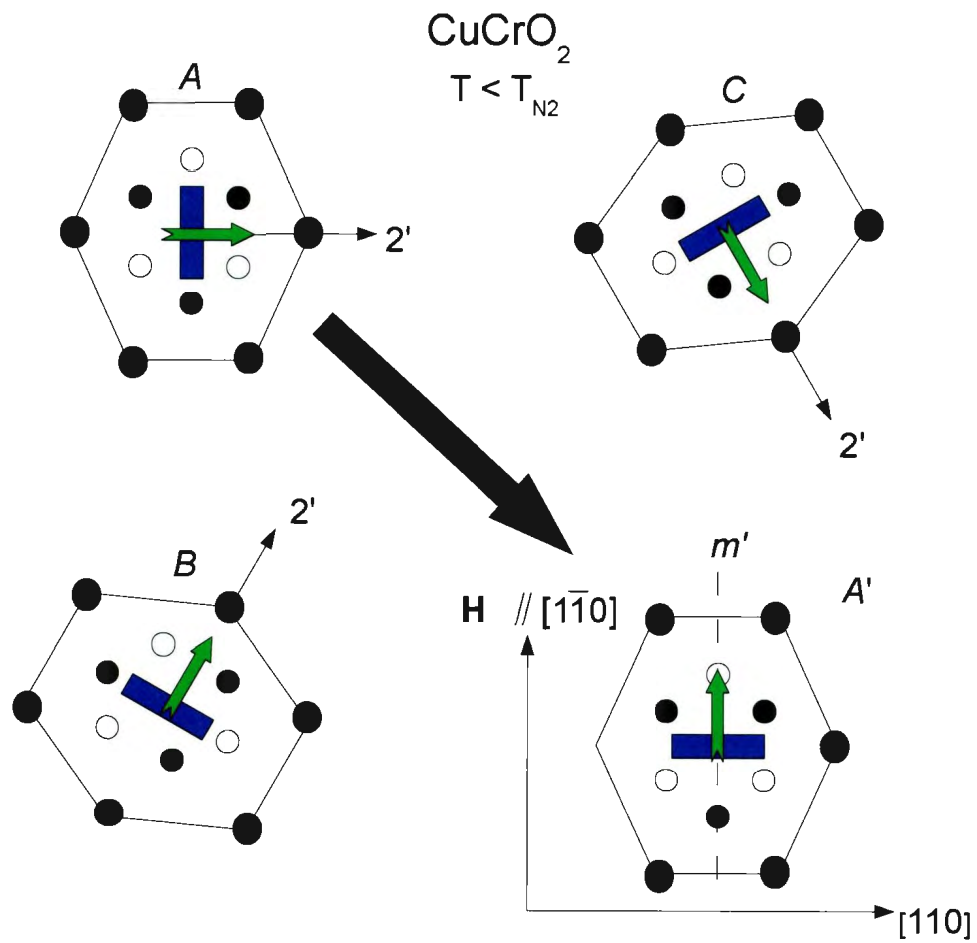
Figure 7.10: Magnetic structural domains A, B, and C in the multiferroic phase of $CuCrO_2$ and the transition from domain A into domain A' at a critical field parallel to the $[1\bar{1}0]$ direction. The figure is identical to Fig. 2.5 and is replotted for convenience.

As seen in Fig. 7.6, the proper screw spin structure in $CuCrO_2$ induces a spontaneous polarization in the direction of the magnetic modulation (see Sec. 2.1.1). Microscopically, the induced polarization is due to a variation of the metal-ligand hybridization [2]. As a result of the 90° flop in the spiral plane in domain A, the spontaneous polarization also flops by 90° [4, 66]. The direction of polarization after the spin flop is shown with the green arrow in domain A'. The 90° flop of the spontaneous polarization can be explained in terms of symmetry arguments [4]. After the spin-spiral flop, the remaining symmetry operation in domain A' is m', a time reversal operation followed by a mirror operation (broken line in A' in Fig. 7.10). Since the system can be polar only parallel to m', an electric polarization is allowed parallel to the $[1\bar{1}0]$ direction. Note that the dielectric constant in the ab plane of $CuCrO_2$ also shows an anomaly at the spin flop transition at low temperatures [27]. In order to determine if the dielectric constant shows similar anomalies at higher temperatures in the proper screw phase, we did a simultaneous measurement of the $\epsilon_{[110]}$ dielectric constant and the transverse acoustic mode $T_{[1\bar{1}0]}P_{[110]}$ as a function 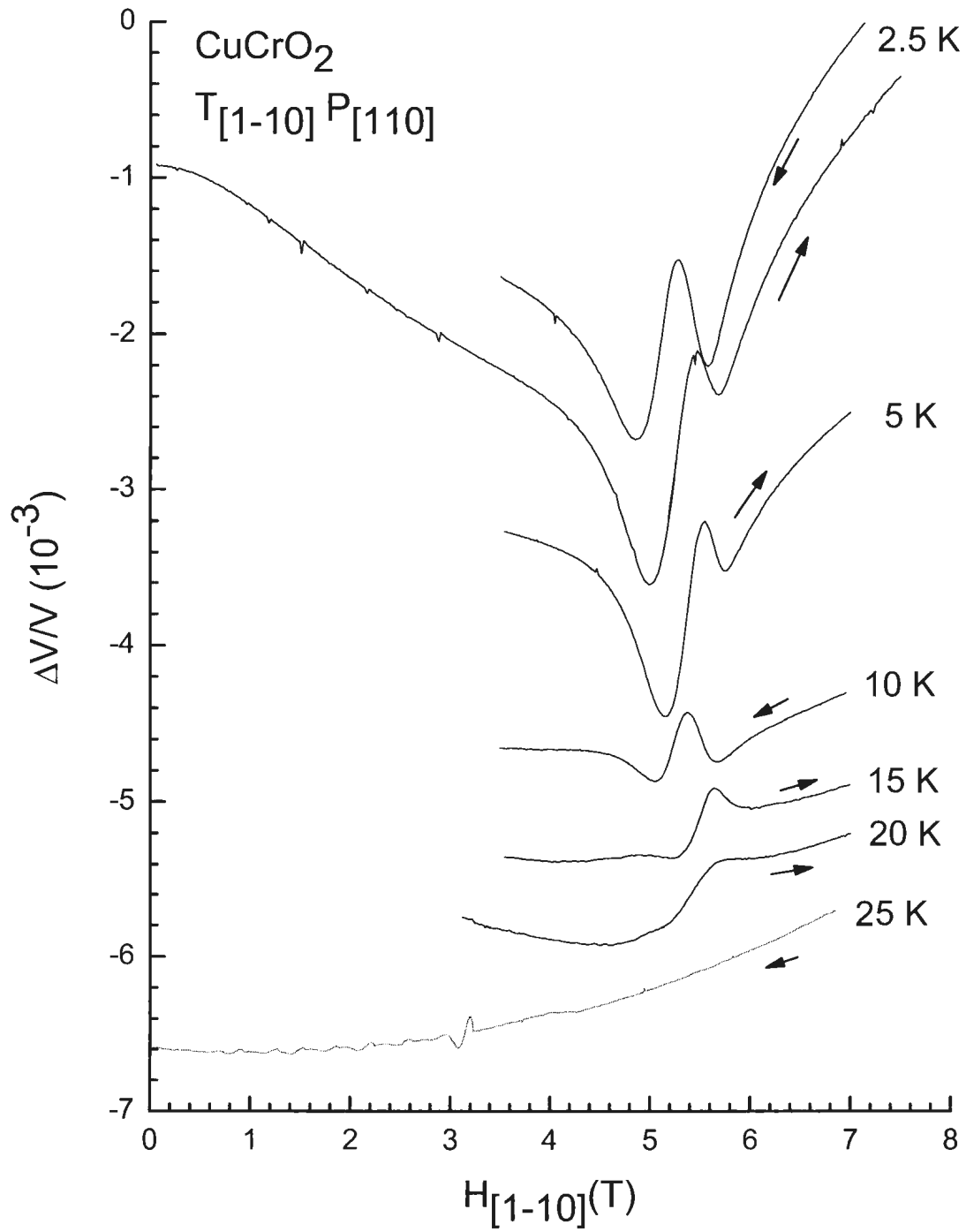of magnetic field parallel to the $[1\bar{1}0]$ direction. Results are shown in Fig. 7.11. Similar to results obtained by Ref. [4], the dielectric constant shows a decrease up to ~ 2 T. The anomaly in the dielectric constant that corresponds to the spin flop transition is at ~ 5.4 T, where the acoustic mode $T_{1\bar{1}0}P_{[110]}$ also shows an anomaly. The variation in the dielectric constant due to the spin flop is much smaller than the variation observed at 2 K [4]. Similar anomaly is also observed when the field scan is performed at 15 K (Fig. 7.11).

Using the data presented in Figs. 7.5, 7.7-7.8, and 7.11, we determine the magnetic phase diagram of $CuCrO_2$ for fields parallel to the $[1\bar{1}0]$ direction shown in Fig. 7.12. At zero field, $CuCrO_2$ is in the paramagnetic phase at temperatures above $T_{N1} = 24.3$ K (squares). Between T_{N1} and T_{N2} (triangles), the magnetic order is thought to be a collinear spin structure [4], which is illustrated in Fig. 7.12. Below T_{N2}, Cr ions order into a proper screw spin structure with a magnetic modulation in the [110] direction. The proper screw structure induces a

134

Figure 7.11: **a)** The dielectric constant along the [110] direction $\epsilon_{[110]}$ simultaneously measured with the transverse acoustic mode $T_{[1\bar{1}0]}P_{[110]}$ in $CuCrO_2$ as a function of magnetic field parallel to the $[1\bar{1}0]$ direction.
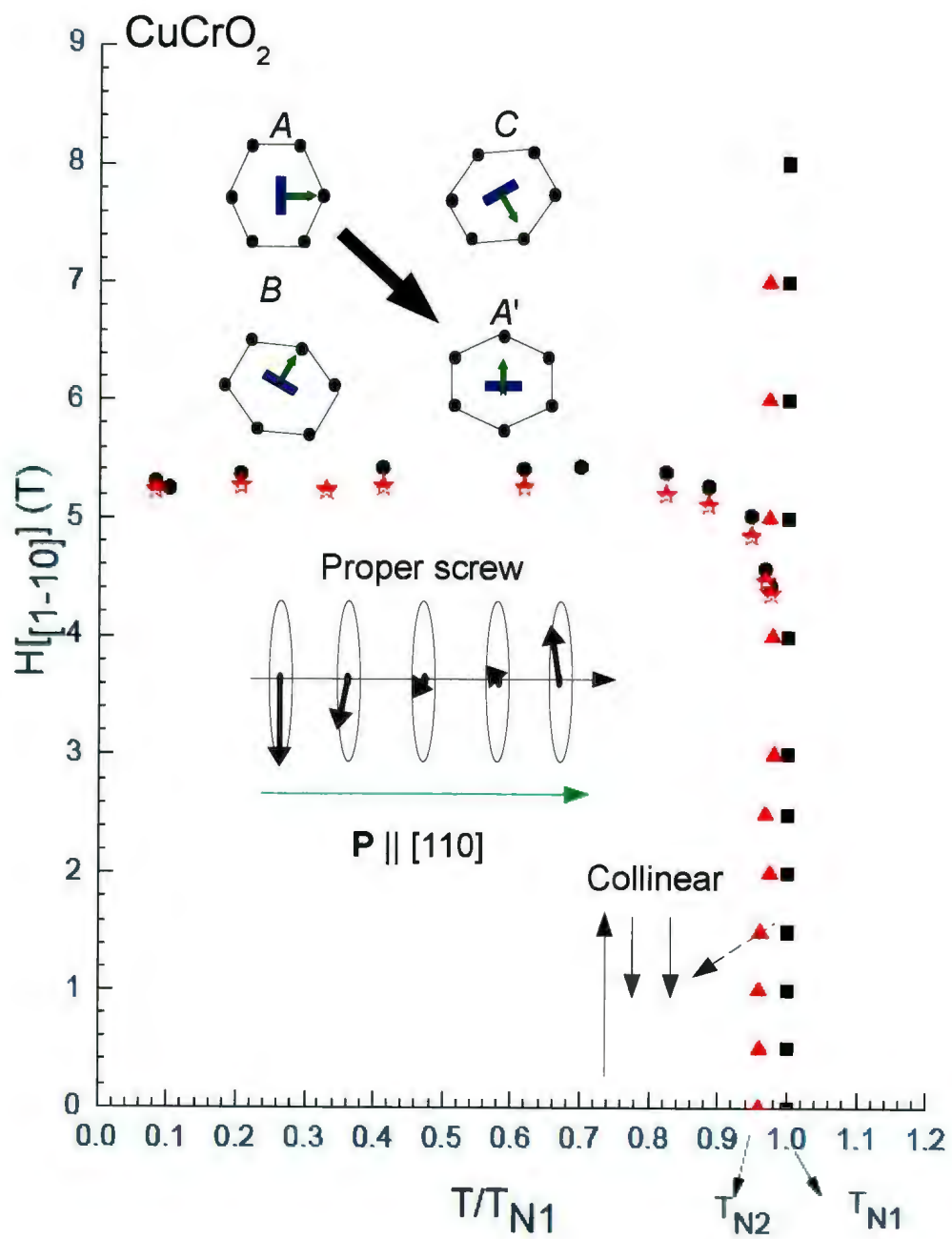
Figure 7.12: Magnetic field vs. temperature phase diagram of CuCrO$_2$ for fields parallel to the [1$\bar{1}$0] direction.

spontaneous polarization in the same direction as shown by a green arrow in Fig. 7.12. Below T_{N2}, acoustic and dielectric measurements as a function of magnetic field shows a spin flop transition. Fig. 7.12, the critical field H_{flop} required for the spin flop is shown with circles and stars for increasing and decreasing fields, respectively. The magnetic structural domains and the spiral plane (rectangle) in each domain are also shown. At H_{flop}, the spiral plane in domain A flops by 90° as shown in domain A'. Upon the spin spiral flop, the spontaneous polarization also flops by 90° (green arrows) [4, 66]. While $H_{[1\bar{1}0]} \approx 4.4$ T is sufficient for the spin-spiral flop at 23.7 K, the same transition is observed at 2 K with $H_{[1\bar{1}0]} = 5.3$ T.

As shown in Fig. 7.5, $\epsilon_{[110]}$ is field dependent for $H\|[1\bar{1}0]$. For comparison, we measured the dielectric constant $\epsilon_{[110]}$ for $H \|[110]$. The temperature scans of the dielectric constant and the velocity of the $(T_{1\bar{1}0}P_{[110]})$ acoustic mode under a magnetic field are shown in Fig. 7.13. The acoustic mode (dashed line), which shows a minimum at T_{N1}, is independent of the magnetic field. Therefore, the relative variation of the acoustic mode is only shown at zero field in Fig. 7.13. Similar to our previous measurements for $\epsilon_{[110]}$ (Fig. 7.4), at zero field the dielectric anomaly is at lower temperature than T_{N1}, indicating the transition at T_{N2}. In addition, the increase in the dielectric constant (~ 2) at the anomaly is also in agreement with our earlier results (Figs. 7.4 and 7.5). As the field is increased, the step like anomaly changes to a Lorentzian line shape. Note that this behavior is different from that observed when the field is applied along the $[1\bar{1}0]$ direction. For $H\|[110]$, T_{N2} is weakly field dependent as illustrated in Fig. 7.14, where triangles represent T_{N2} whereas the squares correspond to T_{N1}.

Dielectric measurements on $CuCrO_2$ were previously performed as a function of fields parallel to the $[110]$ direction at low temperatures [4]. These measurements show no evidence of a flop in the spin-spiral plane. However, it is suggested that a slight reorientation occurs in the spiral planes of domains B and C at intermediate fields, i.e. ~5 T. In order to investigate the reorientation in the spiral planes, we measured $\epsilon_{[110]}$ and the acoustic mode $T_{[1\bar{1}0]}P_{[110]}$ at

Figure 7.13: Temperature dependence of the dielectric constant $\epsilon_{[110]}$ simultaneously measured with the transverse acoustic mode $T_{[1\bar{1}0]}P_{[110]}$ in CuCrO$_2$ at constant fields parallel to the [110] direction.
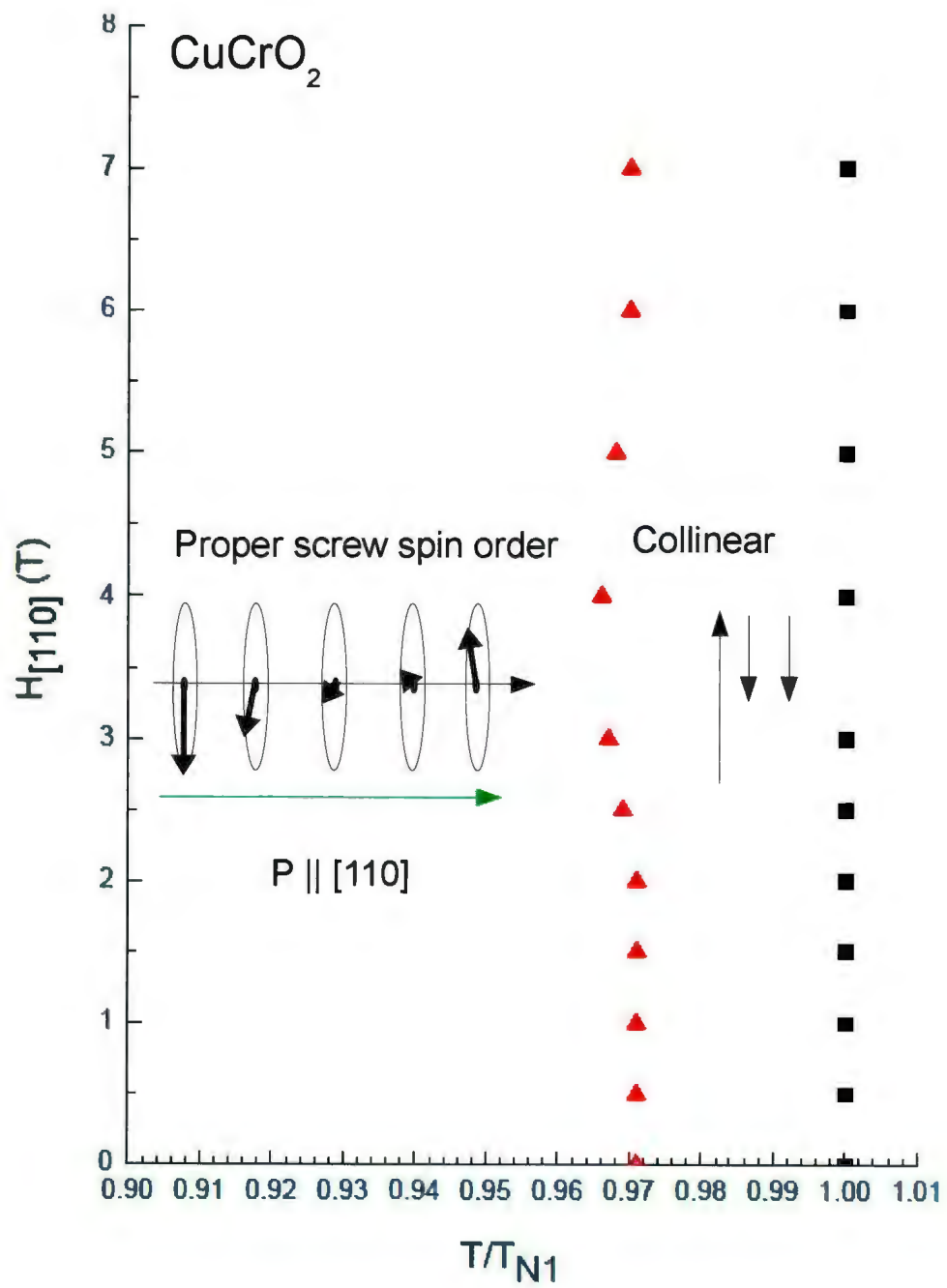
Figure 7.14: $H_{[110]}$ dependence of T_{N1} and T_{N2} in CuCrO$_2$.

139

3 K, 5 K and 20 K as a function of the fields for H $\parallel$ [110]. Results are shown in Fig. 7.15. Measurements performed for increasing and decreasing fields are indicated by arrows above each plot. As shown in Fig. 7.15a, the dielectric constant measured at 3 K and 5 K shows a rapid decrease between 0 T and 2 T, then remains nearly constant up to 7 T. Similarly, at 20 K the dielectric constant shows no variation between 4 T and 7 T. The acoustic mode also shows variations with the field as shown in Fig. 7.15b. At 3 K, the acoustic mode velocity slightly drops down to 2 T and then shows an S-shaped anomaly between 4 and 7 T. At 5 K and 20 K, the acoustic mode behaves similarly when compared to the data obtained 3 K. At 20 K, however the S-shaped anomaly slightly shifts to higher fields, showing its temperature dependence. In Fig. 7.16, we compare the field dependence of the dielectric constant and acoustic mode for H $\parallel$ [110] and H $\parallel$ [1$\bar{1}$0]. The data obtained as a function of the field along the [110] direction are shown with dashed lines whereas those obtained with the field along the [1$\bar{1}$0] direction are shown with continuous lines. At low fields, the dielectric constant behaves similarly for both field directions. However, the small bump in the dielectric constant is noticeable for $H_{[1\bar{1}0]}$, which corresponds to a spin flop transition in domain A (Fig. 7.10), is absent in the data for $H_{[110]}$. The acoustic mode shows a different behavior for $H_{[110]}$ and $H_{[1\bar{1}0]}$. While the spin flop transition observed at $H_{[1\bar{1}0]} \sim 5.4$ is marked with a double minimum feature in the acoustic mode velocity (continuous line), the acoustic mode shows an S-shaped anomaly with $H_{[110]}$. The behavior of the dielectric constant and the acoustic mode for $H_{[110]}$ can be considered as evidence for a reorientation in the spiral planes at ~ 5 T ([27]).
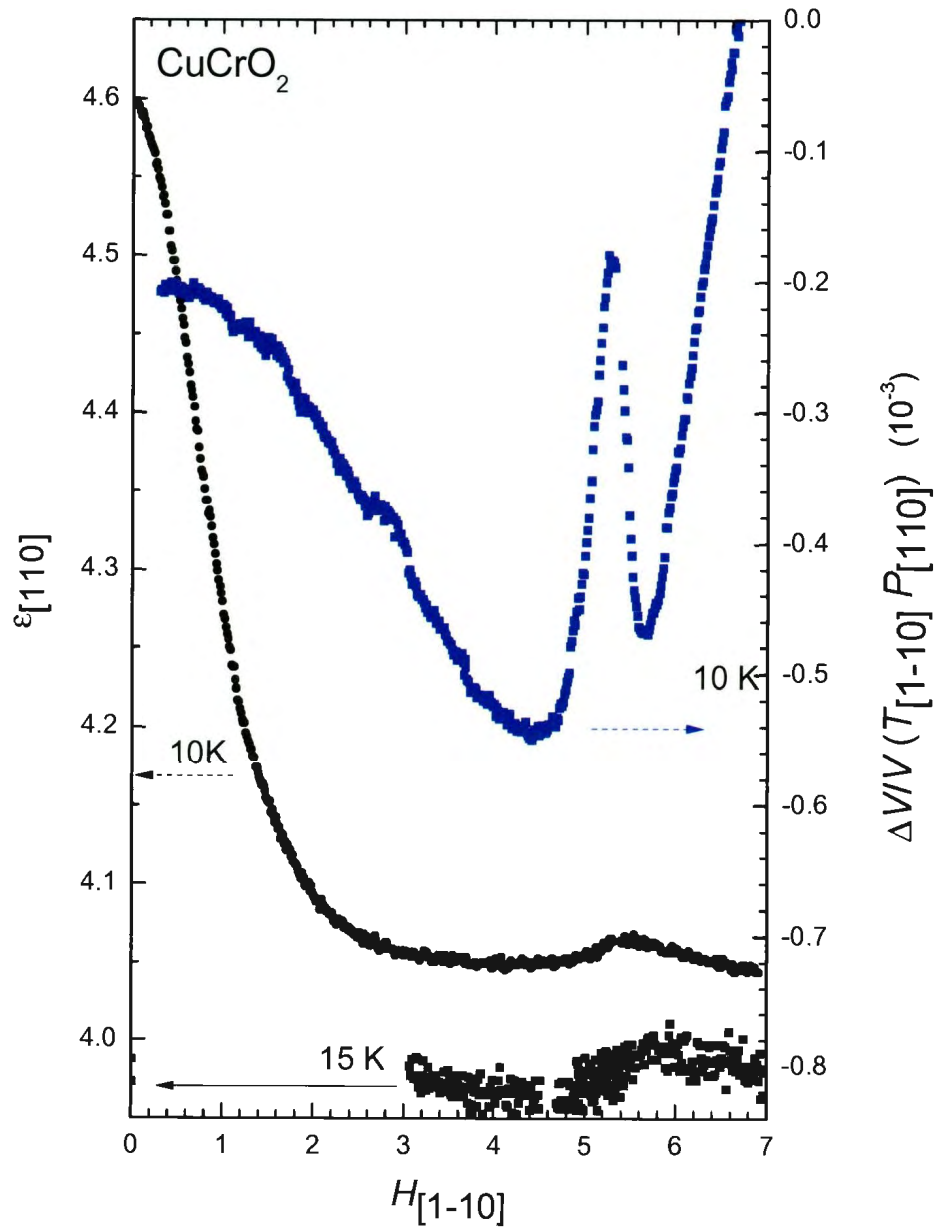
140
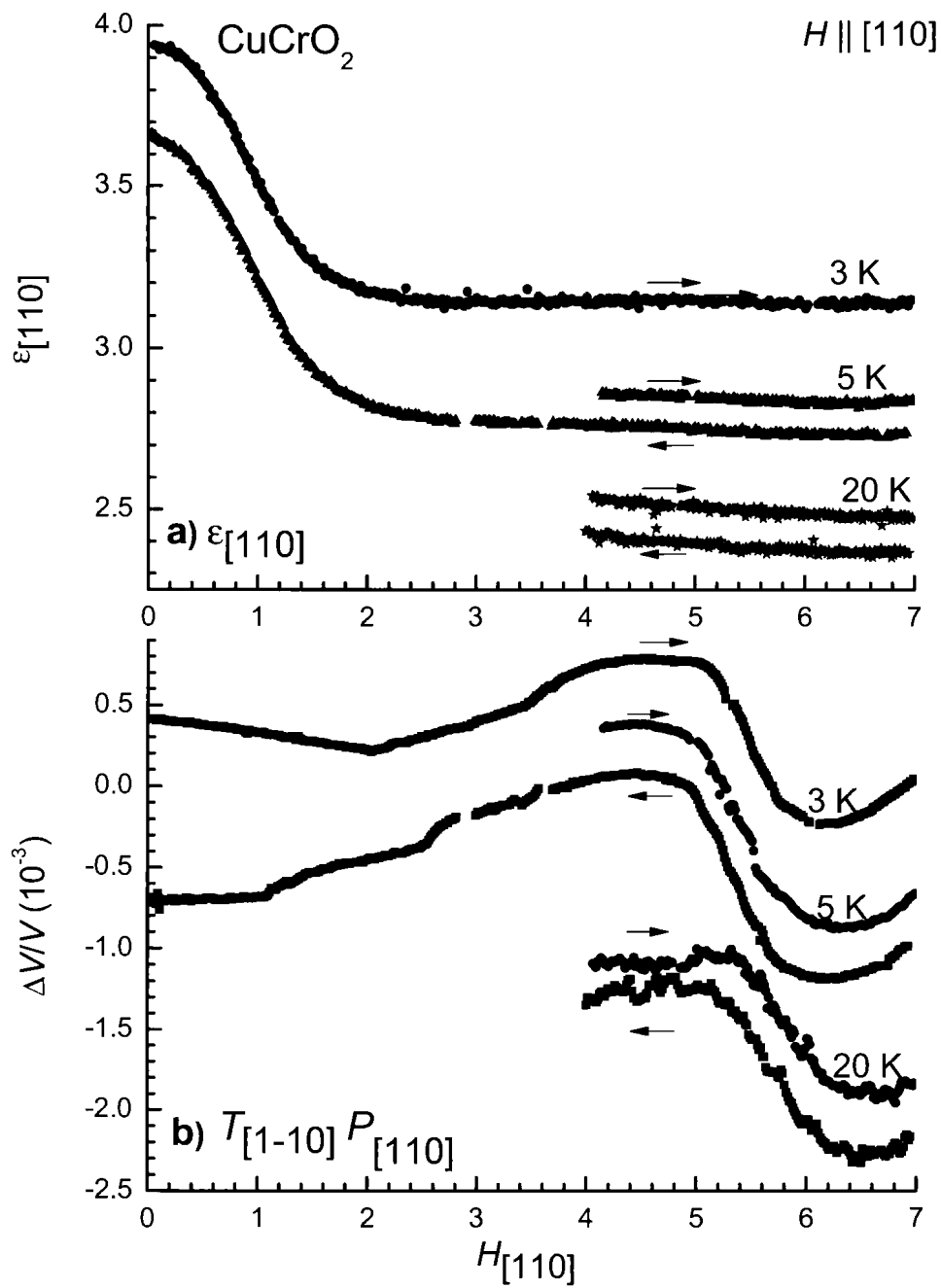
Figure 7.15: **a)** The dielectric constant along the [110] direction ($\epsilon_{[110]}$) simultaneously measured with **b)** the transverse acoustic mode $T_{[1\bar{1}0]}P_{[110]}$ in $CuCrO_2$ as a function of magnetic field parallel to the [110] direction.
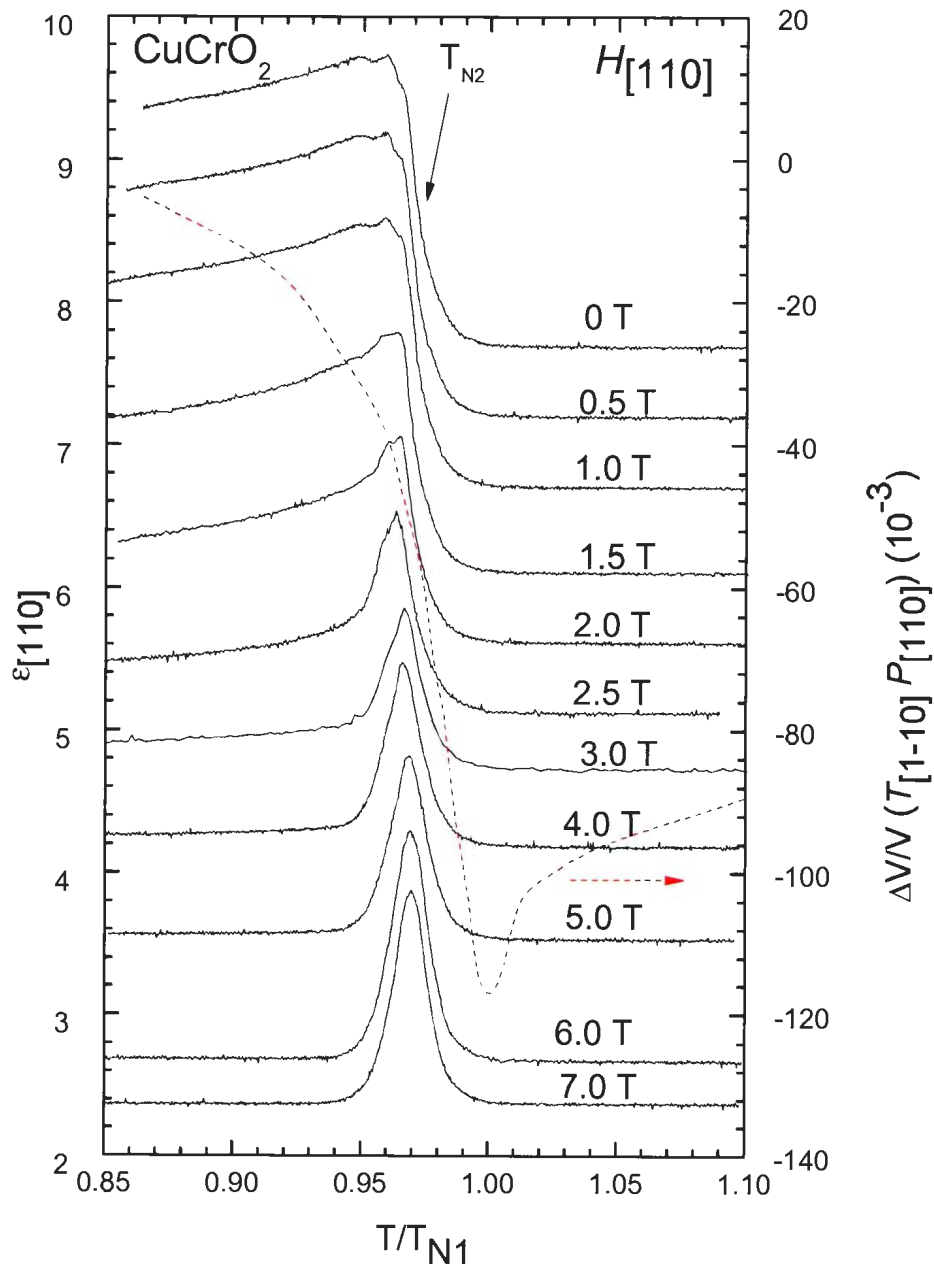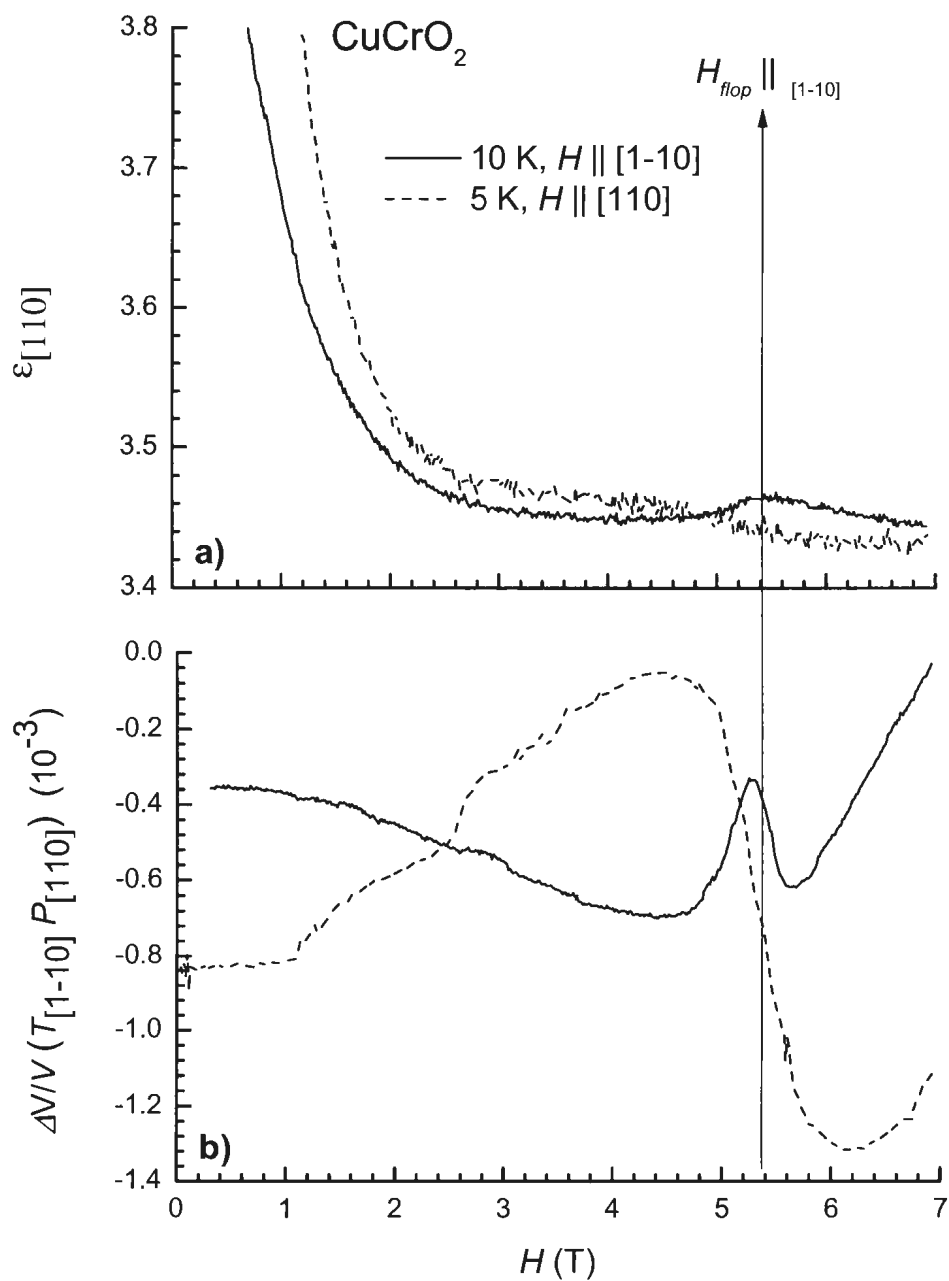
Figure 7.16: Comparison of the $H_{[110]}$ and $H_{1\bar{1}0}$ dependence of **a)** the dielectric constant $\epsilon_{[110]}$ simultaneously measured with **b)** the transverse acoustic mode $T_{[1\bar{1}0]}P_{[110]}$ in CuCrO$_2$.

7.1.2 Comparison of ultrasonic and Brillouin scattering measurements

In this section, we compare the elastic properties of $CuCrO_2$ obtained by Brillouin scattering and ultrasonic pulse-echo method. The mode velocities in Fig. 7.17 are normalized with respect to the velocity maximum measured at high temperatures. According to Table 4.1, Fig. 7.17a-c reflect the temperature dependences of the elastic constants C_{66}, C_{11}, and C_{44}, respectively. The relative velocity variations obtained with Brillouin scattering are represented with symbols. Modes propagating along the y axis are plotted with red squares while those propagating along the x axis are represented with blue triangles. These results are compared to ultrasonic measurements represented with blue and red lines, which correspond to the data for modes propagating along the x and y axes. In Fig. 7.17a and b, the data obtained with Brillouin scattering and ultrasonic measurements show a quantitative agreement down to about 60 K. However, they significantly deviate at low temperatures. In the case of the transverse mode T_yP_z presented in Fig. 7.17c, the velocity variations are in agreement down to 30 K, however it is worth pointing out that the softening observed on this mode is on the order of the experimental uncertainty in Brillouin measurements.

There might be several reasons for the disagreement between both sets of data at low temperatures. First of all, the velocities determined by Brillouin scattering (Fig. 7.17) are calculated with the assumption that the dielectric constants, or the refractive indices, do not considerably change with temperature. However, it could also be related to local heating due to the incident laser beam. In order to test this assumption, we performed Brillouin scattering measurements using different beam power (Fig. 7.18). The data for the T_yP_x and L_y modes obtained with the 10 mW incident beam are shown with red stars whereas those obtained at 20 mW (6400 W/cm^2) are displayed with red squares. As seen in Fig. 7.18, the normalized velocities of the T_yP_x and L_y modes show a larger decrease at a lower beam
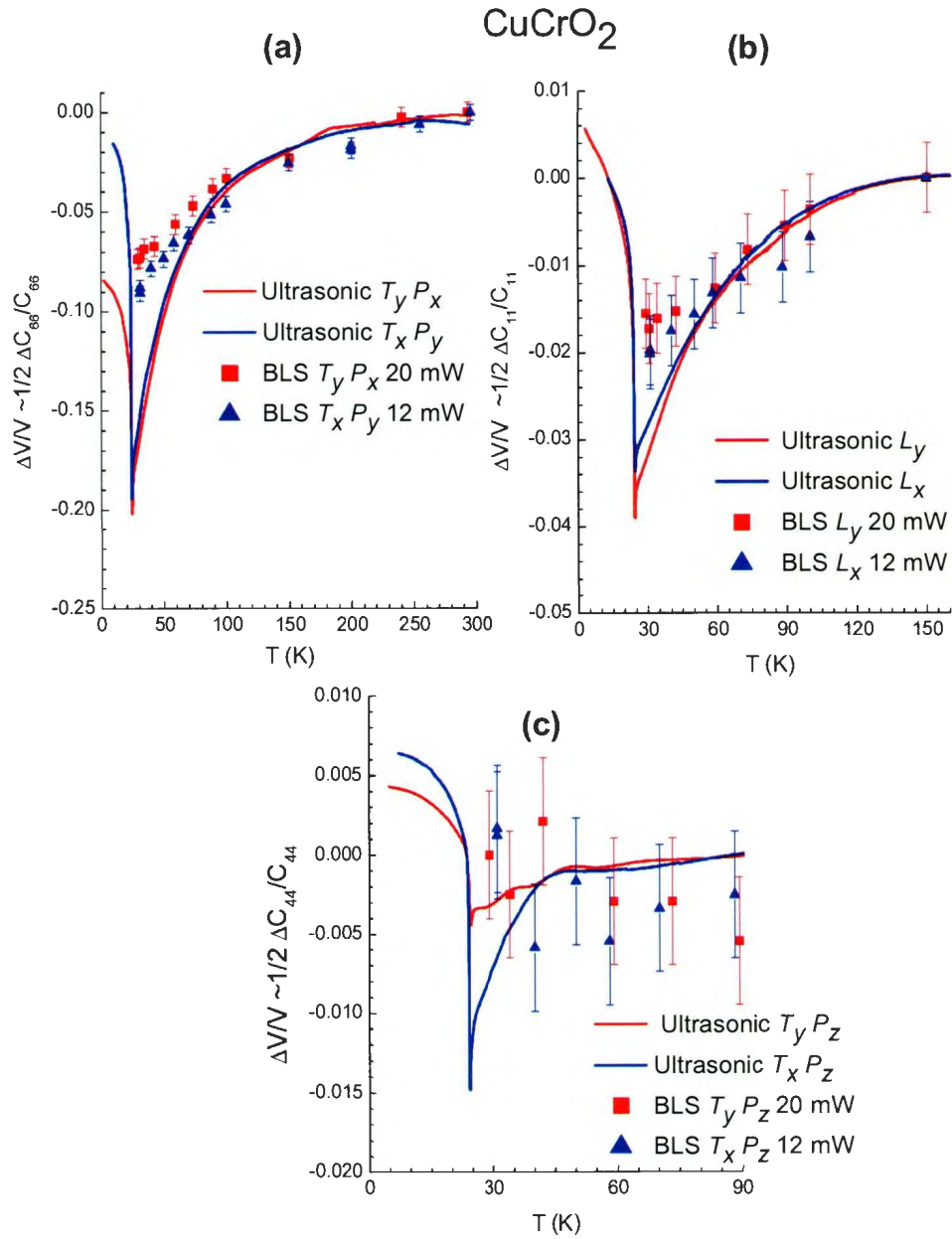
Figure 7.17: Relative velocity variations of bulk acoustic modes observed along the x axis and y axis obtained by Brillouin scattering (symbols) and the ultrasonic pulse-echo method (lines). **a)** $T_x P_y$ and $T_y P_x$ **b)** L_x and L_y **c)** $T_x P_z$ and $T_y P_z$.
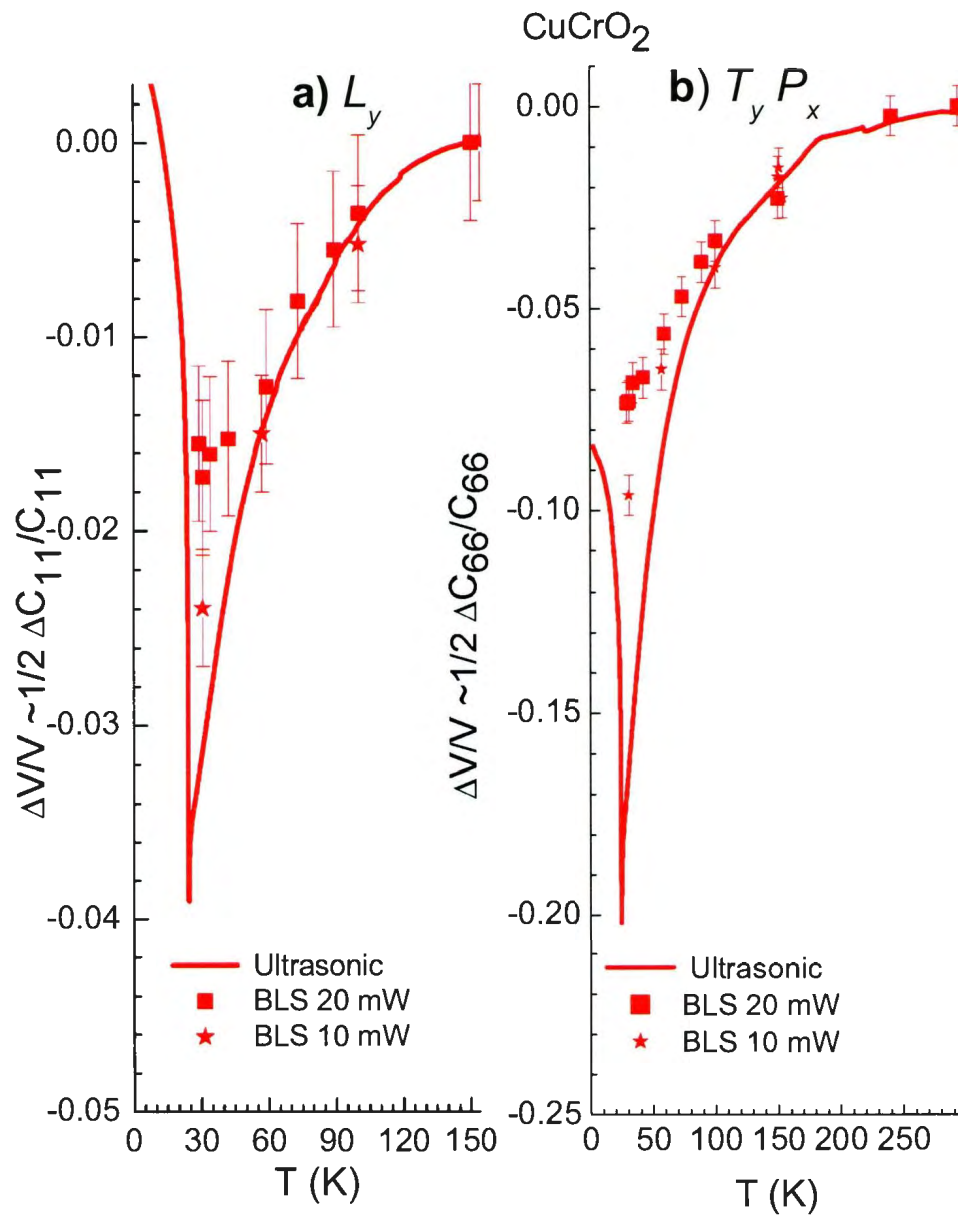
Figure 7.18: Relative frequency variations of the acoustic modes **a**) L_y and **b**) $T_y P_x$ observed with the ultrasonic pulse-echo method and Brillouin backscattering $(x(yu)x)$ using 10 mW and 20 mW incident beam powers.

power. This is particularly evident at 31 K. In the case of $T_y P_x$, the softening is 3% larger with 10 mW (3200 W/cm^2) relative to the result obtained with 20 mW. In the case of the L_y mode, the difference in the softening is about 1%.

In order to further illustrate the effect of local heating on the low temperature Brillouin scattering measurements, we performed a set of measurements at 31 K using different incident beam powers. These measurements were performed in both x and y directions and are shown in Figs. 7.19 and 7.20. With decreasing beam power, longer collection times were required to obtain an acceptable spectrum and measurements with less than 6 mW were not successful. In Fig 7.21, we show the frequency shifts of acoustic modes $T_y P_x$, $T_x P_y$, L_y, and L_x against the beam power density. As seen in Fig. 7.21, the frequencies of both modes increase as the power density increases (Fig. 7.21). For example, the softening observed in the longitudinal modes (Fig. 7.21a) is 2.7% at 1900 W/cm^2, whereas with 11800 W/cm^2 the softening is only 0.7%. The transverse modes, which soften by 20% relative to room temperature (Fig. 7.18), show considerable changes when the power density is increased from 1900 W/cm^2 to 11800 W/cm^2. The respective variations are $\sim$ 5.5% and $\sim$ 11%, corresponding to an increase of almost 60 K in the sample temperature when 11800 W/cm^2 incident beam power is used. Thus, we must conclude that, even at 1900 W/cm^2 local heating in our Brillouin scattering measurements are still significant, which explains why the temperature dependences of the acoustic mode velocities obtained by Brillouin scattering do not agree with those obtained with the ultrasonic pulse echo method.
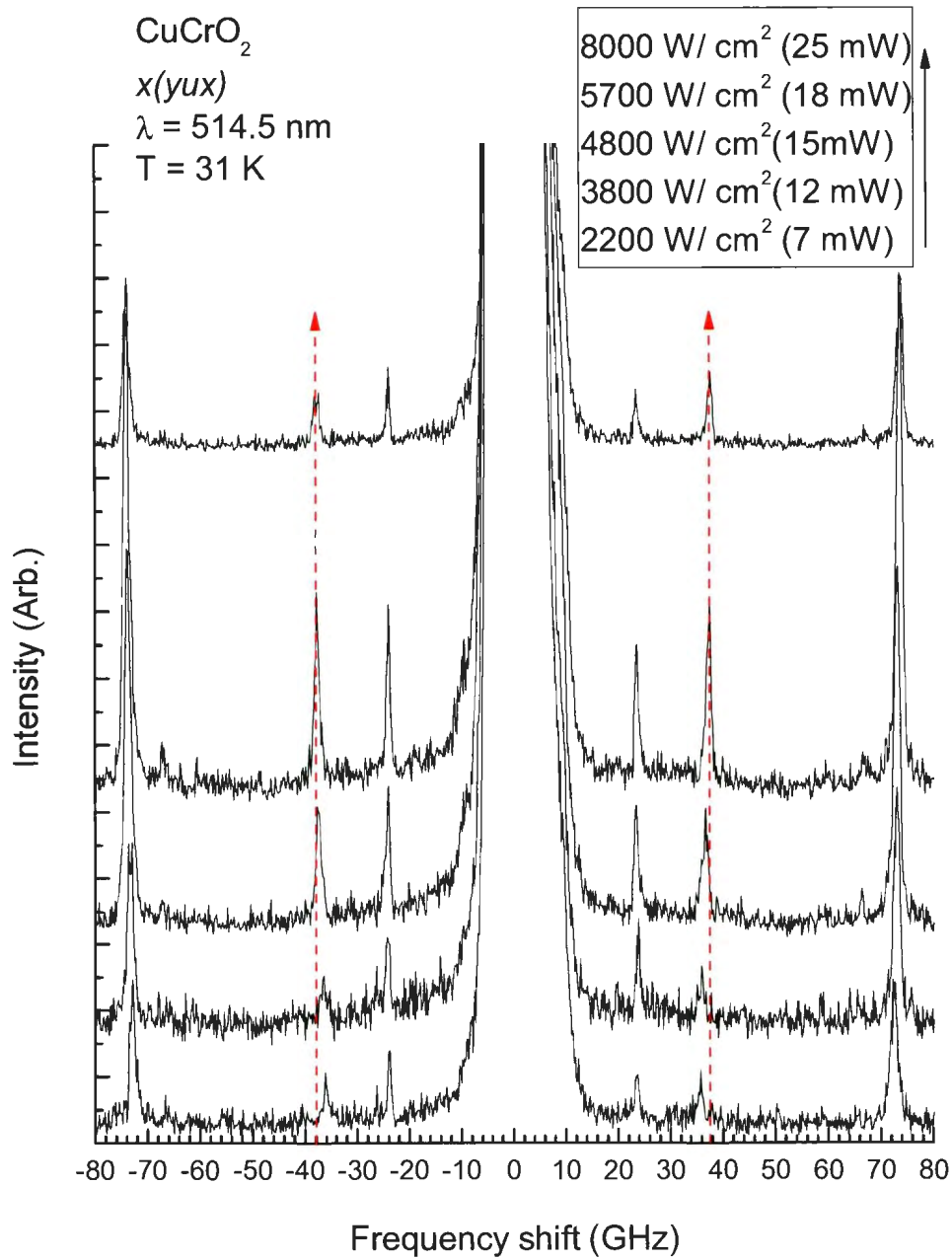
Figure 7.19: Brillouin spectra of CuCrO$_2$ obtained along the x axis at 31 K using different incident beam powers.
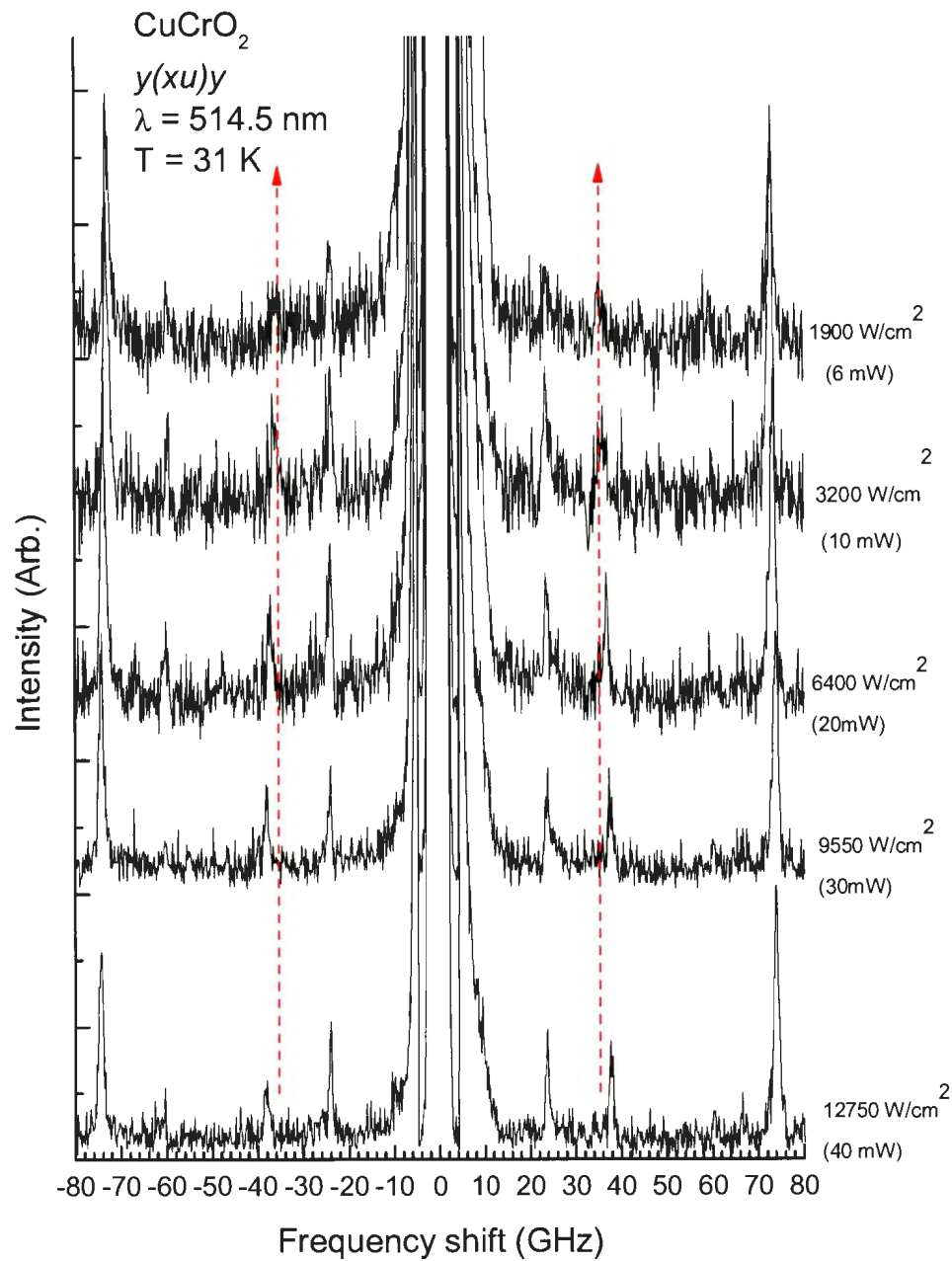
Figure 7.20: Brillouin spectra of CuCrO$_2$ obtained along the y axis at 31 K using different incident beam powers.
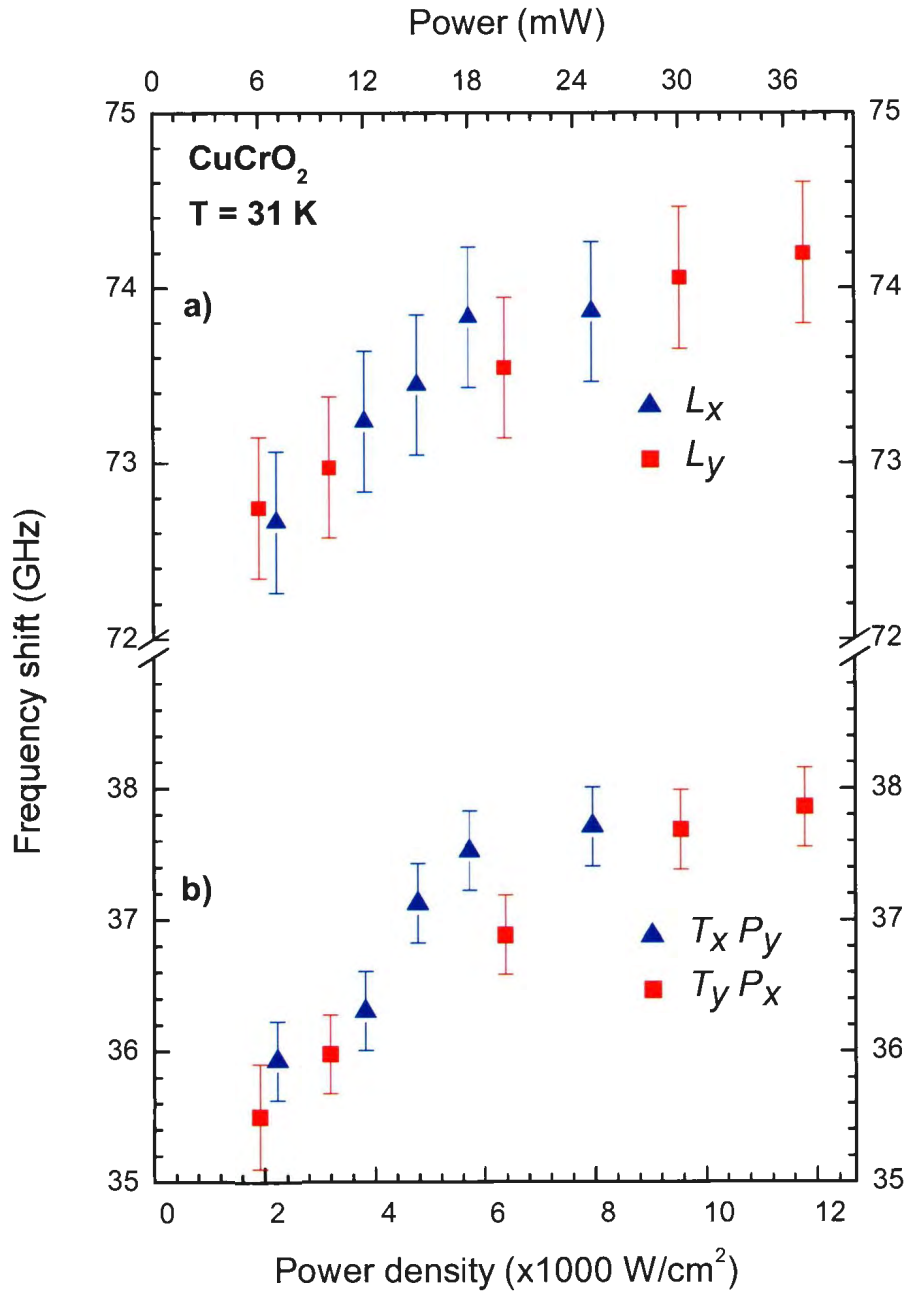
Figure 7.21: The frequency shifts of **a)** the longitudinal modes L_x and L_y and **b)** transverse modes $T_x Py$ and $T_y P_x$ against the incident beam power and density at $T = 31$ K.

Chapter 8

Landau model

As seen in Chapter 7, acoustic modes propagating along the x and y axes in $CuCrO_2$ show softening at T_{N1}. Particularly large softening observed on the $T_y P_x$ and $T_x P_y$ modes, corresponding to a 35% reduction on C_{66}, indicates that the transition at T_{N1} is ferroelastic as observed in $CuFeO_2$ [1] and NaN_3 [105]. However, the fact that the softening is incomplete and a rapid increase in the velocity below T_{N1} (see Fig. 7.1) suggest that the ferroelastic transition is first order as also observed in NaN_3 [105]. Therefore, in order to confirm the nature of the transition observed in $CuCrO_2$, the sound velocity measurements are analyzed using a Landau model based on symmetry arguments. First, we give an introduction to Landau theory and discuss a few Landau potentials that account for first and second order phase transitions.

8.1   Introduction to Landau Theory

Landau theory is a macroscopic thermodynamic model which describes phase transitions without giving any information about the microscopic causes of a phase transition [108]. Here, the discussion will be limited to phase transitions where the symmetry of the low

symmetry phase is a subgroup of the high symmetry space group. A more general description of phase transitions can be found in Ref. [109]. In the context of Landau theory, two new concepts need to be introduced: the order parameter and the excess Gibbs free energy.

The order parameter is a variable that reflects the loss of some symmetry elements below a critical temperature T_c. While its value is zero in the high symmetry phase, it is nonzero in the low symmetry phase. The temperature dependence of the order parameter can reveal the order of a phase transition. For a second order transition, the order parameter changes continuously at T_c while it changes discontinuously for a first order phase transition.

The excess Gibbs free energy simply represents the difference between the Gibbs free energy of the high symmetry phase and that of the low symmetry phase [109]. This energy difference G is then expressed as a Taylor series expansion of the order parameter Q such that

$$G = A_1 Q + \frac{1}{2}AQ^2 + \frac{1}{3}DQ^3 + \frac{1}{4}BQ^4 + \frac{1}{5}cQ^5 + \frac{1}{6}CQ^6 + ... \tag{8.1}$$

Terms with a power larger than 6 are normally ignored since the value of Q is infinitesimal at temperatures close to T_c. In addition, a stable state is associated with the minimum of G which requires that

$$\frac{dG}{dQ} = A_1 + AQ + DQ^2 + BQ^3 + cQ^4 + CQ^5 = 0. \tag{8.2}$$

Given that $Q = 0$ in the high symmetry phase, Eq. 8.2 is only satisfied if $A_1 = 0$. One of the most important characteristics of Landau theory is that the Gibbs free energy has to be invariant under the symmetry operations of the high symmetry phase. For example, assuming that the high temperature phase has a symmetry operation that imposes $Q \rightarrow -Q$, then only even power terms are allowed,

$$G = \frac{1}{2}AQ^2 + \frac{1}{4}BQ^4 + \frac{1}{6}CQ^6. \tag{8.3}$$

In his original theory for second order phase transitions [110], Landau assumed that A is the only temperature dependent coefficient in the expansion such that $A = a(T - T_0)$, where T_0

151

is a transition temperature. Thus, A changes sign at T_0. The coefficient C is always positive for a stable state. Depending on the sign of the coefficient B, Eq. 8.3 can describe second or first order phase transitions as described below.

8.1.1 Second order phase transitions

Whenever $B > 0$, second order transitions can be successfully described considering only the first two terms, hence

$$G = \frac{1}{2}AQ^2 + \frac{1}{4}BQ^4, \tag{8.4}$$

where $A = a(T - T_0)$. The equations that minimize the Gibbs free energy G are

$$\frac{\partial G}{\partial Q} = AQ + BQ^3 = 0, \tag{8.5}$$

and

$$\frac{\partial^2 G}{\partial Q^2} = A + 3BQ^2 \geq 0. \tag{8.6}$$

Here, the first equation means that the free energy corresponds to an extremum, while the second equation ensures that the free energy corresponds to a minimum. Solutions of Eq. 8.5 are given as

$$Q = 0, \quad T > T_0, \tag{8.7}$$

$$Q = \sqrt{\frac{a}{B}(T_0 - T)}, \quad T < T_0, \tag{8.8}$$

corresponding to the order parameter of the high symmetry phase and that of the low symmetry phase, respectively. The variation of G as a function of Q at different temperatures is illustrated in Fig. 8.1. When $T > T_c$, where $T_c = T_0$ is the critical temperature, the equilibrium point is specified by $Q = 0$. Below T_c, the free energy minimum shifts to Q_o. Fig. 8.2 shows the temperature dependence of the order parameter as predicted by Eq. 8.8 with a continuous variation at T_c. Below T_c, the order parameter changes as $(T_c - T)^{1/2}$, where $\beta = 1/2$ is the typical mean field critical exponent for the order parameter.

152
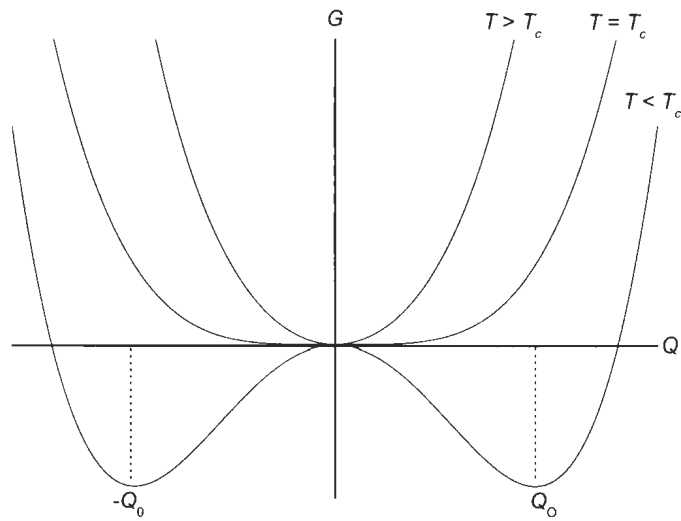
Figure 8.1: Gibbs free energy as a function of Q at various temperatures for a second order phase transition.
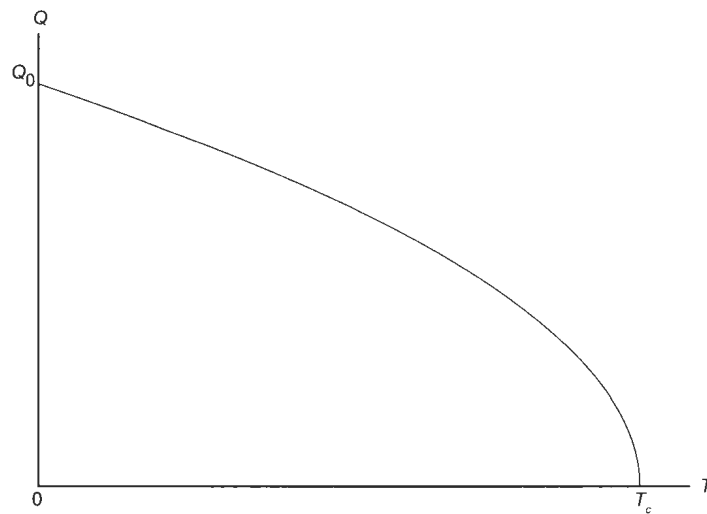
Figure 8.2: Order parameter Q as a function of temperature for a second order phase transition.

8.1.2 First order phase transitions

In this section, we present two Landau potentials that describe first order phase transitions.

2-4-6 potential

The excess Gibbs free energy G in Eq. 8.3 describes a first order phase transition if $B < 0$. Here, we keep the sixth power term so that the free energy has a stable minimum. A stable minimum in G requires that

$$\frac{\partial G}{\partial Q} = AQ + BQ^3 + CQ^5 = 0, \tag{8.9}$$

$$\frac{\partial^2 G}{\partial Q^2} = A + 3BQ^2 + 5CQ^4 > 0. \tag{8.10}$$

Therefore,

$$Q = 0, \quad T > T_0, \tag{8.11}$$

$$Q = \sqrt{\frac{-B \pm \sqrt{B^2 - 4AC}}{2C}}, \quad T < T_0, \tag{8.12}$$

where Eq. 8.12 corresponds to the solution in the low symmetry phase. An important characteristic associated with first order phase transitions is thermal hysteresis. This can be best illustrated by a plot of G as a function of the order parameter Q as shown in Fig. 8.3. When $T \geq T_1$, G is stable at $Q = 0$ (high symmetry phase). At $T = T_1$, a saddle point appears. At T_c, which is called the thermodynamic critical temperature, high symmetry and low symmetry phases become equally stable. However, as a transition to the low symmetry phase would cost energy due to the energy barrier, the transition only occurs at $T = T_0$, when the potential barrier completely disappears. If the temperature is increased, no transition occurs to the high symmetry phase until the temperature reaches T_1. Therefore, as illustrated in Fig. 8.4, the value of Q changes discontinuously at the phase boundaries, which is a characteristic of first order transitions along with thermal hysteresis.
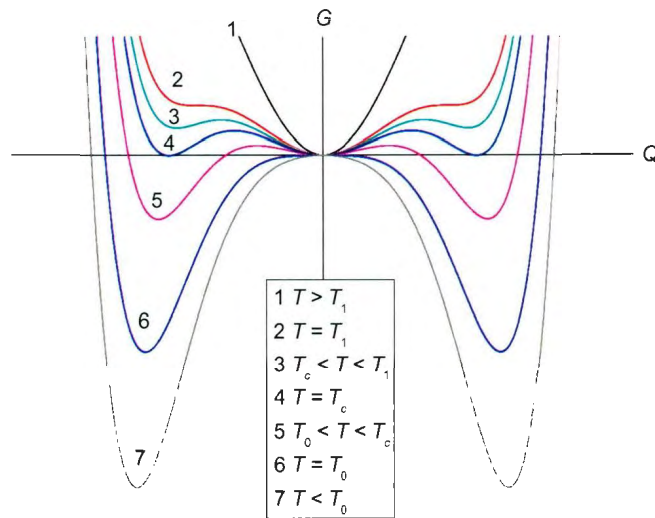
Figure 8.3: Gibbs Free energy as a function of Q at various temperatures for a first order transition.
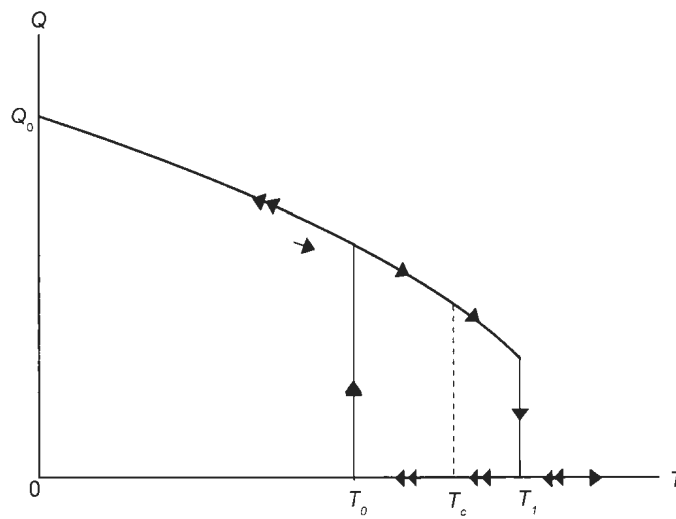
Figure 8.4: Order parameter Q as a function of temperature for a first order phase transition.

155

Given that A is a temperature dependent term in Eq. 8.12, we can determine the characteristic temperatures T_c and T_1 using Eq. 8.12.

Case 1: $B^2 - 4AC < 0$

In this case, substituting $A = a(T - T_0)$ in the inequality, the temperature can be obtained as

$$T > \frac{B^2}{4aC} + T_0 = T_1 \tag{8.13}$$

When Eq. 8.13 is satisfied, Eq. 8.12 describes a stable state with $Q = 0$, which corresponds to the high symmetry phase.

Case 2: $B^2 - 4AC = 0$

Substituting $A = a(T - T_0)$ in the equality, we obtain

$$T = \frac{B^2}{4aC} + T_0 = T_1, \tag{8.14}$$

and

$$Q(T_1) = \sqrt{\frac{-B}{2C}}, \tag{8.15}$$

which describe curve 2 with the appearance of an inflection point (Fig. 8.3).

Case 3: $T = T_c$

At $T = T_c$, both phases are equally stable (curve 4 in Fig. 8.3), requiring that

$$G(Q) = \frac{1}{2}AQ^2 + \frac{1}{4}BQ^4 + \frac{1}{6}CQ^6 = 0. \tag{8.16}$$

Using Eq. 8.16 and 8.12, T_c can be obtained as

$$T_c = \frac{3B^2}{16aC} + T_0. \tag{8.17}$$

2-3-4 potential

If the symmetry of the high symmetry phase allows a third order contribution in G, a 2-3-4 potential such as

$$G = \frac{1}{2}AQ^2 + \frac{1}{3}DQ^3 + \frac{1}{4}BQ^4, \tag{8.18}$$

where $D \neq 0$ and $B > 0$, can account for first order phase transitions. The equations that minimize the free energy G are

$$\frac{\partial G}{\partial Q} = AQ + DQ^2 + BQ^3 = 0 \tag{8.19}$$

$$\frac{\partial^2 G}{\partial Q^2} = A + 2DQ + 3BQ^2 \geq 0. \tag{8.20}$$

Hence, T_1 and T_c correspond to

$$T_1 = T_0 + \frac{D^2}{4AB}, \tag{8.21}$$

and

$$T_c = T_0 + \frac{2D^2}{9aB}. \tag{8.22}$$

8.2 Landau model for an $R\bar{3}m \rightharpoonup C2/m$ ferroelastic transition

In this section, we present a Landau model for an $R\bar{3}m \rightharpoonup C2/m$ ferroelastic transition to analyze the elastic properties of $CuCrO_2$ (see Chapter 7). One would naturally assume that the order parameter of a ferroelastic transition is strains. In that case a linear temperature dependence is expected for the temperature dependence of the elastic constants [35, 36, 37, 105]. Considering that the observed temperature dependence for the acoustic modes in $CuCrO_2$ corresponds to a nonlinear temperature dependence of the elastic constants, we assume that the transition at T_{N1} is pseudoproper ferroelastic, for which the order parameter is associated with another physical quantity that has the same symmetry as the spontaneous strains [1].

The total free energy $G(Q_i, e_j)$, which is a function of the order parameters Q_i and strain components e_j, consists of three distinct contributions

$$G(Q_i, e_j) = G_L(Q_i) + G_e(e_j) + G_c(Q_i, e_j) \tag{8.23}$$

where $G_L(Q_i)$ is the Landau expansion in terms of the order parameters Q_i, $G_e(e_j)$ is the elastic energy associated with the trigonal $\bar{3}m$ point group, and $G_c(Q_i, e_j)$ is the energy due to the coupling between the order parameters and the strains. According to Tol'edano et al. [35], the Landau free energy for an $R\bar{3}m \rightharpoonup C2/m$ ferroelastic transition can be expressed as a function of a two component order parameter (Q_1, Q_2)

$$G_L(Q_1, Q_2) = \frac{1}{2}A(Q_1^2 + Q_2^2) + \frac{1}{3}D(Q_1^3 - 3Q_1Q_2^2) + \frac{1}{4}B(Q_1^2 + Q_2^2)^2. \qquad (8.24)$$

where A is given by $A = \frac{1}{2}a(T - T_0)$ and B and D are constants. Here, T_0 defines the transition temperature in the absence of elastic coupling. For an $R\bar{3}m \rightharpoonup C2/m$ ferroelastic transition, the order parameter belongs to the two dimensional irreducible representation E_g [34], which is represented by

$$(Q_1, Q_2) = \left\{ (x^2 - y^2, xy), (yz, xz) \right\}. \qquad (8.25)$$

The terms allowed in the model have to be compatible with the symmetry properties of the

Table 8.1: Transformation of the order parameter components under the generators of the $\bar{3}m$ point group

	C_{2x}	C_{3z}	$\bar{I}$
Q_1	Q_1	$-\frac{1}{2}Q_1 - \sqrt{3}Q_1$	Q_1
Q_2	$-Q_2$	$\frac{\sqrt{3}}{4}Q_1 - \frac{1}{2}Q_1$	Q_2

high symmetry point group, that is, they have to be invariant under the generators of the $\bar{3}m$ point group, which are a threefold rotation around the z axis C_{3z} (Eq. 4.16), a twofold rotation around the x axis C_{2x} (Eq. 4.17) and a spatial inversion $\bar{I}$ (Eq. 4.18). In Table 8.1, we present how the order parameter components transform under the generators of the $\bar{3}m$ point group (Eqs. 4.16-4.18). Applying the transformation rules given in Table 8.1, it is easy to show that the Landau Free energy $G_L(Q_i)$ is invariant under the $\bar{3}m$ symmetry operations.

In order to calculate the temperature dependence of acoustic modes associated with an $R\bar{3}m \rightharpoonup C2/m$ ferroelastic transition, we have to include the elastic energy of the $\bar{3}m$ point group. The elastic energy $G_e(e_j)$, derived in Chapter 4, is given by

$$G_e(e_j) = \frac{1}{2}C_p(e_1 + e_2)^2 + \frac{1}{2}C_{33}e_3^2 + \frac{1}{2}C_{44}(e_4^2 + e_5^2)$$
$$+ \frac{1}{2}C_{66}e_6^2 + C_{66}(e_1 - e_2)^2 + C_{13}(e_1 + e_2)e_3 + C_{14}(e_1e_4 - e_2e_4 + e_5e_6), \qquad (8.26)$$

where $C_p = \frac{C_{11}+C_{12}}{2}$.

Finally, we include the energy G_c which is due to the coupling between the order parameters and the strains. Here, we only consider the bilinear $(Q_i e_j)$ and linear-quadratic $(Q_i^2 e_j)$ coupling terms. In order to determine the allowed terms, one needs to take into account the transformation of the order parameter components (Table 8.1) and the strains. In Table 8.2, the functional representations of the strains are given in parenthesis in the first column whereas their transformations under the generators C_{2x}, C_{3z}, and $\bar{I}$ are shown in the second, third, and fourth columns, respectively. According to Tables 8.1 and 8.2, we see that the

Table 8.2: Transformation of strains under the generators of the $\bar{3}m$ point group

Strains	C_{2x}	C_{3z}	$\bar{I}$
$e_1(x^2)$	e_1	$\frac{e_1}{4} + \frac{3e_2}{4} - \frac{\sqrt{3}e_6}{4}$	e_1
$e_2(y^2)$	e_2	$\frac{3e_1}{4} + \frac{e_2}{4} + \frac{\sqrt{3}e_6}{4}$	e_2
$e_3(z^2)$	e_3	e_3	e_3
$e_4(yz)$	e_4	$-\frac{e_4}{2} - \frac{\sqrt{3}e_5}{2}$	e_4
$e_5(xz)$	$-e_5$	$\frac{\sqrt{3}e_4}{2} - \frac{e_5}{2}$	e_5
$e_6(xy)$	$-e_6$	$\frac{\sqrt{3}e_1}{2} - \frac{\sqrt{3}e_2}{2} - \frac{e_6}{2}$	e_6

order parameter components (Q_1, Q_2) transform as the strain combinations $\delta_1(e_1 - e_2, e_6) + \delta_2(e_4, e_5)$. Therefore, bilinear coupling terms $\delta_1((e_1 - e_2)Q_1 + e_6Q_2) + \delta_2(e_4Q_1 + e_5Q_2)$, with

δ_1 and δ_2 being coupling coefficients, are allowed in the model. The linear-quadratic terms are $\beta_1(e_1 + e_2)(Q_1^2 + Q_2^2)$ and $\beta_3 e_3(Q_1^2 + Q_2^2)$, giving the coupling energy as

$$G_c(Q_i, e_j) = \delta_1(e_1 - e_2)Q_1 + e_6 Q_2) + \delta_2(e_4 Q_1 + e_5 Q_2) + \beta_1(e_1 + e_2)(Q_1^2 + Q_2^2) + \beta_3 e_3(Q_1^2 + Q_2^2),$$

$$(8.27)$$

where β_1 and β_3 are also coupling coefficients.

The expressions for the strains, in terms of the order parameter components, can be found by minimizing the free energy as

$$\frac{\partial G}{\partial e_j} = 0 \text{ for } j = 1 - 6, \qquad (8.28)$$

which give

$$e_m = \frac{2(\delta_2 C_{14} - \delta_1 C_{44})}{C_a} Q_1,$$

$$e_p = \frac{2(\beta_3 C_{13} - \beta_1 C_{33})}{C_b}(Q_1^2 + Q_2^2),$$

$$e_3 = \frac{2\beta_1 C_{13} - \beta_3(C_{11} + C_{12})}{C_b}(Q_1^2 + Q_2^2),$$

$$e_4 = \frac{-\delta_2(C_{11} - C_{12}) + 2\delta_1 C_{14}}{C_a} Q_1,$$

$$e_5 = \frac{-\delta_1 C_{14} + \delta_2 C_{66}}{C_c} Q_2,$$

$$e_6 = \frac{-\delta_2 C_{14} + \delta_1 C_{44}}{C_c} Q_2, \qquad (8.29)$$

where $e_m = e_1 - e_2$, $e_p = e_1 + e_2$, and

$$C_a = (C_{11} - C_{12})C_{44} - 2C_{14}^2,$$

$$C_b = (C_{11} + C_{12})C_{33} - 2C_{13}^2,$$

$$C_c = C_{14}^2 - C_{44}C_{66}. \qquad (8.30)$$

As illustrated in Fig. 8.4, the order parameters are nonzero below the transition temperature. In order to find the solutions for the order parameters, we minimize the free energy

with the respect to the order parameter components such that

$$\frac{\partial G}{Q_1} = 0, \tag{8.31}$$

$$\frac{\partial G}{Q_2} = 0, \tag{8.32}$$

A simultaneous solution of Eqs. 8.31 and 8.32 leads to three solutions

$$(\mathbf{i})\ Q_1 = Q_2 = 0,$$

$$(\mathbf{ii})\ Q_1 \neq 0 \text{ and } Q_2 = 0,$$

$$(\mathbf{iii})\ Q_1 \neq 0 \text{ and } Q_2 \neq 0. \tag{8.33}$$

Case (**i**) corresponds to the high temperature $R\bar{3}m$ phase. Case (**ii**) corresponds to a structural transition to the monoclinic $C2/m$ phase [111]. According to Eq. 8.29, for $Q_1 = 0$ and $Q_2 \neq 0$, e_1, e_2, e_3, e_5, and e_6 are non-zero, causing deformations along the x, y, z axes and shear deformations in the xz and xy planes, respectively. Case (**iii**) corresponds to a structural transition from the trigonal $R\bar{3}m$ phase to a low temperature triclinic $\bar{1}$ phase.

Therefore, we construct our model for CuCrO$_2$ according to case (**ii**) and consider the scenario in which $Q_1 \neq 0$ and $Q_2 = 0$ (Eq. 8.33). Referring to Fig. 8.4, the transition temperature T_{N1} can be defined as $T_{N1} = T_c$. In order to find the expressions for $Q_1(T_{N1})$ and T_{N1}, we use Eq. 8.31 and the fact that the free energy is zero at $T = T_{N1}$ as illustrated in Fig. 8.3. We obtain

$$Q_1(T_{N1}) = -\frac{2D}{3B},$$
$$T_{N1} = T_0 + \frac{2D^2}{9aB} + \frac{C_f}{aC_a}, \tag{8.34}$$

where

$$C_f = \delta_2^2(C_{11} - C_{12}) - 4\delta_1\delta_2 C_{14} + 2\delta_1^2 C_{44}. \tag{8.35}$$

Here, we set β_1 and β_3 to zero since they do not significantly change T_{N1} and the order parameter Q_1. Even though the temperature dependence of acoustic modes in CuCrO$_2$

suggests a first order transition at T_{N1}, we observe no thermal hysteresis (Fig. 7.1). Therefore, we do not determine the characteristic temperatures T_o and T_1 (see Fig. 8.4). In order to find an expression for the order parameter Q_1 below T_{N1}, we use Eq. 8.31, which gives

$$Q_1(T) = -\frac{D}{2B} - \frac{\sqrt{D^2 + 36aB(T_{N1} - T)}}{36B^2}. \tag{8.36}$$

Next, we derive the temperature dependence of the elastic constants C_{mn} using [112]

$$C_{mn} = \frac{\partial^2 G}{\partial e_m \partial e_n} - \sum_i \frac{\partial^2 G}{\partial Q_i \partial e_m} \left(\frac{\partial^2 G}{\partial Q_i^2}\right)^{-1} \frac{\partial^2 G}{\partial e_n \partial Q_i} \tag{8.37}$$

where $m, n = 1, ...6$ and $i = 1, 2$. Results, as a function of the order parameter $Q_1(T)$, are tabulated in Table 8.3. According to this model, five of the six independent elastic constants show softening due to bilinear coupling between the strains and order parameters. For $T < T_{N1}$, 13 independent elastic constants, compatible with the monoclinic $C2/m$ phase, are obtained (Table 8.3). For these calculations, the elastic energy (Eq. 8.26) is defined relative to the trigonal $R\bar{3}m$ phase using the conventional coordinate system in which the threefold axis is along the z axis with the twofold axis along the x axis [94]. Since an $R\bar{3}m \rightarrow C2/m$ structural transition must preserve the twofold symmetry, the calculated elastic tensor for the monoclinic $C2/m$ phase conserves the twofold symmetry along the x axis as also stated in Ref. [1].

8.2.1   Numerical calculations

In order to estimate some of the model parameters, we use the temperature dependence of the L_x, $T_y P_x$, $T_y P_z$, and $T_x P_y$ modes (Fig. 7.1). In Table 8.5, we show the effective elastic constants of the acoustic modes in the trigonal $R\bar{3}m$ and monoclinic $C2/m$ phases. In Table 8.4, we compare the elastic constants of $CuCrO_2$ obtained using Brillouin scattering (Section 6.2.1) to the numerical values used to get better agreement below T_{N1}. At the most, these values differ from the experimental values by a factor of 2 in the case of C_{66}. Using the

162

Table 8.3: Temperature dependence of elastic constants for an $R\bar{3}m \rightharpoonup C2/m$ ferroelastic transition.

	Trigonal $R\bar{3}m$	Monoclinic $C2/m$
C_{11}	$C_{11}^\circ - \frac{\delta_1^2}{A(T)}$	$C_{11}^\circ - \frac{(\delta_1+2\beta_1 Q_1)^2}{Q_1(D+2BQ_1)+\frac{C_f}{C_a}}$
C_{22}	$C_{11}^\circ - \frac{\delta_1^2}{A(T)}$	$C_{11}^\circ - \frac{(\delta_1-2\beta_1 Q_1)^2}{Q_1(D+2BQ_1)+\frac{C_f}{C_a}}$
C_{33}	C_{33}°	$C_{33}^\circ - \frac{4Q_1^2\beta_3^2}{Q_1(D+2BQ_1)+\frac{C_f}{C_a}}$
C_{44}	$C_{44}^\circ - \frac{\delta_2^2}{A(T)}$	$C_{44}^\circ - \frac{\delta_2^2}{Q_1(D+2BQ_1)+\frac{C_f}{C_a}}$
C_{55}	$C_{44}^\circ - \frac{\delta_2^2}{A(T)}$	$C_{44}^\circ - \frac{\delta_2^2}{\frac{C_f}{C_a}-3DQ_1}$
C_{66}	$C_{66}^\circ - \frac{\delta_1^2}{A(T)}$	$C_{66}^\circ - \frac{\delta_2^2}{\frac{C_f}{C_a}-3DQ_1}4$
C_{12}	$C_{12}^\circ - \frac{\delta_1^2}{A(T)}$	$C_{12}^\circ + \frac{\delta_1^2-4\beta_1^2 Q_1^2}{Q_1(D+2BQ_1)+\frac{C_f}{C_a}}$
C_{13}	C_{13}°	$C_{13}^\circ - \frac{2Q1\beta_3(2Q_1\beta_1+\delta_1)}{Q_1(D+2BQ_1)+\frac{C_f}{C_a}}$
C_{14}	$C_{14}^\circ - \frac{\delta_1\delta_2}{A(T)}$	$C_{14}^\circ - \frac{(\delta_1+2\beta_1 Q_1)\delta_2}{Q_1(D+2BQ_1)+\frac{C_f}{C_a}}$
C_{23}	C_{13}°	$C_{13}^\circ - \frac{2Q_1\beta_3(2Q_1\beta_1-\delta_1)}{Q_1(D+2BQ_1)+\frac{C_f}{C_a}}$
C_{24}	$-C_{14}^\circ + \frac{\delta_1\delta_2}{A(T)}$	$-C_{14}^\circ + \frac{(\delta_1-2\beta_1 Q_1)\delta_2}{Q_1(D+2BQ_1)+\frac{C_f}{C_a}}$
C_{34}	0	$C_{34}^\circ - \frac{2Q_1\beta_3\delta_2}{Q_1(D+2BQ_1)+\frac{C_f}{C_a}}$
C_{56}	$C_{14}^\circ - \frac{\delta_1\delta_2}{A(T)}$	$C_{14}^\circ - \frac{\delta_1\delta_2}{\frac{C_f}{C_a}-3DQ_1}$

Table 8.4: Experimental values of the bare elastic constants in $CuCrO_2$ at room temperature and their comparison with the values used in the model.

Bare values	C_{11}	C_{12}	C_{13}	C_{14}	C_{33}	C_{44}	C_{66}
Experimental (x 10^{10} N/m^2)	24.2	8	-	< 1.4	47	2.35	8.2
Model (x10^{10} N/m^2)	24.2	15	25	-2.3	47	3.5	4.6

Table 8.5: Expressions of ρV^2 for trigonal $R\bar{3}m$ and monoclinic $C2/m$ phases.

Direction	Mode	$R\bar{3}m$ phase	$C2/m$ phase
[100]	L_x	C_{11}	C_{11}
	$T_x P_y$	$\frac{1}{2}(C_{44} + C_{66} - \sqrt{(C_{44} - C_{66})^2 + 4C_{14}^2})$	$\frac{1}{2}(C_{55} + C_{66} - \sqrt{(C_{55} - C_{66})^2 + 4C_{56}^2})$
	$T_x P_z$	$\frac{1}{2}(C_{44} + C_{66} + \sqrt{(C_{44} - C_{66})^2 + 4C_{14}^2})$	$\frac{1}{2}(C_{55} + C_{66} + \sqrt{(C_{55} - C_{66})^2 + 4C_{56}^2})$
[010]	L_y	$\frac{1}{2}(C_{11} + C_{44} + \sqrt{(C_{11} - C_{44})^2 + 4C_{14}^2})$	$\frac{1}{2}(C_{22} + C_{44} + \sqrt{(C_{22} - C_{44})^2 + 4C_{24}^2})$
	$T_y P_x$	C_{66}	C_{66}
	$T_y P_z$	$\frac{1}{2}(C_{11} + C_{44} - \sqrt{(C_{11} - C_{44})^2 + 4C_{14}^2})$	$\frac{1}{2}(C_{22} + C_{44} - \sqrt{(C_{22} - C_{44})^2 + 4C_{24}^2})$

elastic constants reported in Table 8.4, we estimate coupling coefficients using the reductions observed on the elastic constants

$$\frac{\Delta C_{11}(T_{N1})}{C_{11}} = -6.1\%$$
$$\frac{\Delta C_{66}(T_{N1})}{C_{66}} = -34.6\%$$
$$\frac{\Delta C_{44}(T_{N1})}{C_{44}} = -0.88\%,$$
$$\frac{\Delta C_{eff}(T_{N1})}{C_{eff}} = -32.6\%, \tag{8.38}$$

where C_{eff} corresponds to the effective elastic constant associated with the velocity of $T_x P_y$ given in Table 8.5. We also arbitrarily set $a = 1$ and adjust the value of T_0 in order to get a good agreement for the temperature dependence observed above T_{N1}.

The other coefficients are estimated using the values of strains e_1 and e_2

$$e_1(0\text{ K}) - e_2(0\text{ K}) = \frac{2(\delta_2 C_{14} - \delta_1 C_{44})}{C_a} Q_1(0\text{ K}),$$
$$= 5.13 \times 10^{-4} \tag{8.39}$$

$$e_1(0\text{ K}) + e_2(0\text{ K}) = \frac{2(\beta_3 C_{13} - \beta_1 C_{33})}{C_b} Q_1^2(0\text{ K}),$$
$$= -7.0 \times 10^{-6} \tag{8.40}$$

consistent with magnetostriction measurements [33]. Here, we set β_3 to zero since the elastic constants which determine the velocity of the acoustic modes propagating along the x and y axes do not depend on the linear-quadratic coupling term $\beta_3 e_3 (Q_1^2 + Q_2^2)$. The coefficients B and D are determined using the relations (Eqs. 8.34, 8.36).

$$T_{N1} = T_0 + \frac{2D^2}{9aB} + \frac{C_f}{aC_a},$$
$$Q_1(0\text{K}) = -\frac{D}{2B} + \frac{\sqrt{D^2 + 36aBT_{N1}}}{36B^2}. \tag{8.41}$$

All coefficients used in the model are reported in Table 8.6. Using these numerical values, we present in Fig. 8.5 the temperature dependence of the order parameter Q_1. As expected for a first order phase transition, the order parameter shows a discontinuity at the critical temperature T_{N1}. In Fig. 8.6, we present the temperature dependences of the strains, which also show a discontinuity at T_{N1}.

Table 8.6: Values of the coupling and other constants

a	T_0	B	D	δ_1	δ_2	β_1
1	-10	0.183	-3.80	7.97×10^5	-1.24×10^5	874
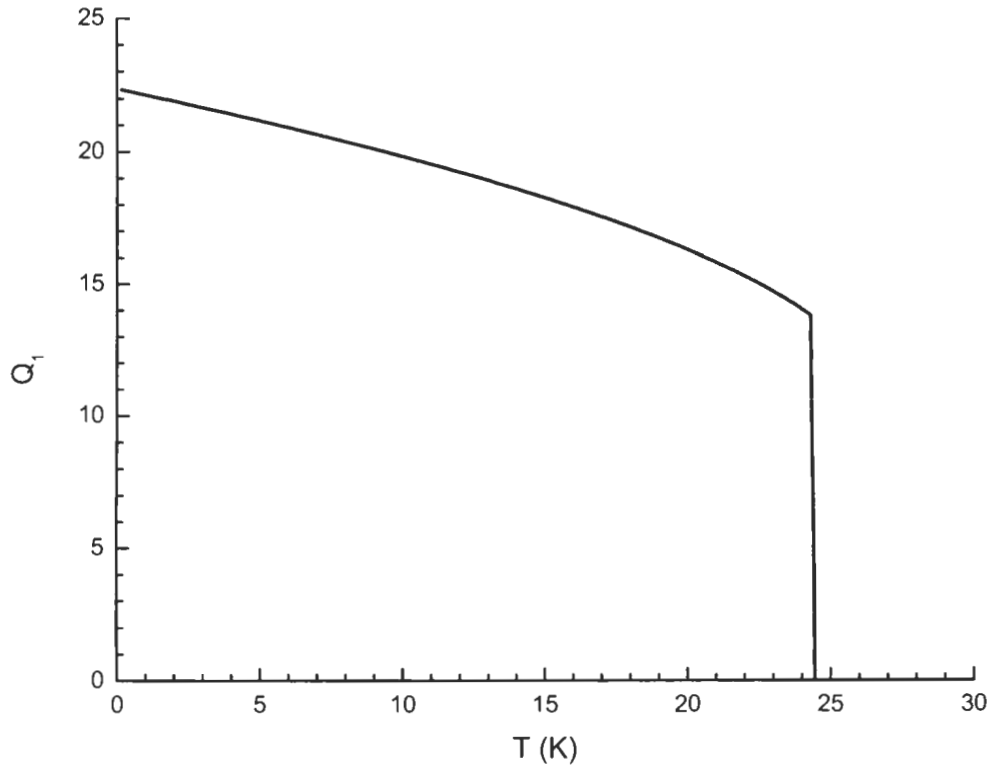
Figure 8.5: Temperature dependence of the the order parameter Q_1 (Eq. 8.36)
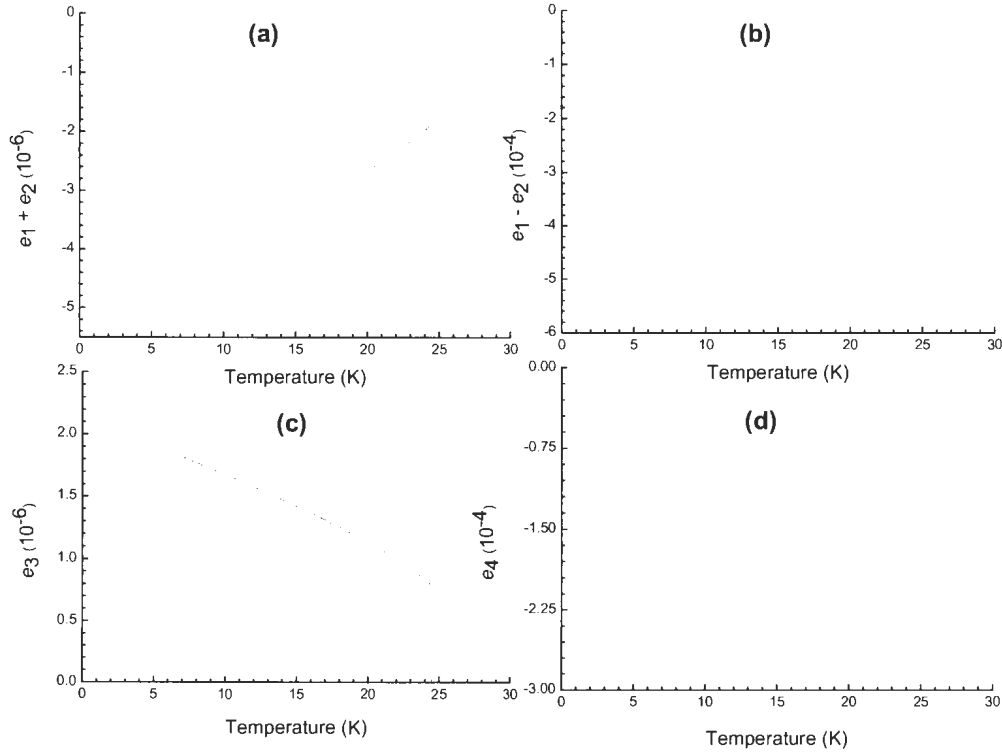
Figure 8.6: Temperature dependence of the strains (Eq. 8.29)

In Fig. 8.7, we compare the temperature dependence of the relative acoustic velocity variations and numerical predictions obtained for a continuous and a first order ferroelastic transition. For a second order phase transition, one can set $B = 0$ and obtain the temperature dependence of elastic constants as reported in Ref. [1]. The experimental data are represented by continuous lines, whereas the numerical predictions of a first and a second order Landau model are shown using dotted and dashed lines, respectively. For clarity all modes are plotted in separate graphs. In Fig. 8.7, a) and b) show the transverse $T_x P_y$ and $T_y P_x$, which mainly depend on C_{66}, whereas c) and d) show the longitudinal modes L_x and L_y, which depend on C_{11}. Finally, we present in e) and f) the transverse modes $T_y P_z$ and $T_x P_z$ the velocities of which are dominated by C_{44}.

Figure 8.7: Temperature dependence of the normalized acoustic mode velocities in $CuCrO_2$ and the predictions of the first and second order Landau models: **a)** $T_x P_y$ **b)** $T_y P_x$ **c)** L_x **d)** L_y **e)** $T_y P_z$ **f)** $T_x P_z$.

The predictions of the first order model (dotted lines in Fig. 8.7) are in good agreement with the data (continuous lines) above T_{N1} except for the transverse mode T_xP_z. However, a good qualitative agreement is still obtained for the model. In general, the softening observed on the modes presented in Fig. 8.7 is due to the bilinear coupling between the order parameter component and strains (Eq. 8.27). At T_{N1}, the steep increase observed in the acoustic mode velocities below T_{N1} is qualitatively reproduced for the modes T_xP_y, T_yP_x, T_xP_z, and L_y (see the inset of Fig. 8.7d). However, for other modes this behavior is not well captured. In order to reproduce this steep increase, higher order coupling terms might be necessary. In the inset of Fig. 8.7c, we notice a change of slope in the velocity of the longitudinal mode L_x just before T_{N1}. This behavior, which is accounted for by the model, is due to the linear-quadratic coupling $\beta_1(e_1 + e_2)(Q_1^2 + Q_2^2)$. The change of slope just above T_{N1} is also apparent in other modes, which cannot be reproduced with the model. Finally, below T_{N1}, the numerical predictions qualitatively capture the temperature dependence of all modes.

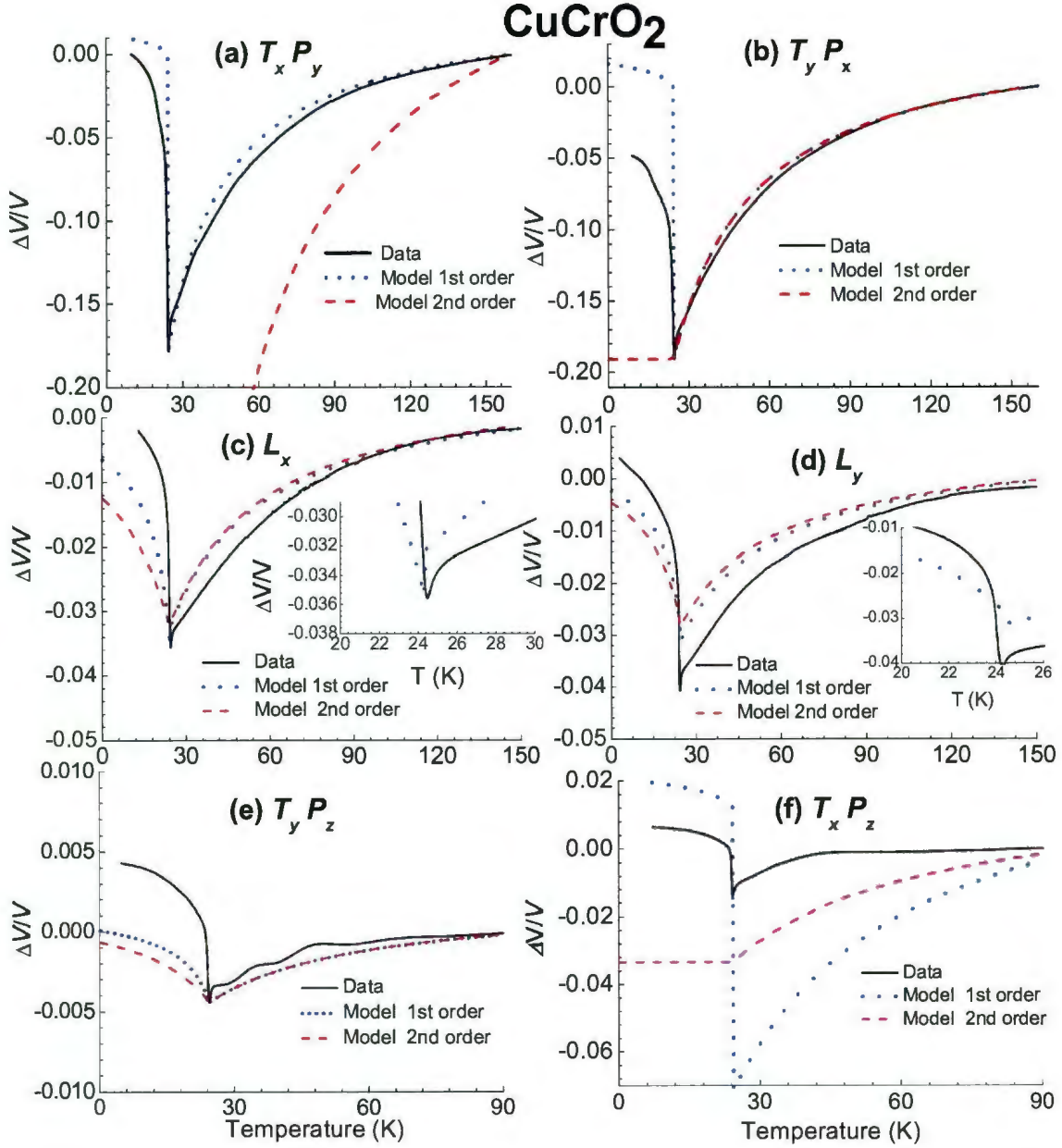The predictions of the second order model (dashed lines in Fig. 8.7) can account for the temperature dependence of some of the modes. However, there are noticeable differences. According to the second order model, the transverse mode T_xP_y should show complete softening at T_{N1}, which significantly deviates from our experimental observations. (continuous line in Fig. 8.7a). The other difference between the numerical predictions and data is that the model does not predict an abrupt increase at T_{N1} in any of the modes, as expected for a second order, or continuous phase transition (see Sec. 8.1). The model also fails to reproduce the temperature dependence of the transverse modes T_yP_x and T_xP_z below T_{N1}.

Considering that the first order model is more compatible with the data (Fig. 8.7), we conclude the transition at T_{N1} is a first order pseudoproper ferroelastic transition. In order to obtain more quantitative agreement between the model predictions and data, we may have to include higher order coupling terms. The fact that the transition is pseudoproper ferroelastic raises the question about the nature of the order parameter Q_1. According to

Ref. [27], the magnetic order between T_{N1} and T_{N2}, is collinear with the magnetic moments oriented along the z axis. In this case, a bilinear coupling term, which accounts for the softening observed on the acoustic modes (Fig. 8.7), is not allowed due to time reversal symmetry. Therefore, the microscopic mechanism that leads to the ferroelastic transition in $CuCrO_2$ still remains unresolved. A possible mechanism in $CuCrO_2$ is investigated in the next chapter.

Chapter 9

Raman Measurements on $CuFeO_2$, $CuCrO_2$, and $CuCrS_2$

This chapter presents the Raman measurements on $CuFeO_2$ and $CuCrO_2$. As mentioned before, sound velocity measurements on $CuFeO_2$ [1, 31] show that the magnetic transition at $T_{N1} = 14$ K is induced by an $R\bar{3}m \rightharpoonup C2/m$ structural transition. According to the Landau analysis [1], the structural transition at $T_{N1} = 14$ K is identified as pseudoproper ferroelastic. Our sound velocity measurements indicate that the isostructural compound $CuCrO_2$ also undergoes an $R\bar{3}m \rightharpoonup C2/m$ ferroelastic transition at $T_{N1} = 24.3$ K (except that the transition in $CuCrO_2$ is first order). Since the order parameter of an $R\bar{3}m \rightharpoonup C2/m$ structural transition belongs to the E_g irreducible representation [34], the transitions in both compounds could be driven by a Raman active E_g mode. Therefore, we performed Raman scattering measurements on $CuFeO_2$ and $CuCrO_2$ down to $T = 5$ K. Another frustrated magnet, $CuCrS_2$, also shows an $R3m \rightharpoonup C/m$ symmetry lowering transition at the antiferromagnetic transition temperature $T_N = 37.5$ K. In that case, the order parameter should belong to the E irreducible representation of the $R3m$ space group [50]. Thus, we also measured the Raman modes in this compound to determine if the transition at T_N is driven by

171

a soft optical mode.

9.1 CuFeO$_2$ and CuCrO$_2$

We first present polarized room temperature spectra of CuFeO$_2$ and CuCrO$_2$ and identify the symmetries of Raman modes in both compounds using Raman tensors. Then, we present the data obtained between room temperature and 5 K and analyze the results to possibly determine the order parameters of the ferroelastic transitions observed in CuFeO$_2$ and CuCrO$_2$ at low temperatures.

9.1.1 Room Temperature Measurements

Delafossite compounds (space group $R\bar{3}m$) such as CuFeO$_2$ and CuCrO$_2$ have one formula unit per unit cell with a total of 12 possible vibrational modes, $A_{1g} + E_g + 3A_{2u} + 3E_u$ [113]. A modes correspond to vibrations of the Cu-O bonds along the hexagonal c axis whereas E modes describe the vibrations in the basal plane (xy plane). Due to the existence of an inversion center, the classification of normal modes is done in terms of their parity [113]. Odd modes, denoted by the subscript u, refer to infrared active or acoustic modes while even modes, denoted by the subscript g, are Raman active. In order to determine the symmetry of the modes observed in CuFeO$_2$ (Fig. 9.1) and CuCrO$_2$ (Fig. 9.2), we performed polarized Raman scattering measurements at room temperature.

Prior to experiments, CuCrO$_2$ and CuFeO$_2$ samples were mechanically polished as described in Chapter 6. In the first set of experiments, performed with the Ar$^+$ laser ($\lambda = 514.5$ nm), the incident beam powers for CuFeO$_2$ and CuCrO$_2$ were 50 mW and 28 mW, respectively. In the second set of experiments on CuFeO$_2$ and CuCrO$_2$, performed by Dr Kim Doan Truong at the University of Sherbrooke, a HeNe laser with a wavelength of 632 nm was used. These measurements were performed using a micro Raman setup with a resolution

of 0.5 cm^{-1}. Apart from the optical elements, the experimental setup consisted of a double grating spectrometer (Jobin Yvon, model Labram-800) and a liquid-nitrogen cooled CCD detector. In order to minimize sample heating, 0.3 mW was focused onto a 3 μm spot size (4000 W/cm^2). All room temperature measurements were performed with a backscattering geometry. The experimental scattering geometries are represented using the Porto notation, $k_i(e_i e_s)k_s$. In Figs. 9.1 and Fig. 9.2, the notation $z(xy)\bar{z}$ indicates that the incident light propagates along the z axis with a polarization along the x axis while the scattered light propagates along the $\bar{z}$ axis with a polarization along the y axis. In addition, the label z' designates a direction making an angle θ relative to the z axis, where $\theta = 50°$ for CuFeO$_2$ while $\theta = 15°$ for CuCrO$_2$. The label y' designates a polarization direction in the yz plane.

To our knowledge, no polarized Raman measurements on CuFeO$_2$ single crystals have been reported so far. At room temperature, the spectrum taken with the Ar$^+$ laser using unpolarized (u) scattered light, Fig. 9.1a, shows modes at 349 cm^{-1} and 690 cm^{-1} in agreement with results obtained on polycrystals [114, 41]. The intensity of the mode at 690 cm^{-1} disappears with cross ($y'x$) polarization while the mode at 349 cm^{-1} remains visible in both ($y'u$) and cross ($y'x$) polarizations. Measurements with the He-Ne laser show Raman modes at 351 cm^{-1} and 692 cm^{-1} and a broad band at 496 cm^{-1} (See Fig. 9.1b). The spectra obtained with the HeNe laser has a much better signal-to-noise ratio than those obtained with the Ar$^+$ laser. This is because in the Hen-Ne setup more scattered light is collected by the large collection cone of the scattered light provided by a lens with a small f-number and short focal length in the micro-Raman setup using the HeNe laser. The mode at 692 cm^{-1} has a strong intensity in the parallel polarization (yy) and disappears in the cross polarization (yx). The intensity of the mode at 351 cm^{-1} is very weak which implies that the He-Ne excitation line at 632.8 nm is not in resonance with the vibrations associated with this mode as observed in LiNiO$_2$ [115]. Despite its weak intensity, it is visible in both polarizations. Moreover, this mode was reproducible down to low temperatures (see Fig. 9.4b).
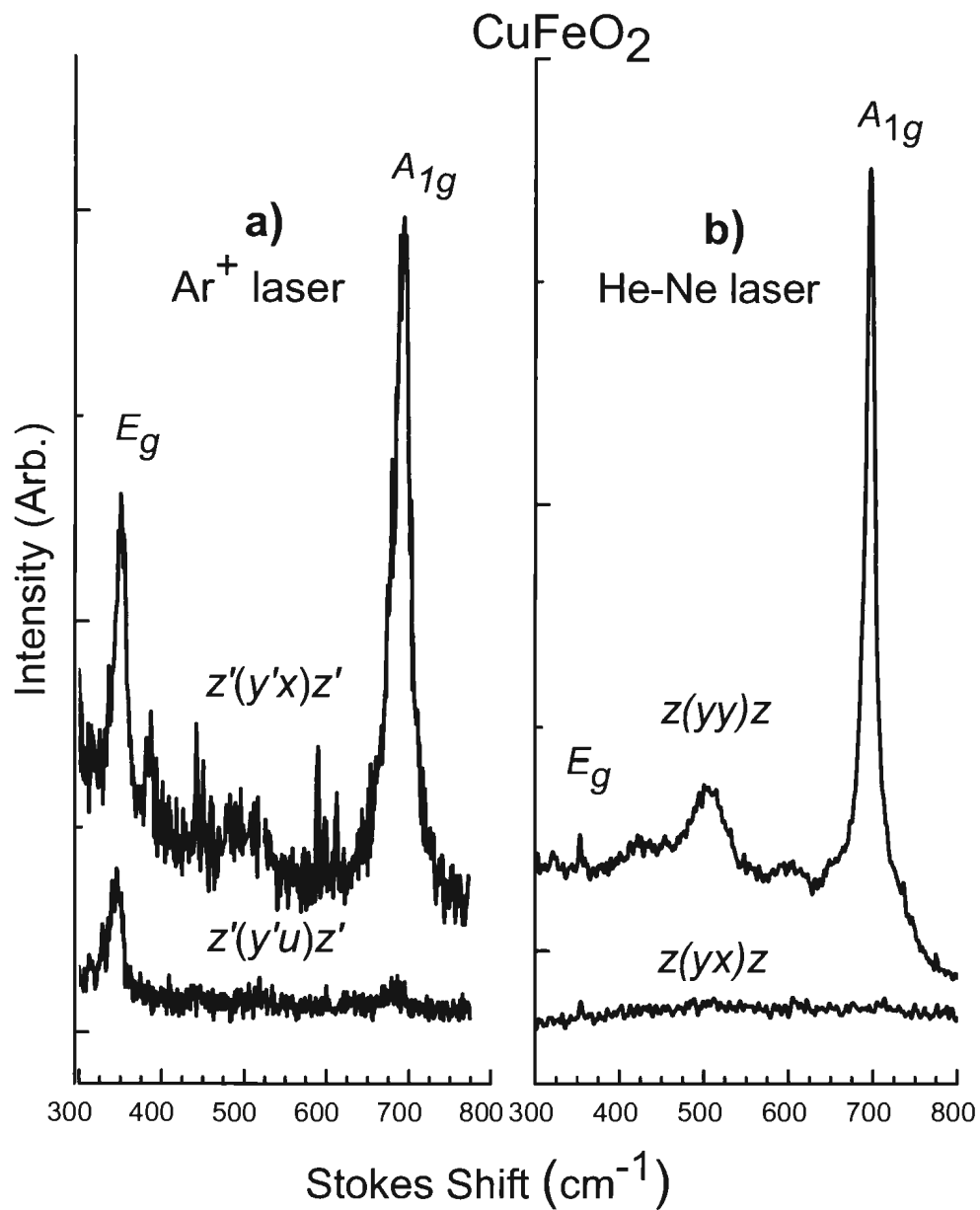
Figure 9.1: Polarized Raman Spectra of $CuFeO_2$ at room temperature obtained using the (a) Ar^+ ($\lambda = 514.5$ nm) and (b)He-Ne ($\lambda = 632.8$ nm) lasers. See text for the description of the scattering geometries. In the spectra obtained with the Ar^+ laser, a plasma line located at 521 cm^{-1} is removed for clarity.

The symmetry of each mode can be identified using the Raman scattering tensors associated with the trigonal point group $\overline{3}m$ (Eq. 9.1 and 9.2) [78, 81],

$$A_{1g}(x) : \begin{bmatrix} a & 0 & 0 \\ 0 & a & 0 \\ 0 & 0 & b \end{bmatrix} \tag{9.1}$$

and

$$E_g(x) : \begin{bmatrix} c & 0 & 0 \\ 0 & -c & d \\ 0 & d & 0 \end{bmatrix}, \quad E_{g(y)} : \begin{bmatrix} 0 & -c & -d \\ -c & 0 & 0 \\ -d & 0 & 0 \end{bmatrix}. \tag{9.2}$$

According to Eqs. 9.1 and 9.2, a cross polarization configuration such as $z(yx)\overline{z}$ allows only E_g modes, while a parallel polarization configuration like $z(xx)\overline{z}$ allows the observation of E_g and A_{1g} modes. Therefore, the mode symmetries are assigned as $\omega_{A_{1g}} = 692$ cm^{-1} and $\omega_{E_g} = 351$ cm^{-1}.

In addition to the vibrational modes observed in CuFeO$_2$, a broad band located at 496 cm^{-1} is also revealed using both laser sources. In the unpolarized $(y'u)$ spectrum obtained with the Ar$^+$ laser, the intensity of this feature is within the background noise. In the parallel polarized spectrum obtained with the He-Ne laser, the broad peak is clearly observed down to 5 K (Fig. 9.4). This broad band is also apparent in the spectra down to 80 K obtained on polycrystals [41]. Polarized spectra obtained with both excitation lines show that the mode at 496 cm^{-1} has A_{1g} symmetry.

Similar to the case of CuFeO$_2$, polarized Raman spectra of CuCrO$_2$ are not available in literature. In Fig. 9.2, we present polarized Raman spectra of CuCrO$_2$ obtained at room temperature. In these spectra, P indicates plasma lines. As in the case of CuFeO$_2$, CuCrO$_2$ should show two Raman modes. However, with unpolarized (u) scattered light (not shown) or a parallel polarization (xx) configuration with the Ar$^+$ laser (Fig. 9.2a), we observe modes at 104 cm^{-1}, 207 cm^{-1}, 382 cm^{-1} 457 cm^{-1}, 538 cm^{-1}, 557 cm^{-1}, 623 cm^{-1}, 668 cm^{-1}, and
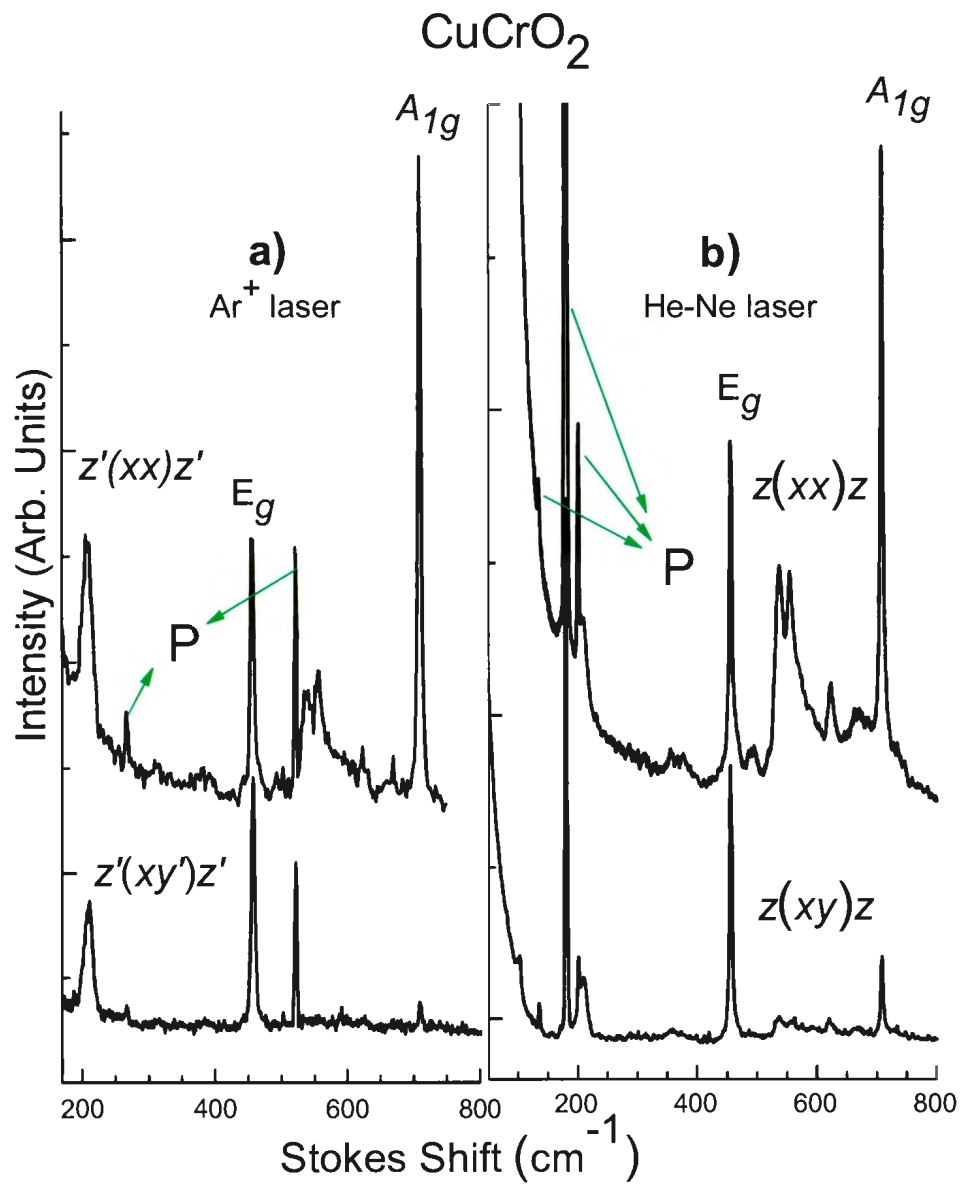
Figure 9.2: Polarized Raman Spectra of $CuCrO_2$ at room temperature obtained using **(a)** the Ar^+ and **(b)** He-Ne lasers. P indicates plasma lines. See text for the description of the scattering geometries.

709 cm^{-1}. Using the He-Ne laser (Fig. 9.2b), a similar spectrum is obtained except for the absence of a mode at 382 cm^{-1} and a new mode at 359 cm^{-1}. The symmetries of these modes can be assigned according to the polarized Raman measurements shown in Fig. 9.2. Since the modes at 104 cm^{-1}, 212 cm^{-1}, and 457 cm^{-1} are observed in both polarization configurations, these modes belong to the E_g irreducible representation. The other modes are therefore assigned to A_g representation since their intensities are weak or disappear in the cross polarization configuration. So far, there have been four publications reporting Raman spectra on CuCrO$_2$ powder samples [42, 43, 44, 45]. Two of these publications show modes at 207 cm^{-1}, 444 cm^{-1}, and 691 cm^{-1} [42, 43]. In addition, one of these works shows additional features with weak intensities at $\sim$540 cm^{-1} and $\sim$560 cm^{-1} [43]. Other publications [44, 45] reveal Raman modes only at 452 cm^{-1} and 703 cm^{-1}. By comparison, our polarized Raman results indicate that the Raman modes in CuCrO$_2$ correspond to $\omega_{A_{1g}} = 709$ cm^{-1} and $\omega_{E_g} = 457$ cm^{-1}.

As mentioned earlier, CuFeO$_2$ and CuCrO$_2$ should only have two Raman modes. However, both compounds show additional features (Figs. 9.1 and 9.2) similar to those observed in other delafossite compounds such as CuAlO$_2$ [116] and CuGaO$_2$ [113]. In agreement with *ab initio* calculations, these additional modes in CuAlO$_2$ are attributed to non-zero wavevector phonons which are normally forbidden by Raman selection rules [116]. As suggested, the selection rules are possibly relaxed by defects such as Cu vacancies, interstitial oxygens or tetrahedrally coordinated Cr^{+3} or Fe^{+3} on the Cu site [116]. Thus, the additional features observed in CuFeO$_2$ and CuCrO$_2$ could have an origin similar to that observed in CuAlO$_2$ [116] and CuGaO$_2$ [113]. They could also be crystal field excitations, which are due to electronic transitions between two orbitals of an atom in a crystal field. The crystal field is simply the electric field arising from the electrons in the orbitals of neighboring ions, which can lift the degeneracy of atomic orbitals. In ABO$_2$ delafossites such as CuCrO$_2$ and CuFeO$_2$, magnetic (Cr^{3+} and Fe^{3+}) ions are in the center of an octahedron formed by the

177

oxygen ions, leading to the overlaps of the $3d$ orbitals of the magnetic ion and the p orbitals of the oxygen ions. This overlap results in energy splitting in the d orbitals (between e_g and t_{2g} orbitals). Crystal field excitations were revealed in the Raman spectra of a number of geometrically frustrated magnets including $R_2Ti_2O_7$, where R = Tb, Dy [117]. In $Tb_2Ti_2O_7$, the Raman shifts of these excitations range between 7 cm^{-1} and 135 cm^{-1} whereas the crystal field excitation observed in $Dy_2Ti_2O_7$ appear at 287 cm^{-1}. All these excitations are due to R^+ ions [117].

9.1.2 Low temperature measurements

Low temperature measurements on $CuFeO_2$ and $CuCrO_2$ were performed using the setups described in the previous section. Measurements using the HeNe laser were performed by Dr. Kim Doan Truong at the University of Sherbrooke. For these measurements, a backscattering geometry with an incident beam power of 0.3 mW was used. With the Ar^+ laser, the scattering geometry for low temperature measurements was different from that used at room temperature. Fig. 9.3 shows a top view diagram of the sample orientation with respect to the incident beam and the direction of observation for low temperature measurements. The crystallographic axes of the samples are also shown. The incident light propagates at 25° relative to the normal ($\hat{n}$) of the sample surface. The scattered light was collected at an angle of 90° with respect to the incident light. In $CuFeO_2$, the focal lengths of the focusing and the collecting lenses were 12 cm and 20 cm (f/4), respectively. For $CuCrO_2$ measurements, the focal lengths were 20 cm (f/4 and f/5, respectively). Such a scattering geometry was preferred over the backscattering geometry in order to avoid the reflected beam from the cryostat windows.

Unpolarized Raman spectra of $CuFeO_2$ obtained using 514.5 nm and 632.8 nm radiation are shown in Fig. 9.4. Spectra using the Ar^+ laser were obtained down to 15 K. As a result,
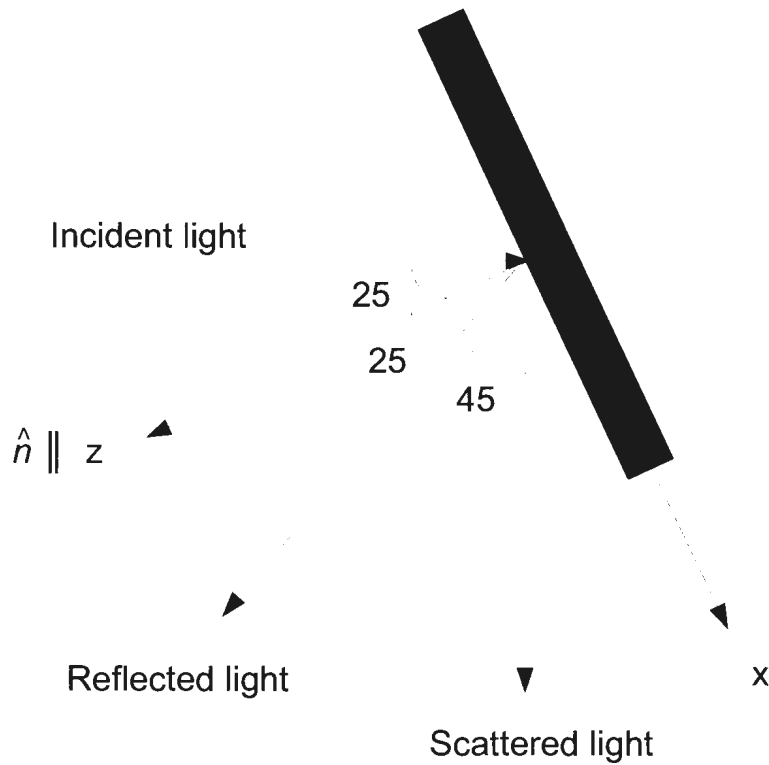
Figure 9.3: A top view of the CuFeO$_2$ and CuCrO$_2$ sample orientation relative to the incident and scattered light for low temperature measurements performed with the Ar$^+$ laser ($\lambda = $ 514.5 nm).

we could not obtain spectra below $T_{N1} = 14$ K with this excitation line. However, using the He-Ne laser, the temperature dependences of the Raman modes were obtained down to 5 K. Spectra obtained with both excitation lines show similar behavior. The intensities of all modes increase in accordance with the decrease in the Raman linewidths. No significant change in the Raman shifts was observed in the temperature range studied. Due to the $R\bar{3}m \rightharpoonup C2/m$ structural transition at T_{N1} [1, 30, 55], spectra obtained below T_{N1} with the He-Ne laser should normally show additional Raman modes. The A_{1g} mode should transform into an A_g mode for the monoclinic space group $C2/m$ whereas one would expect

179
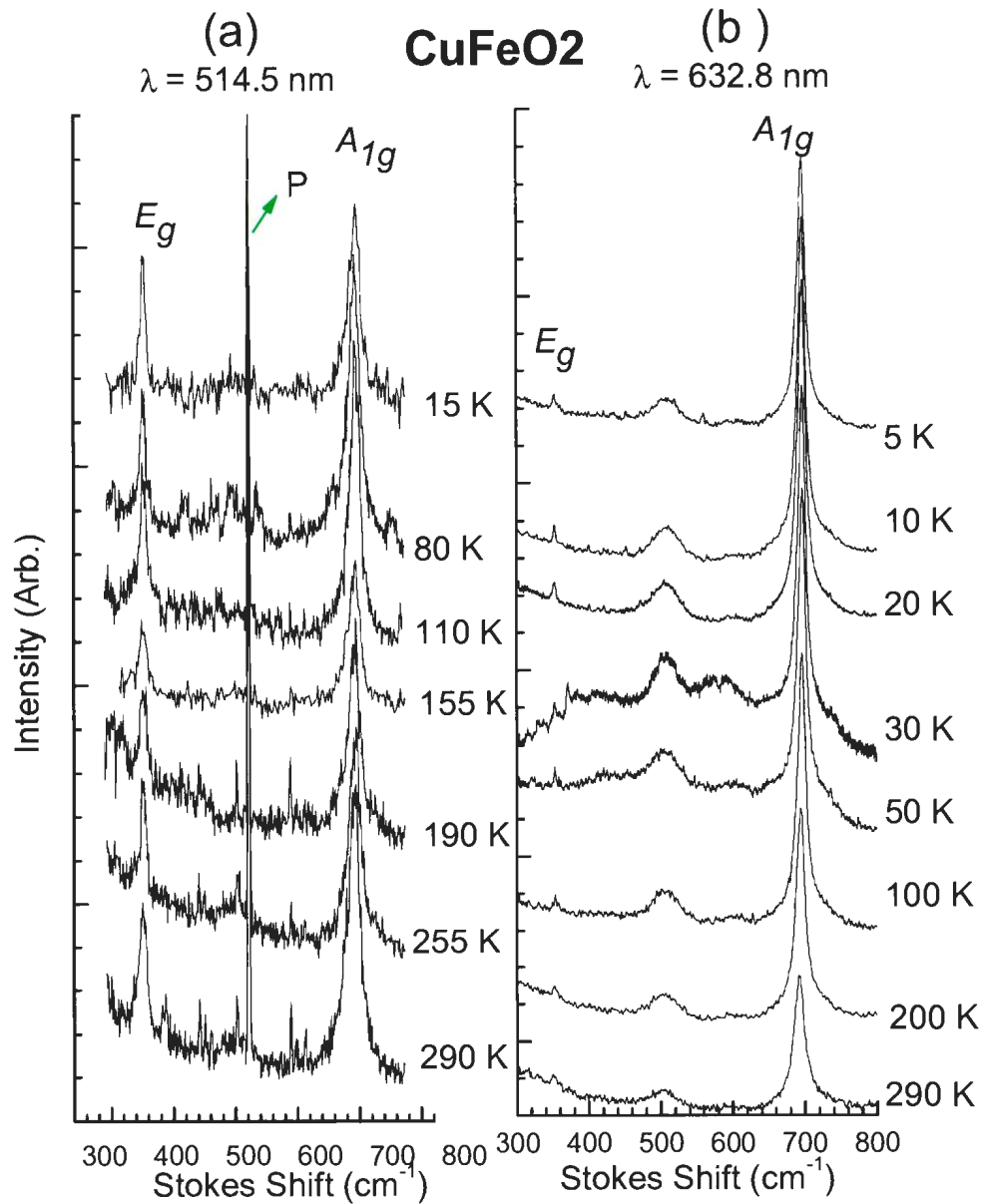
Figure 9.4: Unpolarized Raman spectra of CuFeO$_2$ using (a) the Ar$^+$ laser ($\lambda = 514.5$ nm) (b) HeNe laser ($\lambda = 632.8$ nm) obtained down to 15 K and 5 K, respectively. The HeNe laser measurements were performed by Dr. Kim Doan Truong at the University of Sherbrooke.

the splitting of the E_g mode into an A_g and B_g mode [81]. However, no such splitting is noticeable in the monoclinic phase. We attribute this discrepancy to weak resonance with the He-Ne excitation line, which results in a weak intensity for the E_g mode and makes it difficult to resolve any possible splitting. Another possibility is that the temperature of the sample remains above T_{N1} even with a beam power of 4000 W/cm^2.

Unpolarized Raman spectra of CuCrO$_2$ obtained with the Ar$^+$ and He-Ne excitation lines are shown in Fig. 9.5. While the spectra obtained with the 514.5 nm laser line do not show any significant changes with temperature, the spectra obtained with the HeNe laser display small differences as the temperature is decreased from room temperature down to 8 K. With a close look at the E_g mode (458 cm^{-1}), one can observe that its tail becomes broader on the right hand side below 160 K (Fig. 9.5b). With further cooling, an additional mode is easily distinguished and its frequency increases to 470 cm^{-1} at 8 K. This mode is also observed with parallel and cross polarization configurations as shown in Fig. 9.6. It should be noted that the additional mode is unlikely due to the splitting of the E_g mode since neutron diffraction [30, 55], magnetostriction [33], and sound velocity measurements (Fig. 7.1) do not show any anomaly that could be associated with a structural deformation in the 150 K-200 K temperature range. This mode could be due to crystal field excitations or relaxation of the Raman selection rules because of defects [113, 117]. Moreover, the spectra of CuCrO$_2$ at 8 K and 15 K (Fig. 9.5b) deserve some attention. Unlike the spectra at other temperatures (above T_{N1}), they develop a broad background feature centered at $\sim$550 cm^{-1}. Since it appears below T_{N2}, we could associate it with magnon modes arising from a proper screw ordering observed below T_{N2} [63, 118]. As seen in Fig. 9.6, the broad band is observed using both parallel and cross polarizations. Finally, despite the evidence for an $R\bar{3}m \rightharpoonup C2/m$ ferroelastic transition at $T_{N1} = 24.3$ K in CuCrO$_2$ presented in the earlier chapter, no additional Raman modes are observed below this temperature. Local heating due to incident beam power density (4000 W/cm^2) is a possibility (see Sec. 7.1.2);
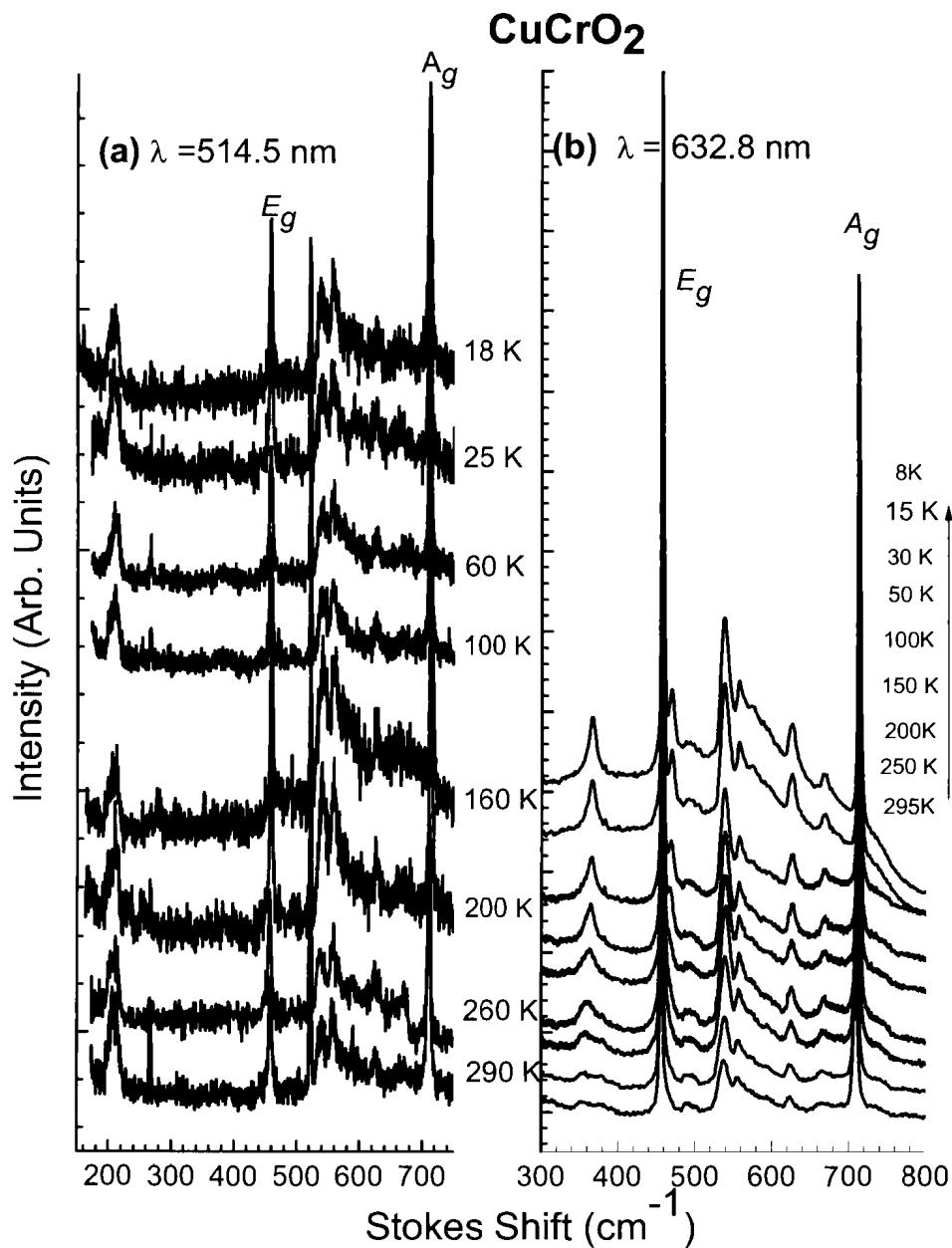
Figure 9.5: Raman spectra of $CuCrO_2$ using (a) the Ar^+ laser ($\lambda = 514.5$ nm) (b) HeNe laser ($\lambda = 632.8$ nm) obtained down to 18 K and 8 K, respectively. The HeNe laser measurements were performed by Dr. Kim Doan Truong at the University of Sherbrooke.

however, the broad band observed in the spectra at 8 K and 15 K (Fig. 9.5) clearly shows that the sample temperatures for these spectra were below T_{N1}. If the additional Raman modes associated with the monoclinic phase below T_{N1} are weak, they might be suppressed by the broad magnon band.
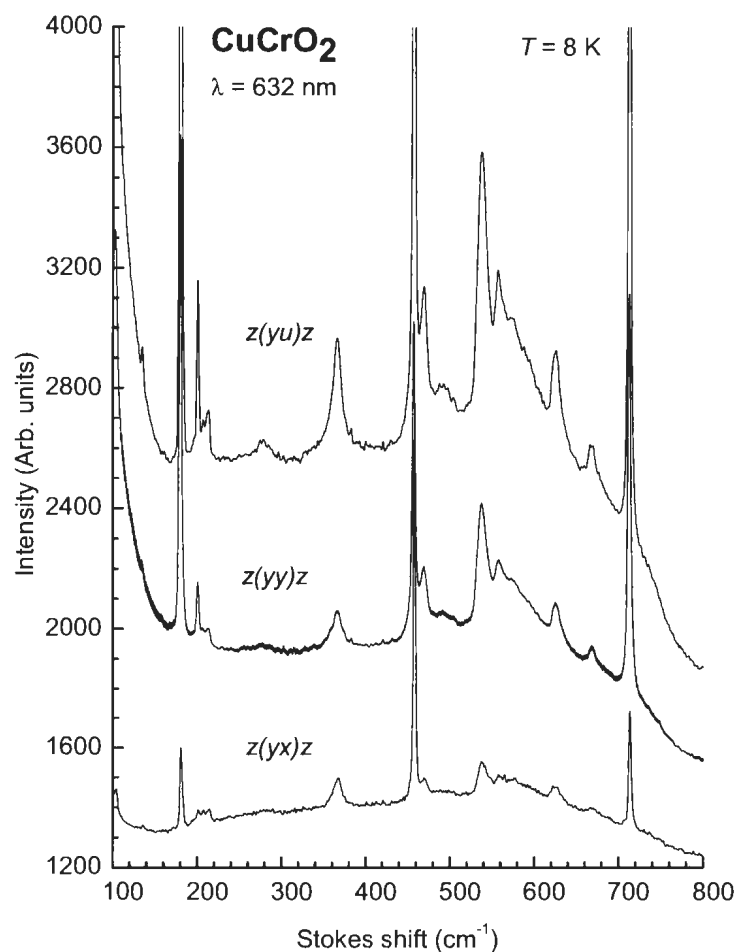
Figure 9.6: Polarized Raman spectra of $CuCrO_2$ obtained at 8 K using the HeNe laser ($\lambda = 632.8$ nm). Data were collected with Dr. Kim Doan Truong at the University of Sherbrooke.

The temperature dependence of the Raman modes in $CuFeO_2$ are presented in Fig. 9.7. Results obtained using both setups show the same variations with temperature; i.e., the frequency of both modes increases as the temperature is reduced. The additional mode at $\omega = 495$ cm^{-1} shows similar behavior with decreasing temperature to those of the Raman modes (not shown). According to the spectra obtained with the Ar$^+$ laser (squares in Fig. 9.7). E_g and A_{1g} mode frequencies show no significant increase between room temperature and 15 K. On the other hand, the results obtained with the HeNe laser (triangles) show that the E_g and A_{1g} mode frequencies increase by 2 cm^{-1} and 5 cm^{-1}, respectively. The differences in the frequency variations obtained from two sets of measurements could be attributed to local heating. Comparing the temperature dependences of the Raman shifts in $CuFeO_2$ (Fig. 9.7) to earlier results obtained between 400 K and 80 K [41], we see that results obtained with the HeNe laser are in quantitative agreement. According to results obtained with the HeNe laser, the frequencies of the A_{1g} and E_g mode in $CuFeO_2$ show no significant variation below $T_{N1} = 14$ K. In addition, the linewidths of all modes in $CuFeO_2$ decrease as the temperature is decreased (not shown).

The frequency variations of the E_g and A_{1g} modes in $CuCrO_2$ are shown in Fig. 9.8. Results obtained with the HeNe laser (triangles) show that both mode frequencies increase between 290 K and 80 K. While the frequency of the A_{1g} mode remains constant between 80 K and 8 K, the frequency of the E_g mode decreases slightly in this range. Results obtained with the Ar$^+$ laser (squares in Fig. 9.8) show the same frequency variation down to 160 K. Below 160 K, both modes show a drop in frequency. While the E_g mode decreases by 1 cm^{-1}, the drop in the A_{1g} mode frequency is 2 cm^{-1}. The origin of the differences below 160 K obtained with the both laser sources is not clear. Interestingly, Raman spectra of $CuCrO_2$ obtained with the HeNe laser shows the appearance of a new mode below 160 K (Fig. 9.5).

According to group theory [34], E_g-symmetric optic modes could be associated with the order parameters of the ferroelastic transitions at T_{N1} in $CuCrO_2$ and $CuFeO_2$ [1]. A typical
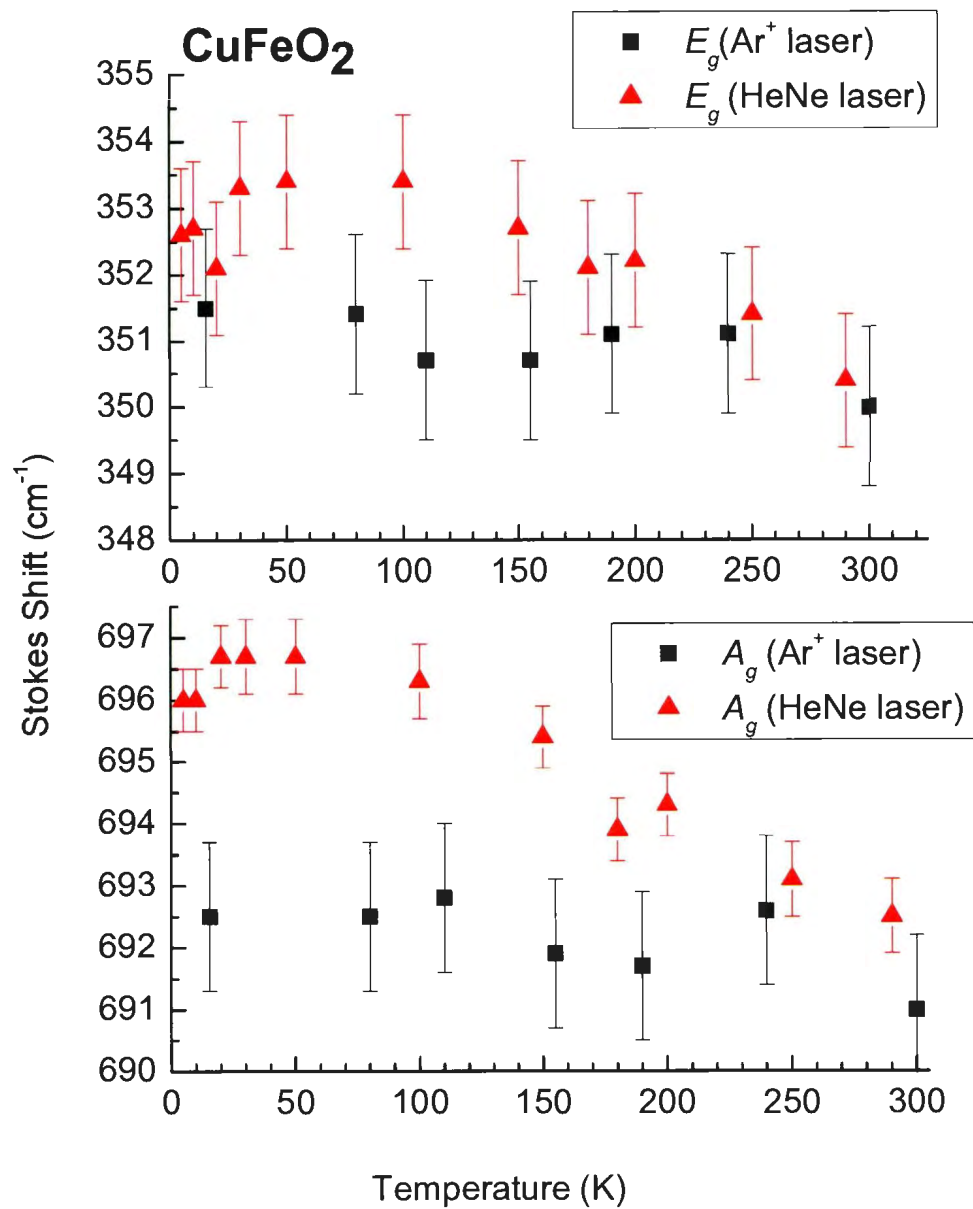
Figure 9.7: Temperature dependences of the Raman shifts in CuFeO$_2$ obtained with Ar$^+$ (514.5 nm) and HeNe (632.8 nm) lasers. Data obtained with the HeNe laser were collected by Dr. Kim Doan Truong at the University of Sherbrooke.
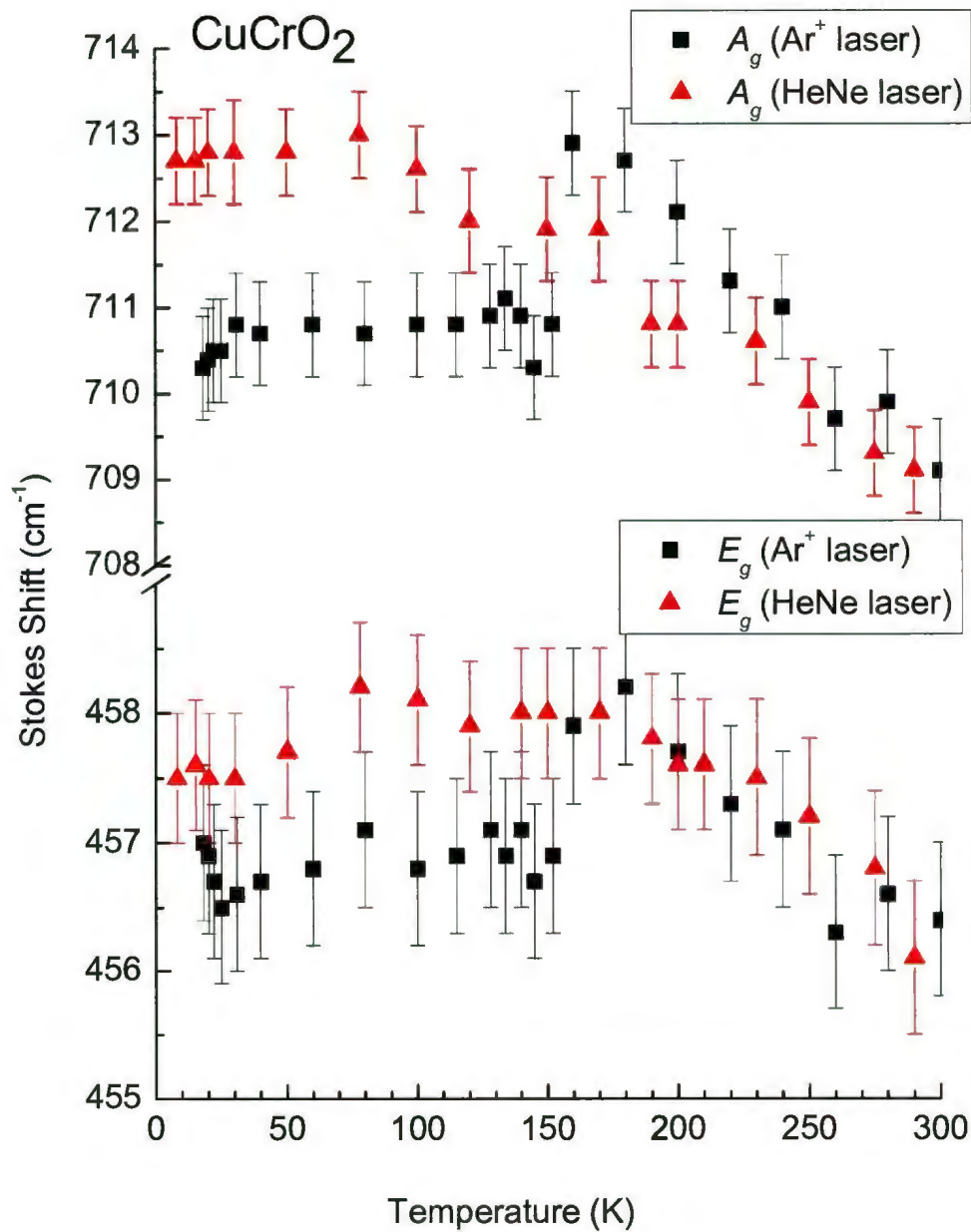
Figure 9.8: Temperature dependences of the Raman shifts in $CuCrO_2$ obtained with Ar^+ (514.5 nm) and HeNe (632.8 nm) lasers. Data obtained with the HeNe laser were collected by Dr. Kim Doan Truong at the University of Sherbrooke.
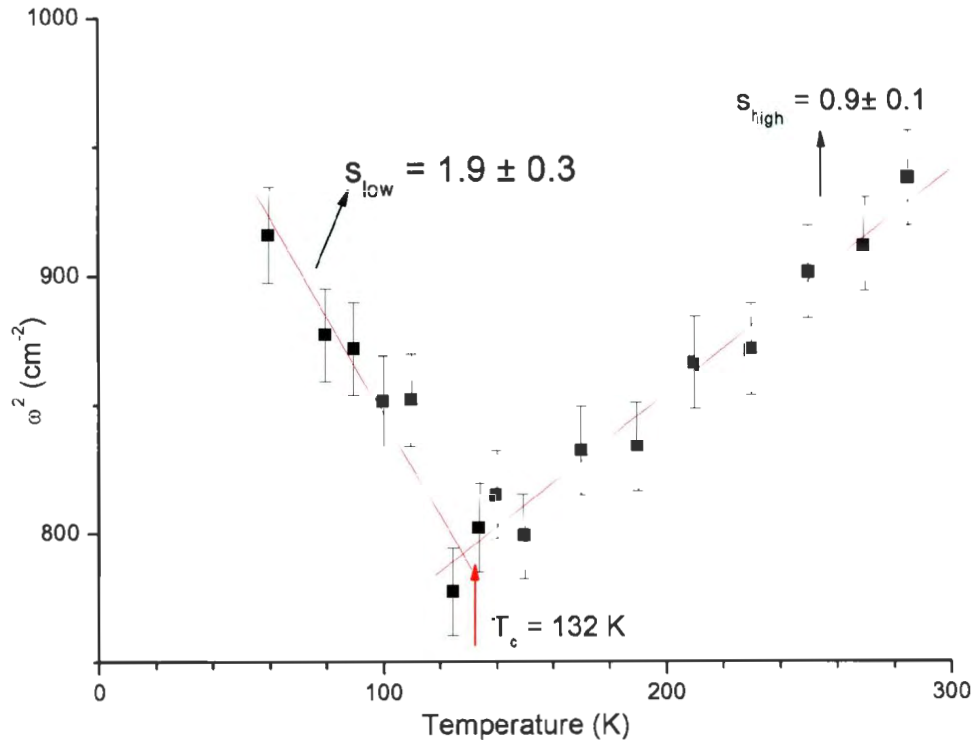
Figure 9.9: Figure is from Aktas et al. [5]. Soft optic mode in the ferroelastic compound RbLiH$_3$(SO$_4$)$_4$.

example of a soft optic mode is shown in Fig. 9.9, where the squared frequency of the B-symmetric soft optic mode in the ferroelastic RbLiH$_3$(SO$_4$)$_4$ compound varies linearly with temperature, with a slope change at T$_{N1}$ [5]. On the other hand, E_g modes in CuFeO$_2$ and CuCrO$_2$ show an increase in frequency with no sign of softening. The temperature behavior of both modes in CuFeO$_2$ and CuCrO$_2$ is rather attributed to anharmonic phonon-phonon interactions, in agreement with the analysis of Pavunny et al. [41]. With a decrease in temperature, anharmonic phonon-phonon interactions are reduced due to a decrease in phonon occupation number. As a result, the strength of the atomic force constant increases,

leading to an increased frequency shift. Based on these results, we conclude that none of the Raman modes in $CuFeO_2$ and $CuCrO_2$ can account for the pseudoproper ferroelastic transitions observed at $T_{N1} = 14$ K in $CuFeO_2$ [1] and at $T_{N1} = 24.3$ K in $CuCrO_2$. While these results do not refute the nature of the ferroelastic transitions in $CuFeO_2$ [1] and $CuCrO_2$ (Figs. 7.1-7.2 and 8.7), they leave the driving mechanisms unresolved.

9.2 Raman scattering measurements on $CuCrS_2$

The triangular lattice antiferromagnet $CuCrS_2$ has one formula unit per unit cell, resulting in 12 vibrational modes, $4A_1 + 4E$ [51]. Since the point group ($3m$) of $CuCrS_2$ lacks inversion symmetry, all modes are Raman and infrared (IR) active [51]. The A_1 modes are associated with the displacements of the Cu and Cr atoms along the c axis with the S atoms moving in the opposite direction. On the other hand, degenerate E modes correspond to the displacements perpendicular to the z axis.

Measurements were performed on single crystals of $CuCrS_2$ provided by Dr. Julia C. E. Rasch at ETH Zurich (Now at VDI/VDE Innovation and Technology GmbH, Berlin). $CuCrS_2$ samples have a platelet geometry with a large area in the basal plane and 200 μm thick along the c axis. Measurements were performed using the 514.5 nm line of a multi mode Ar^+ laser with a beam power of 25 mW.

Fig. 9.10 shows Raman spectra of $CuCrS_2$ obtained between room temperature and 13 K. All spectra were collected using backscattering geometry at an oblique angle of incidence relative to the surface normal of the sample. The scattering geometries can be represented with the Porto notation as $z'(su)z'$ and $z'(pu)z'$. Here z' corresponds to a direction at an angle of 30° relative to the c axis. The notations p and s correspond to light polarizations parallel and perpendicular to the plane of incidence, whereas u corresponds to unpolarized scattered light. (The polarizations s and p do not necessarily correspond to either of the

crystallographic axes since the crystallographic directions in the basal plane in the $CuCrS_2$ are unknown). In Fig. 9.10, the spectra plotted with the same color are collected at the same temperature, which is indicated on the right hand side of the spectrum pair. In each pair of spectra, the lower spectrum is collected with (su) polarization whereas the top spectrum is collected with pu polarization. Spectra at all temperatures show two strong modes at 253 cm^{-1} and 319 cm^{-1}. In addition, a low frequency mode partially hidden in the tail of the laser line is observed at 57 cm^{-1} with (su) polarization. Another mode, which is not easily seen at room temperature reveals itself as the temperature is decreased. A Lorentzian fit to the data gives the frequency shift of this mode as 224 cm^{-1} at 250 K. In order to determine mode symmetry, we compare our results to earlier Raman measurements by Abramova *et al.* [51]. They also calculate expected Raman frequencies using a valence force field model and simulate the Raman spectra of $CuCrO_2$ at room temperature. We refer to these calculations as simulations, which show 8 Raman modes: $4\ A_1 + 4\ E$ [51]. Two of these modes with A_1 and E symmetries are central lines. Three of these modes are located at 198 cm^{-1}, 240 cm^{-1}, and 307 cm^{-1} and belong to the A_1 irreducible representation (IR) [51]. The remaining three modes have E symmetry with frequency shifts at 99 cm^{-1}, 211 cm^{-1}, and 257 cm^{-1}. Raman measurements by Abramova et al. [51] reveal three Raman modes. Similar to our results, two of these modes are located at 257 cm^{-1} and 322 cm^{-1} and are identified as E and A_1 modes, respectively. The third mode appears as a shoulder of the 257 cm^{-1} line and its symmetry is not specified [51]. Comparing our results to Raman spectra and calculated Raman shifts [51], we identify the modes in Fig. 9.10 as $\omega_E = 252$ cm^{-1} and $\omega_{A_1} = 319$ cm^{-1}, and $\omega_E = 57$ cm^{-1}. The mode observed at 224 cm^{-1} could belong to either of the irreducible representations E and A_1, even though simulations [51] show that A_1 mode located at 240 cm^{-1} has a weak intensity. Thus, the mode at 224 is more likely to be an E mode. The remaining A_1 mode which is not observed also has a weak intensity according to simulations [51], which might explain why the spectra of $CuCrS_2$ do not reveal all Raman modes.
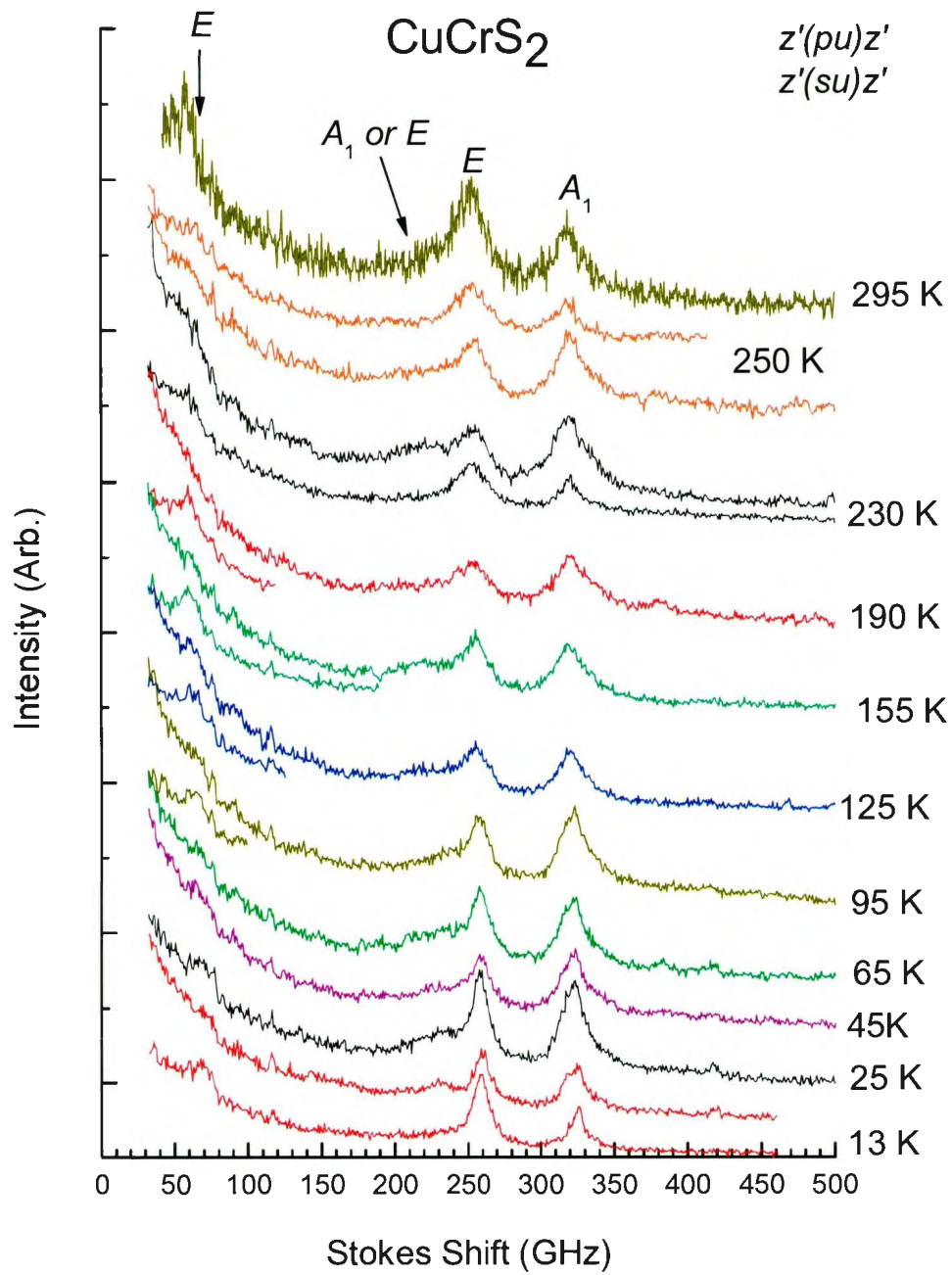
Figure 9.10: Raman spectra of CuCrS$_2$ obtained between 295 K and 13 K.

As the temperature is reduced, Raman spectra do not show significant change except for the appearance of a new mode at 418 cm^{-1} at low temperatures (Fig. 9.10). This mode was observed at low temperatures in the previous measurements and was considered to be due to an electronic transition [51]. As in the case of CuFeO$_2$ and CuCrO$_2$ (Sec. 9.1.1 and 9.1.2), this mode could be due to crystal field excitations or defects [113, 117]. The broad band at 215 cm^{-1} and the low frequency E mode at 57 cm^{-1} become more noticeable at lower temperatures. Below the antiferromagnetic and $R3m \rightarrow Cm$ structural transition temperature $T_N = 37.5$ K [47], spectra do exhibit the splitting of the E mode. Local heating is ruled out due to the low incident beam power density ($\approx$5000 W/cm^2). We conclude that the resolution in our experiments (4 cm^{-1}) is not enough to observe the splitting.

The frequency shift vs. temperature of the four modes is plotted in Fig. 9.11. All modes shift to higher frequencies with decreasing temperature, between 295 K and 90 K and remain almost constant or increase slightly below 90 K. In addition, none of the modes seem to be affected by the structural and antiferromagnetic transition at T_N. These results are similar to those obtained in earlier measurements [51]. However, there are several differences worth mentioning. According to the previous report [51], the broad A_1 mode (at 215 cm^{-1} at room temperature) slightly decreases with a decrease in temperature. In addition, they observe a splitting in the A_1 mode observed at 319 cm^{-1} below 190 K [51]. The frequency separation of the two modes at 78 K is only 3 cm^{-1} [51], which is smaller than our experimental resolution (4 cm^{-1}). Although a minimum at the frequency shifts of the E modes is noticeable at 190 K, we need more data points around this temperature to reach any conclusion. Considering that the frequencies of all the modes increase with decreasing temperatures, similar to those of CuFeO$_2$ and CuCrO$_2$, we attribute the temperature behavior to thermal contraction anharmonic phonon-phonon interactions. As discussed in Sec. 2.2, Aizu [7, 49] classified a $R3m \rightarrow Cm$ structural as a possible ferroelastic transition. The order parameter of such a transition should belong to the E irreducible representation. Our results show that none of
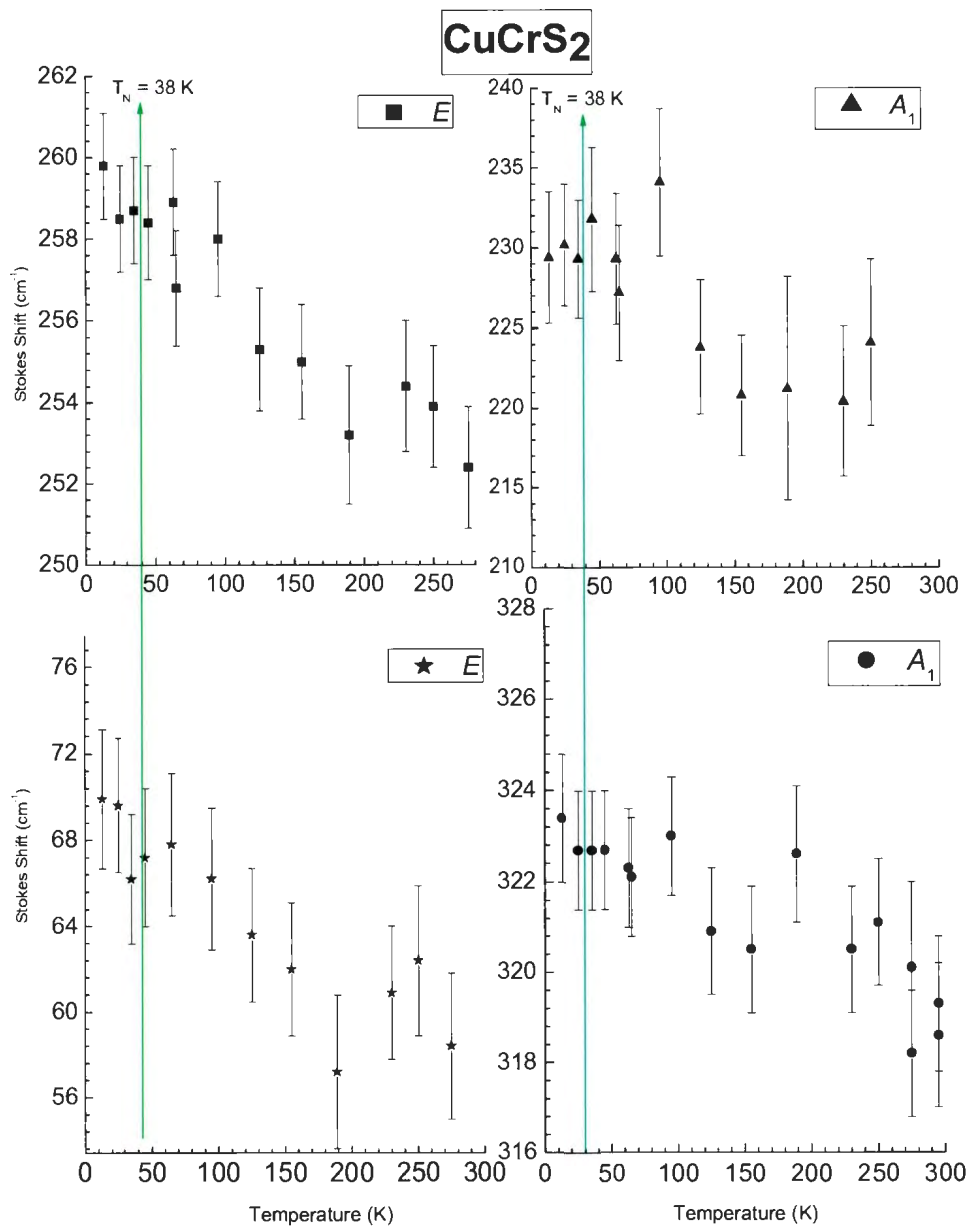
Figure 9.11: The temperature dependences of the frequency shifts of four Raman modes observed in CuCrS$_2$.

the E-symmetric Raman modes in CuCrS$_2$ are associated with the order parameter of the antiferromagnetic and structural transition at T_{N1}.

Chapter 10

Summary and conclusions

In this project, we studied the elastic and structural properties of triangular lattice antiferromagnets $CuCrO_2$, $CuFeO_2$, and $CuCrS_2$ to investigate the role played by the spin-phonon coupling in the magnetic and multiferroic properties of a large class of geometrically frustrated magnets. The emphasis was put on $CuCrO_2$ for comparison with $CuFeO_2$ which was extensively investigated using ultrasonic velocity measurements [1, 3, 31]. Our study consists of three major parts.

The first part was to determine the elastic properties of $CuCrO_2$ and further investigate the elastic properties of $CuFeO_2$. Similar to results obtained on the acoustic modes of $CuFeO_2$ [1], ultrasonic velocity measurements on $CuCrO_2$ show that all acoustic mode velocities decrease as the temperature is reduced down to the first antiferromagnetic transition observed at $T_{N1} = 24.3$ K. The decrease observed in the acoustic mode velocities corresponds to softening of the elastic constants C_{66}, C_{11}, and C_{44}. Particularly, the softening observed in the transverse mode $T_y P_x$ indicates a $\sim 35\%$ reduction on the elastic constant C_{66} at T_{N1} relative to its value at room temperature. Our analysis of the ultrasonic velocity measurements on $CuCrO_2$ using a Landau model indicates that the data are consistent with an $R\bar{3}m \rightharpoonup C2/m$ pseudoproper ferroelastic transition at T_{N1}. In this context, the order parameter, which

belongs to the two dimensional E_g irreducible representation of the trigonal $\bar{3}m$ point group ($R\bar{3}m$ space group), bilinearly couples to spontaneous strains $e_s = \delta_1(e_1 - e_2, e_6) + \delta_2(e_4, e_5)$ and gives rise to softening on the acoustic modes with a nonlinear temperature dependence. In the model, a linear-quadratic coupling term $(\beta_1(e_1 + e_2)(Q_1^2 + Q_2^2))$ is used to account for the drop in the velocity of the longitudinal L_x mode just before T_{N1}. In addition, according to the model, the steep increase in the acoustic velocities below T_{N1} is due to a discontinuous change in the order parameter at the ferroelastic transition at T_{N1}, characteristic of first order phase transitions. More importantly, the incomplete softening of the transverse mode $T_x P_y$ is also due to the first order nature of the pseudoproper ferroelastic transition at T_{N1} in CuCrO$_2$. In a second order ferroelastic phase transition transition, one would expect complete softening in this mode ($T_x P_y$) as suggested in the case of CuFeO$_2$ [1]. Our Brillouin scattering measurements performed on CuFeO$_2$ to determine if this mode shows complete softening were not successful. Due to the opacity of CuFeO$_2$, Brillouin measurements show only surface acoustic modes propagating in the xy and xz planes with a velocity that depends on the elastic constants C_{44} and C_{33}. As a result, we could not confirm the second order nature of the pseudoproper ferroelastic transition in CuFeO$_2$. Brillouin scattering measurements which were also performed on CuCrO$_2$ for comparison with ultrasonic measurements show softening of the acoustic modes. However, local heating, due to incident beam power, does not allow us to observe the actual softening of the acoustic modes in CuCrO$_2$. Even though low temperature Brillouin measurements were not conclusive, room temperature measurements performed using reflection and backscattering geometries provided us with four of the six elastic constants in CuCrO$_2$. The values of the elastic constants were used to fit the model to the experimental data.

In the second part of the study, we determined the magnetic phase diagram of CuCrO$_2$ for magnetic fields applied along the [110] and [1$\bar{1}$0] directions (hexagonal basis). Measurements to determine the magnetic phase diagram of CuCrO$_2$ were performed simultaneously on the

$\epsilon_{[110]}$ dielectric constant and velocities of the $L_{[1\bar{1}0]}$, $T_{[1\bar{1}0]}P_{[110]}$, and $T_{[1\bar{1}0]}P_c$ acoustic modes (hexagonal basis). These measurements show zero-field transitions at $T_{N1} = 24.3$ K and $T_{N2} = 23.8$ K, below which ferroelectricity is induced by a proper screw spin ordering. In addition, measurements with a magnetic field along the $[1\bar{1}0]$ direction confirm the first order transition that was previously observed at low temperatures with magnetization, dielectric constant and polarization measurements [4]. This first order transition, which is attributed to a 90° flop in the spin-spiral from the (110) plane to the $(1\bar{1}0)$ plane, is observed from low temperatures at H = 5.2 T up to T = 23.7 K at H = 4.4 T. Measurements for fields along the $[1\bar{1}0]$ suggest that the minimum in the velocity of the longitudinal L_y mode could be due to the field dependence of magnetic susceptibility [107]. Our dielectric and sound velocity measurements with fields along the [110] direction do not indicate a spin flop transition. However, anomalies observed in the velocity of the $T_{[1\bar{1}0]}P_{[110]}$ mode at H $\sim$5 T suggest a reorientation in the magnetic domains, in agreement with earlier studies [4].

Assuming a collinear magnetic order between T_{N1} and T_{N2} [27], since bilinear coupling between magnetic moments and strains breaks time reversal symmetry, the order parameter cannot be associated with magnetic moments. Therefore, in the last part of our study we investigated the temperature dependence of Raman modes in $CuCrO_2$ and $CuFeO_2$ to possibly determine if the order parameters of the $R\bar{3}m \rightharpoonup C2/m$ ferroelastic transitions at T_{N1} in $CuFeO_2$ [1] and $CuCrO_2$ are associated with an E_g-symmetric Raman active optic mode. Since the $R3m \rightharpoonup Cm$ structural transition at $T_{N1} = 38$ K in $CuCrS_2$ could be driven by an E-symmetric Raman mode, we also measured Raman modes of $CuCrS_2$. Raman measurements on all compounds show that mode frequencies increase with decreasing temperature in accordance with anharmonic phonon-phonon interactions. These results clearly indicate that none of the Raman active E_g modes observed in $CuFeO_2$ and $CuCrO_2$ drive the pseudoproper ferroelastic transitions observed at the Néel temperature T_{N1}. Therefore, the order parameters of the ferroelastic transitions at T_{N1} in $CuFeO_2$ and $CuCrO_2$ are still unknown.

196

Similarly, $CuCrS_2$ does not have any soft optic modes that could be associated with the structural transition at T_{N1}.

Our detailed investigation on the elastic properties of $CuCrO_2$ suggests that a ferroelastic transition at T_{N1} releases the magnetic frustration and stabilizes the antiferromagnetic transition at the same temperature. Another important role of the ferroelasticity in $CuCrO_2$ can be seen if one considers that spin driven ferroelectricity usually appears in low symmetry crystals. The ferroelastic transition reduces the symmetry of the crystal from trigonal ($\overline{3}m$) to monoclinic ($2/m$) at T_{N1}, while at T_{N2} the proper screw spin structure lowers the crystal symmetry to the monoclinic point group 2, inducing a ferroelectric polarization. Thus, a similar ferroelastic transition can be expected in other delafossites such as $AgCrO_2$ and $LiCrO_2$ [26].

In Chapter 8, we analyzed the elastic properties of $CuCrO_2$ using a Landau model which ignores the magnetic degrees of freedom. For a complete quantitative analysis and understanding of magnetoeleastic coupling and its role in $CuCrO_2$ and other delafossites, the free energy has to be expanded to include magnetoelastic coupling terms and possible coupling between strains and magnetic moments. Using the complete model, one can also determine the nature of magnetoelastic coupling at the spin flop transition. Finally, our acoustic velocity measurements as a function of magnetic field show that the ultrasonic pulse echo method can be a useful tool to identify and distinguish between a spin flop transition and spin reorientation.

Bibliography

[1] G. Quirion, M. J. Tagore, M. L. Plumer, and O. A. Petrenko, Phys. Rev. B **77**, 094111 (2008).

[2] T. Arima, J. Phys. Soc. Jpn. **76**, 073702 (2007).

[3] G. Quirion, M. L. Plumer, O. A. Petrenko, G. Balakrishnan, and C. Proust, Phys. Rev. B **80**, 064420 (2009).

[4] K. Kimura, H. Nakamura, S. Kimura, M. Hagiwara, and T. Kimura, Phys. Rev. Lett. **103**, 107201 (2009).

[5] O. Aktas, M. J. Clouter, and G. Quirion, J. Phys.: Condens. Matter **21**, 285901 (2009).

[6] H. Schmid, Ferroelectrics **162**, 317 (1994).

[7] K. Aizu, J. Phys. Soc. Jpn. **27**, 387 (1969).

[8] N. Hur, S. Park, P. Sharma, J. Ahn, S. Guha, and S. Cheong, Nature **429**, 392 (2004).

[9] M. Fiebig, J. Phys. D: Appl. Phys. **38**, R123 (2005).

[10] D. Khomskii, Physics **2**, 20 (2009).

[11] C. Israel, N. D. Mathur, and J. F. Scott, Nat. Mater. **7**, 93 (2008).

[12] A. Roy, R. Gupta, and A. Garg, Adv. in Condens. Matt. Phys. (2012).

[13] S.-W. Cheong and M. Mostovoy, Nat. Mater. **6**, 13 (2007).

[14] T. Kimura, T. Goto, H. Shintani, K. Ishizaka, T. Arima, and Y. Tokura, Nature **426**, 55 (2003).

[15] T. Kimura, Annu. Rev. of Mater Res. **37**, 387 (2007).

[16] Y. Tokura and S. Seki, Adv. Mater. **22**, 1554 (2010).

[17] T. Kimura, G. Lawes, T. Goto, Y. Tokura, and A. P. Ramirez, Phys. Rev. B **71**, 224425 (2005).

[18] H. Katsura, N. Nagaosa, and A. V. Balatsky, Phys. Rev. Lett. **95**, 057205 (2005).

[19] M. Mostovoy, Phys. Rev. Lett. **96**, 067601 (2006).

[20] Y. J. Choi, H. T. Yi, S. Lee, Q. Huang, V. Kiryukhin, and S.-W. Cheong, Phys. Rev. Lett. **100**, 047601 (2008).

[21] Y. Tokunaga, S. Iguchi, T. Arima, and Y. Tokura, Phys. Rev. Lett. **101**, 097205 (2008).

[22] C. Jia, S. Onoda, N. Nagaosa, and J. H. Han, Phys. Rev. B **76**, 144424 (2007).

[23] L. C. Chapon, G. R. Blake, M. J. Gutmann, S. Park, N. Hur, P. G. Radaelli, and S.-W. Cheong, Phys. Rev. Lett. **93**, 177402 (2004).

[24] L. C. Chapon, P. G. Radaelli, G. R. Blake, S. Park, and S.-W. Cheong, Phys. Rev. Lett. **96**, 097601 (2006).

[25] M. Poienar, F. m. c. Damay, C. Martin, V. Hardy, A. Maignan, and G. André, Phys. Rev. B **79**, 014412 (2009).

[26] S. Seki, Y. Onose, and Y. Tokura, Phys. Rev. Lett. **101**, 067204 (2008).

[27] K. Kimura, H. Nakamura, K. Ohgushi, and T. Kimura, Phys. Rev. B **78**, 140401 (2008).

[28] T. Kimura, J. C. Lashley, and A. P. Ramirez, Phys. Rev. B **73**, 220401 (2006).

[29] K. Singh, A. Maignan, C. Martin, and C. Simon, Chem. Mater. **21**, 5007 (2009).

[30] F. Ye, Y. Ren, Q. Huang, J. A. Fernandez-Baca, P. Dai, J. W. Lynn, and T. Kimura, Phys. Rev. B **73**, 220404 (2006).

[31] G. Quirion, M. J. Tagore, M. L. Plumer, and O. A. Petrenko, J. Physs.: Conf. Ser. **145**, 012070 (2009b).

[32] M. L. Plumer, Phys. Rev. B **76**, 144411 (2007).

[33] K. Kimura, T. Otani, H. Nakamura, Y. Wakabayashi, and T. Kimura, J. Phys. Soc. Jpn. **78**, 113710 (2009b).

[34] M. Tinkham, *Group Theory and Quantum Mechanics*, Dover books on Chemistry (Dover Publications, 2003), ISBN 9780486432472.

[35] P. Tolédano, M. M. Fejer, and B. A. Auld, Phys. Rev. B **27**, 5717 (1983).

[36] S. A. T. Redfern and E. Salje, J. Phys. C: Solid State Phys. **21**, 277 (1988).

[37] A. Sawada, M. Udagawa, and T. Nakamura, Phys. Rev. Lett. **39**, 829 (1977).

[38] G. Quirion, W. Wu, O. Aktas, J. Rideout, M. J. Clouter, and B. Mrz, J. Phys.: Condens. Matter **21**, 455901 (2009).

[39] Y. Makita, F. Sakurai, T. Osaka, and I. Tatsuzaki, J. Phys. Soc. Jpn. **42**, 518 (1977).

[40] H. Hellwig, A. F. Goncharov, E. Gregoryanz, H.-k. Mao, and R. J. Hemley, Phys. Rev. B **67**, 174110 (2003).

[41] S. P. Pavunny, A. Kumar, and R. S. Katiyar, J. Appl. Phys. **107**, 013522 (pages 7) (2010).

[42] J. Shu, X. Zhu, and T. Yi, Electrochimica Acta **54**, 2795 (2009).

[43] M. Amami, F. Jlaiel, P. Strobel, and A. B. Salah, Materials Research Bulletin **46**, 1729 (2011).

[44] S. Zheng, G. Jiang, J. Su, and C. Zhu, Mater. Lett. **60**, 3871 (2006).

[45] H. Huang, C. Zhu, and W. Liu, Chinese Journal of Chem. Phys. **17**, 161 (2004).

[46] O. Aktas, K. D. Truong, T. Otani, G. Balakrishnan, M. J. Clouter, T. Kimura, and G. Quirion, J. Phys.: Condens. Matter **24**, 036003 (2012).

[47] J. C. E. Rasch, M. Boehm, C. Ritter, H. Mutka, J. Schefer, L. Keller, G. M. Abramova, A. Cervellino, and J. F. Löffler, Phys. Rev. B **80**, 104431 (2009).

[48] M. Winterberger and Y. Allain, Solid State Commun. **64**, 1343 (1987).

[49] K. Aizu, Phys. Rev. B **2**, 754 (1970).

[50] V. Janovec, V. Dvok, and J. Petzelt, Czechoslovak Journal of Physics **25**, 1362 (1975).

[51] G. M. Abramova, G. A. Petrakovskiy, A. N. Vtyurin, J. C. E. Rasch, A. S. Krylov, J. V. Gerasimova, D. A. Velikanov, V. M. Boehm, and V. Sokolov, J. Raman Spectrosc. **41**, 1775 (2010).

[52] O. A. Petrenko, G. Balakrishnan, M. R. Lees, D. McK. Paul, and A. Hoser, Phys. Rev. B **62**, 8983 (2000).

[53] S. Mitsuda, N. Kasahara, T. Uno, and M. Mase, J. Phys. Soc. Jpn. **67**, 4026 (1998).

[54] H. Kadowaki, H. Kikuchi, and Y. Ajiro, J. Phys.: Condens. Matter **2**, 4485 (1990).

[55] N. Terada, Y. Tanaka, Y. Tabata, K. Katsumata, A. Kikkawa, and S. Mitsuda, J. Phys. Soc. Jpn. **75**, 113702 (2006).

[56] Y. Ajiro, T. Asano, T. Takagi, M. Mekata, H. A. Katori, and T. Goto, Physica B **201**, 71 (1994), ISSN 0921-4526.

[57] N. Terada, Y. Narumi, Y. Sawai, K. Katsumata, U. Staub, Y. Tanaka, A. Kikkawa, T. Fukui, K. Kindo, T. Yamamoto, et al., Phys. Rev. B **75**, 224411 (2007).

[58] M. Poienar, V. Hardy, B. Kundys, K. Singh, A. Maignan, F. Damay, and C. Martin, Journal of Solid State Chem. **185**, 56 (2012).

[59] K. Singh, B. Kundys, M. Poienar, and C. Simon, J. Phys.: Condens. Matter **22**, 445901 (2010).

[60] T. Okuda, Y. Beppu, Y. Fujii, T. Onoe, N. Terada, and S. Miyasaka, Phys. Rev. B **77**, 134423 (2008).

[61] M. Frontzek, J. T. Haraldsen, A. Podlesnyak, M. Matsuda, A. D. Christianson, R. S. Fishman, A. S. Sefat, Y. Qiu, J. R. D. Copley, S. Barilo, Phys. Rev. B **84**, 094448 (2011).

[62] M. Frontzek, G. Ehlers, A. Podlesnyak, H. Cao, M. Matsuda, O. Zaharko, N. Aliouane, S. Barilo, and S. V. Shiryaev, J. Phys.: Condens. Matter **24**, 016004 (2012).

[63] M. Poienar, F. Damay, C. Martin, J. Robert, and S. Petit, Phys. Rev. B **81**, 104411 (2010).

[64] M. Soda, K. Kimura, T. Kimura, and K. Hirota, Phys. Rev. B **81**, 100406 (2010).

[65] B. Kundys, A. Maignan, D. Pelloquin, and C. Simon, Solid State Sci. **11**, 1035 (2009).

[66] H. Yamaguchi, S. Ohtomo, S. Kimura, M. Hagiwara, K. Kimura, T. Kimura, T. Okuda, and K. Kindo, Phys. Rev. B **81**, 033104 (2010).

[67] S. Seki, Y. Yamasaki, Y. Shiomi, S. Iguchi, Y. Onose, and Y. Tokura, Phys. Rev. B **75**, 100403 (2007).

[68] T. Nakajima, S. Mitsuda, S. Kanetsuki, K. Tanaka, K. Fujii, N. Terada, M. Soda, M. Matsuura, and K. Hirota, Phys. Rev. B **77**, 052401 (2008).

[69] J. T. Haraldsen and R. S. Fishman, Phys. Rev. B **82**, 144441 (2010).

[70] N. Terada, S. Mitsuda, T. Fujii, K. ichiro Soejima, I. Doi, H. A. Katori, and Y. Noda, J. Phys. Soc. Jpn. **74**, 2604 (2005).

[71] F. Engelsman, G. Wiegers, F. Jellinek, and B. V. Laar, Journal of Solid State Chem. **6**, 574 (1973).

[72] C. Davis, *Lasers and Electro-optics: Fundamentals and Engineering* (Cambridge University Press, 1996).

[73] J. Liu, *Photonic Devices* (Cambridge University Press, 2005).

[74] W. Hayes and R. Loudon, *Scattering of Light by Crystals*, Wiley Interscience publication (Wiley, 1978).

[75] D. Steele, *Theory of Vibrational Spectroscopy*, Studies in Physics and Chemistry (Saunders, 1971).

[76] C. Raman and K. Krishnan, Nature **121**, 501 (1928).

[77] G. Landsberg and L. Mandelstam, Naturwissenschaften **16**, 557 (1928).

[78] R. Loudon, Adv. Phys. **13**, 423 (1964).

[79] A. Anderson, *The Raman Effect: Principles* (M. Dekker, 1971).

[80] Optical Spectroscopy Group, *Facilities at the University of Bath: Introduction to Raman spectroscopy @ONLINE* (2012), URL `http://people.bath.ac.uk/pysdw/newpage11.htm`.

[81] J. Decius and R. Hexter, *Molecular Vibrations in Crystals* (McGraw-Hill, 1977).

[82] J. Ferraro and K. Nakamoto, *Introductory Raman Spectroscopy* (Academic Press, 1994), ISBN 9780122539909.

[83] F. Arecchi, E. Schulz-Dubois, and M. Stitch, *Laser Handbook* (North-Holland Pub. Co., 1972).

[84] M. Cardona and G. Güntherodt, *Light Scattering in Solids II: Basic Concepts and Instrumentation*, Topics in Applied Physics (Springer, 1982).

[85] J. R. Sandercock, Phys. Rev. Lett. **28**, 237 (1972).

[86] A. Dervisch and R. Loudon, J. Phys. C: Solid State Phys. **9**, L669 (1976).

[87] M. H. Kuok, S. C. Ng, and V. L. Zhang, J. Appl. Phys. **89**, 7899 (2001).

[88] M. Musgrave, *Crystal Acoustics: Introduction to the Study of Elastic Waves and Vibrations in Crystals*, Holden-Day Series in Mathematical Physics (Holden-day, 1970).

[89] T. C. Lim and G. W. Farnell, J. Acoust. Soc. Am. **45**, 845 (1969).

[90] G. W. Farnell W. Mason and R. Thurston, *Properties of Elastic Surface Waves*, in Physical Acoustics: Principles and Methods V. 6, edited by W. Mason, R. Thurston (Academic Press, 1970).

[91] J. K. Krüger, L. Peëtz, R. Siems, H.-G. Unruh, M. Eich, O. Herrmann-Schönherr, and J. H. Wendorff, Phys. Rev. A **37**, 2637 (1988).

[92] S. Speziale, F. Jiang, C. Caylor, S. Kriminski, C. Zha, R. Thorne, and T. Duffy, Biophys. J. **85**, 3202 (2003).

[93] L. C. Parsons and G. T. Andrews, AIP Advances **2**, 032157 (pages 12) (2012).

[94] E. Dieulesaint and D. Royer, *Elastic Waves in Solids: Applications to Signal Processing* (J. Wiley, 1980), ISBN 9780471278368.

[95] N. Balshaw, *Practical Cryogenics: An Introduction to Laboratory Cryogenics* (Oxford Instruments, Scientific Research Division, 1996).

[96] S. Omeiri, B. Bellal, A. Bouguelia, Y. Bessekhouad, and M. Trari, J. Solid State Electr. **13**, 1395 (2009).

[97] M. Seikh, C. Narayana, S. Parashar, and A. Sood, Solid State Commun. **127**, 209 (2003).

[98] L. Bjerkan and K. Fossheim, Solid State Commun. **21**, 1147 (1977).

[99] R. Kragler, Solid State Commun. **35**, 429 (1980).

[100] R. Vacher and L. Boyer, Phys. Rev. B **6**, 639 (1972).

[101] V. Rodriguez, M. Couzi, A. Tressaud, J. Grannec, J. P. Chaminade, and C. Ecolivet, J. Phys.: Condens. Matter **2**, 7387 (1990).

[102] R. Doe, *Material properties @ONLINE* (2012), URL http://www.cvimellesgriot.com/products/Documents/.

[103] G. Carlotti, D. Fioretto, G. Socino, and E. Verona, J. Phys.: Condens. Matter **7**, 9147 (1995).

[104] J. Sartwell and C. J. Eckhardt, Phys. Rev. B **48**, 12438 (1993).

[105] T. Kushida and R. W. Terhune, Phys. Rev. B **34**, 5791 (1986).

[106] Y. Shapira, Phys. Rev. **187**, 734 (1969).

[107] G. Quirion, X. Han, and M. L. Plumer, Phys. Rev. B **84**, 014408 (2011).

[108] J. Tolédano and P. Tolédano, *The Landau Theory of Phase Transitions: Application to Structural, Incommensurate, Magnetic, and Liquid Crystal Systems*, World Scientific Lecture Notes in Physics (World Scientific, 1987).

[109] E. Salje, *Phase Transitions in Ferroelastic and Co-elastic Crystals*, Cambridge Topics in Mineral Physics and Chemistry (Cambridge University Press, 1993).

[110] L. Landau and E. Lifshitz, *Statistical Physics*, in Course of Theoretical Physics (Pergamon Press, 1969).

[111] J.-C. Tolédano and P. Tolédano, Phys. Rev. B **21**, 1139 (1980).

[112] W. Rehwald, Adv. Phys. **22**, 721 (1973).

[113] J. Pellicer-Porres, A. Segura, E. Martínez, A. M. Saitta, A. Polian, J. C. Chervin, and B. Canny, Phys. Rev. B **72**, 064301 (2005).

[114] S. P. Pavunny, A. Kumar, R. Thomas, N. M. Murari, and R. S. Katiyar, Mater. Res. Soc. Symp. Proc. 1183, 63 (2010).

[115] C. Julien and M. Massot, Solid State Ionics **148**, 53 (2002).

[116] J. Pellicer-Porres, D. Martínez-García, A. Segura, P. Rodríguez-Hernández, A. Muñoz, J. C. Chervin, N. Garro, and D. Kim, Phys. Rev. B **74**, 184301 (2006).

[117] T. T. A. Lummen, I. P. Handayani, M. C. Donker, D. Fausti, G. Dhalenne, P. Berthet, A. Revcolevschi, and P. H. M. van Loosdrecht, Phys. Rev. B **77**, 214310 (2008).

[118] R. Kajimoto, K. Nakajima, S. Ohira-Kawamura, Y. Inamura, K. Kakurai, M. Arai, T. Hokazono, S. Oozono, and T. Okuda, J. Phys. Soc. Jpn. **79**, 123705 (2010).